University of Padova

Academic year 2018-2019 (796$^{\text{th}}$)

Department of Information Engineering (DEI)

Doctoral thesis in Information Engineering

Multimodal underwater networks

Author: Filippo Campagnaro

Supervisor: Michele Zorzi

To all the people who have always supported me, in particular my grandmothers, my parents, my uncles, my cousins and my beautiful girlfriend.
A tutte le persone che mi hanno supportato durante questi anni, in particulare le mie nonne, i miei genitori, i miei zii, i miei cugini e la mia bellissima ragazza.

Abstract

The recent level of maturity reached by broadband underwater non-acoustic communication technologies paves the way to the development of new applications, such as wireless remote control for underwater vehicles and the possibility to retrieve a massive quantity of data from underwater sensor networks. Indeed, an optical link can support the transmission of high-traffic demanding data (e.g., video streams) in real time, but its reach can hardly exceed 100 meters. Also radio frequency electromagnetic communications can provide a high transmission rate, however, in salty sea-waters their maximum range is less than 7 meters. Therefore, when considering either optical or radio frequency communications, a low-rate long-range acoustic link still has to be employed. Although this backup link cannot be used to transmit high data traffic, it can still keep the minimal quality of service needed to monitor the status of the underwater network. This thesis presents how optical and acoustic communications can be combined in the so-called multimodal networks, by testing such solutions with DESERT Underwater, a simulation and experimentation framework for underwater networks. Optimal routing and data-link layers for multimodal networks are analyzed, as well as a switching algorithm that decides which technology to employ for transmitting the data packets, depending on the type of data and the channel quality. These protocols are evaluated via both simulation and field experiments.

Sommario

Il recente livello di maturità raggiunto dalle comunicazioni non acustiche sottomarine a banda larga ha aperto la strada allo sviluppo di nuove tecnologie, quali telemetrie senza fili per veicoli sottomarini e la possibilità di reccogliere grandi moli di dati da sensori subacquei. Infatti, un link ottico sottomarino può trasmettere una grande quantità di dati in brevissimo tempo, ma il suo range di copertura difficilmente supera il centinaio di metri. Anche i segnali radio hanno la capacità di supportare comunicazioni a banda larga, tuttavia, in acque salate raggiungendo un range massimo di 7 metri. In un'installazione sottomarina, quindi, è sempre necessario combinare un sistema di comunicazione a banda larga con un modem acustico a lunga gittata, da utilizzare come link secondario a basso rate, così da garantire una minima qualità di servizio anche quando il link principale risulti fuori range. Questa tesi presenta come comunicazioni ottiche ed acustiche possono essere combinate per creare una rete multimodale, capace di supportare sia la trasmissione di grosse moli di dati, sia link long range robusti, da utilizzare per inviare messaggi di monitoring essenziali all'operatività della rete stessa. Protocolli multimodali ottimizzati di routing ed accesso al mezzo sono stati implementati, simulati e testati sul campo, usufruendo del framework DESERT Underwater, nella sua versione modificata per supportare la sperimentazione di reti multimodali ottiche ed acustiche sottomarine.

Contents

List of Acronyms

ACK	Acknowledge
APD	Avalanche Photodiode
ASV	Autonomous Surface Vehicles
AUV	Autonomous Underwater Vehicle
BER	Bit Error Rate
CH	Cluster Head
C-CDF	Complementary Cumulative Distribution Function
CDF	Cumulative Distribution Function
CMRE	Centre of Marine Research and Experimentation
CSMA	Carrier-Sense Multiple Access
CTD	Conductivity, Temperature and Depth
FSK	Frequency-Shift Keying
EM	Electro-Magnetic
EETTM	Expected Transmission Time
HDPE	high-density polyethylene

HF	High-Frequency
IM	Instant Message
LF	Low-Frequency
LFM	Linear Frequency Modulated
LED	Light Emitting Diode
LUT	Lookup Table
MAC	Medium Access Control
MACA	Multiple Access Collision-Avoidance
MF	Mid-Frequency
MI	Magneto-Inductive
MTF	Matched Filter
NFNP	Near-Far Node Pairs
NF-TDMA	Near-Far Spatial Reuse TDMA
NTP	Network Time Protocol
OMS	Optimal Multimodal Routing
OMS	Optimal Multimodal Scheduling
PCHIP	Piecewise Cubic Hermite Interpolation
PDD	Packet Delivery Delay
PDR	Packet Delivery Ratio
PER	Packet Error Rate

PHY	Physical Layer
PMT	Photomultiplier
PoC	Proof-of-Concept
RBF	Gaussian Radial Basis Function
RF	Radio Frequency
ROV	Remotely Operated Vehicle
RMSE	Root-Mean Square Error
RSSI	Received Signal Strength Indicator
RTE	Radiative Transfer Equation
SIR	Signal To Interference Ratio
SiPMs	Silicon Photomultipliers
SINR	Signal To Interference and Noise Ratio
SNR	Signal To Noise Ratio
SVM	Support Vector Machines
SVR	Support Vector Regression
TDMA	Time-Division Multiple Access
UWAN	Underwater Acoustic Network
WFS	Wireless for Subsea

List of Figures

List of Tables

Chapter 1

Introduction

When referring to underwater communication and networks, it is usually implied that acoustic technologies are employed for wireless information transfer. Indeed, acoustic communication schemes and systems have been widely researched and studied, and many practical modem implementations and commercial products exist that deliver acoustic communications for general-purpose or niche applications [4].

Acoustic modems are generally characterized by a convenient mix of long transmission ranges, fair reliability and robustness. These features vary depending on the application. For example, in high-reliability scenarios, the user is more willing to sacrifice the link data rate in favor of better protection against channel distortion and errors. On the contrary, non-mission critical high-rate transmission operations such as underwater habitat inspection and surveying may require the transmission of bulk data in the form of underwater video or images, which may be carried out in quasi-real time through a modem that provides a sufficiently high bit rate at the price of lower reliability.

Owing to the advancement of acoustic telemetry and communications [5–7], to their capability to cover different scenarios, as well as to the establishment of the first underwater communication standard [8–10], acoustic communications have become a de-facto solution for several applications, from biology, oceanography and meteorology, to coastal surveillance, anti-submarine warfare, and ecological relief operations. Still, underwater acoustic links are typically limited in terms of bandwidth (which decreases with the maximum coverage distance), and resilience to multipath distortion. Moreover, high bit rates become available only in specific scenarios, and typically over short-range, benign channels. To overcome these issues, other underwater communication technologies based on, e.g., optical [11–19], radio-frequency [20–22] or magneto-inductive signals [23, 24] have been considered. Each of them comes with its own pros and cons: for example, optical signals achieve extremely high bit rates within very short reach (up to a few meters, or a few tens of meters in dark and clear waters), whereas radio-frequency signals incur very strong attenuation in conductive ocean waters, but achieve reasonable bit rates at short range (higher than acoustic systems within a few meters) and are not affected by misalignment issues, unlike optical links.

Given the interest in the development of diverse technologies for underwater scenarios, it has recently been proposed that communication devices may incorporate multiple, non-mutually-interfering transceivers, possibly involving multiple technologies [25–28], into what is referred to as a *multimodal communication system*. This makes it possible for each node to leverage more flexibility in face of a changing communication context, at the price of a generally bulkier system prototype, that requires further integration efforts and additional logic to exploit the advantages of each technology. Relevant examples, in this respect, include the utilization of underwater optical and acoustic communications to enable very high-rate data transfer at short range, or the integration of bandwidth-disjoint acoustic systems that cover, e.g., both high-rate short-distance and low-rate long-distance communications.

In this chapter, we provide an overview of recent advances in the domain of multimodal underwater communications and networks. Specifically, in Section 1.1 we present a review of the state of the art for physical communication technologies per se and, in Section 1.2, their integration into multimodal networks. Finally, in Section 1.3, we present the structure of this Thesis.

1.1 Underwater communication technologies

The prominent technologies for underwater wireless transmission to date are acoustics, RF and optics. In this section, we survey commercial products and research prototypes based on these technologies, and provide some details on their expected performance.

The most studied and used underwater telecommunication technology to date is based on acoustic signals, and provides sufficiently long transmission ranges compared to typical application requirements, fair reliability and robustness. Indeed, the large number of applications that can be potentially supported by underwater acoustic communications has prompted the research and commercial development of several acoustic transceivers. Until recently, such transceivers used to be mostly optimized for long-range communications at a low bit rate. For example, the Benthos ATM 90 [29] can transmit up to 2.4 kbps at 6 km and 15 kbps at 1.5 km; the LinkQuest UWM series covers from 1.5 kbps at 5 km to 17.8 kbps at 1.5 km; the EvoLogics S2CR 7/17 modem [30] can achieve a coverage range of up to 8 km with a maximum bit rate of 6.9 kbps; the AQUATEC AQUAmodem1000 [31] has a maximum transmission range of 10 km with a data rate of 100 bps to 2 kbps; the Sercel MATS3G [32] covers 2.3 km at 16.5 kbps, or 16.5 km at 100 bps; and the

Develogic HAM.NODE [33] can transmit up to 30 km with a bit rate of 145 bps. Further, it has been shown that it may be possible to achieve a communication link of 100 to 400 km at 1 bps in the Arctic [34] using the WHOI MicroModem [35].

Over the last ten years, underwater acoustic communications have emerged also as a practical solution for telemetry, where a higher bandwidth is required for communication at intermediate, order-of-km ranges. Several solutions for this application are available off the shelf, such as the EvoLogics S2CR 18/34 modem [36] (13.9 kbps at up to 3.5 km), and the Subnero modem [37] (15 kbps at up to 3 km). Short-range acoustic communication systems were typically restricted to research purposes. For example, the Hermes FAU acoustic modem [38] is reported to achieve a bit rate of 87 kbps up to 120 m, whereas MIT developed a prototype able to achieve more than 100 kbps up to 200 m in a controlled scenario [39]. Despite the research efforts, neither of [38,39] has developed into a commercial prototype.

Only very recently did short range underwater communications start to be of interest. This is mainly due to an increasing number of foreseen applications for underwater scenarios, with special reference to those involving one or more submerged vehicles that exchange high-rate data streams with fixed nodes or human controllers, and therefore require short-range, high-rate underwater communication systems. Very promising prototypes and some off-the-shelf high-rate acoustic modems have been developed along these lines. Northeastern University developed the SEANet modem prototype [40], able to transmit 41 kbps. Given the current hardware specification, they estimate that the prototype should be able to reach a data rate of 250 kbps by utilizing a bandwidth of 100 kHz at a range of a few meters. BaltRobotics demonstrated low-quality video streaming with their acoustic prototype [41], which communicates at 115 kbps within a range of up to 200 m. EvoLogics also developed their S2CM HS modem [42], which achieves 63 kbps up to 300 m.

Although acoustic modems are the typical solution for underwater digital communications, their bandwidth is very limited; in addition, horizontal transmission in shallow-water scenarios often results in poor, environment-dependent performance, even in short range. For this reason, alternative technologies are being studied that may fit better in some scenarios: the need for high speed communications under water has pushed the realization of electro-magnetic (EM) and optical devices that can transmit, in short range links, data at a bit rate on the order of one or more Mbps. For instance, EM radio-frequency (RF) and magneto-inductive (MI) underwater modems are able to perform broadband communication at very short range. RF communications can achieve high transmission bit rates under water, although their communication range is still very limited. Indeed, the performance of RF modems is immune to most environmental conditions that affect the propagation of acoustic waves, including refraction-inducing temperature/pressure

Table 1.1: List of performance figures declared by the manufacturer for representative acoustic, EM/RF/MI, and optical underwater transceivers

Tech	Manufacturer and model	Range	Bit rate	Tech Pros	Tech Cons
Acoustic	AQUATEC AQUAmodem1000 [43]	10 km	{0.1,2} kbps	Proven technology No need for LOS Range up to 30 km Robust in deep water vertical link Availability of good channel models for simulation purposes	Affected by acoustic noise and multi-path High power consumption Order-of kbps bit rates Poor in shallow waters Affected by sound speed gradient High latency May impact marine life
	Arctic transmission [34]	100 km	1 bps		
	BaltRobotics Prototype [41]	100 m	115 kbps		
	Benthos ATM 90 [29]	{1.5,6}	{15,2.4} kbps		
	Develogics HAM.NODE [33]	30 km	145 bps		
	EvoLogics S2C R series [30, 36, 42]	{0.35,7} km	{64,7} kbps		
	FAU Hermes modem [38]	150 m	87.7 kbps		
	LinkQuest UWM series [44]	1.5,5 km	{5,17.8} kbps		
	MIT Prototype [39]	200 m	100 kbps		
	Northeastern SEANet [40]	10s m	{41,250} kbps		
	Sercel MATS3G [32]	{2.3,16.5} km	{16.5,0.1} kbps		
	Subnero WNC [37]	3 km	15 kbps		
EM / RF / MI	CoSa WiFi [20]	10 cm	{10,50} Mbps	High Bandwidth Low Latency Good performance in fresh shallow water Crosses air/water/ seabed boundaries No need for LOS	Very short range (<10 m) Affected by water salinity and conductivity Few modems available Susceptible to EMI High power MI may impact marine life
	Dalhousie Univ. Prototype [24]	10 m	8 kbps		
	CoSa EF Dipole [20]	{1,8} m	{0.2,1} Mbps		
	INESC TEC Dipole [21]	1 m	1 Mbps		
	WFS Seatooth S200 [22]	{10,40} m	100 bps		
	WFS Seatooth S300 [22]	{4,10} m	{156,25} kbps		
	WFS Seatooth S500 [22]	10 cm	10 Mbps		
Optical	Aquatec AQUAmodem Op1 [11]	1 m	80 kbps	Mbps bit rates High bits per Joule capacity Good performance in clear dark water Low latency	Short range (<100 m) Affected by turbidity, marine fouling and ambient light Needs LOS and good alignment
	ENEA PoC [12]	1 m	{0.25,2} Mbps		
	Keio optical modem [13]	3 m	2 Mbps		
	IST Medusa Optical Modem [14]	10m	{20,200} kbps		
	MIT low power led modem [15]	{6.5,8} m	{10,1} Mbps		
	Penguin Automated Systems [16]	{10,300} m	{100,1.5} Mbps		
	Sonardyne BlueComm 500 [17]	{7,150} m	{500,10} Mbps		
	SPAWAR optical modem [18]	2 m	10 Gbps		
	Sant'Anna OptoCOMM [19]	{5,7} m	10 Mbps		
	Ifremer optical modem [45]	60 m	3 Mbps		
	MIT AquaOptical modem [3]	50 m	4 Mbps		

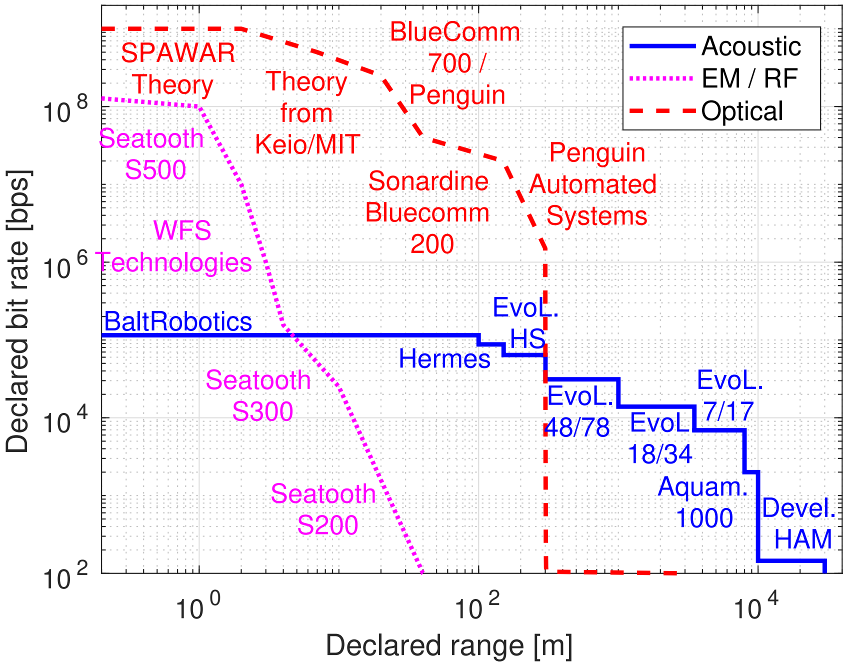

Figure 1.1: Nominal bit rate vs. range for the best among the mature technologies listed in Table 1.1.

gradients, sea state, bottom sediments, etc. However, RF communications suffer from RF interference and are prone to very strong attenuation in salted waters, where the conducibility of the medium is larger than in fresh waters. This can be seen from the bit rates declared for several RF modems and reported in the Table 1.1. For instance, the Wireless for Subsea (WFS) Seatooth S500 [46] RF modem provides a bit rate up to 100 Mbps up to a range of 10 cm. This modem can be employed in docking stations to quickly download data from an autonomous underwater vehicle (AUV) with no need for physical cables [47]. Similarly, the INESC Tec institute of the University of Oporto, developed a dipole antenna prototype [21] to support 1 Mbps communication at 1 m, and the Lubeck University of Applied Science developed a prototype for WiFi communication underwater [20], with a rate of 10-50 Mbps up to 10 cm. The University of Applied Sciences also developed a dipole [20] antenna, to communicate with a rate of 0.2 to 1 Mbps and a range of 1-8 m, depending on the water conditions (i.e., 1 meter in salty water, 8 meters in fresh water). On the other hand, Dalhousie University developed a MI prototype that achieves 8 kbps at 10 m [24], to perform low-rate low-latency communications.

Unlike RF communications (which are very effective at short range and are not affected by multipath or alignment issues), optical communications are more suitable for ranges between 5 and 100 m, especially in deep dark waters. However, turbid and shallow ocean waters represent a challenging environment for optical communication systems. In fact, high turbidity scatters and attenuates the optical field, whereas ambient light may become a significant source of noise, making transmissions close to the sea surface more difficult. For example, the Sonardyne BlueComm 200 [17] achieves a transmission rate of 20 Mbps up to a distance of 200 m, but only in deep, dark waters. The same modem would poorly perform in presence of light noise, due to the saturation of the receiver. Therefore, the same company designed an ultraviolet version of this modem, able to achieve a maximum range of 75 m even in the presence of high ambient light. Another model, the BlueComm 100, can be used in all water conditions, including shallow water daytime, to transmit at a rate of 5 Mbps at a maximum distance of 20 m. Blue and green lights, which have a wavelength of 470 and 550 nm respectively, are the most widely used for underwater optical communication [18]. The light source can be either a laser or a matrix of light emitting diodes (LEDs). The high-power off-the-shelf Sonardyne Bluecomm modem line employs either or both wavelengths, depending on the model [17]. Laser sources can provide a very high bandwidth and a bit rate up to 0.5 Gbps (as is the case, e.g., for the Bluecomm 500). Still, lasers need very good alignment between the transmitter and the receiver. LED-based modems like the Bluecomm 200 offer a tradeoff in this respect, with a lower bit rate (tens of Mbps) with much looser alignment requirements. Another commercial off-the-shelf optical modem is the AQUAmodem Op1 [11], which achieves 80 kbps at 1 m. Although its performance is not as high as that of the Bluecomm line, it has a lower power consumption and a different application target. Customized LED-based optical modems are also developed by Penguin ASI [16, 48]; the maximum performance of their system is order-of-100 Mbps at hundreds of meters, but comes at the price of very bulky and expensive modems that are only suitable for extremely specialized applications. Data muling applications often rely on small and cost-effective AUV designs [49]. To reduce costs, these AUVs mount a custom optical modem built using low-cost off-the-shelf components for high-rate communications [12, 14, 19], rather than a commercial one.

The details of the modems presented in this subsection are summarized in Table 1.1. A summary of the bit rate as a function of range for current state-of-the-art optical, electro-magnetic, and acoustic modems is provided in Fig. 1.1, where we can observe that optical technologies are the preferred choice up to a distance of about 100 m (that might be reduced to 30:50 m, depending on the water conditions), whereas acoustics would be the best performing technology from that point onward. We also note that RF modems are consistently outperformed by optical or acoustic modems, and have the only advantage that RF transmissions are omnidirectional (unlike optical ones) and not prone to environmental characteristics (unlike acoustic ones). For this reason in this thesis, from here onwards, we consider only acoustic and optical multimodal networks. The acoustic and the optical underwater channels are briefly described in Section 1.1.1 and 1.1.2, respectively. Although high frequency acoustic modems can provide bitrates up to few hundreds of kbps, in very short ranges they are topped by optical modems. In addition, optical systems, when in range, usually offer a very stable link, while high frequency acoustic modems suffer of multipath and wind noise in shallow water scenarios. Still, acoustic modems should be included in a multimodal system, as optical links are affected by different environmental conditions, such as water turbidity and sunlight noise, that do not disturb acoustic communications. Therefore, in such challenging scenarios for optical communications, high frequency acoustic modems can at least provide a data rate that is high enough to perform, for instance, the transmission of a slide-show like low quality video streaming composed by still-frames. In the case neither optical nor high frequency acoustic are in range, instead, medium and low frequency acoustic modems should be employed to at least maintain the system connectivity, although with a significant drop in performance.

1.1.1 Basics of underwater acoustic communications

Substantial differences exist between long-range deep water acoustic communications and short-range shallow water acoustic communications. Since multimodal systems are used for relatively short ranges of a few km, we focus on the latter. The shallow water underwater channel is a time-varying frequency-selective channel, characterized by a long delay spread [50] and a coherence time on the order of tens of ms [5]. Given the low transmission rate (common systems achieve a few kbps [51]), such long channel and short coherence time pose a challenge for channel equalization [52]. Since the sea surface is continuously in motion, individual channel taps are affected by a Doppler shift that, depending on the carrier frequency, may vary up to tens of Hz [53]. Due to the low sound speed (roughly 1500 m/s), this Doppler shift affects the duration of the received signal and, therefore, cannot be fully compensated by a phase-locked loop. Instead, interpolation is generally required [54]. The key parameters to predict the integrity of acoustic communications are the number of channel taps, their power and propagation delay, and the variation of these characteristics over time.

The power attenuation in the channel is governed by propagation loss and absorption loss. Propagation loss is a function of the channel structure. Acoustic propagation is a highly non-linear process [55], which may create convergence zones where an acoustic signal is clearly received, as well as shadow zones where signals are much more attenuated than what is expected from the free space spherical propagation law [56]. Moreover, the propagation of sound between layers characterized by different sound speed values (mostly created by changes in the water pressure or temperature) refract the sound wave and may lead to additional attenuation or convergence [57]. Absorption loss is a function of the carrier frequency of the transmitted signals, and is mainly affected by the water temperature, salinity, and acidity [57]. Since propagation loss and absorption loss cannot be separated at the receiver, the overall attenuation level is used to predict the channel conditions.

Besides the channel impulse response and the power attenuation, acoustic communications is also highly affected by the channel ambient noise. The ambient noise is usually modeled as an isotropic colored Gaussian noise whose power spectral density reduces by 10 dB per octave [58]. However, the acoustic ambient noise may also include location-dependent, non-isotropic noise which may affect the performance of acoustic communications. The sources of such noise are acoustic transmissions from nearby ships, short noise transients from marine fauna such as snapping shrimps, and wide-band noise from breaking waves, especially when the receiver is close to the water surface [59]. Thus, besides the noise level itself, the time-varying characteristics of the noise also affect the performance of acoustic communications.

The SNR (in dB) of a transmission performed at a frequency f_a over a distance d between the transmitter and the receiver is found as [57]

$$SNR(d, f_a) = 10 \log_{10} \left(\frac{P_a}{N(f_a)\, \delta f_a} \right) - A(d, f_a)\,, \tag{1.1}$$

where P_a is the source power, $N(f_a)$ is the noise level, $A(d, f_a)$ is the power attenuation in dB, and δf_a is a narrow band around f_a where we can assume $A(d, f) = A(d, f_a)$ and $N(f) = N(f_a)$.

1.1.2 Basics of underwater optical communications

Light traveling in the water interacts with the particulates and dissolved materials within the water as well as the water molecules themselves. These interactions produce light attenuation (modeled via an attenuation rate per unit length traveled by the wave, and termed c) that will determine the underwater light field, or radiance, denoted as L, and defined as the measure of light energy leaving an extended source in a particular direction. The definition of radiance is given by flux per unit area per unit of solid angle in a given direction in W m^{-2} sr^{-1} such that

$$L = \frac{\varphi}{\Omega A \cos(\theta)}\ , \tag{1.2}$$

where φ is the radiant flux or power defined as the radiant energy flow per unit time (measured in W), θ is the angle between the surface normal and the specified direction, A is the area of the source (m^2) and Ω is the solid angle (sr) subtended by the measurement.

The parameters L and c are related through the radiative transfer equation (RTE), which relates the apparent and inherent optical properties of the medium [60]. The light attenuation rate c, the optical absorption rate a, and the loss rate due to scattering processes b are related as

$$c = a + b \; . \tag{1.3}$$

If the inherent optical properties of the medium depend only on depth, inelastic processes are ignored, and there are no internal sources, the time-dependent RTE is described as [61]

$$\begin{aligned} \cos\theta \frac{dL\left(z,\lambda,\theta,\phi\right)}{dz} =& - c(z,\lambda)L(z,\lambda,\theta,\phi) + \\ &+ \int_{4\pi} \beta\left(z,\lambda,\theta',\phi' \rightarrow \theta,\phi\right) L\left(z,\lambda,\theta',\phi'\right) \, \mathrm{d}\Omega' \, , \end{aligned} \tag{1.4}$$

where $\beta(\,\cdot\,)$ is called the volume scattering function and describes how the medium scatters light per unit length and solid angle. The polar angle θ and the azimuthal angle ϕ of a spherical coordinate system specify the scattered light direction, whereas the coordinates (θ', ϕ') inside the integral convey the direction of the incident light. The integration limit denotes that the integral is computed over the unit sphere surface, and we recall that $\mathrm{d}\Omega' = \sin\theta' \, \mathrm{d}\theta' \, \mathrm{d}\phi'$. At a given depth and wavelength, L is usually referred to as the radiance distribution. The first term on the right hand side of (1.4) represents the loss of radiance in the direction (θ, ϕ) due to scattering and absorption, while the second term provides the gain in radiance from all other directions (θ', ϕ') into the direction (θ, ϕ). Analytical solutions of the RTE (1.4) are possible only if scattering is negligible. Otherwise, as in the present work, (1.4) must be solved numerically. The most complete and accurate method to do so is the successive-orders-of-scattering solution used in radiative transfer modeling software such as Hydrolight [61].

Because radiance is difficult to measure, most light field measurements involve integrals of the radiance distribution. For this study, we are interested in scalar irradiance, E_0, i.e., the irradiance measured over all directions, obtained by integrating radiance over the whole sphere as

$$E_0(z,\lambda) = \int_{4\pi} L(z,\lambda,\theta,\phi) \, \mathrm{d}\Omega \; . \tag{1.5}$$

In the case of light transmission for underwater optical communications, this will be affected by the ambient light, considered as noise. The ambient light noise power N_A is obtained as

$$N_A = \left(S \cdot E_0 \cdot A_r\right)^2 \, , \tag{1.6}$$

where S is the sensitivity of the receiver and A_r is the receiver area.

1.2 Underwater multimodal networks

The concept of multimodal underwater communication is, in some way, akin to the deployment of multiple radio systems on board the same node in the context of terrestrial radio networks. In the underwater environment, one of the first multimodal systems was employed in [25], which presents a data muling system where an AUV equipped with acoustic communications processes the video feed of an underwater camera to align with underwater sensors, and downloads data through optical communications. Acoustic communications are employed for control, synchronization and parameter setting.

The variable-depth moored acoustic nodes presented in [26] can surface to exploit radio communication links. The system balances between the energy required for the node to reach the surface and the energy consumption of underwater acoustics, and chooses either strategy depending on data transmission requirements. The autonomous underwater exploration device presented in [62] can rely on different underwater communication capabilities. The authors discuss the tradeoffs between frequency-shift keying (FSK)-based modem technology and custom low-cost modems [63].

A notable feature of multimodal systems is that the composition of multiple powerful physical layers may not be necessary to achieve good performance. For example, [64] considers a multimodal optical/acoustic system, where the optical part is implemented through an infrared modem assembled from inexpensive off-the-shelf components. The optical modem provides an alternative communication channel, and is shown to substantially improve the performance of underwater acoustic networks in terms of synchronization and TCP connections.

MURAO [65] is the first routing protocol to employ multimodal optical and acoustic communications. It assumes a clustered underwater network structure, where acoustic communications enable cluster formation and management, whereas intra-cluster communications are carried out using optical systems. Q-learning [66] is employed to set up and iteratively improve the routing structure and topology.

The above approaches are tailored to specific scenarios, or offer solutions for stable networks. However, they may suffer from bottlenecks and delays in realistic multimodal networks, where PHY performance changes over time and space due to mobility and environmental conditions, and does so in different ways for different PHYs. A scheduling mechanism that can optimize the use of the multimodal network's resources is therefore needed. To address the above challenges, we propose the optimal multimodal scheduling (OMS) protocol [67]. OMS manages transmissions through any set of PHYs by jointly setting transmission time slots in a per-technology time-division multiple access (TDMA) fashion, and divides the data load among the PHYs to optimize link utilization and transmission delay. In addition, OMS organizes transmission slots to favor packet routing and enforce a fair number of transmission opportunities per node. We tested the performance of OMS against benchmark schemes in numerical simulations and in a sea experiment using multimodal nodes encompassing different acoustic PHYs. The results show that OMS achieves better throughput, packet delivery delay, and fairness in resource allocation.

OMR [68] has been proposed as an optimal approach to convey data packets through a converge-casting network topology, in such a way that the utilization of multimodal links is highest while respecting the forwarding capabilities of intermediate relays, and while ensuring some degree of fairness to all nodes. Optimal decisions are made in a distributed fashion. The MARLIN routing protocol for underwater networks [69] relies on a reinforcement learning approach to identify the multihop routes that provide an overall minimum delay or highest degree of reliability through an underwater network. The system learns both the optimal hop sequence and which of the multiple available acoustic devices should be used by each relay. OMR and OMS are detailed in Chapters 5 and 6, respectively.

In the hybrid optical/acoustic multimodal networks considered in [70], real-time video streaming is serviced through optical channels, whereas acoustic communications provide a feedback channel to, e.g., send acknowledgments and coordinate the alignment of optical modems. Acoustic communications also provide a fallback solution in turbid waters, where optical systems would not be able to establish reliable links. Such a hybrid solution is shown via simulations to outperform both optical and acoustic communications alone.

In [71], the authors consider a mobile AUV in the spirit of [25], and propose to optimize the path of the AUV in order to maximize the value of the information retrieved from the sensor nodes, which loses value as time goes by. The AUV uses optical communications to retrieve data, whereas acoustic communications are employed to notify the AUV of new data being generated.

The efficient management of multimodal underwater links often requires to be able to automatically switch among different communication technologies using only locally available information. In the context of the wireless remote control of a remotely operated vehicle (ROV), [28, 72] provide a few policies that achieve such switching. In [73], more complex scenarios are implemented using the free-access DESERT underwater framework [74] and evaluated in a diver cooperation scenario.

The authors in [49] propose hybrid acoustic/optical devices to be employed in the coordination of swarms of AUVs, as well as to transfer information among the members of the swarms. The custom design of both the acoustic and the optical modem is also discussed. The authors in [75] exploit a custom re-configurable underwater acoustic modem to implement a “bilingual” modem concept. Such modem switches between two available modulation schemes, namely the NATO standard JANUS [9, 10] and a higher-rate MFSK modulation format. JANUS provides a first-contact scheme and a robust fallback, whereas the MFSK scheme was used to achieve higher data rates when channel conditions so allowed.

The optimal assignment of data traffic to different communication technologies in a multimodal underwater network is related to the design of multipath routing schemes in multihop multi-channel networks [76]. The motivation behind these protocols is typically to exploit additional network resources to improve reliability, increase throughput or achieve load balancing across different sections of a wireless network. The problem implies several challenges related to interface assignment and switching, routing metric design, and mobility [77]. In the literature on terrestrial radio networks, few works design protocols to optimally assign a data flow to a specific path in a network of multi-channel nodes [78–80].

Among basic schemes, the CA-AODV [78] protocol proposes to combine channel assignment with AODV [81] using one channel to exchange route requests and reply packets. Thus, the route discovery mechanism automatically finds the information required to make flow assignment decisions. Hyacinth [79] is a protocol for wireless mesh networks that spans trees from gateway nodes and routes data based on either hop count, gateway link capacity or minimum residual bandwidth over a given path. The multi-radio link quality source routing protocol chooses forwarding paths via an expected transmission time metric [80]. A very similar approach is employed in [82] to find multipath routes and optimally allocate video data flows over a wireless mesh network.

The terrestrial radio approaches above focus on relatively stable wireless networks and on the optimization of link reliability or load balancing for large networks. Unlike these approaches, underwater networks are commonly small and have a limited number of hops. The main challenge with underwater multimodal routing is how to combine transmissions over the technologies available to a node in the settings of poor physical layer reliability, where both transmissions and acknowledgments often fail.

The approach and metric proposed in [80] are often considered in the literature as a benchmark for performance evaluation of multipath, multichannel routing protocols (e.g., see [79, 82]). We will also consider a version of the method in [80] as a benchmark in our simulation study, as described in Chapter 5.3.1.

1.3 Structure of the Thesis

The remainder of this thesis is organized in other nine chapters. Chapter 2 presents a protocol that leverages the long propagation delay and the near-far effect of the acoustic networks: these properties, usually treated as disadvantages, can actually be exploited to design MAC protocols where multiple nodes can transmit at the same time without colliding at the receiver. The near-far approach results in an improved temporal use of the channel with respect to what is normally achieved. Chapter 3, instead, describes the underwater optical channel, and how it can be simulated with high reliability, by integrating analytical models with field measurements. This model has been included into the DESERT Underwater network simulator, enabling the possibility to perform simulations of multimodal acoustic and optical networks. In Chapter 4, the statistical relationship between optical and acoustic channels is analyzed, by training a support-vector machine with data retrieved during 12 days of field campaign in open and littoral sea and ocean waters. The results show that it is feasible to accurately predict the SNR of optical links based upon acoustic measurements and a suitable classifier.

Optimal multimodal routing and optimal multimodal scheduling protocols are presented in Chapters 5 and 6, respectively. Both protocols have been evaluated via simulation and real field experiments. Chapter 7 describes how a remotely operate vehicle can be controlled with a multimodal optical and acoustic wireless remote control system, to overcome constraints imposed by use of umbilicals. Chapter 8, instead, states how the range of this remote control can be extended up to 30 km with a multimodal and multihop network, composed by two different types of acoustic modems working at different frequencies. The other topics addressed during the research activity have been presented in Chapter 9. Finally, in Chapter 10 we draw our concluding remarks.

Notes

Part of the content of this chapter has been published in [83].

Chapter 2

Leveraging the near-far effect in underwater acoustic network

2.1 Introduction

The design of medium access control (MAC) protocols for underwater acoustic networks (UWANs) faces several challenges [7, 84], usually summarized into the concept of space-time uncertainty. The significant delays induced by the low propagation speed of underwater acoustic signals imply that channel access decisions are not optimal when informed only by instantaneous channel sensing. Rather, a considerable amount of wait time would be required to safely gain channel access and ensure collision avoidance [85]. Otherwise, packet collisions are possible, where a collision is defined as the superposition of one or more packets at the receiver, possibly impeding the correct reception of some or all of them.

We consider time-division multiple access (TDMA)-based scheduling, which largely fits UWANs with demand for high packet transmission rates [5]. Our system model includes network nodes transmitting information to a sink, as well as exchanging information among themselves. Considering that UWANs serve for status exchange of information as well as for transmitting occasional data, we consider two types of traffic demands: *status packets*, whose target is the sink, and whose minimum reception rate must be guaranteed; and *opportunistic packets*, whose destination can be any node and that are randomly generated and handled on a best-effort basis. This general framework can be embodied by a number of applications, e.g., a team of divers and/or AUVs performing underwater work. This can be the case for rescue operations for a damaged ship, oil recovery from a wrecked tanker, or industrial work to install or maintain pipes, infrastructures, and communication lines. In all cases, the divers send periodic (P) status reports to a surface vessel, which serves as a sink; in addition, they exchange opportunistic (O) control packets to coordinate and assist one another. The former are served in a contention-free fashion, whereas the latter are transmitted less frequently and at random times, and are served in an opportunistic way. Fig. 2.1 shows a diagram of this scenario, where some divers are connected to a "cluster head" (CH) diver: the two divers on the left are sending P messages to the CH; at the same time, another diver on the right transmits an O message to its peer further down.

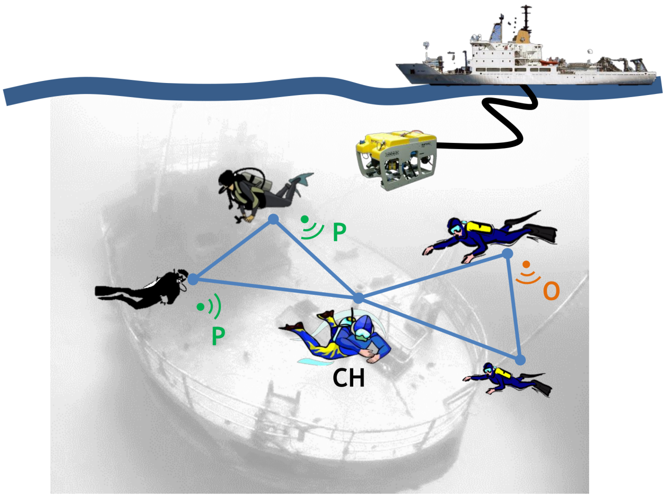

Figure 2.1: Sketch of our considered application scenario.

In TDMA, to guarantee collision-free reception, each time slot includes a guard interval whose duration is given by the maximum propagation delay in the network plus an additional guard period to compensate for possible clock drifts. Since, in underwater acoustics, propagation delays are much greater than clock drifts, the network performance is weakly affected by poor time synchronization among the nodes. Still, in TDMA the channel utilization is low. To overcome this problem, a possible solution is offered by spatial-reuse TDMA channel access schemes. Under some assumptions, such as the knowledge of the propagation delays among the nodes [86, 87] or of the local network topology [88], these schemes substantially improve the channel utilization by allowing mutually harmless communication sessions to co-exist. This is achieved either by leveraging on the propagation delays to decouple reception over time at the receiver, or by exploiting different attenuation figures over different distances to ensure that no harmful collisions take place at active receivers.

One of the most common sources of collisions is the so called near-far effect, whereby a node located farther from the receiver is jammed by a closer node. This scenario is very common in UWANs, where the large attenuation per unit distance traveled by an acoustic signal is likely to create near-far scenarios. In the available literature on MAC protocols for UWANs, the main approach is to avoid near-far events by designing protocols so that the collision of a signal by a "near" node on the transmission by a "far" node can be avoided [87], or at least limited to a minimum. The latter has been achieved, e.g., via power control [89], orthogonal signals [90] spatial diversity [91], or interference alignment [92]. On the contrary, in this chapter we argue that near-far scenarios are in fact a resource that can be leveraged to improve the performance of UWANs, e.g., via multipacket reception techniques using successive interference cancellation. Yet, as we show in our field experiment, even when interference cancellation is limited or unavailable, since transmissions from a farther node do not substantially affect the reception of signals from a closer node, the two nodes can still be allowed to transmit simultaneously, as long as the destinations of the two nodes are different.

Allowing transmissions of near-far node pairs (NFNPs) to different destination nodes in a spatial-reuse TDMA fashion opens the possibility to overcome one of the most limiting assumptions in scheduling UWANs, namely, that the network can support the transmission of only a single packet type. Specifically, while most existing channel access protocols allocate transmissions considering either contention-based communications (e.g., Carrier-Sense Multiple Access–CSMA, and Multiple Access Collision-Avoidance–MACA) or contention-free communications (e.g., TDMA and spatial-reuse TDMA), opportunistic transmissions of NFNPs allow different communications patterns to co-exist. In particular, the messages that are not subject to stringent delivery constraints can be allocated for opportunistic transmissions, so that they do not have to wait for pre-assigned slots; similarly, scheduled transmissions with tighter constraints can co-exist with opportunistic traffic without being harmed by the latter.

In this chapter, we describe a scheduling MAC algorithm for both contention-free and opportunistic transmissions. Our algorithm, referred to as the *near-far spatial reuse TDMA* (NF-TDMA), maximizes the network throughput and minimizes the delivery delay by allowing multiple nodes to transmit in the same time slot. To that end, given information on the network topology and the NFNPs (e.g., provided by an initial topology discovery phase), we formulate an optimization problem that yields collision-free scheduling for a target minimum packet transmission rate. Moreover, we allow each transmitting node to locally choose the best communication type for each time slot, and provide it with guidelines to prioritize transmissions.

To the best of our knowledge, together with our recent work [93] about leveraging on the near-far effect in handshake-based MAC protocols, our NF-TDMA algorithm is the first attempt to exploit the near-far effect to achieve a performance improvement in underwater acoustic networks, and the first attempt to explicitly consider this phenomenon in an optimized scheduling protocol. We prove our argument both in simulations and in a sea experiment, in order to show the practicality of our approach. Our contribution is three-fold:

1. A method to exploit the near-far effect to increase the network throughput, even when all nodes are directly connected to the same sink and spatial reuse is seemingly not possible, and even without interference cancellation capabilities;
2. A scheduling algorithm to service both contention-free and opportunistic communications, each having different objectives;
3. A combination of a centralized schedule with a distributed one to obtain an optimal channel utilization for a given interference cancellation capability of the system.

We compare our results against those achieved by a basic TDMA protocol, as this is the solution all currently available collision-free spatial-reuse TDMA schemes would fall back to when all nodes are directly connected to a single sink. Our results show that our NF-TDMA achieves much better throughput and delivery delay. This comes at a slight cost in terms of fairness in opportunistic transmission chances. These results are verified and our assumptions are validated in a field experiment, where we demonstrate our algorithm in real time using off-the-shelf acoustic modems.

The remainder of this Chapter is organized as follows. In Section 2.2 we survey relevant related work in the area. Section 2.3 introduces the system model along with some assumptions and preliminary definitions of the relevant network metrics considered in this chapter. Section 2.4 proposes our NF-TDMA protocol and the algorithm to obtain a scheduling solution given a network topology. Section 2.5 shows preliminary simulation results, which are instrumental to proving the superior capabilities of our protocol with respect to plain TDMA before testing our solution in a field experiment (Section 2.6). Finally, we offer some concluding remarks in Section 2.7.

2.2 Related works

To compensate for the low channel utilization of TDMA, UWAN-MAC [94] proposes to schedule sleep/transmit/receive epochs among the nodes via a network discovery mechanism, and to adaptively shift these epochs over time in case joining nodes cause receive-receive collisions. Similarly, I-TDMA [95] proposes to postpone colliding transmission schedules by assuming that the propagation delay is known (something which was not strictly needed in UWAN-MAC). However, these solutions are prone to uncontrolled drifts in the sleeping schedules of the nodes [96]. The authors in [97] propose a centralized and a distributed scheduling scheme. The former prioritizes the nodes that need to occupy the channel for a shorter amount of time. The latter is based on clustering and on centralized scheduling in each cluster. Clustering is employed also in [98], where a hierarchy of two nested TDMA schedules is proposed: the outer one is used for surface radio/acoustic gateway stations, whereas the inner one is used by underwater nodes. Mobility is supported by reserving a pre-allocated slot for opportunistic cluster membership packets. In [99], it is proposed to distribute 2-hop topology information and to schedule nodes based on their ID, by adapting the TDMA frame length to the transmission requirements, whereas [100] bases its scheduling choices on a priority list known a priori and on a tight scheduling of the nodes without guard times in each slot. The authors in [101] take a different approach by assuming that time is slotted and that each node in a single broadcast domain network can transmit in any slot with a given probability. A linear program is solved to compute the optimal transmission probabilities for all nodes. The advantage of this approach over a uniform transmission probability assignment is shown to increase with increasing packet size. Under the same system assumptions, the approach in [102] also proposes heuristic policies based on the exchange of neighboring node counts. A hybrid protocol that alternates TDMA-scheduled slots and unscheduled slots is proposed in [103], where the slot length also includes the maximum propagation delay.

Exploiting the propagation delay to avoid receiver-side collisions has been shown to be a promising approach in [104]. The STUMP protocol [105] extends this approach by scheduling transmissions in a multihop network so that all types of primary conflicts can be avoided. The design assumes that the nodes are aware of propagation delays and transmission requirements in their 2-hop neighborhood. STUMP-WR [106] adds routing to the picture, which operates on links instead of rings and therefore requires only the solution of a simpler link scheduling problem. The ST-MAC protocol [107] solves a similar space-time scheduling problem by avoiding conflicts and including a capture model. The optimal solution is compared to a simpler heuristic where the node whose transmission would be completed last is scheduled first. DOS [108] further extends ST-MAC with an on-demand mechanism to update transmission schedules over a hierarchical topology. The approach is shown to outperform ST-MAC when the latter is re-designed to improve fairness. The approach in [109] introduces a time-evolving conflict graph which is exploited by centralized algorithms to schedule transmissions under different cost functions, leading to fair, traffic-based or most-heavily-loaded-first scheduling. Scheduling in the broader context of a converge-casting network was considered in [110–112]. In particular, [110] presents a Receiver-Oriented Sleep Scheduling (ROSS) protocol, where the network is designed to operate data fusion. Sibling nodes on the converge-casting tree coordinate with their parent nodes in case of scheduling conflicts, and the coordination process is allowed to escalate upstream until the conflict is resolved. Similarly, [111] organizes the scheduling of transmissions over the converge-casting tree tier by tier, in a way that reduces the latency of the aggregation process. A number of combinations between scheduling and routing policies are compared in [112], where the best performance was yielded by fair scheduling coupled with a relay selection policy that favors the less interfered node.

The work in [113] takes a fundamental approach by showing that optimal schedules in any network with a single broadcast domain are status, and that the maximum achievable throughput is $N/2$, where N is the number of nodes. The authors provide a computationally efficient algorithm to obtain good schedules. The same result has been shown to extend to complex topologies in [114]. Based on the above work, [115] adds realistic modem constraints and shows that an implementation of the scheme proposed in [113] actually works in practice in simple topologies. The approach in [88] further observes that any scheduling approach which relies on topology and propagation delay information may incur excessive overhead or even fail when such information is subject to change due to even limited mobility or channel variability. For this reason, a topology-transparent schedule is taken as the basis to create a topology-based schedule which is also robust to topological changes. The results are successfully tested both in simulations and in a field experiment. In [93], we describe a heuristic method to limit the exposed terminal problem by allowing near and far nodes to engage in simultaneous communication sessions to different destinations. However, this approach was tailored to handshake-based communications, and is not suitable for networks with heavy traffic requirements such as those considered here.

Unlike all previous approaches, in this chapter we argue that not all collisions are harmful, and that near-far communication scenarios can be in fact exploited to decouple interfering transmissions. As we show in our field experiment, such opportunity is available even when the system does not have interference cancellation capabilities. This goes to the benefit of network performance, as a spatial reuse algorithm can afford to schedule transmissions more often, on average. With the above in mind, we propose a scheduling algorithm that is specifically designed to exploit near-far transmission opportunities. Additionally, our algorithm supports the management of packets of different types, with different service constraints. We introduce our scheduling design by starting from some preliminary definitions in Section 2.3.

2.3 System model

In this section, we introduce the system model and the objectives for resource allocation considered in this work. Our system includes a group of nodes (e.g., divers or submerged devices) represented by a set $\mathcal{N} = \{i_1, \ldots, i_{N-1}\}$ of nodes. Each of the nodes is directly connected to a single node, i_0, referred to as the *cluster head*, or *sink*. However, a node $i_n \in \mathcal{N}$ may or may not be connected to a node $i_m \in \mathcal{N}$, $m \neq n$. Each node in $\mathcal{N}$ is assumed to always have a status packet to transmit to node i_0, and occasionally may also have an opportunistic packet to transmit to one of its one-hop neighbor nodes (including node i_0). Status packets convey the status of the node (location, energy level, air supply, mission progress, etc.) and are to be transmitted in a contention-free manner. In addition, status packets are transmitted and should be received by the cluster head at least once every T_L seconds. On the contrary, the transmission of opportunistic packets takes place randomly. Since we aim to reduce the transmission delay of opportunistic packets, as long as the minimal rate for the transmission of status packets is maintained, the transmission of opportunistic packets is preferred. All nodes are allowed to send opportunistic packets to any node, whereas status packets are transmitted by all nodes except the cluster head, which is instead the common destination. A node is assumed to always have a status packet to transmit, whereas opportunistic packets are less frequent.

2.3.1 Problem definition

We are interested in a collision-free TDMA-based periodic transmission schedule for each node $i_n \in \mathcal{N}$ with respect to the cluster head. The time frame of this schedule consists of time slots allocated to nodes for transmissions. The time frame is set by the cluster head node, i_0, which in turn broadcasts the solution to its one-hop neighbors, i.e., to the nodes in $\mathcal{N}$. While this is a centralized solution, the special position of node i_0 ensures fast and reliable sharing of the scheduling solution with all nodes. To ensure that the network can easily adapt to the motion of nodes, we target a scheduling solution with low communication overhead. The nodes are assumed to only evaluate their one-hop neighbor list and share it with the sink node. An example of a process to obtain this information is presented in [116], where nodes transmit in a pre-determined manner during the network setup phase, such that by receiving packets, a node can build its own one-hop list. Given one-hop information, the sink node evaluates the network topology and replies only with the schedule. Moreover, we allow all nodes to locally decide which packet type (i.e., either status or opportunistic) to transmit. That is, the nodes can maintain their own packet queue and service it locally. With respect to the network performance, we are interested in maximizing the network throughput, minimizing the transmission delay, and obtaining high network fairness. In the following we define these objectives.

Throughput – Status packets

Let us assume that a status packet consists of N_{bit} bits. Also, call x_n^{s} the number of successfully received status packets sent by node i_n to node i_0 over a given time interval of duration T seconds. Since every node always has a status packet to transmit to node i_0, the network throughput of status packets is defined as

$$\rho_{\text{through,s}} = \frac{1}{T} \sum_{n=1}^{N-1} x_n^{\text{s}} N_{\text{bit}} \ . \tag{2.1}$$

Let $t_{n,j}^{\text{s}}$ be the time when the jth status packet of node i_n is received by the sink. Considering the objective of receiving status packets at least once every T_L seconds, we maximize $\rho_{\text{through,s}}$ under the constraint that

$$t_{n,j+1}^{\text{s}} - t_{n,j}^{\text{s}} < T_L, \ \forall n, j \ . \tag{2.2}$$

In this work we do not directly optimize the fairness in scheduling status packets. Instead, we consider a *minimum fairness* of status packets by defining a vector $\mathbf{c}$ of minimal number of receptions over one time frame of the schedule.[1]

$$x_{n,0}^{\text{s}} \geq c_n, \ \forall n \ . \tag{2.3}$$

We choose $c_n \geq 2, \ \forall n$, such that each node is allocated at least two packets to transmit. Hence, as long as the time frame of the schedule is smaller than T_L, a node can allocate both status and opportunistic packets in the same time frame.

Scheduling delay – opportunistic packets

Define $x_{n,m}^{\text{o}}$ as the number of opportunistic packets generated by node i_n and successfully received by node i_m, and define a set $\mathcal{M}_n$ such that $m \in \mathcal{M}_n$ if and only if $x_{n,m}^{\text{o}} > 0$. Also let $t_{n,m,j}^{\text{o}}$ be the delay from the time an opportunistic packet j is transferred to the MAC layer of source i_n until it is successfully delivered to its destination i_m. That is, $t_{n,m,j}^{\text{o}}$ captures both the end-to-end transmission delay and the queuing delay. The average per-node scheduling delay of opportunistic packets is defined as (recall that the cluster head can also send opportunistic packets)

$$\rho_{\text{delay,o}} = \frac{1}{N} \sum_{n=0}^{N-1} \frac{1}{|\mathcal{M}_n|} \sum_{m \in \mathcal{M}_n} \frac{1}{x_{n,m}^{\text{o}}} \sum_{j=1}^{x_{n,m}^{\text{o}}} t_{n,m,j}^{\text{o}} \ . \tag{2.4}$$

Fairness – opportunistic packets

We measure fairness by comparing the differences in the per-node throughput of the opportunistic packets. By applying Jain's fairness index [117], we

---

[1] Throughout this chapter, we indicate vectors via bold lower-case letters (e.g., $\mathbf{a}$), matrices via bold upper-case letters (e.g., $\mathbf{A}$), and matrix/vector entries via indices subscripted to the non-bold version of the same matrix/vector name (e.g., a_j, $A_{x,y}$).

define the throughput fairness of opportunistic packets to be

$$\rho_{\text{fair,o}} = \frac{\left(\sum_{n=0}^{N-1} \sum_{m=0, m\neq n}^{N-1} x^{\text{o}}_{n,m}\right)^2}{N \sum_{n=0}^{N-1} \left(\sum_{m=0, m\neq n}^{N-1} x^{\text{o}}_{n,m}\right)^2} . \tag{2.5}$$

2.3.2 Topology information

With respect to the cluster head, i_0, the information about the *receiver-side topology* is given in the form of an $(N-1) \times (N-1)$ matrix $\mathbf{M}$. Specifically, the diagonal elements of $\mathbf{M}$ represent the direct links between node i_0 and its neighbor nodes, while the rest of the matrix entries indicate the possibility of receiving in the presence of interference from another node. More specifically, the (x, y)th entry, $M_{x,y}$, equals 1 if node i_0 can successfully receive a packet from node i_x even while node i_y is transmitting, and 0 otherwise.[2]. To form $\mathbf{M}$, we require a probability matrix $\mathbf{P}$ whose entry $P_{x,y}$ represents the probability of successful reception of packets from node x while node y is transmitting. Then, $M_{x,y} = 1$ if $P_{x,y} \geq \theta$, where θ is a target packet reception probability. Both matrices $\mathbf{M}$ and $\mathbf{P}$ are inputs to our algorithm, and can be measured during an initial phase for topology discovery.[3] During the same process, the nodes in $\mathcal{N}$ obtain their list of one-hop neighbor nodes and share it with the cluster head. As a result, the cluster head is able to evaluate the network topology.

In case $M_{x,y} = 1$ and $M_{y,x} = 1$, nodes i_x and i_y can be scheduled for simultaneous transmissions, as neither would impede the reception of the other. However, in case $M_{x,y} = 1$ but $M_{y,x} = 0$, if transmitting together, node i_x will overshadow (or jam) the transmissions of node i_y, i.e., the near-far effect occurs. Note that the former case is only possible when the receiver holds multiple packet reception capabilities or applies interference cancellation techniques. However, the latter case does not involve interference cancellation techniques. An example of a topology exhibiting a near-far scenario is illustrated in Fig. 2.2a. In this example, node i_1 is much closer to node i_0 than node i_2 and jams the transmissions of the latter. In this chapter, we specifically assume that there is at least one near-far scenario across the network.

---

[2] We assume that the cluster head only has information about NFNPs. The event that more than two nodes transmit simultaneously is still possible, and managed as explained in Section 2.4.2

[3] Topology information can be obtained by measuring the rate of successful packets [118, 119] or by estimating the SINR through measuring the distances among the nodes and applying an attenuation model [87]. This process is beyond the scope of this chapter.

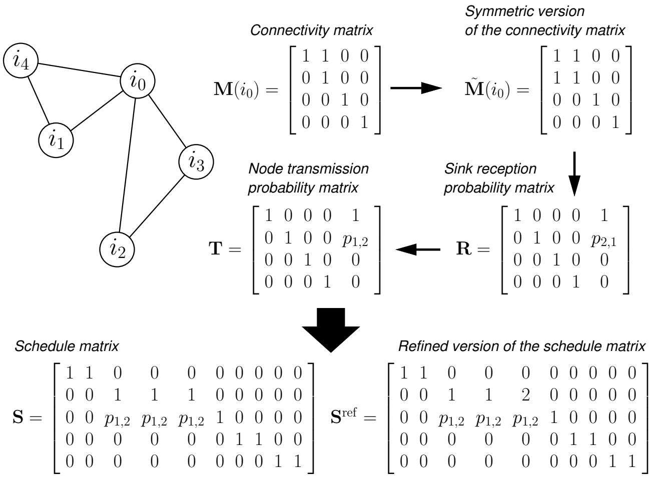

$$\mathbf{M}(i_0) = \begin{bmatrix} 1 & 1 & 0 & 0 \\ 0 & 1 & 0 & 0 \\ 0 & 0 & 1 & 0 \\ 0 & 0 & 0 & 1 \end{bmatrix} \longrightarrow \tilde{\mathbf{M}}(i_0) = \begin{bmatrix} 1 & 1 & 0 & 0 \\ 1 & 1 & 0 & 0 \\ 0 & 0 & 1 & 0 \\ 0 & 0 & 0 & 1 \end{bmatrix}$$

$$\mathbf{T} = \begin{bmatrix} 1 & 0 & 0 & 0 & 1 \\ 0 & 1 & 0 & 0 & p_{1,2} \\ 0 & 0 & 1 & 0 & 0 \\ 0 & 0 & 0 & 1 & 0 \end{bmatrix} \longleftarrow \mathbf{R} = \begin{bmatrix} 1 & 0 & 0 & 0 & 1 \\ 0 & 1 & 0 & 0 & p_{2,1} \\ 0 & 0 & 1 & 0 & 0 \\ 0 & 0 & 0 & 1 & 0 \end{bmatrix}$$

$$\mathbf{S} = \begin{bmatrix} 1 & 1 & 0 & 0 & 0 & 0 & 0 & 0 & 0 & 0 \\ 0 & 0 & 1 & 1 & 1 & 0 & 0 & 0 & 0 & 0 \\ 0 & 0 & p_{1,2} & p_{1,2} & p_{1,2} & 1 & 0 & 0 & 0 & 0 \\ 0 & 0 & 0 & 0 & 0 & 0 & 1 & 1 & 0 & 0 \\ 0 & 0 & 0 & 0 & 0 & 0 & 0 & 0 & 1 & 1 \end{bmatrix} \quad \mathbf{S}^{\mathrm{ref}} = \begin{bmatrix} 1 & 1 & 0 & 0 & 0 & 0 & 0 & 0 & 0 & 0 \\ 0 & 0 & 1 & 1 & 2 & 0 & 0 & 0 & 0 & 0 \\ 0 & 0 & p_{1,2} & p_{1,2} & p_{1,2} & 1 & 0 & 0 & 0 & 0 \\ 0 & 0 & 0 & 0 & 0 & 0 & 1 & 1 & 0 & 0 \\ 0 & 0 & 0 & 0 & 0 & 0 & 0 & 0 & 1 & 1 \end{bmatrix}$$

(a)

```
Algorithm 1: The NF-TDMA algorithm
input: $\mathbf{M}, \mathbf{P}, \mathbf{c}, T_L$
/* Preliminary Step I                                    */
$\mathcal{R} = \emptyset, \tilde{\mathbf{M}} = \mathbf{M}$
for $n, m \leftarrow 1$ to $N,\ n \neq m$ do
    if $M_{n,m} = 0$ and $M_{m,n} = 1$ then
        $\mathcal{R} \leftarrow \{\mathcal{R},\ (i_n, i_m)\}$
        $\tilde{M}_{n,m} = 1$
$\mathrm{X}(\tilde{\mathbf{M}}) \leftarrow$ element wise complement of $\tilde{\mathbf{M}}$
/* Preliminary Steps II and III                          */
$\mathbf{R} \leftarrow$ independent sets of $\mathrm{X}(\tilde{\mathbf{M}})$ as columns;   $\mathbf{T} \leftarrow \mathbf{R}$
for $k \leftarrow 1$ to $|\mathbf{R}|$, $n \leftarrow 1$ to $N$ do
    for $m$ such that $(i_n, i_m) \in \mathcal{R}$ do
        if $R_{n,k} = 1$ and $R_{m,k} = 1$ then
            $R_{n,k} \leftarrow R_{n,k} P_{n,m}$
            $T_{n,k} \leftarrow T_{n,k} P_{m,n}$
/* Determine the NF-TDMA schedule                        */
Solve (10) to obtain $\hat{\mathbf{a}}$
$\mathbf{S} \leftarrow \emptyset$
for $k := 1$ to $|\hat{\mathbf{a}}|$ do
    $\mathbf{r}(k) \leftarrow [T_{1,k}, \ldots, T_{N,k}]^{\mathrm{T}}$
    $\mathbf{S} := \Big[\mathbf{S}, \underbrace{\mathbf{r}(k), \ldots, \mathbf{r}(k)}_{\hat{a}_k}\Big]$
```

(b)

Figure 2.2: (a) Example for the illustration of the NF-TDMA algorithm. (b) Pseudocode of our proposed NF-TDMA algorithm.

2.4 The Near-Far scheduling solution

In this section, we discuss in detail our spatial reuse scheduling algorithm that exploits the near far effect. We start by describing the key idea behind our solution, and then present our algorithm. We discuss the details of forming the scheduling TDMA frame, how to determine the types of packets transmitted, and how to set the list of destinations of opportunistic packets. For a clearer description of our algorithm, throughout the following subsections we refer step-by-step to the example given in Fig. 2.2a. There, the cluster-head i_0 has to compute a schedule for all its connected nodes $i_1, \ldots, i_4$, where some nodes are subject to the near-far effect: for example, a transmission by node i_2 would be shadowed by a transmission from i_1, if the two corresponding signals are received at the same time. The following subsection highlights the key idea and operation of our algorithm, whereas Section 2.4.2 describes the algorithm's details.

2.4.1 Key idea

Our solution is based on the observation that in a near-far situation, only one collision occurs and the jammer can still transmit. Then, the receiver can directly decode the packet from the jammer while applying interference cancellation techniques to decode the jammed packet. In that sense, our solution is similar to cognitive radio schemes, where secondary nodes are allowed to transmit in the band of primary nodes. Since interference cancellation is not always feasible, we also allocate transmission epochs where the reception of packets of each node is guaranteed. In these transmission epochs, we allow the jammer to transmit only if it employs power control to ensure the reception of the transmission from the jammed node. Moreover, as we demonstrate in our field experiment, even without interference cancellation capabilities, spatial reuse is still possible by utilizing information about NFNPs and guiding the jammer and jammed nodes to transmit packets to different destinations.

Our NF-TDMA algorithm is unique in the sense that although (like any other TDMA scheduling algorithm) it is designed for the contention-free communication of status packets, it also serves the transmission of opportunistic packets. To that end, while the basic schedule is set by the cluster head, nodes can distributedly decide whether to transmit a status packet or an opportunistic packet. This is determined while satisfying a minimum transmission rate of status packets and depending on opportunistic packet arrivals. To avoid collisions, in the case of opportunistic packets, a node decides upon the destination node from a list of possible candidates offered by the cluster head already at the initial stage when the scheduling solution is derived.

We expect the near-far situation to persist even when the receiver, jammer, and jammed nodes slowly move, which is the common case in UWANs. This is motivated by the results in [120] which shows that there is a strict boundary between the cases of low and sufficient signal-to-interference ratio (SIR) to correctly receive a packet belonging to a NFNP. This implies that exploiting the near-far effect in spatial reuse scheduling algorithms does not strictly require frequent topology and schedule updates.

2.4.2 NF-TDMA

The output of the NF-TDMA scheduling algorithm is an $N \times L$ matrix $\mathbf{S}$ to allocate the transmissions of N nodes over L time slots. Given $\mathbf{S}$, a node i_n is allowed to transmit in time slot ℓ with probability $S_{n,\ell}$. Then, the case of $\sum_{n=0}^{N-1} S_{n,\ell} > 1$ for some ℓ (i.e., more than one nodes are allowed to transmit together in one or more slots) is typically referred to as spatial-reuse TDMA, and the case where $\exists\, i_m, i_n, \ell \ \mid \ S_{n,\ell} > 0,\ S_{m,\ell} > 0,\ M_{m,n} \neq M_{n,m}$ characterizes NF-TDMA. The latter case means that between two nodes that transmit in a given slot, only one can be received (say only m). In the following, we describe the procedure to obtain $\mathbf{S}$. The steps of the algorithm are listed in Algorithm 1, Fig. 2.2b. Our implementation of the algorithm is published for reproducibility.[4]

---

[4] `http://marsci.haifa.ac.il/share/diamant/NearFarPublishCode.zip`

Preliminary steps

Before obtaining the schedule, the cluster head i_0 performs three preliminary steps to rearrange the topology information in matrix $\mathbf{M}$ towards scheduling transmissions. First, node i_0 constructs a list $\mathcal{R}$ of all node pairs involved in a near-far situation. This list is found by inspecting non-symmetric entries in matrix $\mathbf{M}$. Referring to the example in Fig. 2.2a, these would be nodes (i_2, i_1). To formalize this,

$$(i_n, i_m) \in \mathcal{R} \quad \text{if } M_{n,m} = 0 \text{ and } M_{m,n} = 1 \;, \tag{2.6}$$

where the second node i_m is the jammer node (see lines 1–4 in Algorithm 1, Fig. 2.2b).

For each far node $i_n \in \mathcal{R}$ and its near peer i_m, node i_0 is able to estimate an interference cancellation probability, $p_{n,m}$. The latter is the probability of properly decoding a packet from i_n while simultaneously receiving a packet from node i_m.[5] Note that if i_m is the jammer, then $p_{n,m} < p_{m,n}$. Clearly, $p_{n,m}$ is a function of the SNR and of the superposition of the packets. Instead of avoiding the near-far effect, we exploit it by allowing nodes i_n and i_m to transmit simultaneously. For this, we "fill up the gaps" and create a symmetric version of $\mathbf{M}$, namely $\tilde{\mathbf{M}}$, such that

$$\tilde{M}_{n,m} = \begin{cases} 1 & , \quad (i_n, i_m) \in \mathcal{R} \\ M_{n,m} & , \quad \text{otherwise} \end{cases} \tag{2.7}$$

(see line 5 in Fig. 2.2b). Matrix $\tilde{\mathbf{M}}$ for our example is given in Fig. 2.2a.

Second, we find all the possible collision-free transmission scheduling solutions in the network. For this, we form the symmetric matrix $\mathrm{X}(\tilde{\mathbf{M}})$, where $\mathrm{X}(\cdot)$ denotes the element-wise 1-complement operator. In case entry $\mathrm{X}(\tilde{\mathbf{M}})_{i,j} > 0$, then both nodes i and j may transmit together. Next, we convert $\mathrm{X}(\tilde{\mathbf{M}})$ into a connected graph, where nodes are vertices, and non-zero entries are edges. The list of all independent sets of this graph (see also [121]), $\mathbf{w} = \{\mathbf{w}^{(1)}, \ldots, \mathbf{w}^{(K)}\}$, represents all the combinations of nodes that can transmit together. To find the best possible collision-free transmission scheduling solution in the network, our goal is to choose those independent sets from $\mathbf{w}$ that lead to the maximum link utilization while guaranteeing the minimal required per-node transmission rate. These independent sets will then form the TDMA schedule time frame. Consider for example that $\hat{K}$ independent sets are chosen from $\mathbf{w}$. Then, the schedule time frame consists of $\hat{K}$ time slots such that in the kth time slot, only nodes that are included in $\mathbf{w}^{(k)}, \; k = 1, \ldots, \hat{K}$ can transmit. Each entry $n, \; n = 1, \ldots, N-1$ in an independent set $\mathbf{w}^{(k)}$ can have the following three values:

---

[5] The interference cancellation probability can be found by calculating or measuring the signal-to-interference-pulse-noise ratio (SINR) for each of the received symbols and setting a threshold for the target symbol error rate probability (e.g., see [88]).

1. $w_n^{(k)} = 0$: node i_n can not transmit;
2. $w_n^{(k)} = 1$: node n can transmit, and the reception of its packet will not be affected by interference with probability 1;
3. $w_n^{(k)} = p_{n,k}$: node n can transmit, and the reception of its packet will not be affected by interference with probability $0 < p_{n,k} < 1$.

Note that the third case can occur when there is another node, i_m, who forms a near-far pair with node i_n and for which $w_n^{(k)} > 0$. That is, the third case applies when

$$\exists\, i_m \;\mid\; (i_n, i_m) \in \mathcal{R} \;\wedge\; w_m^{(k)} > 0 \; .$$

In this case, we set $p_{n,k} = p_{n,m}$. Clearly, without interference cancellation capabilities we have $p_{n,k} = 0$. As a first-order approximation, near-far scenarios with a jammed node and more than one jammer nodes are considered by setting $(1 - p_{n,k})$ as a multiplication of all the relevant near-far error probabilities. For example, if node i_n is the "far" node with respect to both nodes i_m and i_q, and $w_m^{(k)} > 0$, $w_q^{(k)} > 0$, $w_n^{(k)} > 0$, we set $p_{n,k} = 1 - (1 - p_{n,m})(1 - p_{n,q})$. The K different vectors $\mathbf{w}$ are arranged in columns to form an $(N-1) \times K$ *sink reception probability* matrix $\mathbf{R}$, whose entry $R_{n,k}$ is the probability that the cluster head node i_0 receives a packet from node i_n for the kth transmission set (see lines 7–11 in Fig. 2.2b). Matrix $\mathbf{R}$ for our example is presented in Fig. 2.2a.

Third, we form an $(N-1) \times K$ *node transmission probability* matrix $\mathbf{T}$, whose entry $T_{n,k}$ represents the probability that node i_n transmits in the kth possible transmission combination. For a node i_n for which $w_n^{(k)} = 1$, we set $T_{n,k} = 1$. However, for a node pair $(i_n, i_m) \in \mathcal{R}$ and time slot k for which $w_n^{(k)} > 0$ and $w_m^{(k)} > 0$, we prefer to allow the jammer node i_m to always transmit. In this case, the probability that the jammed node i_n transmits depends on the ability of i_0 to receive the jammer (rather than the jammed node). Hence, we set $T_{m,k} = 1$ and $T_{n,k} = p_{m,n}$. As will become clear in the next section, this preference is because when probability $p_{n,m}$ is low, our scheduling solution would allocate at least one exclusive transmission slot to the jammed node. When this happens, the jammer would be allowed to actually transmit along with its jammed node pair only when it employs power control. For our example, matrix $\mathbf{T}$ is shown in Fig. 2.2a.

Forming the schedule

The stage is now set to present our NF-TDMA algorithm to obtain the scheduling matrix $\mathbf{S}$. We observe that $\rho_{\text{through,s}}$ and $\rho_{\text{delay,o}}$ in (2.1) and in (2.4), respectively, can be optimized by maximizing the channel utilization, which corresponds to maximizing the number of collision-free transmissions.

That is because both the number of received packets and the time a packet is delayed in transmission queues are affected by the number of collision-free transmissions. Hence, in the setting of spatial-reuse TDMA, the schedule converges to allocating the maximum possible number of transmission time slots while ensuring that packets arrive without collisions. To that end, we denote a $K \times 1$ vector $\mathbf{a}$, whose entries a_j represent the number of times column j from $\mathbf{T}$ is chosen in the scheduling solution. In matrix form, we obtain the *reception vector*

$$\mathbf{r}(\mathbf{R}, \mathbf{a}) = \mathbf{R}\mathbf{a} \ , \tag{2.8}$$

such that for row n in matrix $\mathbf{R}$, $r_n(\mathbf{R}, \mathbf{a})$ packets are sent by node i_n and successfully received at node i_0.

To allow a minimum number of transmissions (including at least one status packet) by each node i, we fix the number of time slots in one time frame to be

$$L = \frac{T_L \cdot \max_i c_i}{T_s} \ , \tag{2.9}$$

where T_s is the duration of the time slot. Then, considering the scheduling constraints in (2.2) and (2.3), the scheduling problem can be written as

$$\hat{\mathbf{a}} = \underset{\mathbf{a}}{\operatorname{argmax}} \sum_{n=1}^{N-1} r_n(\mathbf{R}, \mathbf{a}) \tag{2.10a}$$

$$\text{s.t.} \ \sum_{n} a_n = L \ , \tag{2.10b}$$

$$r_n \geq c_n, \ \forall n \in \mathcal{N} \ . \tag{2.10c}$$

Note that by (2.5), the goal in fairness is to equalize the transmission opportunities of nodes. While we do not explicitly optimize fairness in (2.10), we relate to the fairness by imposing constraint (2.10c) to satisfy requirement (2.3). This way, a node i_n gets a minimum of c_n contention-free transmission slots per frame, which ensures some fairness in the transmission of status packets. However, the fairness of opportunistic packets is not considered. Problem (2.10) is an NP-hard integer linear program, whose worst-case complexity grows exponentially with the size of $\mathbf{a}$. However, as shown in [122, 123], it can be solved in polynomial time (on average) via the branch-and-bound algorithm.

The solution $\hat{\mathbf{a}}$ from (2.10) is readily used to find the schedule matrix $\mathbf{S}$. Let $\mathbf{T}_j$ represent the jth column of the node transmission probability matrix $\mathbf{T}$, and $\hat{a}_j$ be the jth element of $\hat{\mathbf{a}}$. We have

$$\mathbf{S} = \Big[\underbrace{\mathbf{T}_1, \ldots, \mathbf{T}_1}_{\hat{a}_1}, \underbrace{\mathbf{T}_2, \ldots, \mathbf{T}_2}_{\hat{a}_2}, \ldots, \underbrace{\mathbf{T}_K, \ldots, \mathbf{T}_K,}_{\hat{a}_K} \Big] \ , \tag{2.11}$$

i.e., the jth column of $\mathbf{T}$ is replicated $\hat{a}_j$ times. Since our objective is to maximize the network throughput, the solution for (2.10) and the definition in (2.11) are set by considering matrix $\mathbf{R}$, i.e., the packet reception requirement rather than the packet transmission requirement. In turn, schedule $\mathbf{S}$ indicates which node can transmit in each time slot and the probability that it will actually transmit. Hence, the solution of (2.10) is readily transformed into the scheduling matrix $\mathbf{S}$, whose columns are replicas of the columns of the node transmission probability matrix $\mathbf{T}$.Therefore, the scheduling solution matrix $\mathbf{S}$ contains $\hat{a}_k$ replicas of $\mathbf{T}_k$ (see lines 13–17 in Fig. 2.2b). In Fig. 2.2a, we show the resulting scheduling solution $\mathbf{S}$ for our example, where we consider $L = 10$, $c_n = 2\ \forall n$, see (2.10c), $p_{1,2} = 1$, and $p_{2,1} = 0.3$. Here, entry $S_{n,\ell}$ is the probability that node i_n transmits in slot ℓ.

Determining the packet type

In each time slot, t, a node scheduled to transmit can send either a status packet or an opportunistic packet. Considering the need to send status packets, opportunistic packets are transmitted only if there is a high probability to transmit a status packet in the next few time slots such that constraint (2.2) is met. To formalize this, let $t_m,\ m = 1, 2, \ldots$ be a future time slot index such that $t_m > t$ and $S_{n,t_m} > 0$. Also denote as $\mathcal{E}_{n,t,t_m}$ the event for which node i_n will transmit between the current time slot t and a future time slot t_m. The probability that event $\mathcal{E}_{n,t,t_m}$ occurs is

$$\mathbb{P}[\mathcal{E}_{n,t,t_m}] = 1 - \prod_{i=1}^{m} (1 - S_{n,t_i}) \ . \tag{2.12}$$

Let $\hat{m}$ be the smallest subindex for which $\mathbb{P}[\mathcal{E}_{n,t,t_m}] > \Theta_{\text{Tx}}$, where Θ_{Tx} is a fixed threshold. Then, node i_n will transmit an opportunistic packet in time slot t if there is an opportunistic packet in the queue, and if the time elapsed from the previous time slot where node i_n transmitted a status packet (say, t_ℓ) until the future time slot $t_{\hat{m}}$ is smaller than the required value T_L, see (2.2). Formally, if $\exists\, \hat{m}$ such that

$$t_{\hat{m}} \cdot T_s + T^{\max} - t_\ell \cdot T_s < T_L \ , \tag{2.13}$$

where $T^{\max}$ is the maximum propagation delay in the network. Otherwise, a status packet is transmitted. The condition in (2.13) makes sure that the time elapsed between transmissions of status packets would not exceed T_L seconds. However, no consideration is given to the case where fewer transmission slots than opportunistic packets are available. In the latter case, opportunistic packets are queued up, and transmitted in a first-come-first-served fashion. The delay induced by this event is considered in the definition of the scheduling delay metric in (2.4), and is analyzed in our numerical results and field experiment.

Refinement

Note that the utility function in (2.10) considers the packet reception probability, while the scheduling solution sets the transmission probability of the nodes. As we mentioned above, in case the kth transmission set is chosen multiple times (i.e., $\hat{a}_k$ is large), this allows the reception of at least c_n packets for a node i_n whose reception probability $p_{n,k}$ at the cluster head is low. That is, the solution in $\mathbf{S}$ may avoid some simultaneous transmissions by the near-far nodes i_m and i_n if these transmissions may reduce the chances of the jammed node i_n to be received below its required flow constraints. This comes directly from the solution of (2.10) by choosing $\hat{\mathbf{a}}_{k^\star} \geq 1$ for at least one transmission set $k^\star$ in which node i_n can be received without interference. However, these avoided simultaneous transmissions can still be allowed if the jammer i_m reduces its transmission power such that although i_n and i_m simultaneously transmit, the packets of i_n are still received. Hence, considering a node pair $(i_n, i_m) \in \mathcal{R}$, for which only node i_n is scheduled to transmit in set $k^\star$, we observe that a refinement is possible.

To further improve the network throughput, we allow the jammer node i_m to transmit in set $k^\star$ only if it employs power control. Such power control should still ensure the reception of node i_n. Let P_n be the reception power of a packet from a node i_n at the cluster head i_0, such that the power ratio between the jammed packet and the jamming packet is

$$\rho_P(n, m) = \frac{P_n}{P_m} \ . \tag{2.14}$$

It follows that to transmit in set $k^\star$, node i_m must reduce its power by a factor $\rho_P^2(n, m)$. This will lead to an *inverse* near-far scenario where node i_n becomes the jammer and node i_m becomes the jammed node.

After obtaining solution $\mathbf{S}$ through (2.10), we performed a refinement by identifying all the transmission sets $k^\star$ according to the following procedure $\forall (i_n, i_m) \in \mathcal{R}$. The following algorithm identifies the transmission sets $k^\star$ in $\mathbf{S}$ in which near-far simultaneous transmissions are avoided, and mark them in a new refined scheduling matrix $\mathbf{S}^{\text{ref}}$:

1. Initialize $\mathbf{S}^{\text{ref}} = \mathbf{S}$.
2. Form a matrix $\tilde{\mathbf{R}}$ of all maximal independent sets of the symmetric matrix $\tilde{\mathbf{M}}$ (see (2.7)).
3. Identify a column $k^\star$ in $\mathbf{S}$ not included in $\tilde{\mathbf{R}}$ such that $S_{n,k^\star} = 1$ and $S_{m,k^\star} = 0$.
4. Make an indication $S^{\text{ref}}_{m,k^\star} = n$.

To execute the refined NF-TDMA algorithm, instead of $\mathbf{S}$, the sink node communicate $\mathbf{S}^{\text{ref}}$ to the other nodes. Then, a node i_m for which $S^{\text{ref}}_{m,k^\star} > 1$ is allowed to transmit in time slot $k^\star$ only if it reduces its transmission power by a factor $\rho_P^2(n,m)$ from (2.14). In Fig. 2.2a, we denoted $S_{1,5}^{\mathrm{ref}} = 2$. This means that node i_1 is allowed to transmit in the 5th time slot only if it reduces its transmission power by a factor $\rho_P^2(2,1)$. Naturally, power control can be performed only if i_m can locally calculate factor (2.14) or is explicitly told which power to use, and thus this refinement may not always be performed.

Destination of opportunistic packets

While nodes make the decision whether to transmit a status packet or an opportunistic packet distributedly, they can be guided to choose the destination node of their packets properly. Since the cluster head is aware of the connectivity list of each of its one-hop neighbor nodes, for each node and for each time slot, the cluster head can suggest a list of possible destination nodes. More specifically, consider two nodes m and n scheduled to transmit in time slot k. Also assume that nodes m and n are directly connected to a node r. Since neither m, n or the cluster head knows whether m and n are NFNPs with respect to r, to be on the safe side the cluster head will advise nodes m and n not to transmit to node r. These nodes may choose to transmit to another node from the given list or to transmit a status packet to the cluster head.

2.4.3 Discussion

Note that our NF-TDMA algorithm is a combination of an optimal centralized solution with a distributed sub-optimal schedule. On the one hand, it uses available information at the cluster head in the form of network topology and NFNPs to optimally schedule status packets given the interference cancellation probability. On the other hand, our algorithm opportunistically allows nodes to transmit packets to their one-hop neighbors while preserving the collision-free reception of status packets. In our NF-TDMA algorithm, we assume a global round-robin TDMA schedule where slots are determined based on the maximum propagation delay, which is in turn determined by the system transmission range. This schedule allows some tolerance to motion as the information exchanged between the nodes and the sink node is only in the form of one-hop neighbor lists. Naturally, additional information can be used to refine the schedule at the cost of sensitivity to motion and channel conditions. Since our NF-TDMA only allocates transmission time slots, it can be readily implemented also on such an improved schedule.

Low communication overhead is one immediate benefit yielded by the combination of centralized schedule optimization and distributed transmission decisions. Specifically, our solution does not require nodes to share their time-varying transmission requirements, so that in turn the sink does not need to broadcast the packet type and destination for each scheduled transmission.

This is because, in our solution, each node can build its own near-far list and does not need to explicitly share it with the other nodes. Instead, when forming the near-far matrix, the only overhead is represented by the transmission of one-hop connectivity lists by the nodes, a total of $(N-1) \cdot (N-1)$ bits, and by the transfer of the resulting optimized schedule, $\mathbf{S}$, from the sink to the nodes. To transmit $\mathbf{S}$, the sink is required to transmit a total of $(N-1) \cdot (N-1)$ probability values. In our implementation, each probability value is represented by 1 byte. This calculation does not include the overhead needed for obtaining the one-hop neighbor lists and the list of near-far node pairs, which is out of the scope of this chapter and can be addressed with a per-node overhead of $\log(N)$ bits re-transmitted roughly N times by methods such as, e.g., [116].

The fact that our algorithm serves both contention-free and opportunistic transmissions is utilized to increase throughput even in cases where the system does not have interference cancellation capabilities. In fact, in case a node already served the transmission of status packets, it can further utilize the channel to opportunistically transmit packets. This decision is performed distributedly, and the cluster head guides nodes to properly choose the destination of their opportunistic packets. As a result, although TDMA is traditionally convenient only when the packet transmission rate is high, our algorithm remains a convenient choice also when the packet transmission rate is low. The advantages of this hybrid feature of our algorithm come from a specific application of cross-layer network design: using available information of both the contention-free and the opportunistic communication types, the overall performance can be improved. However, the distributed choice of the packet type has its drawbacks. Specifically, since the transmission of i_n in slot k is set randomly according to probability $S_{n,k}$, there is a chance that $\mathbb{P}[\mathcal{E}_{n,t,t_m}]$ in (2.12) is greater than the threshold Θ_{Tx} while no transmission is issued. In this case, node i_n will issue an opportunistic packet while constraint (2.2) is not fulfilled. However, this risk is low, as the exploitation of spatial reuse and of the near-far effect provides a large number of transmission slots to each node. In fact, we never encountered such occurrence in our extensive simulations, nor in the outcome of our sea experiment (see Section 2.6).

2.5 Numerical results

In this section, we discuss the performance of our NF-TDMA algorithm. We measure the performance in terms of throughput of status packets, $\rho_{\mathrm{through,s}}$ from (2.1), scheduling delay of opportunistic packets, $\rho_{\mathrm{delay,o}}$ from (2.4), and throughput fairness of opportunistic packets, $\rho_{\mathrm{fair,o}}$ from (2.5). We show results for three configurations of the NF-TDMA protocol, namely: 1) *Ideal NF-TDMA*, where the interference cancellation probability is ideal and both the jammer and the jammed nodes of each NFNP are assumed to be decoded with probability 1; 2) *Realistic NF-TDMA*, where the interference cancellation probability is set according to the evaluated SINR; and 3) *Limited NF-TDMA*, where nodes do not have interference cancellation capabilities.[6] The case of Limited NF-TDMA is further explored in our field experiment. For clarity, for all three schemes we do not apply the power control mechanism described in Section 2.4.2. The performance of the power control refinement is explored instead in the results of the lake experiment in Section 2.6. We compare our results with the performance of the simple round-robin TDMA protocol (*TDMA*) where in each time slot only one node can transmit. For a fair comparison with the NF-TDMA algorithm, we duplicate the frame of the simple TDMA schedule to match that of the NF-TDMA schemes (i.e., $L = T_L/T_s$). Since we consider a star topology, where all nodes are directly connected to the cluster head node i_0, all other available spatial-reuse collision-avoidance protocols that use only topology information would converge to the simple TDMA protocol. This is because, without taking advantage of the near-far effect, a star topology means that the sink node would not be able to receive packets if simultaneous transmissions occur.

2.5.1 Simulation setup

Our simulation setup includes a Monte-Carlo set of 200 topologies. In each simulation run, $N = 8$ nodes are placed uniformly at random in a volume of 5×5 km^2 with a water depth of 100 m. The volume includes four horizontal obstacles and one vertical obstacle at uniformly distributed locations with uniformly distributed length in the range $[100, 200]$ m. For each node pair in line-of-sight, we perform a Bellhop run [124, Ch. 3] for shallow waters of depth 100 m, flat sand bottom, fixed sound speed 1500 m/s, and carrier frequency 10 kHz. The Bellhop model outputs a multipath structure from which the power attenuation level can be derived. Using the estimated power attenuation level, we calculate the SNR of the line-of-sight node pair considering a source level of 170 dB re (1 μPa at 1 m), a noise level of 40 dB re (1μPa^2/Hz), and a transmission rate of 1000 bps. Then, for the calculated SNR level and considering BPSK communications at a transmission rate of 1000 bps, we set a link between a line-of-sight node pair if the bit error rate is less than 10^{-3}. In case two or more packets are simultaneously received, the SNR level of each packet is used to calculate the signal-to-interference-plus-noise ratio (SINR) level of each packet, which in turn is used to calculate the bit error rate.

For status packets, we consider a target transmission rate of one packet every $T_L = 100$ s, see (2.2). Considering available commercial acoustic

---

[6] Recall that, even with no interference cancellation capabilities, multiple nodes can transmit simultaneously if the destinations of their packets are different and certain interference conditions are satisfied.

modems [51], we set the maximum transmission range to be 3000 m, corresponding to a maximum propagation delay of 2 s. Then, considering the transmission of synchronization signals, a training sequence, 1000 data bearing bits, and guard time for possible clock drifts, we set the time slot to be $T_s = 5$ s.

Each simulation run includes 1000 time slots. For each time slot i, a node n for which $S_{n,i} \geq x$ where $0 \leq x \leq 1$ is drawn uniformly at random, can transmit either a status packet or an opportunistic packet. Status packets are always available and are transmitted to node i_0. The arrival times of opportunistic packets are distributed according to a Poisson process of rate $\lambda = 1$ packet per minute per node, and these packets are stored in the node's local queue. The type of packet to be transmitted is determined via (2.13) in Section 2.4.2, where we set $\Theta_{\text{Tx}} = 0.8$.

2.5.2 Simulation results

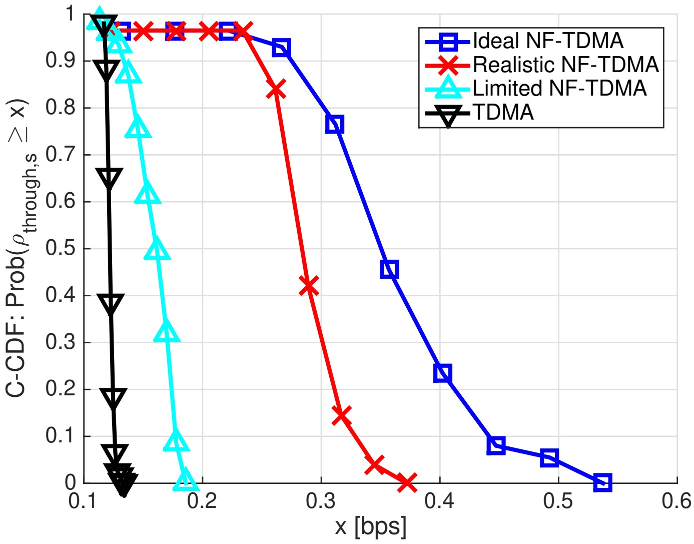

Figure 2.3: Empirical C-CDF of $\rho_{\text{through,s}}$ from (2.1).

In Fig. 2.3, we show the empirical complementary cumulative distribution function (C-CDF) of $\rho_{\text{through,s}}$ from (2.1) for status packets. Clearly, since TDMA does not depend on the specific network topology but only on the number of nodes, and since status packets are always available, the network throughput of TDMA changes negligibly across different runs. Compared to the performance of TDMA, we observe a significant improvement using our schemes, where even without interference cancellation capabilities (i.e., for Limited NF-TDMA) the network throughput increases by 40%, whereas with perfect interference cancellation the improvement can be as large as a factor of 4. Since no status packets collide at the cluster head when using Ideal NF-TDMA, the results are expectedly better than those for Realistic NF-TDMA. However, even for the latter, the network throughput improves by a factor of 3 compared to TDMA. We note that we are mainly concerned about the delay of opportunistic packets, as long as the minimum transmission rate of status packets is maintained, see (2.2). Hence, the opportunistic packets are scheduled whenever possible, and the resulting $\rho_{\text{through,s}}$ would not change considerably when using the refinement mechanism in Section 2.4.2.

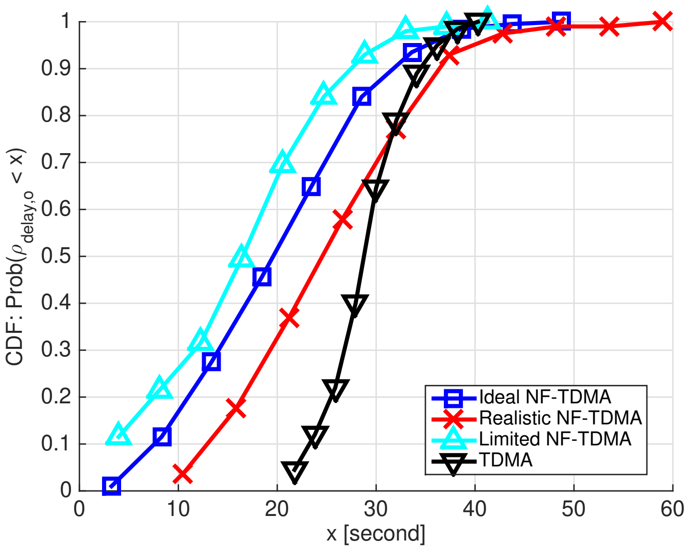

Figure 2.4: Empirical CDF of $\rho_{\text{delay,o}}$ from (2.4).

The empirical CDF results of $\rho_{\text{delay,o}}$ from (2.4) are shown in Fig. 2.4. Here we observe that, on average, the scheduling delay is roughly 30 s for TDMA. Since $L = T_L/T_s = 20$ slots and $N = 8$, this result comes directly from the fact that 1.5 opportunistic packets can be scheduled in each TDMA frame on average. We observe that interference cancellation capabilities improve the delay performance of Realistic NF-TDMA and Ideal NF-TDMA by respectively 1.8 and 3.6 times, compared to TDMA. In addition, the results show that a more significant improvement exists for the Limited NF-TDMA scheme. This surprising result is because opportunistic packets are sent to one-hop neighbor nodes but not to the cluster head, and since the schedule only ensures collision-free reception of status packets, opportunistic packets are prone to collisions. Because in Limited NF-TDMA fewer opportunistic packets are transmitted than in Realistic NF-TDMA and Ideal NF-TDMA, fewer collisions occur, and the scheduling delay decreases.

To comment on the fairness in scheduling opportunistic packets, in Fig. 2.5 we show C-CDF results of $\rho_{\text{fair,o}}$ from (2.5). Since TDMA evenly allocates

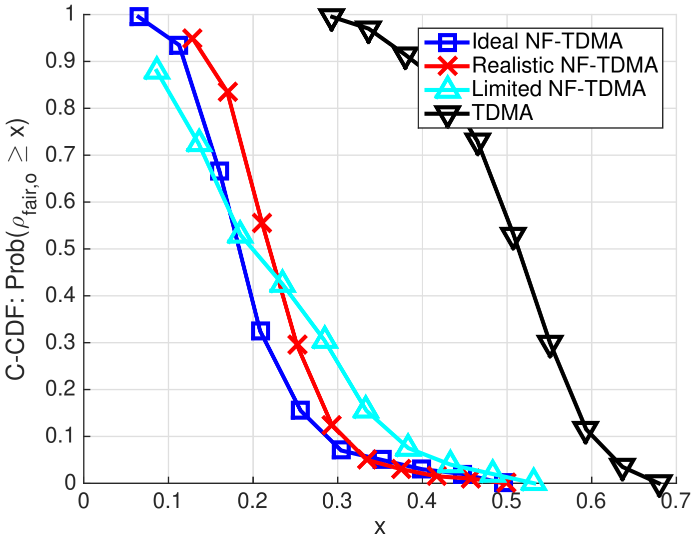

Figure 2.5: Empirical C-CDF of $\rho_{\text{fair,o}}$ from (2.5).

opportunistic packet transmissions, its fairness $\rho_{\text{fair,o}}$ is far better than that of the NF-TDMA schemes. Not much difference is observed between the three different NF-TDMA schemes. Yet, Realistic NF-TDMA consistently outperforms Ideal NF-TDMA. This is because, as seen from the results of Fig. 2.3, the latter correctly allocates more opportunistic packet transmission opportunities to nodes located close to the cluster head. We also observe that the fairness of Limited NF-TDMA varies compared to that of Realistic NF-TDMA and Ideal NF-TDMA. This is because, in terms of fairness, the performance of Limited NF-TDMA strongly depends on the topology. Specifically, for a certain NFNP with respect to the cluster head, spatial reuse in Limited NF-TDMA is determined by the ability of the far node to find a destination which is not connected to the near node. In some topologies, such destination nodes are found for only one or a few nodes, which adversely impacts fairness; conversely, in other topologies several far nodes can find proper destination nodes, and fairness improves as a consequence.

2.6 Field experiment

In our numerical results, we showed the performance of the NF-TDMA algorithm in terms of network throughput, scheduling delay, and service fairness. To apply our simulations, we used a simple flat bathymetry. In addition, due to the use of this simple model and to avoid additional assumptions, in our simulations we did not consider the use of the refined scheme described in Section 2.4.2. To verify our insights, in this section we present results from a field experiment using off-the-shelf acoustic modems with and without the power control mechanism. These modems do not have interference cancellation capabilities and can thus verify our conclusions for the interesting (and realistic) case of Limited NF-TDMA. The experiment also demonstrates the effectiveness and practicality of our scheme, which can be easily implemented on top of any existing physical layer.

2.6.1 Experiment setup

The setup of the experiment is shown in Fig. 2.6. The experiment was conducted in Dec. 2015, in lake Garda, Italy. The experiment included five nodes, communicating using EvoLogics modems. Our algorithm was implemented using the emulation capabilities of the ns2-based DESERT Underwater framework [74] and a real time synchronized scheduler connecting the application layer to the acoustic modems. The modems had no interference cancellation capability and in a near-far scenario can thus receive at most one packet. The nodes were deployed from harbor docks and from boats. By moving the two boats we created the four different network topologies shown in Fig. 2.6. Nodes 2 and 3 were deployed from harbor docks 75 m from each other and at water depth of 2 m and 4 m, respectively (all topologies). Nodes 1 and 5 were placed 10 m from each other and were deployed from a small boat at water depth 10 m and distance ∼700 m from node 2 (Topologies 1, 2, 3) and at water depth 2 m and distance ∼50 m from node 2 (Topology 4). Node 4 was deployed from an additional boat at water depth 5 m and distance 200 m (Topology 1), 700 m (Topology 2), and 600 m (Topologies 3, 4) from node 2. When the boats were distant from the harbor, the water depth was roughly 30 m, where the water depth at the harbor was between 2 and 4 m.

In each of the tested topologies, the network was fully connected. Node 1 was set as the designated cluster head. With respect to the cluster head, in Topology 1 node 5 was the jammer of NFNPs including nodes 2, 3 and 4. In Topology 2, both nodes 4 and 5 were the jammers of NFNPs including nodes 2 and 3, but $(4, 5)$ was not a NFNP. In Topology 3, node 5 was jamming nodes 2, 3 and 4, and node 4 was jamming nodes 2 and 3. In Topology 4, nodes 2, 3 and 5 were jamming node 4, and node 5 was jamming nodes 2 and 3. At the beginning of each topology test, to verify our setting, we performed a “discovery check” where we tested the links and the possible NFNPs. Then, the refined NF-TDMA algorithm (see Section 2.4.2) was tested for 1000 s, followed by another 1000 s where we also tested the more conservative NF-TDMA algorithm in (2.10) (i.e., without power control). Nodes transmitting without power control used the maximum source level of 182.5 dB re (1 μPa @ 1 m), while nodes for which $S_{n,k} = n$, $n \neq 1$ transmitted using a source level of 162.5 dB re (1 μPa @ 1 m).

Taking into account the propagation delay and the delay of the modem for decoding the packets, we used a time slot duration of $T_s = 5$ s. As a

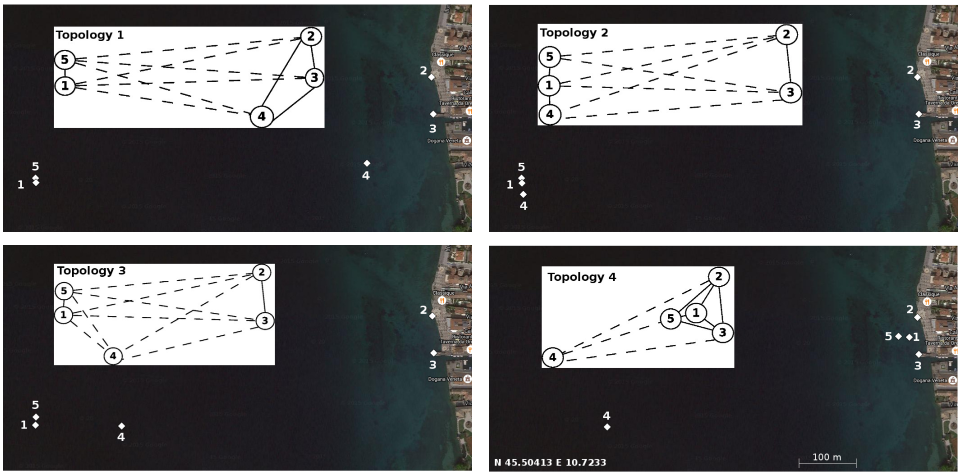

Figure 2.6: Setting of the lake experiment. Geographical maps show the location of the nodes. The white panel in each map conveys the logical topology of the network. Near-far connections with respect to node 1 are shown using dashed lines. The bottom-left corner in all maps corresponds to the geographical coordinates (45.50413°N, 10.7233°E). (Maps courtesy of Google Maps.)

limitation to the rate of transmitting status packets, we considered $T_L = 100$ s (see (2.2)). The resulting TDMA frame contained $T_L/T_s = 20$ time slots, and each run was configured to involve a total of 10 TDMA frames. In each of these frames, each node from 2 to 5 sent at least one status packet to node 1. As discussed in Sections 2.4.2 and 2.4.2, each node from 2 to 5 also sent several unicast opportunistic packets to other nodes in each TDMA frame. Both the status and the opportunistic packets included 64 information bytes, which were transmitted at a rate of 500 bps, so that the total duration of each packet was roughly 1 s. Due to the fully connected topology and the maximum range of 700 m between the nodes, this ensures that collisions are bound to occur whenever two nodes transmit in the same time slot.

Even though the lake surface was calm during the experiment, the very shallow water depth and the many reflections from the harbor's concrete walls resulted in a high overall packet error rate, which was measured to be roughly 20%. As a result, the performance of the simple TDMA procedure[7] is limited to the reception of 8 status packets by node 1, and to a per-node reception of 32 opportunistic packets. The latter is calculated by taking into account that $(20 - 4) \cdot 3/4$ time slots are available at each node for reception of opportunistic packets in each TDMA frame, out of which on average 1/3 are directed to the specific node and only 80% are successful. A summary of the relevant communication features and environmental characteristics

---

[7] Recall that due to the fully connected network, simple TDMA is the method to which all spatial-reuse TDMA methods which do not utilize near-far converge.

Table 2.1: Relevant hardware and environmental features.

Info	**Value**
Modem model	Evologics S2RC 18/34
Carrier frequency	26 kHz
Bandwidth	16 kHz
Source level	162.5 to 182.5 dB re 1 μPa @ 1 m
Processing delay	0.15 s
Bit rate	976 bps
Estimated data rate	512 bps
Packet size	512 bits
Water temperature	7 to 12 °C
Water salinity	350 ppm
Sound speed	≈1448 m/s
Further information	No wind, no waves, no shipping noise

experienced during the trial is reported in Table 2.1.

2.6.2 Experiment results

The results are shown in Table 2.2. For each topology, we show the per-node number of status packets received (Column of Node 1), and the per-node number of opportunistic packets received (Columns of Node 2-5). For the opportunistic packets, in brackets we show the number of exposed terminal problems solved. These are the number of time slots a node was allowed to transmit beyond the guaranteed $c_n = 2$ time slots (see (2.10)) in each TDMA schedule time frame. We note that the average per-node number of status packets received by node 1 was 8.5 and 6.5 with and without power control, respectively. We note that the numbers in Table 2.2 were obtained through offline processing of the reception logs of each node, and involved no additional overhead during network operations.

As expected, on average more opportunistic packets were received when power control was applied. This is supported also by the larger number of exposed terminal problems resolved when using power control. However, we observe that in some cases better results are obtained without applying power control. This is because the modems supported a maximum source level reduction of 20 dB, which was not always sufficient. As a result, interference occurred and packets were dropped. Compared to the expected results of TDMA, we note the significant increase in the average number of received opportunistic packets using the two versions of our NF-TDMA algorithm. Namely, roughly 75% and 50% additional opportunistic packets were received

Table 2.2: Lake experiment results. Numbers indicate status packets Rx by node 1 and opportunistic packets Rx by all other nodes.
(In parentheses: number of exposed terminal problems solved.)

Topology	**Method**	**Node 1**	**Node 2**	**Node 3**	**Node 4**	**Node 5**
T1	**Power control**	11	36 (0)	62 (0)	13 (17)	10 (44)
	No Power Control	10	33 (0)	72 (0)	13 (17)	10 (32)
T2	**Power control**	16	62 (7)	34 (19)	44 (49)	43 (52)
	No Power Control	9	35 (7)	59 (19)	65 (7)	21 (24)
T3	**Power control**	22	89 (0)	113 (0)	55 (25)	10 (44)
	No Power Control	20	85 (0)	102 (0)	63 (17)	10 (32)
T4	**Power control**	89	118 (68)	46 (42)	78 (34)	15 (44)
	No Power Control	67	81 (0)	29 (30)	71 (34)	18 (32)
Avg	**Power control**			56.5 (27.8)		
	No Power Control			47.9 (15.7)		

with and without power control, respectively. Considering the results in Fig. 2.3 for limited interference cancellation, these experimental outcomes validate our simulations.

2.7 Conclusions

In this chapter, we focused on the problem of transmission assignment in UWANs. We considered a time slot-based scheduling approach for a network topology where primary conflicts are not allowed and all nodes are directly connected to the sink. Exploiting the near-far effect, we proposed a spatial reuse scheduling solution that allows concurrent transmissions even when interference cancellation is not available. We formalized the problem of resource allocation for a given interference cancellation model and solved it optimally to achieve a collision-free scheduling solution while maintaining a minimum required packet transmission rate. Our scheduling algorithm is unique in the sense that it services both contention-free and opportunistic communications, each having different objectives. For the former, the objective is to maximize the network throughput, whereas for the latter scheduling delay and throughput fairness are of concern. Our numerical results show that in terms of all three objectives our schedule significantly outperforms the TDMA protocol, to which all current spatial-reuse scheduling protocols converge under the considered network topology. For the realistic case of no interference cancellation capability, we verified our results and demonstrated the effectiveness of our system in a field experiment. The results confirmed the high benefit of utilizing information about near-far node pairs to increase network throughput.

Notes

Part of the content addressed by this chapter has been published in [93] and [125].

Chapter 3

Modeling the underwater optical channel

3.1 Introduction

Underwater optical communications are currently gathering increasing interest. Many recently developed optical modems are commercially available (e.g., [17, 126]) and used in deep water Oil&Gas assets. However, most of these systems do not exist as commercial off-the-shelf products, but rather as customized implementations which typically require an expensive development phase. Several universities and research institutes proposed low-cost underwater optical proof-of-concept (PoC) modems (e.g. [14, 49]); however, none of them has been made commercially available, or reportedly employed in a complex networking experiment so far.

Before a real deployment of an underwater optical network, a preliminary system evaluation involving system-level analysis and simulations is required. During the simulations, it is essential to consider realistic scenarios, based not only on theoretical models, but also on field measurements with real hardware. Only in this way can the simulation results provide the first evaluation of a real system with high accuracy. Several theoretical models for underwater optical communications, either analytical or based on Monte Carlo approaches, have already been addressed in the literature [127, 128]. However, they typically do not address time-varying optical channels or depth-varying ambient light noise, and they are typically based on physical models that require complex computations [18, 129]. The Woods Hole Oceanographic Institution has performed several sea trials to evaluate their optical modem under different water conditions. These include deep water scenarios [130] and shallow water scenarios at night [131] as well as in daytime conditions [132]. During the design phase in [131], they have also performed some preliminary simulations of optical transmissions. In [133], the authors present their hybrid optical and acoustic communications system, and employ the system in data-muling and vehicle control operations. Although these results are very interesting and demonstrate the effectiveness of the device, the authors have not released any underwater acoustic and optical network simulator based on the performance figures obtained this way.

In this chapter, we aim to propose a solution to address the need for an optical communication model that is amenable to network simulations. Specifically, we propose the first underwater optical network simulator based on real measurements of optical propagation in ocean waters of different types. Such parameters were measured during the ALOMEX'15 research cruise, organized by the NATO STO Centre of Marine Research and Experimentation (CMRE). The ALOMEX'15 campaign spanned 13 days and covered a total route of about 2800 km, starting from Cartagena, Spain, down to the West Saharian sea, and with final destination Las Palmas de Gran Canaria, Spain (see Fig. 3.1). During the cruise, the research vessel R/V Alliance has been navigated to 39 different stations to collect measurements. In each site, the measurements included the down-welling solar light irradiance, the optical attenuation and absorption coefficients, and the water temperature throughout the water column. The measurements have been explicitly taken at different locations and times of day, in order to encompass diverse environmental conditions and water properties.

All measurements have been processed and embedded in the multi-modal acoustic and optical DESERT Underwater Network Simulator [134] in the form of lookup tables (LUTs), which are used to characterize the optical channel. An example of such data is reported in Fig. 3.2, that shows the absorption rate a, the scattering rate b and the total attenuation rate c. The latter quantity models the light energy loss due to propagation as a function of distance, and depends on depth. This data is reported for stations 3 and 25 in Fig. 3.1, which are representative of very different water types. The simulator also supports the connection to both acoustic and optical real underwater modems, such as all the EvoLogics S2C acoustic modems [135] and the ENEA optical modem prototype, to perform multi-modal sea trials, and thus also serves as a network emulator or proof-of-design system for new technologies [74].

The content of this chapter is the following. Section 3.2 describes the implementation details of the optical simulator, by centering our study on a sample scenario (depicted in Section 3.2.3): this model has been included into the open access DESERT Underwater network simulator, used to carry out the simple simulation study reported in Section 3.2.4. This study makes it possible to assess the impact of different ambient light and water conditions on the performance of optical links, based on real data. In Section 3.2.5, we perform preliminary experiments using the PoC optical modem of the Italian ENEA research institute [49] both in dark water and in very shallow water during a sunny day, and measured the packet delivery ratio in both conditions. The preliminary optical communication simulations and the results of the

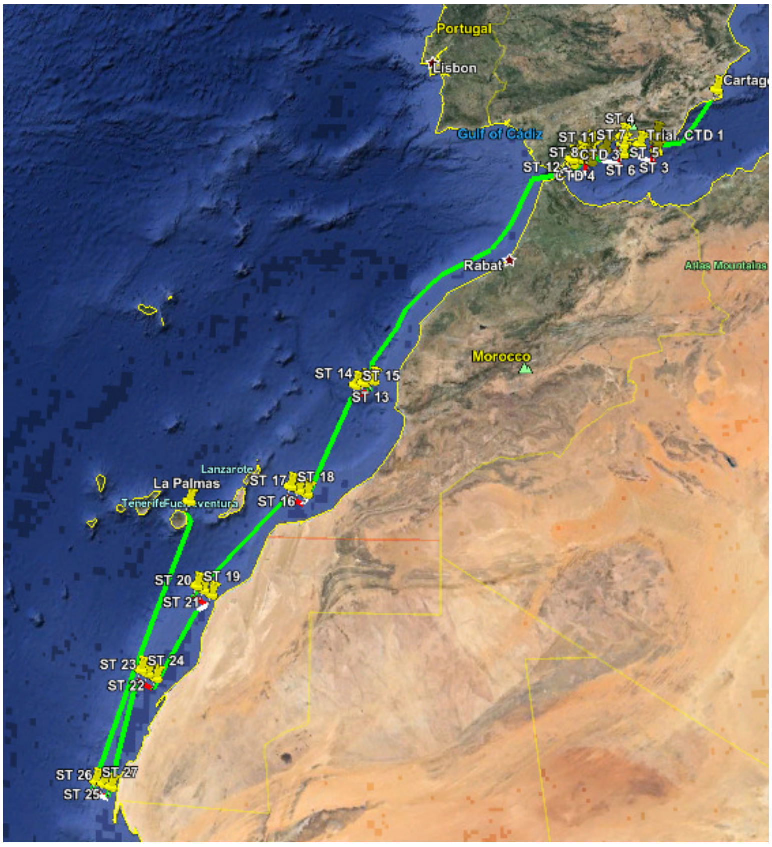

Figure 3.1: Cruise plan of the NATO ALOMEX'15 research cruise.

optical modem tests in sunny shallow waters served as an estimate of the ENEA modem performance in the presence of a filter to attenuate the solar light noise, and motivated the development of such filter for the next version of the modem. During the last years, several other modems with a higher level of maturity have been evaluated in real field experiments: Section 3.3 presents how performance and beam pattern of these modems have been included in the DESERT Underwater simulator in the form of lookup tables. Section 3.3.1 presents both the implementation details and how the LUTs extraction has been performed. The physical layer model so obtained takes into account the alignment between the transmitter and the receiver, and both the variation of the sunlight noise and the water turbidity along the water depth: the results, presented in Section 3.3.2, demonstrates the gap between such a realistic model and a simpler model based on the average water conditions of a certain area. Finally, in Section 3.4 we present our conclusions.

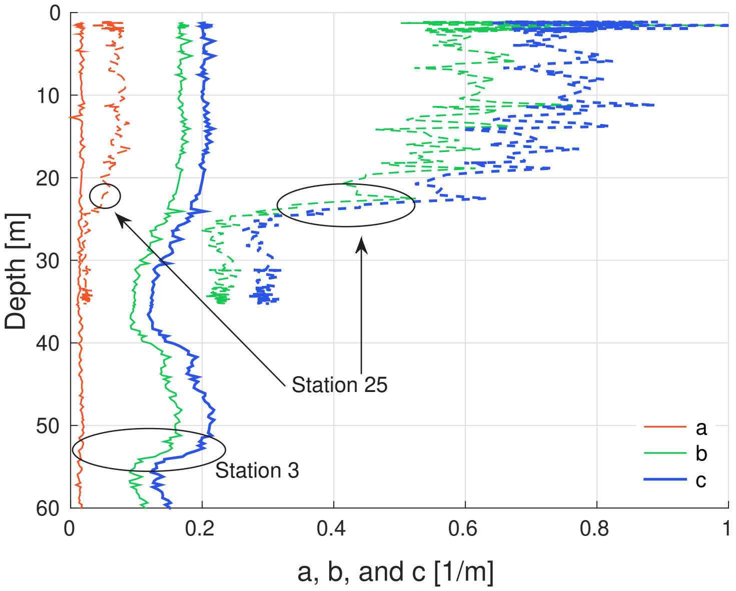

Figure 3.2: Measured light absorption (a, red) scattering (b, green) and total attenuation (c, blue) coefficients for stations 3 and 25 in Fig. 3.1.

3.2 Measurement-based optical simulator

We start from the implementation of a measurement-based optical communication simulator. This tool has been included in the DESERT Underwater framework [134], a state of the art underwater multimodal acoustic and optical network simulator and emulator. The optical transmission model is described in [127]: we extended such model in order to include the most important variable optical parameters of the channel, namely, the attenuation coefficient c, the scalar irradiance of the solar light E_0 and the temperature t, as lookup tables. In the following subsections we describe how these LUTs have been obtained from the raw data acquired during the ALOMEX'15 NATO cruise, and how they have been integrated in the optical propagation simulator. In Table 3.1 we list the optical parameters employed in the optical SNR formula.

3.2.1 Attenuation coefficients and received power

The optical absorption a and attenuation coefficients c of the water were measured using a Wet Labs Conductivity, Temperature and Depth (CTD) system equipped with an additional AC-s meter [136]. The measurement was carried out at different depths and covered the whole water column. Additionally, the coefficients a and c were measured at different wavelengths, from 400 nm to 735 nm. In a scenario where both the receiver and the

Table 3.1: Optical properties: notation and meaning

Notation	Meaning	Value
P_0	Source-radiated optical power	100 W
B	Signal bandwidth	100 kHz
A_t	Transmitter area	10 mm^2
θ	Transmitter's semi-aperture	1 rad
A_r	Receiver area	1.1 mm^2
S	Receiver sensitivity	0.26 A/W
R	Receiver's shunt resistance	1.43 GΩ
I_d	Photodetector's dark current	1 nA
q	Elementary charge	1.6 10^{-19} C
K	Boltzmann constant	1.38 10^{-23} JK^{-1}
T	Temperature	From measurements
E_0	Scalar irradiance of the solar light	From measurements
a	Absorption rate	From measurements
b	Scattering rate	From measurements
c	Total attenuation rate	From measurements

transmitter are placed at the same depth d, the value of c is constant, and the attenuation of a light beam in water can be calculated as (3.1)

$$P(r) = P_0 \cdot e^{-c(d)\cdot r}, \tag{3.1}$$

where $P(r)$ is the light power propagated to the receiver, assumed to be r meters from the transmitter. However, in case the transmitter and receiver are located at different depths, respectively d_{tx} and d_{rx}, c can vary largely. For this reason, we integrated the depth dependence of the parameter c along the the water column as in (3.2) below:

$$P(r) = P_0 \cdot \prod_{k=K_0}^{K_N} e^{-c(d_k)\cdot\Delta_r(d_k)}, \tag{3.2}$$

where $d_{K_0} = d_{\text{tx}}$ and $d_{K_N} = d_{\text{rx}}$, and $\Delta_r(d)$ is the distance covered by the beam around depth d_k where c can be assumed constant and equal to $c(d_k)$. Moreover, $\sum_{k=K_0}^{K_N} \Delta_r(d_k) = r$. When the CTD was cast, it measured values for c and d along the water column every 30 cm on average. With this granularity, the variability of two consecutive values of c is always less than 10%, and 0.8% on average. Hence, it is reasonable to employ linear interpolation to obtain the values of $c(d)$ at depths for which a measurement was not collected. Finally, following the model in [127] and assuming a perfect alignment between the transmitter and the receiver, call θ the transmitter's beam semi-aperture angle, A_r the receiver area and A_t the transmitter area. The optical power sensed by the receiver is computed as

$$P = P(r) \cdot \frac{2A_r}{\pi r^2(1-\cos\theta) + 2A_t}. \tag{3.3}$$

3.2.2 Optical noise: solar light noise and temperature gradient

The downwelling radiance of the sunlight has been measured with the free-falling Satlantic Hyperpro II radiometer [137] along the so-called euphotic zone, while the boat was moving straight at a constant speed. The data was collected at several wavelengths from 400 nm to 735 nm throughout the water column. Since the HyperPro measures only the downwelling radiance per unit wavelength E_d in W/(cm^2 nm), in the second case we applied a conversion based on the relation between the ratio E_0/E_d and the ratio between the scattering coefficient and the absorption coefficients b/a [138, page 180]. The scattering coefficient has been obtained from the relation $b = c - a$, while the ambient light noise at the receiver is calculated as $N_A = E_0(d)A_rS$.

The CTD also provided measurements of the temperature T of the water throughout the water column. The temperature at the receiver is employed to compute the amount of the thermal noise affecting the reception, which is related to the shunt resistance, the series resistance and the load resistance: $I_j = \sqrt{4KTB/R}$, where R is the shunt resistance, that approximates well the combination of the resistances described above. Finally, the optical SNR is computed as

$$SNR = \frac{P \cdot S}{2q(I_d + S \cdot P)B + 4KTB/R + N_A^2} \,. \tag{3.4}$$

The optical measurements included in our simulations are presented in Figure 3.3.

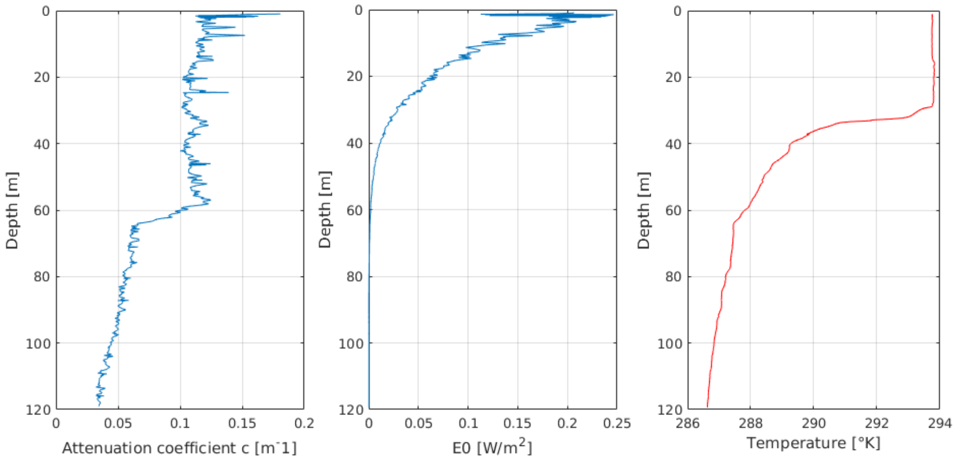

Figure 3.3: Variation of the optical parameters along the water column. From left: attenuation coefficient c, sunlight noise irradiance E_0 and water temperature T.

In order to emphasize how the variation of the sunlight noise irradiance E_0 and of the total attenuation coefficient c affect optical propagation in a real scenario, we report in Fig. 3.4 the coverage area of an omni-directional transmitter, represented as a red diamond, placed at a depth of 15 m, 45 m and 75 m in a water column of about 120 m. The coverage area is defined as the region of the watercolumn where the SNR would be higher than 20 dB. The coverage area is shown both in the presence of sunlight noise (black line) and for night-time operations in dark waters (blue line), when the sunlight noise is considered to be negligible. The results in Fig. 3.4 highlight the asymmetric shape of the coverage region, and the fact that the region broadens when the transmitter is placed at a deeper location. The latter is due both to the trend followed by c, which tends to decrease with depth regardless of the presence of sunlight noise, and to the lower sunlight noise irradiance.

3.2.3 Simulation scenario and system configuration

We simulate a scenario akin to those presented in [25] and [139] (Fig. 3.5), where one or more AUVs perform data-muling operations along a network of submerged sensors clusters. A similar scenario is also considered in [27], where the authors focus on optimizing the AUV trajectory to maximize both throughput and power efficiency. In our scenario, each cluster acts as an autonomous data collection entity, and is disconnected from other clusters. The distance between two adjacent clusters is 400 m, each cluster is deployed at different water depths, from 15 to 125 m, and therefore incurs different water conditions. A clusterhead is elected within each cluster to be the only node which can directly talk with a passing AUV.

In this context, acoustic communications are employed to exchange low-rate data when the AUV is cruising from one node to another; high-rate optical communications, instead, support short-distance message transmission at a very high bit rate, and can be exploited whenever the AUV is sufficiently close to a node. A signaling mechanism to automatically detect when to switch between optical and acoustic communications is employed in the communications stack. Such mechanism has been described first in [140], where we proved the effectiveness of adding a signaling system to a switching strategy based on the perceived power, in a scenario where all the nodes are placed at the same depth and with the same optical channel conditions.

In our case, a purely threshold-based switching algorithm cannot be employed, due to the high variability of the water conditions. In our solution, the AUV probes the optical channel every time it approaches a node, and the switch between acoustic and optical communications occurs only when such probe exchange is successful. To reproduce this behavior, we estimate the distance between the transmitter and the receiver based on the perceived acoustic power: the probing system starts when the estimated distance is

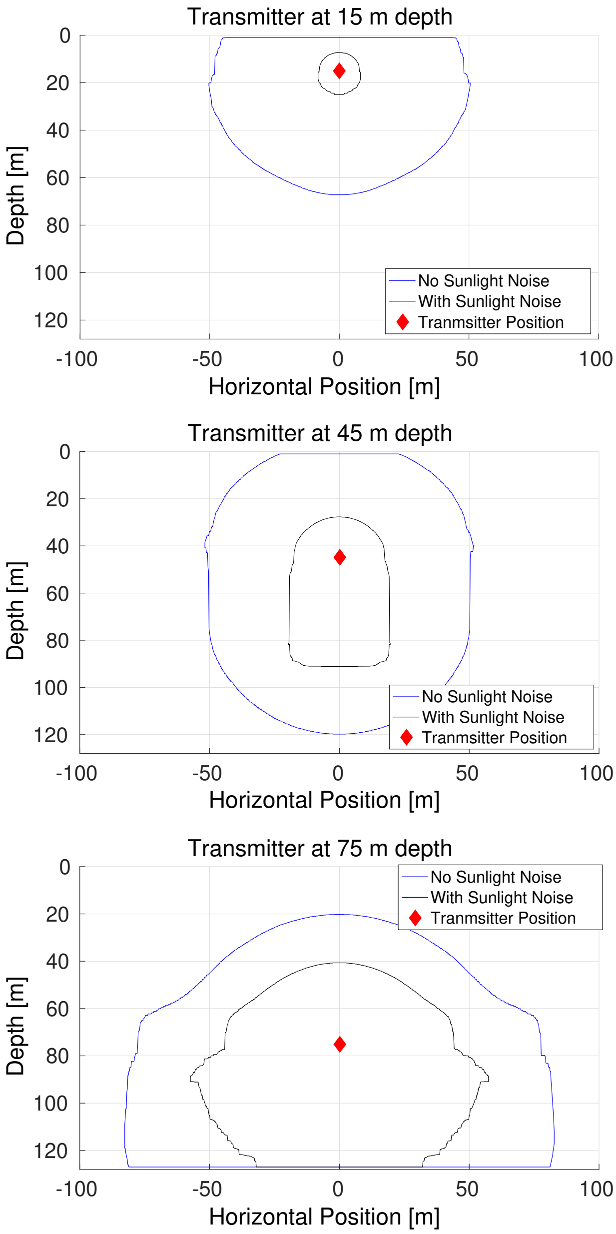

Transmitter at 15 m depth

Transmitter at 45 m depth

Transmitter at 75 m depth

Figure 3.4: Optical modem coverage area, depending on the transmitter depth. When the transmitter is deeper the region broadens due to a lower c and a lower E_0 (in the presence of sunlight noise).

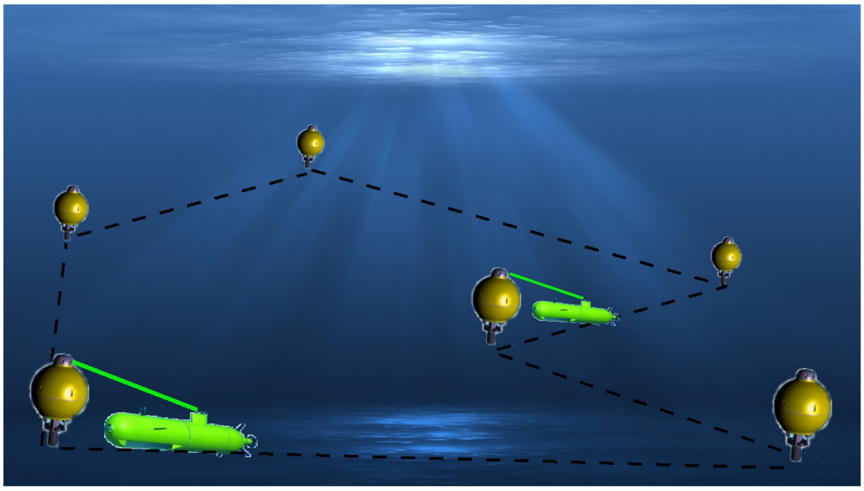

Figure 3.5: Simulation scenario with two AUVs and six sensor clusters deployed at different depths. The AUVs hover through the network area and collect data from the clusters. The trajectory of the AUVs is shown as a dashed line.

smaller than or equal to the maximum optical communication range. On the other end, as soon as the AUV does not receive any packets for a fixed period, it probes the optical channel again. If the probe fails due to packet loss, it switches back to acoustics. Such a system largely fits any applications where the traffic is strongly asymmetric. For example, this is the case when underwater nodes are expected to send large amounts of data to the AUV, whereas the latter only transmits sporadically, such as in a data-muling application.

In our simulation, the speed of sound under water is assumed to be constant and equal to 1500 m/s, while the speed of light is set to $\simeq 2.25 \cdot 10^8$ m/s. We simulate the behavior of the EvoLogics HS acoustic modem [42] for acoustic communications; this modem works at a carrier frequency of 150 kHz and provides a bandwidth of 60 kHz, a nominal maximum transmission rate of 62.5 kbps (as reported in the modem data sheet [42]), a maximum transmission power of 10 W and a nominal operational SNR of 10 dB. The acoustic bit rate is set to 40 kbps, with a source level of 150 dB re μPa at 1 m from the source.

The optical transmission model is implemented according to the description in Section 3.2, assuming an optical wavelength $\lambda = 532$ nm. The SNR threshold for optical reception is set to 20 dB. The optical transmitter has a transmission rate of 1.5 Mpbs and a transmission power of 100 W. In addition, although our simulator can consider directional beams and non line of sight optical communications as well, we force perfect alignment between transmitter and receiver, which fits well optical transceiver architectures

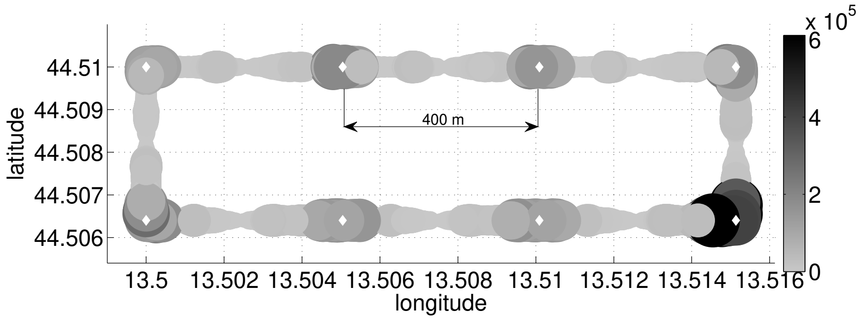

Figure 3.6: Throughput of the link between the AUV and the node closest to it. The white diamonds represent the node locations.

made of multiple emitting and receiving elements arranged, e.g., in a hemispherical topology. The sunlight noise and the temperature gradient have been taken into account as explained in Section 3.2.2. The maximum optical range in such scenario is 62 m, that corresponds to an acoustic threshold of 120 dB re μPa^2 at 1 m from the source. When the mean received power passes such threshold, we assume that the AUV is approaching a node and the probing mechanism described above begins. The results of such simulations are shown in Section 3.2.4.

3.2.4 Results and performance comparison

In order to highlight the benefits of an optical communication simulator based on real channel measurements with high variability of attenuation coefficient and solar noise along the water column, we deploy the nodes at different depths, and set the corresponding AUV waypoints to match such depths. In particular, the northwest node is placed at a depth of 20 m, and the southeast node is placed at a depth of 120 m, whereas the other nodes are placed at intermediate depths.

Fig. 3.6 represents the instantaneous throughput as a function of the AUV position: the thinner the line and the lighter its gray color shade, the lower the throughput. Fig. 3.6 shows that the switching mechanism described in Section 3.2.3 is effective: when the AUV approaches a node, the system switches from acoustic to optical communications, and the throughput becomes higher. On the other hand, when the AUV covers the distance from one node to the following one, it switches back to acoustic communications, in order to maintain an active link with the closest node. We can observe a very high throughput close to the deepest node, i.e., the node located at the bottom-right position in the figure. This is due to the fact that solar light noise is negligible at a depth of 120 m, and in addition the attenuation coefficient is much smaller than close to the water surface.

Such a behavior is further detailed in Fig. 3.7, where we report the cumulative distribution function (CDF) of the instantaneous throughput at the receiver, for communications at a depth of 20 to 80 meters from the surface (solid line) and at a depth of 80 to 120 meters (solid line with diamond markers). The difference between the two cases is not very large for a distance above 85 m, where the optical communications cannot be employed; on the contrary, the achievable throughput is much higher in a deep water scenario when the distance decreases below 85 m.

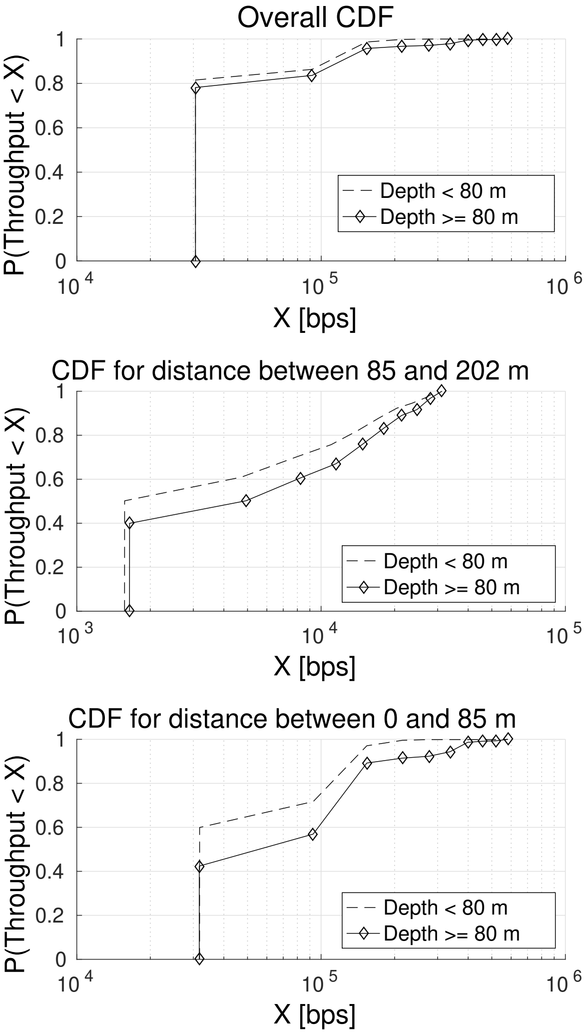

Figure 3.7: Cumulative distribution function of the throughput between the AUV and the node closest to it.

This simulation study suggests that the impact of sunlight noise on the performance of underwater optical communication systems is very large. These results were discussed with the optical communications team of the ENEA Casaccia research center in Italy, who are developing an underwater optical modem prototype for underwater robotic networks. The prototype was tested in a lake experiment in very shallow waters before proceeding further with the development in order to assess the impact of sunlight noise on the receiver. The next section reports on these experiments and the related conclusions.

3.2.5 Real measurements of optical communication

We performed a lake test of ENEA's proof-of-concept (PoC) optical modem prototype from October 10 to October 12, 2016 at the Bracciano lake, Italy. The PoC modem has three sides, as seen in Fig. 3.8, which make it possible to achieve virtually omni-directional communications. The modem can transmit packets within short ranges, at a bit rate of up to 1 Mbps. The transceiver of the modem has been made using off-the-shelf photo-sensors with human-eye wavelength sensitivity, and blue and white high power LED matrix emitters, usually employed for night lighting. An Arduino Mega board [141] provides the electronics and logic to drive the transceiver. In this preliminary stage, both the transmit power and the receiver-side signal acquisition thresholds are manually set and calibrated. Such calibration was one of the main issues for the experiment, as the external conditions were not stable. The new version of the prototype will employ a self-calibrating system.

The modem was powered with a 48 V external DC power supply, and the data to be transmitted was transfered from a laptop to the modem via an Universal Serial Bus (USB) cable. The test has been carried out with a bit rate of 0.5 Mbps and a packet size of 224 bits. The maximum packet size was determined based on the charging time of a capacitor in the low-pass filter employed by the receiver hardware. Such capacitor became fully charged a few milliseconds after the reception started, which made it impossible to detect longer packets correctly. This design shortcoming was set to be revised for the next version of the PoC modem.

In our setting, the distance between the transmitter and the receiver was approximately 1.5 m, and the water depth 1.3 m. The water was very clear fresh water, the sky was also clear of clouds and the whole experiment was carried out around noon in strong sunlight conditions (see Fig. 3.9).

The DESERT Underwater emulator was employed to perform transmission and reception of the packets via the PoC optical modem. Details and packet delivery ratio (PDR) figures for five different tests carried out during the experiment are reported in the list below.

1. During the fist dry test we performed the transmissions in darker conditions and in the absence of background lighting: this resulted in the successful transmission of 60% of the packets.

2. A second dry test has been carried out in the presence of blurred background light: in these conditions, the PDR achieved by the modem

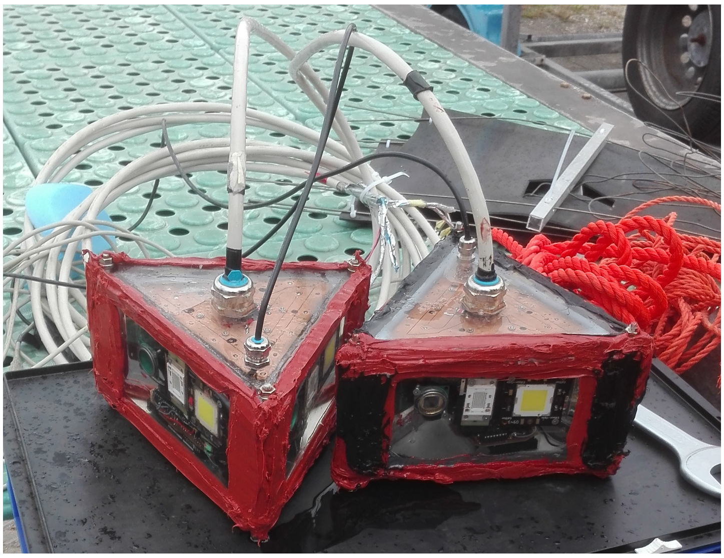

Figure 3.8: ENEA's proof-of-concept optical modem.

was around 50%.

3. A final dry test was carried out in the presence of a strong background light, which led to a PDR of 5%, in addition to an unstable behavior caused by the saturation of the receiver electronics.

4. A first lake test was carried out by operating the modems in the shade offered by the pier from where the equipment was deployed. The obtained PDR in these conditions was about 10%.

5. A second lake test faced strong sunlight noise, and yielded a PDR of 2% or less. This figure was partly due to the strong sunlight noise, and partly to the saturation of the receiver.

The third dry test and both the lake tests have been performed in unstable conditions, and for this reason the obtained PDR was very small. In both the third dry test and the latter lake test, the strong background light noise caused the saturation of the receiver and the consequent loss of packets. On the other hand, although in the former lake test we exploited the shade offered by the pier, the sunlight noise effect was still very strong. Indeed, we were not able to obtain a uniform and stable shadow due to both the small size of the pier (Figure 3.9) and the shifting of the sun.

The PoC version of the ENEA Casaccia modem was not designed to withstand the pressure of deeper waters. However, these preliminary results already highlight that the impact of sunlight noise on underwater optical communications cannot be neglected, and possibly requires a carefully designed sunlight noise cancellation mechanism at least to avoid the saturation

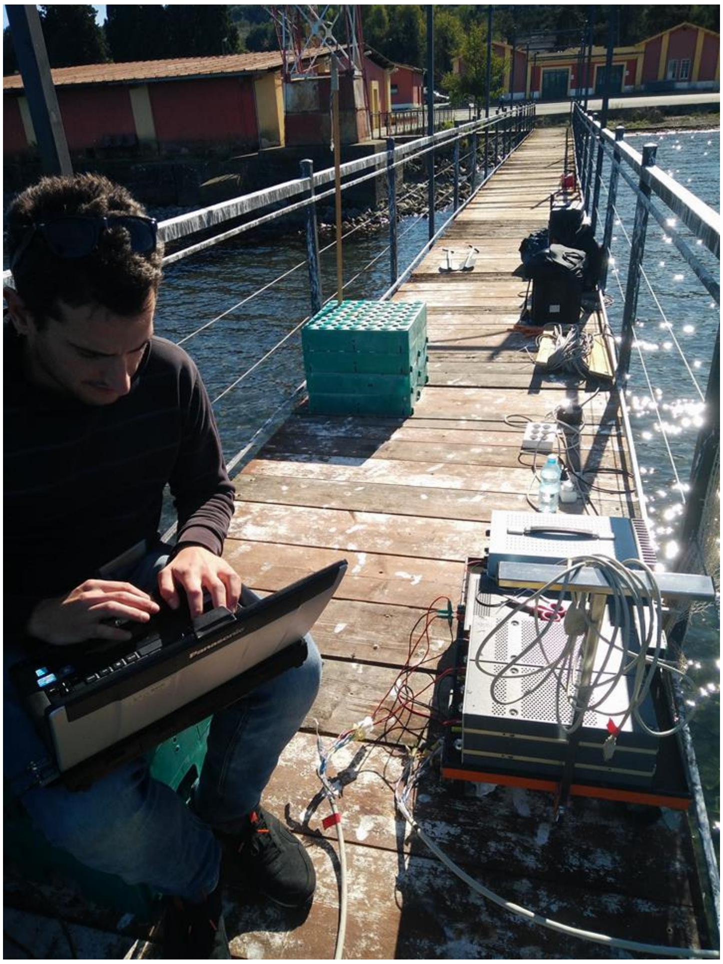

Figure 3.9: Sunlight conditions during the lake experiment.

of the light detector at the receiver. An automatic mechanism to adaptively calibrate the reception threshold would also reduce wrong signal detections and trigger packet reception optimally in different illumination scenarios. Both improvements are under development at ENEA and will be incorporated in the next version of the modem.

3.3 Beam pattern and real performance of underwater optical modems

Performing a simulation of underwater optical communications that matches well the actual performance of real optical modems is very challenging, as each manufacturer, as well as each research institute that developed its own modem prototype, employs a different transmitter light source and a different receiver, that cannot be modeled in the same way due to the different physical properties. For instance, in [127] the authors employed a set of blue light emitting diodes (LEDs) as a transmitter, and a Si-PIN photo-diode [142] as a receiver, while in [3] the receiver choice was an avalanche photodiode (APD) [143]. Instead, in [17] the authors used a prism of blue LED matrices as transmitter and a receiver based upon a photomultiplier (PMT) [144]. In [2], they used a LED-based transmitter and a Silicon Photomultipliers (SiPMs) [145] receiver. In [146], the authors employed a blue and a white LED matrices as transmitter, and a photo-sensors with human-eye wavelength sensitivity receiver. Instead, both in [147] and [128], they employed a laser transmitter and a PMT receiver.

Another challenging aspect is to predict how underwater optical communication reacts to the surrounding light noise. Direct light noise to the modem may saturate the receiver, causing the loss of the signal. Some companies and research institutes propose a modem able to limit this effect, with a noise compensation system [11, 17, 146]. However, most of these mechanisms are patented or proprietary, and therefore it is not possible to model them with free access.

Many models for simulating underwater optical communications have been presented in the literature, as already presented in this chapter. Monte Carlo-based models ([147], [128]) are computationally expensive, specially for emitters composed by multiple light sources, such as matrices of LEDs. The Beer-Lambert's exponential law [127] based on the attenuation coefficient `c` is used very often, however, neither an LED nor a laser is a perfect Lambertian light source. In addition, in [45] the authors state that the parameter `c` should only be used in the case of a narrow collimated light beam, such as a laser diode. Instead, in the case of an uncollimated beam emitter, like an LED, `c` does not characterize the light propagation adequately, and should be replaced by the diffuse attenuation coefficient $\mathtt{K}_d$. Section 3.2.1 presents how the optical properties of the water varies along the water column. For this reason, in Section 3.2 we included a database of water properties to characterize real scenarios, and modeled underwater optical communications by integrating the Beer-Lambert's law along the water column. In this section, we extended this approach by including a database of modem performance figures, in order to match the behavior of real transmissions, by overcoming the problem of the Beer-Lambert's law. This model has been included in the DESERT Underwater simulator [74], available online [148].

3.3.1 Implementation details in DESERT Underwater

In this section we describe how the real performance of underwater optical communications has been modeled. In Section 3.3.1, we describe the performance lookup tables extrapolation, while in Section 3.3.1 we present the optical beam pattern model that has been implemented in the DESERT

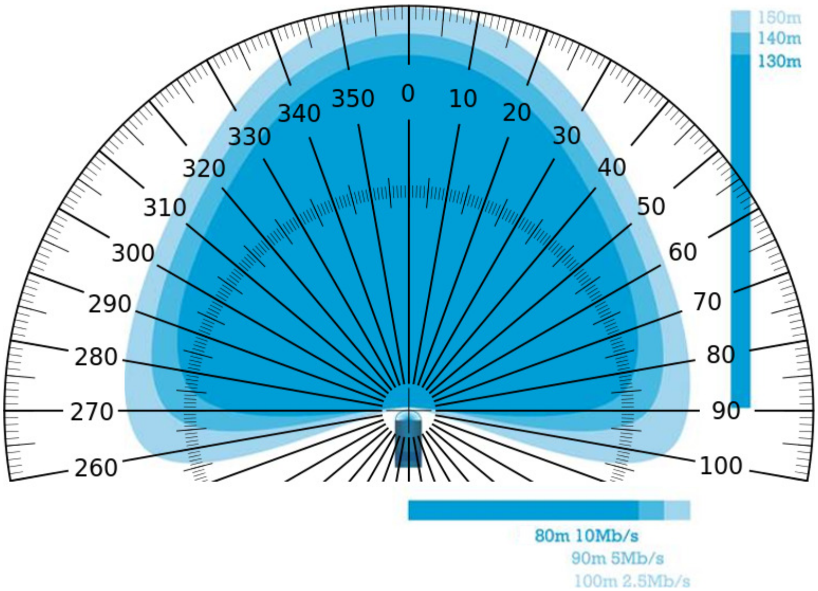

Figure 3.10: BlueComm 200 operational area [1] in ideal water conditions.

Underwater simulator.

Lookup table extraction

In order to include the performance figures of an optical modem in the DESERT Underwater simulator, we extrapolated a set of LUTs from the beam pattern of some state of the art transceivers. For example, the BlueComm 200 beam pattern in ideal water conditions, for different levels of bit rate, namely 2.5, 5 and 10 Mbps, is presented in Figure 3.10 [1], and the Ifremer optical modem beam pattern is depicted in Figure 3.11 [2], when transmitting at 3 Mbps. From this figure we extrapolated the LUT of the beam pattern section (LUT$_{bp}$), composed of inclination angle from the transmitter with respect to the receiver (θ) and the normalized maximum range achievable at that angle ($n_r(\theta)$). n_r has been calculated as

$$n_r(\theta_k) = R(\theta_k)/R(0), \tag{3.5}$$

where $R(\theta)$ is the maximum transmission range when the inclination between transmitter and receiver is $\theta = \theta_k$, and $R(0)$ is the maximum transmission range when transmitter and receiver are perfectly aligned. OPT transmitters and receivers may have a different operational area, and therefore a different LUT$_{bp}$. This is the case of the MIT AquaOptical prototype [3] (Figure 3.12). The 3D beam pattern is obtained from the rotation of the provided performance figures along the transmitter direction.

We then built the LUT of the maximum range achievable in different water conditions (LUT$_{cr}$) for that modem. For instance, the maximum range

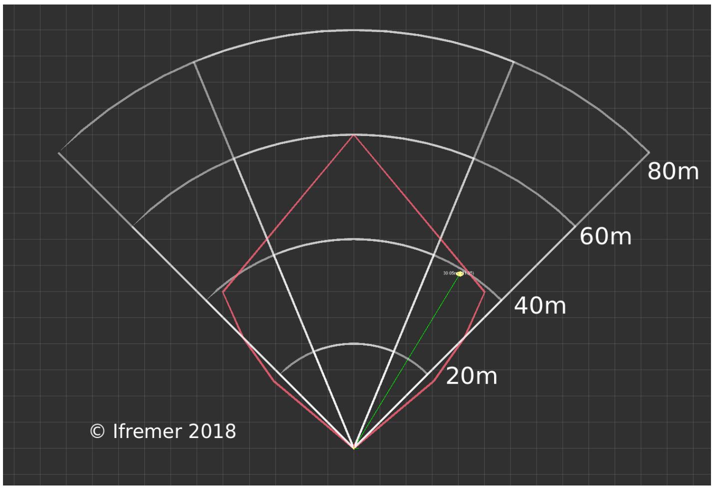

Figure 3.11: Ifremer optical modem operational area when transmitting at 3 Mbps [2] in shallow water at night, turbidity Jerlov I ($c \simeq 0.02\ m^{-1}$).

$\mathbf{c}$ $[\mathbf{m}^{-1}]$	$\mathbf{R}_{deep}$ [m]	$\mathbf{R}_{nigth}$ [m]
0.0001	150	100
0.02	140	90
0.65	87	70
2	32	30

Table 3.2: BlueComm 200 maximum transmission range at different water conditions, when transmitting at 2.5 Mbps.

of the BlueComm 200 is reported in Figure 3.13 in the case of deep water (red line) and shallow water (blue line) scenarios, during night operations close to the coast. In the latter case, the light noise caused by moon, stars, coastal and ship lighting lowers the maximum transmission distance of underwater optical communications. In order to create a more fine-grained LUT, we employed the MatLab Piecewise Cubic Hermite Interpolation (PCHIP) [149], that allowed us to smoothly fit the samples (Figure 3.13).

Beam pattern model

Given a 3D space, we set the transmitter at the origin of the axes and we compute the inclination angles between the transmitter and the receiver. To find the maximum transmission range we compute both the inclination angle θ^{tx} between the (X-Y) plane and the straight line connecting transmitter and receiver, and the angle θ^{tx}_{XY} between the x-axis and the projection on the (X-Y) plane of the straight line connecting the transmitter and the receiver. A visualization of the inclination angles used in the model is reported in

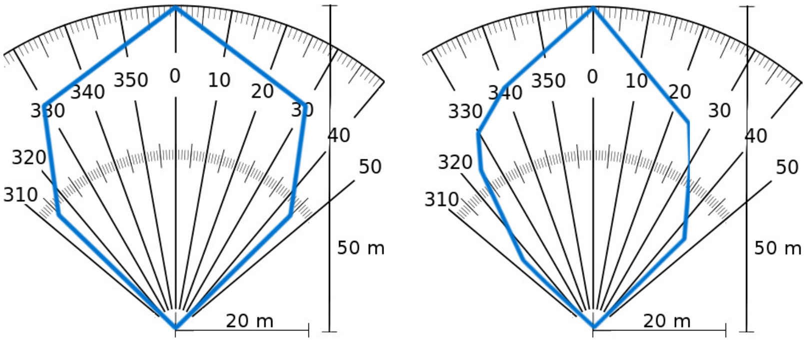

Figure 3.12: The MIT AquaOptical modem operational area when the transmitter position is fixed and the receiver changes the position pointing to the transmitter (left hand side) and when the receiver is fixed and the transmitter changes the position pointing to the receiver (right hand side) as reproduced from [3]. The experiment took place in a pool, transmitting at 4 Mbps in shallow water at night, turbidity Jerlov I ($c \simeq 0.02\ m^{-1}$).

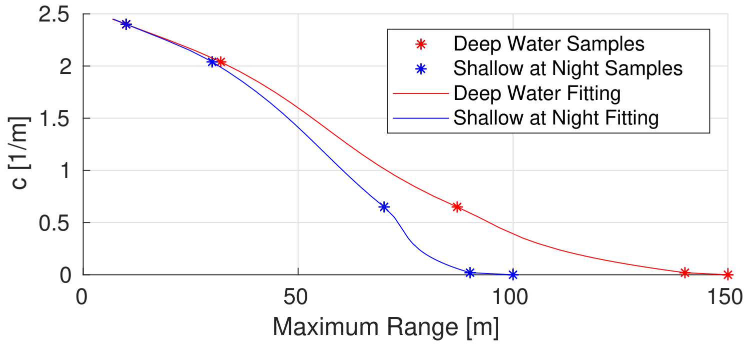

Figure 3.13: BlueComm 200 maximum transmission range in different water conditions, when transmitting at 2.5 Mbps.

Figure 3.14. In general, considering a spherical coordinate system, θ is the polar angle and θ_{XY} is the azimuthal angle. These angles have to be computed both from the transmitter's point of view and from the receiver's point of view. By default, we suppose the modem of each node to be placed in the (X-Y) plane and directed along the x-axis. We define the direction of the modem as the direction of the maximum transmission range $R(0)$, presented in Section 3.3.1. In our model, the modem can be rotated with a rotation angle α along the (X-Z) plane. α is used to point the transmitter and receiver towards each other. Positive values of α correspond to a clockwise rotation and negative values of α to a counterclockwise rotation, i.e., with $\alpha = \pi/2$ the modem is directed toward the positive values of the z-axis and with $\alpha = -\pi/2$ rad the modem is directed toward the negative values of the z-axis, by considering the modem at the origin of the 3D space. Transmitter and receiver have their own rotation angles, α_{tx} and α_{rx} respectively.

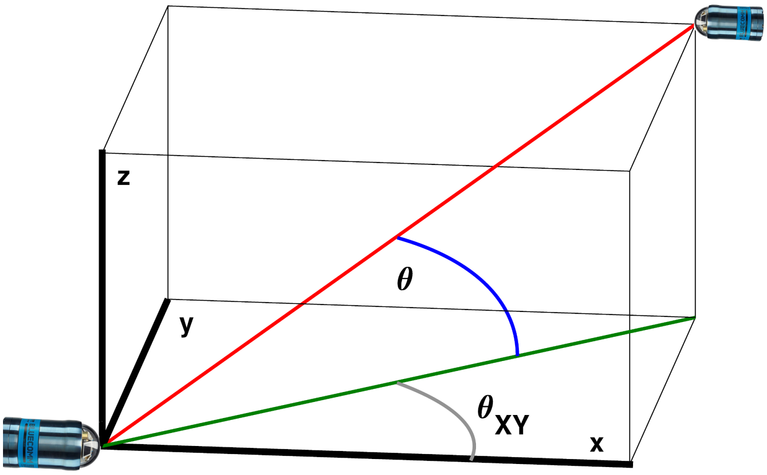

Figure 3.14: Representation of the angles θ and θ_{XY}.

First of all we compute the polar and the azimuthal angles from the transmitter's point of view, i.e., we compute θ^{tx} and θ^{tx}_{XY}. Given the position of the transmitter (x_{tx},y_{tx},z_{tx}) and the position of the receiver (x_{rx},y_{rx},z_{rx}), to apply our model we first compute the new coordinates of the receiver by considering the transmitter as the origin of our new 3D space:

$$\begin{aligned}\Delta^{rx}_x &= x_{rx} - x_{tx}\\ \Delta^{rx}_y &= y_{rx} - y_{tx}\\ \Delta^{rx}_z &= z_{rx} - z_{tx}.\end{aligned} \tag{3.6}$$

We consider the rotation angle of the transmitter equal to α_{tx}. As the first step, to compute θ^{tx} and θ^{tx}_{XY}, we perform the rotation of the axes by an angle $-\alpha_{tx}$ with respect to the y-axis. In this way the new reference system has the x-axis in the direction of the transmitter modem. The position of the receiver in the new reference system is given by

$$\begin{aligned}\tilde{\Delta}^{rx}_x &= \Delta^{rx}_x \cos(-\alpha_{tx}) - \Delta^{rx}_z \sin(-\alpha_{tx})\\ \tilde{\Delta}^{rx}_y &= \Delta^{rx}_y\\ \tilde{\Delta}^{rx}_z &= \Delta^{rx}_x \sin(-\alpha_{tx}) + \Delta^{rx}_z \cos(-\alpha_{tx}).\end{aligned} \tag{3.7}$$

To compute the inclination angle θ^{tx}, first we compute

$$d^{rx}_{XY} = \sqrt{(\tilde{\Delta}^{rx}_x)^2 + (\tilde{\Delta}^{rx}_y)^2}, \tag{3.8}$$

then, if $d^{rx}_{XY} = 0$, θ^{tx} is given by

$$\theta^{tx} = \begin{cases} \pi/2 & \text{if } \tilde{\Delta}^{rx}_z > 0 \\ -\pi/2 & \text{if } \tilde{\Delta}^{rx}_z < 0 \end{cases} \tag{3.9}$$

Otherwise, if $d^{rx}_{XY} > 0$, θ^{tx} is given by

$$\theta^{tx} = \arctan \frac{\tilde{\Delta}^{rx}_z}{d^{rx}_{XY}}. \tag{3.10}$$

To compute θ^{tx}_{XY}, if $\tilde{\Delta}^{rx}_x = 0$, the inclination angle is given by

$$\theta^{tx}_{XY} = \begin{cases} \pi/2 & \text{if } \tilde{\Delta}^{rx}_y > 0 \\ -\pi/2 & \text{if } \tilde{\Delta}^{rx}_y < 0 \end{cases} \tag{3.11}$$

otherwise, if $\tilde{\Delta}^{rx}_x > 0$, the angle is equal to

$$\theta^{tx}_{XY} = \arctan \frac{\tilde{\Delta}^{rx}_y}{\tilde{\Delta}^{rx}_x}. \tag{3.12}$$

where the inverse tangent must be suitably defined to take the correct quadrant of the (X-Y) plane into account.

In a similar way, we compute the inclination angles from the receiver's point of view, i.e., θ^{rx} and θ^{rx}_{XY}. In this case we set the receiver to be at the origin of our new 3D space. We compute the inclination angle θ^{rx} between the (X-Y) plane and the straight line connecting transmitter and receiver, and the angle θ^{rx}_{XY} between the x-axis and the projection on the (X-Y) plane of the straight line connecting the transmitter and the receiver. The rotation angle of the receiver modem is α_{rx}. To set the receiver at the origin of the 3D space, the coordinates of the transmitter become

$$\begin{aligned} \Delta^{tx}_x &= x_{tx} - x_{rx} \\ \Delta^{tx}_y &= y_{tx} - y_{rx} \\ \Delta^{tx}_z &= z_{tx} - z_{rx}. \end{aligned} \tag{3.13}$$

Then we perform a rotation of the axes with respect to the y-axis by an angle $-\alpha_{rx}$. The coordinates of the transmitter in the new reference system become

$$\begin{aligned} \tilde{\Delta}^{tx}_x &= \Delta^{tx}_x \cos(-\alpha_{rx}) - \Delta^{tx}_z \sin(-\alpha_{rx}) \\ \tilde{\Delta}^{tx}_y &= \Delta^{tx}_y \\ \tilde{\Delta}^{tx}_z &= \Delta^{tx}_x \sin(-\alpha_{rx}) + \Delta^{tx}_z \cos(-\alpha_{rx}). \end{aligned} \tag{3.14}$$

Using these coordinates, the way to compute θ^{rx} and θ^{rx}_{XY} is the same employed for the transmitter. From the LUT$_{bp}$ of the transmitter and the LUT$_{bp}$ of the receiver, we obtain the normalized attenuation coefficients $n^{tx}_r(\theta^{tx})$, $n^{tx}_r(\theta^{tx}_{XY})$, $n^{rx}_r(\theta^{rx})$, $n^{rx}_r(\theta^{rx}_{XY})$. If the angle obtained with the previous computations is not an entry of the LUT$_{bp}$, a linear interpolation is performed to find the actual attenuation coefficient.

The last step is to find the maximum transmission range for the given water conditions. If transmitter and receiver are at the same depth d, we retrieve the value of c in the LUT related to this depth. If the actual value of d is not an entry of the LUT, a linear interpolation is performed. If the transmitter and the receiver are at different depths, we compute the equivalent value of the attenuation coefficient (c_{eq}), and find the maximum transmission range for c_{eq}. Given d_N and c_N the depth and the attenuation coefficient of the deeper node and d_1 and c_1 the values related to the other node, c_{eq} is computed as the weighted average of c, using as weights the depth between 2 values of c in the LUT:

$$c_{eq} = \frac{1}{d_N - d_1} \sum_{k=1}^{N-1} \frac{c_k + c_{k+1}}{2} (d_{k+1} - d_k). \tag{3.15}$$

If the maximum transmission range for the given c_{eq} is $R(0)$, the actual transmission range considering the relative position of the transmitter and receiver is

$$R = R(0) \cdot n_r^{tx}(\theta^{tx}) \cdot n_r^{tx}(\theta_{XY}^{tx}) \cdot n_r^{rx}(\theta^{rx}) \cdot n_r^{rx}(\theta_{XY}^{rx}). \tag{3.16}$$

3.3.2 Resulting beam pattern in real scenarios

In this section we present the results for the maximum transmission range of the Bluecomm 200 simulated in a real scenario. In this case we suppose that LUT$_{bp}$ is the same for the transmitter and the receiver. For each scenario, we placed the transmitter in a static position, with the rotation angle $\alpha_{tx} = 0$ rad, and moved the receiver in different positions to find the maximum transmission range in which receiver and transmitter still communicate. In all the positions, the receiver has a rotation angle $\alpha_{rx} = \pi$ rad. We used the values of the attenuation coefficient c and noise measured during the ALOMEX'15 research cruise in 2 different locations. For each location, the average value of the attenuation coefficient $\bar{c}$ has been calculated along the water column, using Equation (3.15) with $d_1 = 1$ m and d_N equal to the maximum depth of the water column. The resulting beam pattern has been computed in four cases:

1. case 1: variable attenuation coefficient for different depths in the presence of surrounding light noise during a night operation;

2. case 2: variable attenuation coefficient for different depths in deep dark water;

3. case 3: $c = \bar{c}$, in the presence of surrounding light noise during a night operation;

4. case 4: $c = \bar{c}$, in deep dark water.

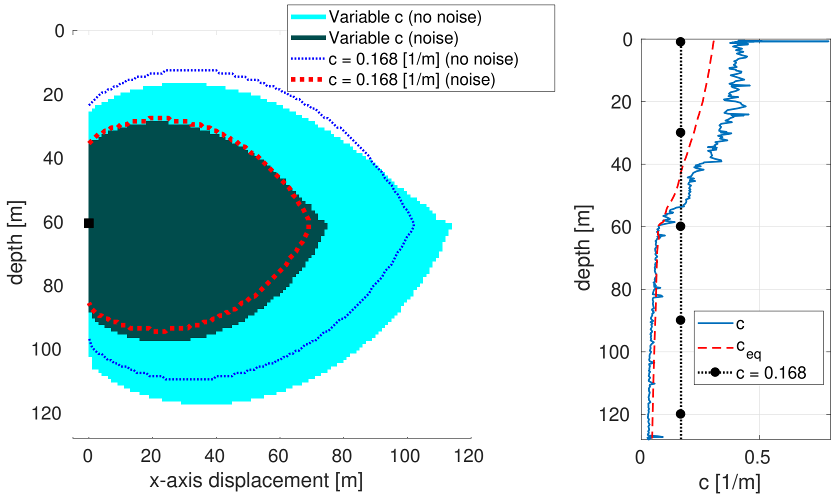

Figure 3.15: Maximum transmission range in a water column of 128 m, left hand side, and the corresponding values of the attenuation coefficient and c_{eq}, right hand side.

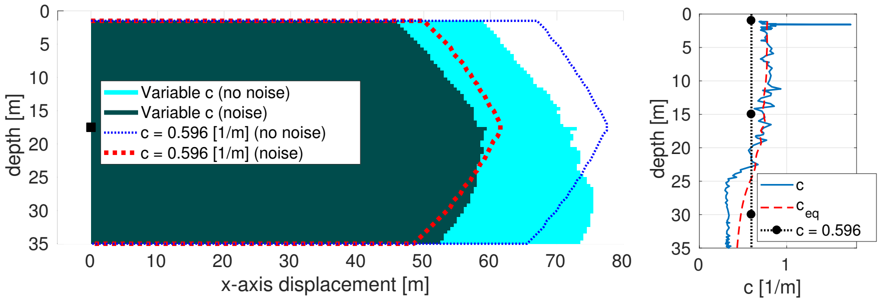

Figure 3.16: Maximum transmission range in a water column of 35 m, left hand side, and the corresponding values of the attenuation coefficient and c_{eq}, right hand side

The first location has latitude 30°42.52′ N and longitude 10°18.68′ W, offshore the coast of Morocco. In this scenario the water column depth is 128 m and the transmitter is placed at a depth of 60.5 m. In Figure 3.15, right hand side, both the values of the attenuation coefficient for each depth (solid blue line) and the values of c_{eq} (dashed red line) computed from the transmitter point of view are depicted. In this location $\bar{c} = 0.168$ m^{-1}, and the maximum transmission range is reported in Figure 3.15. We can observe that in both case 3 (dotted red line) and case 4 (dotted blue line), the maximum transmission range is symmetric with respect to the transmitter depth. In cases 1 (dark green region) and 2 (turquoise region), instead, for depth bigger than the transmitter depth, the transmission range is wider than in cases 3 and 4, because the values of c_{eq} are smaller than $\bar{c}$. On the contrary, for a depth lower than the depth of the transmitter, the transmission range is smaller with respect to cases 3 and 4, as c_{eq} is greater than $\bar{c}$.

The second location has latitude 23°50.41′ N and longitude 16°09.86′ W, offshore the coast of Western Sahara. In this location the water column is 35 m deep and the transmitter is placed at a depth of 17.5 m. In Figure 3.16, right hand side, both the actual values of c for each depth (solid blue line) and the values of c_{eq} computed from the transmitter point of view (dashed red line) are presented, and $\bar{c} = 0.596\ \text{m}^{-1}$. The maximum transmission range has been computed in the 4 cases and is reported in Figure 3.16, left hand side. Similarly to the previous case, the transmission range becomes bigger at increased depth, following the trend of the attenuation coefficient. In this scenario, the maximum transmission range along the x-axis is lower than in the first location, because the attenuation coefficient in this area is bigger than in the previous one, due to the high turbidity of the water.

3.4 Conclusions

In this chapter, we presented a measurement-driven optical channel model and its implementation as part of the DESERT Underwater network simulator. The model incorporates samples of three different optical parameters: the temperature, the total attenuation coefficient of the water, and the downwelling solar light irradiance. Such samples have been collected in the context of the NATO STO CMRE ALOMEX'15 scientific cruise. Both parameters are included as part of a depth- and distance-dependent signal-to-noise ratio model that can be used to simulate the performance of optical links. In addition, real modems' beam patterns have been added into the simulator, thus including into the model the realistic effect of the alignment between the transmitter and the receiver as well. Through a simulation study, we proved the model's capability to simulate different water conditions and depth-dependent optical performance.

Notes

Part of this work has been published in [12] and [150].

Chapter 4

Relationship between underwater optical and acoustic channels

4.1 Introduction

In the last decade, ocean exploration has increased considerably through underwater surveys. The purposes of these surveys include bathymetry mapping and natural resource prospection, maintenance (environmental monitoring and structural inspection of underwater facilities such as drilling devices and pipelines), and securing marine infrastructures against intruders. The ability to wirelessly exchange information among submerged devices is a key enabling technology to perform these tasks. As already discussed in Chapter 1, the two top technologies for underwater wireless transmission are underwater acoustic communications and underwater optical communications. Acoustic communications are characterized by long-range (in the order of tens of km) but low-data-rate transmissions (up to a few kbps), and can support only low-traffic demanding applications due to the limited bandwidth, long delay spread, short channel coherence time, and dispersiveness that characterize the acoustic channel [151]. Optical communications feature high data rates (in the order of Mbps), but is only suitable over much shorter transmission ranges (in the order of tens of meters, as presented in Chapter 3).

Acoustic and optical communications are driven by different physics. The former, as detailed in Chapter 2, involves the propagation of a pressure wave and is modeled, e.g., via the so-called normal modes [55, 57] or empirical equations [124], whereas the latter (described in Chapter 3) is performed via electromagnetic waves whose propagation is driven by the radiative transfer equations [60]. The sources of noise in the underwater acoustic channel are also much different than those that affect the optical channel [72].

While shipping noise and sea waves are the main sources of noise in acoustic communications [57], the irradiance and scattering of sunlight in the water are the main factors that affect optical communications. Although these models are seemingly unrelated, it is of theoretical interest to show if there exists a combination of underwater acoustic properties that can be exploited to predict the state of the underwater optical link. Specifically, we are mainly interested in finding a relationship between the measured physical characteristics of the underwater acoustic link and the following two estimates:

1. a binary (good/bad) state of optical channel at a certain range and depth;
2. the signal-to-noise ratio (SNR) of optical communications at a given range and depth.

The first item is a classification problem, whereas the second item implies a regression and prediction problem.

While finding a relation between the acoustic and optical channel is of theoretical interest per se, such relation also has several practical applications. First, it would assist in predicting the characteristics of optical through acoustics. This will significantly reduce the cost and complexity of obtaining optical measurements, which otherwise require specialized equipment [136,137]. Second, by predicting the quality of optical through acoustics, a mobile node which holds both communication systems can be guided to a location where both technologies can be efficiently used. This application is specifically important for multimodal underwater communication systems, where both optical and acoustics are utilized [73]. For example, by predicting the properties of optical communications, an autonomous underwater vehicle (AUV) equipped with both technologies [152] can be directed to the maximal[1] range and depth still allowing reliable communication with the hub. Third, exploiting a relationship between optical and acoustic communications would enable more effective switching mechanisms than the current range-based triggering of optical, which only reflects the communication system specifications, and not the actual characteristics of the communication channel [72].

In this work, we study the relationship between optical and acoustic channels from a statistical point of view. Specifically, we investigate whether, for a given range and depth, the properties of an underwater acoustic link can be used for classifying optical link quality and for predicting the SNR over optical links. We limit our application to environments like the open sea, where it can be assumed that the properties of the optical link change slowly in time and space. While we were unable to find a theoretical/mathematical explanation for the relation between the acoustic and the optical channels, we present statistical evidence that this relation exists. It is our hope to stimulate further theoretical investigations in this direction.

---

[1] For safety reasons, the AUV should avoid a close contact with the receiver.

Our study is based on a large dataset of acoustic and optical link properties simultaneously measured over a prolonged time span and over different frequency bands. Our dataset was obtained during the ALOMEX'15 experiment led by the NATO STO CMRE, La Spezia, Italy. Using this dataset, we trained different learning models based on support vector machines (SVMs) [153], with the goal of classifying the corresponding quality of the optical link and predicting the optical SNR at various distances and depths. The learning system was designed and tuned to maximize the classification and prediction accuracy, while at the same time avoiding overfitting.

Our results show a strong correlation between the properties of the underwater acoustic link and the overall quality of optical communications. Moreover, using the acoustic properties as predictors, we show that the SNR of the optical link can be estimated with a sufficient degree of accuracy to enable ambient intelligence in underwater communication systems. This surprising result not only provides a tool for combining acoustic and optical communications, but also justifies further theoretical studies targeting the relationship between the underwater acoustic and optical links. Our contribution is therefore three-fold and includes:

1. an extensive quantitative study of the relationship between acoustic and optical channels;
2. a comparison between such relation at different acoustic frequency bands;
3. a dataset freely shared with the community for further investigation of the link between underwater acoustics and optics, and for the design of multimodal systems.

The remainder of this chapter is organized as follows. The basics of the machine learning techniques employed for data analysis are presented in Section 4.2, while Section 4.3 provides an intuitive explanation of the correlation between acoustic and optical channels. A detailed description of the acquired dataset is given in Section 4.4. The methods and results of the quantitative study are described in Section 4.5. Finally, we draw our conclusions in Section 4.6.

4.2 Machine learning approaches used for data analysis

In this chapter, we focus on a particular class of supervised learning methods that can be formally characterized using the statistical learning theory framework [154]. Statistical learning approaches aim to infer the function that maps input data to output data, such that the learned function can be used to predict the output from future input. In order to guarantee that the learned model generalizes well to unseen data, statistical learning algorithms try to limit the complexity of the resulting model to prevent overfitting. In particular, we use an efficient class of learning algorithms called SVM [153]. An SVM tries to achieve the best separation between patterns belonging to different classes by finding the maximum-separation hyperplane that has the largest distance to the nearest training data point of any class. In general, the larger the distance margin, the lower the generalization error of the classifier and the risk of overfitting the data. As a result, this learning framework is particularly indicated when the available data is limited. A similar framework can be applied in the case of real-valued outputs (regression tasks) using a variant called Support Vector Regression (SVR) [155]. While our database is quite broad in terms of surveyed area, it is limited in terms of number of measurements. For this reason, we have chosen SVM and SVR for the tasks of classification and regression, respectively.

We consider both linear and non-linear SVMs. In linear SVM, we assume that the patterns are linearly separable, and find two parallel hyperplanes whose distance is as large as possible to separate the two classes of data. The equation of a linear SVM is expressed in the form

$$f(x) = \langle \vec{w}, \vec{x} \rangle + b \; , \tag{4.1}$$

where $\langle \, , \, \rangle$ denotes the inner product in $\mathbb{R}^n$, and the vector w and scalar b are used to define the position of the maximum-margin separating hyperplane. Geometrically, the distance between the two external hyperplanes is $2/\|\vec{w}\|$, so in order to maximize their distance we want to minimize $\|\vec{w}\|$. As we also have to prevent data points from falling into the margin, we add the following constraints $\forall\, i$:

$$\begin{cases} \vec{w} \cdot \vec{x}_i - b \geq 1 & \text{if } y_i = 1 \\ \vec{w} \cdot \vec{x}_i - b \leq -1, & \text{if } y_i = -1 \end{cases} . \tag{4.2}$$

These constraints state that each data point must lie on the correct side of the margin. By introducing Lagrange multipliers α_i, the SVM training procedure amounts to solving a convex quadratic problem. The solution is a unique globally optimum result, for which

$$\vec{w} = \sum_{i=1}^{N} \alpha_i y_i \vec{x}_i \tag{4.3}$$

The terms $\vec{x}_i$ are called *support vectors*. Once an SVM has been trained, the decision function can simply be written as

$$f(\vec{x}) = \operatorname{sign}\bigg(\sum_{i=1}^{N} \alpha_i y_i (\langle \vec{x}, \vec{x}_i \rangle) + b \bigg) . \tag{4.4}$$

The non-linear SVM uses the so-called *kernel trick*, implicitly mapping the inputs into higher-dimensional feature spaces. The resulting algorithm is formally similar to the linear SVM, except that every dot product is replaced by a non-linear kernel function $K(\vec{x}, \vec{x}_i)$. This allows the algorithm to fit the maximum-margin hyperplane in a transformed feature space. In this work we use the popular Gaussian Radial Basis Function (RBF) kernel:

$$K(\vec{x}, \vec{x}_i) = \exp\Big(- |\vec{x} - \vec{x}_i|^2 / (2\sigma^2) \Big) \,. \tag{4.5}$$

4.3 Intuitive explanation for a correlation between acoustic and optical communications

This chapter focuses on presenting evidence about a correlation between acoustic and optical channels that allows the classification of optical and the prediction of its SNR based on acoustic data. In the absence of a well established theory for the relation between the two channels, in this section we give our intuitive explanation for this correlation. Our main claim is that the quality of optical is mostly affected by the turbidity of the water, and that this turbidity is generated by channel parameters that also affect acoustics.

We start with the connection between acoustic noise and optical links. The acoustic noise at shallow water is dominated by the acoustic noise generated by the surface waves. Close to the surface, these waves generate water bubbles and are a main contributor to the optical turbidity. Hence, the noise level and the acoustical SNR are expected to have some relation with optical communications. Similarly, the quality (or integrity) of acoustic communications that is affected by the acoustic noise is expected to have some link to optical communications as well.

The optical turbidity is also very much affected by the number of scatterers in the water column, for example plankton and floating sediments. These scatterers often also serve as acoustic volume reflectors, which affect the structure of the underwater acoustic impulse response. Hence, we expect that parameters like the channel's length, the delay spread, and the number of taps, will have some connection with the optical turbidity and therefore with the quality of optical links. We also see a relation between the number of scatterers in the water, which affects both technologies. Specifically, the volume scatterers affect the optical propagation in water as well as the RMS of the acoustic channel taps. Moreover, the number of scatterers in the channel is proportional to the acoustic power absorption, and thus affects the received signal level of the acoustic link.

Last, we note that the time dependency of acoustic communications is mostly affected by the motion in the channel. In turn, this motion creates circulation in the water, that highly affects the water's turbidity. Hence, we

Figure 4.1: Location of the measurement sites during the ALOMEX'15 cruise. Some stations were sampled at the same location but at different times.

expect to find a connection between the optical channel and measures like the channel coherence time and the noise level coherence time that reflect the time-dependency of the channel.

4.4 Description of the acquired dataset

To validate our system we used a data set collected during the NATO ALOMEX'15 mission, already introduced in Chapter 3. The ALOMEX'15 experiment spanned 13 days across 2800 km from southern Spain to west Africa. During this expedition, we measured both acoustic and optical link properties in the nine different stations marked in Fig. 4.1. Some stations were sampled in the same locations but at different times. In each station, a data collection lasting over an hour took place. The locations noted in Fig. 4.1 were chosen to represent different channel conditions, as reported in Table 4.1. Note that Stations 1-4 were located in the Mediterranean Sea, while Stations 5-9 were sampled in the Atlantic Ocean.

The measurement equipment was hosted on board the 93 m-long R/V Alliance. The optical properties were evaluated by probing the water column from the bow of the Alliance, while the transmissions took place from the stern. In two locations, the acoustic transmissions were performed from a work boat located approximately 1000 m from the Alliance. Referring to Fig. 4.1, these locations were Station 3, in the Alboran Sea ($35°47.0453'$ N, $004°51.0284'$ W), and Station 4, in the Atlantic Ocean along the Moroccan

Table 4.1: Experimental measurement stations

#	Location	Date	Time	Temp.	Depth	Range	Notes
1	37°35.3729'N, 00°58.7448'W	Nov 1	13:40	18°C	20 m	21 m	Cartagena Harbor, instruments calibration
2	36°25.0708'N, 01°40.0358'W	Nov 2	14:00	21°C	128 m	52 m	Rough sea, average wave height of 1 m
3	35°45.4758'N, 04°55.6935'W	Nov 4	12:30	19°C	129 m	57 m	Calm sea
4	35°47.0453'N, 04°51.0284'W	Nov 4	16:30	20.5°C	119 m	1.3 km	Calm sea, working boat
5	30°42.5113'N, 10°18.6613'W	Nov 6	09:00	20.5°C	127 m	1 km 583 m	Calm ocean, working boat
6	30°28.5720'N, 10°16.5030'W	Nov 6	15:30	20.5°C	126 m	59 m	Calm ocean
7	23°51.1912'N, 16°19.4189'W	Nov 9	15:30	19.5°C	40 m	45 m	Shallow/warm/ turbid waters (Sahara sandstorm)
8	25°04.0009'N, 15°20.4917'W	Nov 10	09:30	22°C	44 m	51 m	Calm ocean with clear waters
9	25°13.1351'N, 15°30.1324'W	Nov 10	13:45	22°C	77 m	53 m	Calm ocean with clear waters

coast (30°42.5113′ N, 010°18.6613′ W). Acoustic measurements were obtained by transmitting and receiving acoustic signals covering two different frequency bands. In all cases, the receiver and transmitter were deployed horizontally.

The dataset employed in this study is available online at `http://marsci.haifa.ac.il/share/diamant/DataToShare.zip` in the form of two 3-D matrices for the acoustic and optical data. Each matrix contains the time-varying measured acoustic and optical properties for each experiment station. Below, we describe the measured acoustic and optical properties in more detail.

4.4.1 Acoustic properties

In the absence of a theory connecting underwater acoustics and underwater optics, to statistically explore the relation between acoustic and optical channels we utilize all acoustic properties we could measure. The analysis below will show that no specific acoustic property is individually dominant

Table 4.2: Acoustic properties measured during the trial.

#	**Parameter**	**Measurement**
		Lower frequency range
1	Noise level (LF)	Average value of $\rho_{\mathrm{MTF}}(\tau)$ before the arrival of the first path
2	RSSI (LF)	Value of the first valid peak in $\rho_{\mathrm{MTF}}(\tau)$
3	Delay spread (LF)	RMS of delay of valid peaks in $\rho_{\mathrm{MTF}}(\tau)$
4	RMS tap amplitude (LF)	RMS of valid peaks in ρ^{i}_{MTF}
5	Number of paths (LF)	Number of valid peaks in $\rho_{\mathrm{MTF}}(\tau)$
6	SNR (LF)	Ratio between the received energy and the noise level
7	Channel length (LF)	Difference between the arrival delays of the last and first valid peaks in $\rho_{\mathrm{MTF}}(\tau)$
8	Noise coherence (LF)	Average time for which the cross-correlation between noise level measurements decreases below 90%
9	Coherence time (LF)	Average time $x\,T_s$ for which the cross-correlation between $\rho_{\mathrm{MTF}}(\tau)$ and $\rho_{\mathrm{MTF}}(\tau+\Delta)$, for some Δ, decreases below 90%
		Higher frequency range
1	Noise (HF)	Measured noise level
2	RSSI (HF)	Indicator for the received signal strength
3	Delay spread (HF)	RMS of delay of measured channel taps
4	RMS tap amplitude (HF)	RMS of measured channel taps
5	Number taps (HF)	Number of measured channel taps
6	Integrity (HF)	Indicator for link quality

to characterize the quality of an optical link. The acoustic dataset includes a total of 9 and 6 properties for the LF and HF bands, respectively, due to the different parameter set that the LF and HF devices could measure. A summary of the properties is provided for reference in Table 4.2.

The acoustic measurements were collected in a lower frequency (LF) band of 8-16 kHz, and in a higher frequency (HF) band of 18-34 kHz. LF involved the transmission of 200 consecutive linear frequency modulated (LFM) signals of duration 0.1 s and with a guard interval of 0.1 s. The LFM LF signals were transmitted through an omni-directional ITC projector at a source level of 181 dB Re 1 μPa @ 1 m (with a ripple of 3 dB in the frequency range considered), and received by two omni-directional Cetacean C57 hydrophones with flat receiver sensitivity, one placed at a depth of 5 m and a second one placed at a depth of 10 m. The pre-amplification level of these two hydrophones was 20 dB. In parallel to the transmissions in the LF band, the acoustic properties in the HF band were measured by a pair of EvoLogics S2C acoustic modems in the range 18-34 kHz, transmitting omni-directionally with a source level of 184 dB re 1 μPa @ 1 m (with a ripple of about 5 dB in the frequency range considered), both deployed at a depth of 10 m. The modems set their pre-amplification level automatically based on the level of the first received signal, and reception was also omni-directional with a flat receiver sensitivity.

Lower Frequency (LF) Band — The LFM signals recorded by the hydrophone were cross-correlated to estimate the channel impulse response and to evaluate the noise characteristics. To that end, we used a matched filter (MTF). Let $s(t)$ $0 < t \leq T_s$ be a transmitted LFM signal of unit energy and duration T_s s, and let $y(t),\ 0 < t \leq T_s + T_d$ be the corresponding signal at the output of the channel, with T_d being the delay spread of the channel. The non-normalized MTF output is given by

$$\rho_{\mathrm{MTF}}(\tau) = \left| \int_0^{T_s} s(t) y(t-\tau)\, \mathrm{d}t \right| . \tag{4.6}$$

Since $s(t)$ is a wideband LFM and since the SNR is high, ρ_{MTF} is an approximation of the channel impulse response $h(\tau)$ [156]. This is because, assuming that the channel impulse response $h(\tau)$ is linear, the following simplification may be made:

$$\int_0^{T_s} s(t)y(t-\tau)\mathrm{d}t = \int_0^{T_s} s(t)\left(s(t) * h(t-\tau)\right)\mathrm{d}t \approx \int_0^{T_s} \delta(t)h(t-\tau)\mathrm{d}t = h(\tau)\ , \tag{4.7}$$

where $\delta(t)$ is the Dirac delta function, and $*$ denotes convolution.

To evaluate which of the peaks in ρ_{MTF} corresponds to true arrivals, we used a constant false alarm threshold. Since setting a threshold directly on the response ρ_{MTF} requires the evaluation of the noise power spectral density (psd), which can be time-varying and hard to track, we used the normalized MTF whose response is

$$\rho_{\mathrm{NMTF}} = \frac{\left|\int s(t)y(t)\,\mathrm{d}t\right|}{\sqrt{\int s^2(t)\,\mathrm{d}t \int y^2(t)\,\mathrm{d}t}}\ . \tag{4.8}$$

As presented in [157], given a target false alarm probability, P_{fa}, a threshold x_T can be set without the need to estimate the noise characteristics. This threshold is calculated by

$$P_{\mathrm{fa}} = 1 - B\left(x_T^2, \frac{1}{2}, \frac{N-1}{2}\right)\ , \tag{4.9}$$

where N is the product of the signal bandwidth and duration T_s, and

$$B(a,b,z) = \int\limits_0^a t^{b-1}(1-t)^{z-1}\,\mathrm{d}t$$

denotes the regularized incomplete beta function [158]. As the locations of the valid peaks in ρ^i_{NMTF} correspond to those in ρ^i_{MTF}, these peaks are used to determine the acoustic properties. As the acoustic properties affecting optical communications are unknown, we have chosen to employ all main

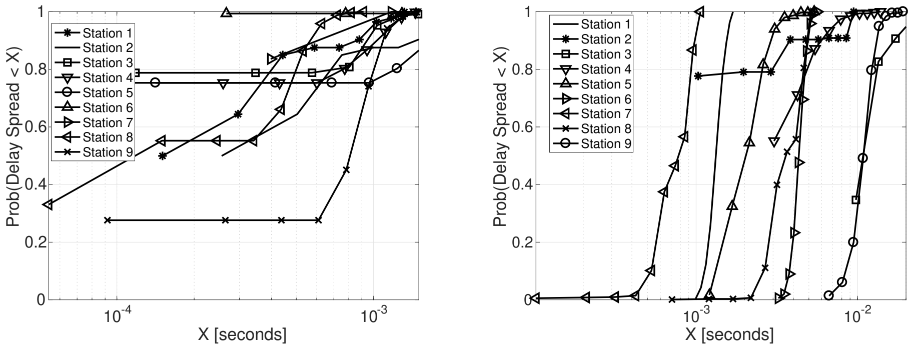

(a) Low frequency band (b) High frequency band

Figure 4.2: CDF of the delay spread in the LF and HF bands for the measurement stations (note the different x-axis scale).

acoustic link properties which could be extracted from the received LFM signals. This list is described in Table 4.2.

Higher Frequency (HF) Band — The acoustic properties in the HF band were calculated by the firmware of the EvoLogics modem. For each communication packet, the modems provide an estimate of the received signal strength indicator (RSSI), the power and delay of the most significant multipath arrivals, the noise level, the propagation delay, and an empirical evaluation of the communication link's integrity. The latter measurement reflects the SNR, hence the bit error rate. The acoustic properties given by the EvoLogics modems in the HF band are the received energy, the noise level, the SNR, the number of paths, the delay spread, and the integrity.

In Figs. 4.2a and 4.2b, we show the per-site cumulative distribution function (CDF) of the delay spread parameter in the LF and HF bands, respectively. The results highlight significant differences across the sites. For example, we observe an order of magnitude difference between the delay spread of the HF at site 6 compared to site 9, and the variance of the delay spread of the LF at site 8 is much bigger than that at site 4. This corroborates the requirement to perform measurements in different environments. This inter-site variability guarantees that the learning algorithms extract robust statistical correlations among the signals, which can be validated on separate, different subsets of patterns used during the test phase.

While the number of measurements and the number of parameters available at HF are relatively small, the SVM and the SVR can learn robust models even with a very small number of training samples [159, 160]. In our case, this is also supported by the fact that the measurements at HF are distributed fairly equally across all the sites, thereby representing a heterogeneous distribution.

4.4.2 Optical properties

The optical parameters of the water were measured using a Wet Labs Conductivity, Temperature and Depth (CTD) system with an AC-s meter [136], and the free-falling Satlantic Hyperpro II radiometer [137]. The CTD provided measurements of the optical absorption and attenuation coefficients, water salinity, conductivity, temperature and sound speed throughout the water column. The optical profiler measured the downwelling radiance along the so-called euphotic zone while the boat was moving straight at a constant speed. The data was collected at several wavelengths from 400 nm to 735 nm.

Using these devices, we obtained a set of physical characteristics for different depth and wavelength including the absorption rate, a, the attenuation rate, c, and the water temperature, T. Using a and c, the scattering rate b is calculated via (1.3). Parameters c and T were processed to evaluate the SNR of the underwater optical link at different depths, wavelengths, and distances from the source. In particular, following the model in [127] and assuming a perfect alignment between the transmitter and the receiver, the optical SNR at range r and depth d is computed as

$$SNR_o(r,d) = \frac{P_0 S \frac{2A_r}{\pi r^2(1-\cos\theta)+2A_t} \exp(-c(d)\cdot r)}{(E_0(d)A_r S)^2 + 2q(I_d+I_\ell)B + 4KTB/R}\,, \tag{4.10}$$

where the notation and the values assigned to each parameter are summarized in Table 4.3.

At each measurement site, the optical SNR was evaluated for four ranges and four depth values, namely $r \in \{5, 10, 15, 20\}$ m and $d \in \{5, 10, 20, 35\}$ m, and at a single wavelength of 532 nm.

In (4.10), the parameter E_0 has been chosen to represent two cases:

1. *Dark waters*: optical transmission during the night. Here we set $E_0 = 10^{-6}$ W/m^2 as a realistically low value that represents a negligible light background.

2. *Daytime*: optical transmission in the presence of solar light noise. Here, E_0 is computed based on the output of the HyperPro profiler.

Since the HyperPro measures only the downwelling radiance per unit wavelength E_d in W/(cm^2 nm), in the second case we applied a conversion based on the relation between ratio E_0/E_d and ratio b/a [161, page 180]. This relationship is illustrated in Fig. 4.3a. Our dataset includes one set of optical parameters measured at each site per depth and wavelength. From this data, we evaluate one SNR value per pair of depth and transmission distance.

Two example measurements of the parameters a, b and c obtained at Stations 2 and 7 of the ALOMEX'15 campaign are shown in Fig. 4.3b. The variation of a with depth is depicted via a light gray line, the variation of b via a dark gray line, and the variation of c via a black line. The mixed

Table 4.3: Optical properties: notation and meaning

	Meaning	Value
P_0	Source-radiated optical power	30 W
S	Receiver sensitivity	0.26 A/W
A_r	Receiver area	1.1 mm^2
A_t	Transmitter's area	10 mm^2
θ	Transmitter's semi-aperture	0.5 rad
E_0	Scalar irradiance of the solar light	From measurements
q	Elementary charge	1.6 10^{-19} C
I_d	Photodetector's dark current	1 nA
I_ℓ	Incident light current	1 μA (upper bound)
B	Signal bandwidth	100 kHz
K	Boltzmann constant	1.38 10^{-23} JK^{-1}
T	Temperature	From measurements
R	Receiver's shunt resistance	1.43 GΩ
a	Absorption rate	From measurements
b	Scattering rate	From measurements
c	Total attenuation rate	From measurements

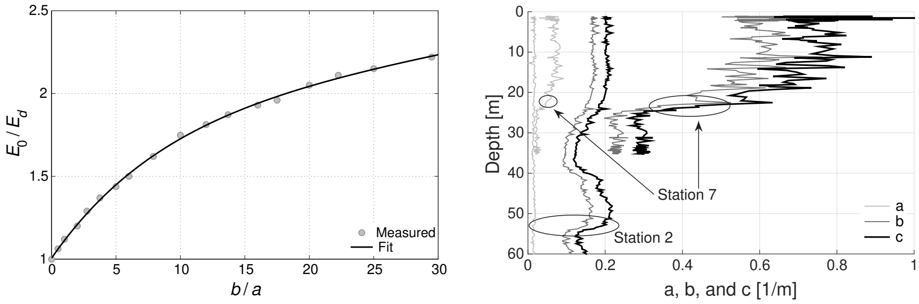

(a) Relationship between E_0/E_d and b/a, used to measure E_0 in the presence of solar light.

(b) Measured absorption (a, light gray) scattering (b, dark gray) and total attenuation (c, black) coefficients for stations 2 and 7.

Figure 4.3: Parameters of underwater optical communications: (a) E_0/E_d vs. b/a; (b) sample plots of a, b and c at two stations.

waters of Station 2 are reflected by some irregularities in the variation of b with depth. The turbid waters of Station 7 display a higher scattering coefficient b at all depths, characterized by spikes at some depths. With reference to Table 4.1, we observe that the mixed waters of Station 2 confer a mildly irregular variation with depth to b. On the contrary, the highly turbid waters of Station 7 are characterized by higher values of b and more irregular variations with depth. In both cases, b is the dominating parameter concurring to $c = a + b$.

4.5 Results for evaluating the relationship between acoustic and optical channels

In this section, we discuss *i*) the results of the learning methods used to find the set of acoustic properties that can predict the reliability of the optical link, and *ii*) the pairs of acoustic and optical properties that show a trend of high correlation. Since the optical data included only one set of measured parameters per site, we have only performed classification and prediction from the acoustic properties to the optical properties.

In the results presented below, performance figures are shown for both a linear SVM (Lin) and a non-linear kernel (RBF). Input for classification and prediction are the LF acoustic measurements at 5 m depth (LF5), the LF acoustic measurements at 10 m depth (LF10), and the HF acoustic measurements (HF). To assess the robustness of the proposed learning system, we repeated the analysis several times, shuffling the training and test patterns before each run. Error bars in the figures indicate standard deviations computed for 10 different repetitions of this process.

4.5.1 System model

In this work, all data processing was performed offline, including both training and testing procedures. However, the database formed by the measured acoustic and optical channel properties can also be processed online later. In this case, training is performed offline before system deployment while testing (i.e., classification) takes place online. For online applications, it is important to use a testing database containing a very diverse set of measurements. Otherwise, overfitting may occur in the training phase and online classification may fail. Since the experiment involved data collection from multiple sea and ocean environments and during both daytime and nighttime, we believe that our database achieves such diversity.

It should be noted that the performance of real optical systems depends not only on the channel parameters but also on the characteristics and deployment of optical modems. Naturally, these characteristics cannot be predicted from the acoustic channel properties. However, online prediction of the channel-based optical link quality and SNR does provide a method to evaluate optical link variation over range and depth. Such a prediction tool can facilitate reliable communication by informing the transmitter's selection of depth and range to the receiver.

To calculate the optical SNR we make use of (4.10). As noted in Table 4.3, (4.10) depends on some fixed properties and some measured properties. The latter include the attenuation coefficient c, the temperature T, and the light noise irradiance E_0. The measured optical properties show, in most cases, a negligible relationship with longitude, latitude, time and depth (in line, e.g., with [162]), whereas in other cases the change with depth and location is more pronounced (as is the case, e.g., for parameter b). In both cases, we limit our study to environments where the difference in the optical properties across the locations where the acoustic and optical equipment were deployed is manageable by our model. Still, we expect to find differences in the prediction accuracy of the optical SNR and the classification of the optical link as a function of depth and range. The expected difference as a function of the depth is due to the fact that c, T, and E_0 are depth-related, and thus different correlation with the acoustic properties yields changes in the prediction accuracy. We also expect that the prediction accuracy decreases with range, as the impact of non-accurate prediction increases with range.[2]

While we argue that the measured optical properties do not change much in space and time, this is not the case for the acoustic properties. Because the acoustic channel is space and time-dependent, there may be a difference between the relation of the measured acoustic properties and the optical channel at different time instants. Yet, we assume that the basic characteristics of the acoustic channel are indeed distinctive of different sea/ocean environments. For example, within a small area we expect the acoustic noise level to remain roughly the same, and similarly the average delay spread. We therefore aim to explore the relation between these basic (slowly changing in time and space) acoustic and optical characteristics. To that end, we do not perform prediction based on the instantaneous values of the acoustic parameters. Instead, for each test site we consider a large dataset of acoustic properties measured over tens of minutes, subdivide them into consecutive time windows, and perform prediction based on the average value of the acoustic parameters taken over each window.

To avoid prediction bias and overfitting, we performed multiple training and testing attempts. In each attempt, a random subset of the data was

---

[2] We remark that our evaluation is limited to the sets of distances and depths considered in Section 4.4.2. These sets could be extended to include further values, provided that a different classifier is trained for the corresponding optical data. A different approach would be to train a regression model of the optical parameters $c(d)$ and $E_0(d)$, substitute them into Eq. (4.10), and use the latter to predict the SNR for any r. As c can vary highly with depth (see Fig. 4.3b), this approach is expected to require a much larger training set, and is left as future work.

chosen for training and the rest for testing. Two prediction types were considered: 1) classification where using the properties of the acoustic channel we identified optical communications as “good” or “bad” at different ranges and depths, and 2) prediction where we used acoustic channel properties to predict the SNR of the optical link at different ranges and depths. In the following, we describe the details of these procedures.

4.5.2 Training procedure and evaluation details

For the acoustic data, the time series describing each acoustic property were first pre-processed. This included scaling individual properties to be within the interval $[0, 1]$, windowing, and averaging. Since the diversity of the measurements is important to achieve a robust classification, the window size was determined as the one that achieved the maximum average variance of the elements within each window. This window size was determined separately for each property in each frequency band and for each experiment station. For each window, the mean and variance values were given as input to the classifier. The result is a set of 18 properties for the LF band, and a set of 12 properties for the HF band. In total, the database included 1370 patterns for the LF data at 5 meters, 2320 patterns for the LF data at 10 meters, and 297 patterns for the HF data.

Since the optical data was used as labeling for training and testing only, no pre-processing was performed. In the context of multimodal systems, we focused only on classifying and predicting the optical SNR during both nighttime and daytime (see Section 4.4.2). However, the same procedure can be carried out for all 16 properties listed in Table 4.3. An example for the latter is given below for parameter b.

The training procedure involved a threshold to label the trained optical dataset as “good” or “bad.” With the aim of showing the relation between acoustic and optical channels, the choice of this threshold is not necessarily related to the needs of actual optical systems, but is rather determined such that the number of “good” and “bad” training links is equalized to avoid overfitting. For the same reason, we considered only those depths and ranges that yielded a sufficient number of positive and negative optical links during the training procedure. With this in mind, for daytime measurements, we chose a fixed threshold level of 15 dB, and considered classification only for the depth-distance pairs $(10, 5)$ m and $(25, 10)$ m. For nighttime measurements, we chose a fixed threshold level of 10 dB, which allowed classification for all the combinations of depth $\in \{5, 10, 15, 25\}$ m and distance $\in \{10, 15, 20\}$ m. In Fig. 4.4, we show the evaluated SNR of the measured optical links during daytime and nighttime. The values shown lead to a variation of roughly 70 dB in the range of SNR. Naturally, this produces a large change in the number of “good” and “bad” optical channels. More specifically, the choice of these threshold levels yielded on average a ratio between “good” and “bad”

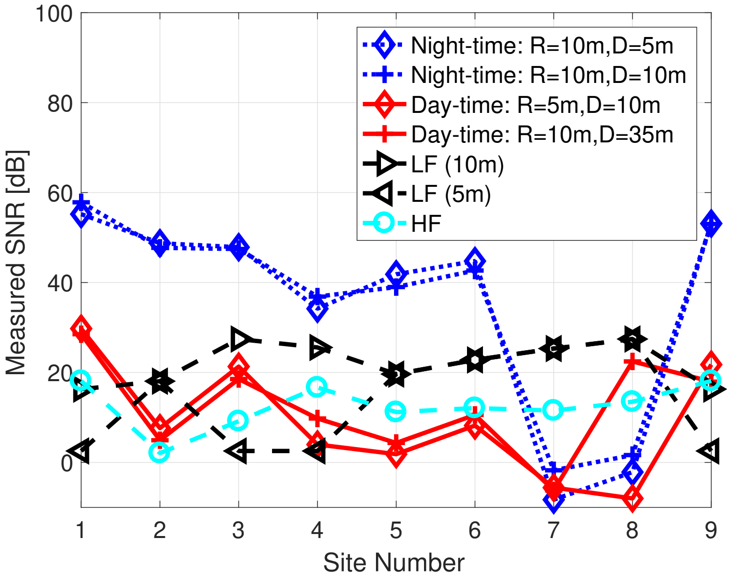

Figure 4.4: Average values for the optical and acoustic SNR measured at the different experimental sites. Results show a range of roughly 70 dB during nighttime, and 40 dB during daytime for optical SNR. Correlation between the optical SNR and the acoustic SNR is not clear.

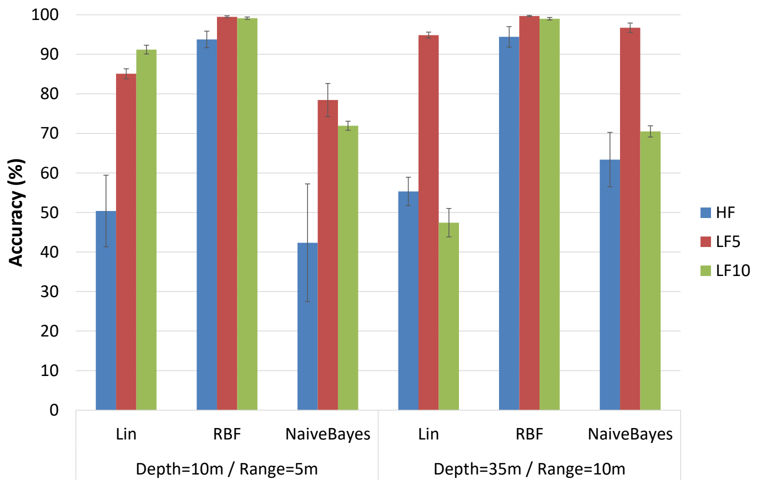

Figure 4.5: Classification accuracy for daytime optical communications, obtained using linear SVM, RBF SVM, and a simple Naive Bayes classifier. Results suggest a clear non-linear relationship between acoustic properties (mostly LF5) and optical links.

channels of 62% for daytime and 65% for nighttime. Note that thresholding is required only for classification. For regression, instead, the whole dataset was used to train the system and predict the SNR of optical links.

Training was performed separately for the acoustic LF recordings at 5 m, the acoustic LF recordings at 10 m, and the acoustic HF recordings (10 m). The aim of training was twofold: 1) discriminating the corresponding quality of the optical signal (binary-valued classification task), and 2) predicting the corresponding optical values (real-valued regression task). To that end, the dataset was first divided into training sets (75% of the patterns) and test sets (25% of the patterns), and the latter were used to test the generalization capability of the models. We considered two kernel functions: the simple linear SVMs, and the non-linear RBF kernel. To set the learning hyperparameters, we adopted a k-fold cross-validation procedure, where one fold was randomly selected and left out to test the current settings of the hyperparameters. Based on the amount of available data, we used 3 folds for LF at 5 m, 4 folds for LF at 10 meters, and 5 folds for HF. To evaluate the robustness of our approach and to reduce the risk of overfitting, each SVM was trained 10 times, and we report the mean classification accuracy and the corresponding standard deviations.

4.5.3 Classification results

The classification accuracy for the test sets is reported in Fig. 4.5 for both the linear SVM and the non-linear SVM with the RBF kernel. We explore classification using all three types of acoustic measurements. In all cases, the marked difference between the linear SVM and the RBF kernel suggests that the relation between the acoustic properties and the optical link quality is non-linear. In order to better assess the robustness of the findings, as a control simulation we also performed the same classification task using a Naive Bayes classifier [163]. The average accuracy obtained using this alternative type of algorithm was closely aligned with that obtained with the linear SVM (see Figure 4.5). For this reason, in the following experiments we only considered the SVM models. Moreover, overall the results indicate that the LF measurements provide a more accurate prediction of the quality of the optical link, approaching 100% of classification accuracy for the non-linear SVM. The LF measurements yield a much higher accuracy also for the linear SVM, except for the condition corresponding to a depth of 35 m and a range of 10 m, where the performance of LF10 is similar to that obtained using HF.

The classification accuracy for the test sets to predict the optical SNR during nighttime is reported in Fig. 4.6. Here, many more values of optical SNR can be predicted. Also in this case, the non-linear kernel clearly outperforms the linear SVM, achieving 100% for all the target properties. In fact, for many properties, the performance of the linear SVM in Fig. 4.6 is close

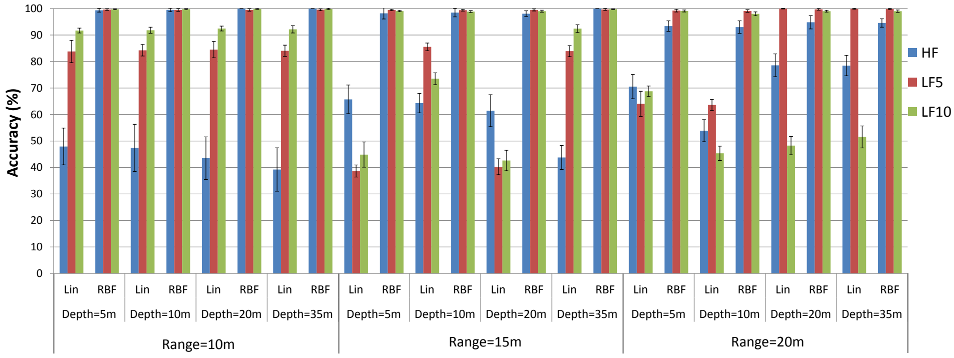

Figure 4.6: Nighttime optical SNR. Results suggest a clear non-linear relation between acoustic properties and optical link quality.

Table 4.4: Precision, recall and specificity values for all the classification tasks.

	Range (m)	Depth (m)	Linear SVM									Non-linear RBF kernel								
			HF			LF5			LF10			HF			LF5			LF10		
			Prec	Recall	Specif	Prec	Recall	Specif	Prec	Recall	Specif	Prec	Recall	Specif	Prec	Recall	Specif	Prec	Recall	Specif
Daytime	**5**	**10**	0.37	0.38	0.58	0.76	0.93	0.79	0.88	0.95	0.87	0.93	0.90	0.96	0.99	0.99	1.00	0.99	0.99	0.99
	10	**35**	0.53	0.40	0.70	0.57	0.97	0.95	0.27	0.44	0.49	0.96	0.92	0.96	1.00	0.96	1.00	0.98	0.99	0.99
Nighttime	**10**	**5**	0.75	0.51	0.39	0.96	0.85	0.77	1.00	0.91	0.96	0.99	0.99	0.97	1.00	1.00	0.98	1.00	1.00	0.98
		10	0.76	0.51	0.31	0.96	0.85	0.79	0.99	0.92	0.94	0.99	0.99	0.97	1.00	1.00	0.97	1.00	1.00	0.98
		20	0.82	0.46	0.21	0.96	0.85	0.81	0.99	0.92	0.92	1.00	1.00	1.00	0.99	1.00	0.97	1.00	1.00	0.99
		35	0.83	0.42	0.14	0.96	0.85	0.77	0.99	0.92	0.92	1.00	1.00	1.00	1.00	1.00	0.98	1.00	1.00	0.99
	15	**5**	0.81	0.74	0.32	0.37	0.21	0.59	0.52	0.45	0.45	0.98	0.98	0.95	0.99	1.00	0.99	0.99	1.00	0.98
		10	0.80	0.72	0.39	0.96	0.87	0.78	0.83	0.82	0.46	0.99	0.99	0.96	1.00	1.00	0.97	0.99	1.00	0.96
		20	0.76	0.72	0.25	0.40	0.23	0.61	0.49	0.38	0.49	0.99	0.99	0.96	0.99	1.00	0.99	0.98	1.00	0.98
		35	0.84	0.45	0.29	0.96	0.84	0.80	1.00	0.92	0.97	1.00	1.00	1.00	1.00	1.00	0.99	1.00	1.00	0.98
	20	**5**	0.79	0.80	0.48	0.58	0.86	0.45	0.64	0.92	0.44	0.96	0.96	0.89	0.99	1.00	0.99	0.98	1.00	0.98
		10	0.51	0.67	0.42	0.57	0.87	0.43	0.21	0.36	0.49	0.95	0.95	0.95	0.99	1.00	0.99	0.99	0.94	0.99
		20	0.84	0.85	0.65	0.99	1.00	1.00	0.24	0.39	0.52	0.99	0.99	0.98	0.94	1.00	1.00	0.96	1.00	0.99
		35	0.84	0.87	0.59	0.98	0.99	1.00	0.25	0.40	0.56	0.99	0.99	0.98	0.97	1.00	1.00	0.96	1.00	0.99

to chance level (50%). Similar to the case of daytime optical transmission, in the nighttime scenario the LF measurements (LF5 in particular) are better predictors for the quality of the optical link. However, when using the linear SVM, HF sometimes still outperforms LF10, especially for the conditions corresponding to long distances (range = 20 m). This suggests that in nighttime conditions the HF signal can be more reliable than in daytime conditions, approaching a prediction accuracy of 100% for the non-linear SVM and of 80% for the linear SVM at long ranges.

The high classification accuracy obtained for both the daytime and the nighttime prediction of the quality of the optical link suggests a strong relationship between the acoustic properties and the optical link quality. This relation seems to be non-linear, as the greatest accuracy is achieved by the SVM using the RBF kernel. In order to better evaluate the classifier per-

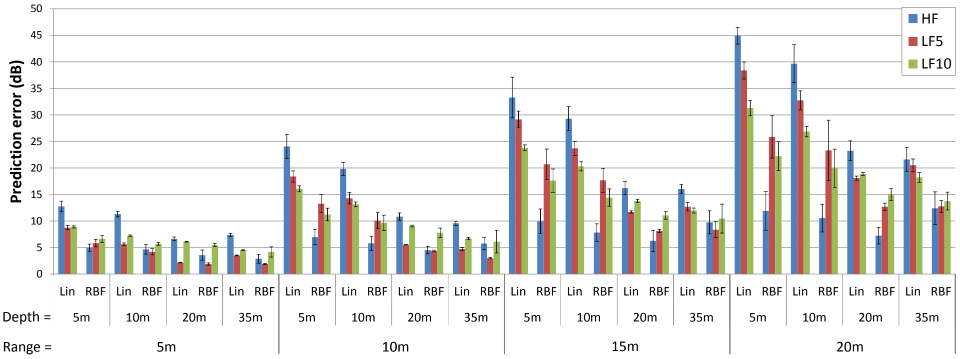

Figure 4.7: Prediction error for the daytime optical SNR. Compared to the range of optical SNR, results suggest a good non-linear prediction of the optical link quality from the acoustic properties.

formance across different conditions, three additional performance measures were also computed from confusion matrices [164]: precision (i.e., class agreement of the data labels with the positive labels given by the classifier), recall (i.e., effectiveness of the classifier to identify positive labels), and specificity (i.e., effectiveness of the classifier to identify negative labels). The complete results are reported in Table 4.4. Precision, recall and specificity values are consistent across conditions, and fully aligned with the accuracy results reported in Fig. 4.5 and Fig. 4.6. In particular, results show that indeed the non-linear classifier achieves much better performance on all metrics, and has no biases for any particular class.

Interestingly, the data seem to suggest that linear classification using LF measurements improves close to the surface. This needs to be investigated further, as not all collected data shows this same trend, and we have no further evidence to prove it. However, we still conjecture that linear classification might be in fact more precise near the surface. A possible explanation can be a high concentration of biological particles such as plankton in the upper water layer, which would scatter the acoustic wave and, during daytime, also sunlight. The collection of additional data in this specific scenario would be a necessary step to verify this conjecture.

4.5.4 Prediction results

Classification results show evidence of a relationship between acoustic properties and optical link quality. The strength of this relationship can be evaluated by prediction. The optical SNR prediction errors for the test sets for all the 16 range-depth pairs of the daytime optical data are reported in Fig. 4.7. Refer to Fig. 4.4 for the true optical SNR values at the different sites and for daytime and nighttime data collection. The results are given in terms of the root mean squared error (RMSE), measured in dB, for each type of acoustic dataset. As observed in the classification results, the non-linear kernel outperforms the linear SVM when predicting SNR. Notably, the RMSE of optical SNR achieved by the non-linear SVM is always around or below 5 dB at any measured depth when the range is 5 m. Contrary to the classification task, using HF acoustic data to train the RBF SVM for regression yields, in most cases, results that are better than those achieved using LF acoustic data. This result might be due to the fact that the binary classification task is easier to perform than the fine-grained regression task, which could be more challenging to fulfill at high accuracy. The larger number of samples in the LF dataset might have introduced noise that was detrimental only for the fine-grained predictions performed with the non-linear SVM.[3]

The optical SNR measured at several depths and ranges as well as the average measured acoustic SNR values are shown in Fig. 4.4. No clear correlation is visible at this point between the optical and acoustic SNR values for the different testing sites. The optical SNR varies between −10 dB and 60 dB for nighttime, and between −10 dB and 30 dB for daytime optical links. Within such broad ranges, being able to predict the optical SNR based on acoustic SNR measurements within roughly 5 dB of RMS error strongly suggests the existence of a relationship between acoustic and optical channels. We also observe that the accuracy of the prediction decreases with increasing range, and is lowest for the longest range of 20 m. Such a range is akin to the maximum operational range of several practical underwater optical modems. Therefore, the accuracy decrease is expected, and mainly due to the SNR decrease as a result of absorption and scattering of light power in water.

For the nighttime scenario, the prediction errors of the test sets for all the 16 range-depth pairs are reported in Fig. 4.8. Similar to the case of daytime optical transmission, we observe that the non-linear kernel operates far better than the linear one. When using RBF, the regression results obtained using the HF dataset are better than those obtained using LF5 and LF10, which might be due to overfitting. Although this trend was observed also in daytime conditions, this difference is much more marked in nighttime conditions.

We now consider optical-SNR prediction accuracy as a function of depth. By analyzing the trends in Fig. 4.8, we observe that for the RBF kernel, the prediction error at a fixed distance (i.e., for each different range) gradually decreases with depth. Hence, the optical signal becomes more predictable as we move deeper in the water. However, this interesting trend holds only for the first three depths, while at a depth of 35 m we notice that the prediction

---

[3] Another possible explanation is that the HF regression training was overfitting the results. We have found a marked difference between an accuracy of 0.5 dB in training and 2 dB in testing that may support this, where on the contrary, the LF error was comparable between training and test sets. However, since the test performance of the non-linear SVM using HF was often lower than that obtained with LF, this explanation is not supported by sufficient evidence.

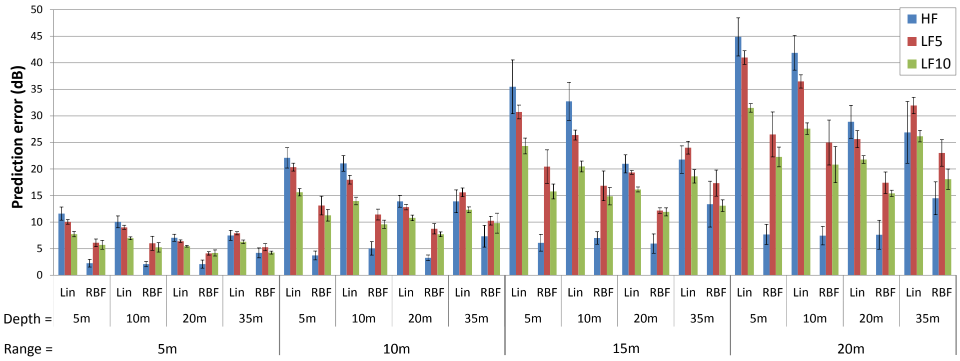

Figure 4.8: Prediction error for nighttime optical SNR. Compared to the range of optical SNR, results suggest a good non-linear prediction of the optical link quality from the acoustic properties.

error remains about the same or slightly increases. This phenomenon occurs for prediction using both LF and HF acoustic measurements, and means that, up to a certain depth, the optical SNR becomes more predictable. We argue that this effect is due to the scattering coefficient b which decreases with depth up to a certain value, as seen in Fig. 4.3b. As long as b decreases, the exponential parameter in (4.10) becomes less dominant, and predicting the optical SNR becomes easier. Note that this effect appears even if the actual value of b cannot be predicted accurately per se. In order to test this hypothesis, we trained the RBF SVM to predict the observed parameter b. The results shown in Fig. 4.9 imply that it is harder to predict the value of b at a depth of 35 m. The reason behind this is that scattering tends to happen mostly in the euphotic zone of the water column, whose boundaries are limited to specific water depths. When optical measurements are performed deeper than the euphotic zone, b tends to drop, as observed, e.g., from Station 7 data in Fig. 4.3b. Such a drop may not be captured by the training over the rest of the data set, which explains the RMSE increase in Fig. 4.9 at a depth of 35 m. Remarkably, this does not greatly affect the accuracy of the SNR prediction, because a lower b also means that the SNR would be less affected by the exponential parameter in (4.10).

4.5.5 Impact of single properties on prediction accuracy

We now wish to explore if there are certain acoustic properties which are more closely related to the optical properties and are thus more informative for optical channel quality prediction. We therefore investigate the influence of each individual acoustic property on the prediction accuracy of the optical SNR. To that end, in this section, instead of performing prediction based on the full set of nine (LF) and six (HF) acoustic properties, we perform prediction based on each of the measured properties independently.

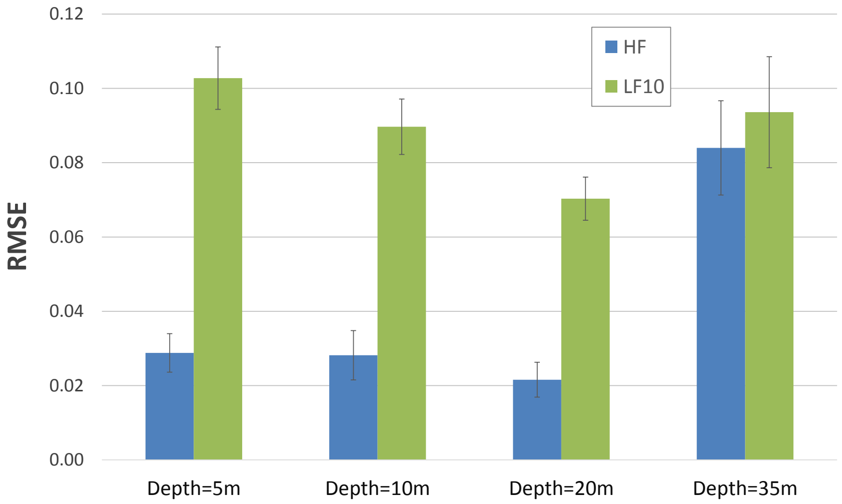

Figure 4.9: RMSE for the prediction of the scattering parameter b using the RBF SVM kernel.

In Fig. 4.10, we show the daytime and nighttime prediction error of the optical SNR, respectively, evaluated for a transmission range of 5 m, and averaged across the four considered depth values. The enumerated properties match those in Table 4.2. As expected, the average prediction accuracy decreases when using only a single acoustic property as the predictor. For the nighttime case, this result is observed when using both the lower and the higher frequency acoustic properties. However, for regression of the optical SNR during daytime, this performance decrease is mostly observed when using the HF data, and the decrease when using the LF data is only marginal. Compared with the prediction performance when using all properties (column "All param" in Fig. 4.10), we note that the prediction error increases only by roughly 3 dB. This result suggests that even when not all considered acoustic properties are available, the relationship between acoustic and optical channels is sufficiently marked to allow the prediction of the optical SNR. (Recall the intuitive explanation for this result given in Section 4.3.)

From Fig. 4.10, we observe that the average error is fairly constant across all single acoustic properties. This suggests that the acoustic properties used have a similar correlation with the optical properties. That is, no specific acoustic parameter is dominant for predicting the SNR of the optical link. Yet, exploiting the whole set of parameters yields better performance, as the prediction error decreases from 5–8 dB to 3–5 dB. In particular, the first set of bars in each panel of Fig. 4.10 ("All param"), show that for the range of 5 m, the prediction error performance is about 5 dB. From this result, we conclude that the theoretical relations between the acoustic and optical channels are quit complex and cannot be simplified based on a single

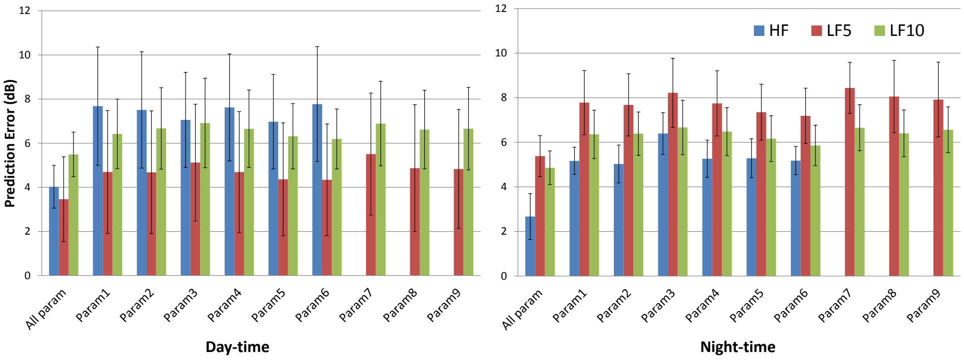

Figure 4.10: Prediction error of the optical SNR for range 5 m averaged for all depths (5, 10, 20 and 35 m). Results obtained using the SVM with the RBF kernel, trained with either all acoustic properties or a single property at a time.

acoustic parameter.

From Figs. 4.7 and 4.8, we observe that the prediction performance improves as the range decreases. As is even clearer from the average results shown in the first column of Fig. 4.10 ("All param"), we also observe that the prediction results for the nighttime optical SNR are generally better than for the daytime SNR at 5 meter ranges. Performing this same analysis for ranges of 10 m, 15 m, and 20 m also revealed generally better optical-SNR prediction results at night. Both trends are explained due to a more complex connection between acoustic and optical channels as range and sunlight increase. Both make predictions more demanding as an accurate evaluation of the parameters c and E_0 is respectively required in these cases (see Table 4.3).

4.5.6 Implications for multimodal technology switch mechanisms

Given the range of the optical SNR as shown in Fig. 4.4, the results for both nighttime and daytime classification and regression show a fairly accurate prediction of the optical SNR. This performance not only strengthens the evidence of a connection between the acoustic properties and the optical ones, but also implies that the practical application of directing an AUV to the optimum range and depth for optical communications is realistic. That is, the AUV can head directly to a location predicted to have good optical SNR, while still being deep enough and far enough from the vessel it communicates with for safety reasons. In this context, the mission of the AUV will be to communicate optically when in range, by keeping a safe distance to the communicating vessel.

For a target optical SNR, $\mathrm{T_h}$, the following algorithm can be applied:

1. Train an acoustic-optical classifier and predictor based on collected data (the database openly shared with this chapter);
2. Collect acoustic properties to form an input data set;
3. Given range and depth, classify the quality of the optical link and predict the optical SNR, $\mathrm{SNR}_o(r, d)$;
4. Direct the AUV to a location at range $\hat{r}$ and depth $\hat{d}$ for which optical is classified as a good link, and for which $\mathrm{SNR}_o(\hat{r}, \hat{d}) > \mathrm{T_h}$, and switch from acoustic to optical technology.

4.6 Conclusions

In this work, we explored the statistical relationship between the properties of underwater acoustic and optical links for the purpose of classifying the underwater optical link and predicting its SNR. We based our analysis on a large database including both optical and acoustic measurements, collected in nine different sea environments during a 13-day expedition. Our results indicate a clear relation between the acoustic properties and the quality of the optical link. In particular, using the RBF classifier, with the acoustic measurements we were able to predict the quality of the optical link with an accuracy close to 100%. Moreover, for the range of 5 m, we were able to predict the SNR of the optical link with an accuracy of about 5 dB within a dynamic range of 70 dB. Our results further show that in most cases, the higher frequency measurements of the acoustic channel can better predict the optical channel. Our classification and prediction algorithms can already serve as a switching mechanism for multimodal systems that combine underwater acoustic and optical communications. While our results provide strong evidence about the connection between acoustic and optical channels in the water, we could not develop the mathematical relation between the two channels, and this requires further exploration. As an additional future research direction, we plan to include an initial unsupervised phase, which might discover useful patterns in the data and thereby better support multiple supervised tasks. As a future direction, unsupervised learning, e.g., deep belief networks [165, 166], may discover other useful patterns in the data such as meaningful clustering of the data, and that can adaptively set the classification thresholds. Successful application of these approaches to communication systems [167, 168] motivates their use in our context as well.

Notes

The content of this chapter has been published in [169] and [170].

Chapter 5

Fair and throughput-optimal multimodal routing

5.1 Introduction

A key role, in multimodal communication systems, is played by the logic that decides how to switch between the available PHYs. While multimodal point-to-point links are manageable with relatively simple policies [72], organizing multimodal nodes into a network requires a change of perspective. In fact, the nodes may connect to different neighbors using (possibly partially overlapping) subsets of their PHYs. These subsets may change over time according to a variety of circumstances, that depend, e.g., on environmental conditions, mobility, and on the traffic requirements of the nodes. In this chapter, we design a specific component of the multimodal PHY usage logic: the multihop routing algorithm. In this context, we propose Optimal Multimodal Routing (OMR), a routing solution that fully utilizes the available PHY technologies in an optimized fashion. Specifically, by considering the different PHY technologies as another layer of network resources, we formalize the routing problem as a maximization problem where each node tries to extract the most from all its available PHYs. The solution to this problem leads to a routing protocol that is distributed and fair, and avoids bottlenecks. OMR is valid in any network topology, and can be applied to any combination of available PHY technologies, including when different nodes incorporate different technologies.

Our contribution is twofold, and includes:

- A novel distributed routing algorithm for multimodal underwater networks, which maximizes the amount of information transmitted through all technologies available to each node, while at the same time balancing the traffic flow through the network and pursuing a fair network utilization for all nodes;

- A broad quantitative evaluation, which proves that our distributed algorithm performs very close to a globally optimum benchmark relying on full network topology knowledge, and that it outperforms both straightforward solutions to exploit multimodal links and more complex multi-technology routing solutions inherited from the terrestrial radio networking domain.

We evaluate the performance of OMR by means of numerical simulations and through several field experiments performed in a lake north of Berlin, Germany. To the best of our knowledge, ours is the first reported trial for multimodal routing schemes.

5.2 Network model and Optimal Routing

We consider a converge-casting network of multimodal underwater nodes, where data traffic has to be routed towards a common sink node. This is a very common network topology arrangement, that is found in several practical applications, from long-term data monitoring in a given area, to underwater infrastructure monitoring [171] and to Internet-accessible underwater networks [172]. We desire to obtain good performance in all key aspects of the multimodal network. In particular, we are interested in maximizing the network goodput while limiting the end-to-end transmission delay. Since underwater networks usually face energy limitations, we are also interested in minimizing the packet transmission overhead. On the other hand, to keep network traffic flow smoothly and reduce bottlenecks, we are interested in the full exploitation of the available network links. With the goal of obtaining a favorable tradeoff among the above quality measures, in this chapter we propose the first optimal multimodal routing (OMR) scheme for underwater networks.

5.2.1 Key idea

The key idea behind our distributed routing scheme is that the available multimodal links should be fully exploited, while at the same time avoiding that some relays become bottlenecks for the routing process. To do so, the nodes should *i*) avoid forwarding an excessive amount of traffic towards the relays upstream and *ii*) favor nodes with fewer valid routes to the sink during the data relaying process. We achieve this by having the nodes estimate the capability of their relays to forward traffic further, and by having these relays distribute a minimal amount of information about the current backlog of data bits in their queues. This allows each network node to separately solve an optimization problem, and to find the number of bits to be transmitted to its neighbors through each multimodal link. We note that our approach does

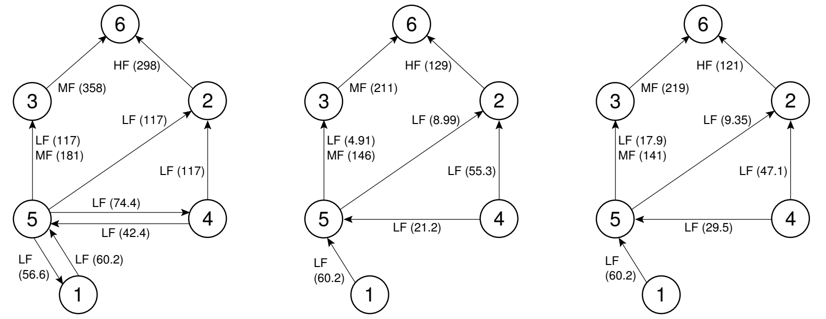

(a) Flooding (b) OMR (c) OMR–FF

Figure 5.1: Per-link transmission rates in bytes/s using flooding (a) and our OMR algorithm (b). OMR is also compared with the OMR–FF benchmark (c), where the full topology is assumed to be known at no cost.

not resort to flooding, as we explicitly want to avoid unnecessary redundant transmissions of the same data.

Even without topology information, this approach balances traffic much better with respect to a baseline algorithm that, e.g., floods all data through all available technologies. This can be observed in Fig. 5.1, where we report the per-link transmission rates required to convey the same number of packets to the sink. We consider three multimodal routing solutions: flooding, where all links and all available technologies are used and packets are re-transmitted; our OMR method to achieve fairness with only one-hop topology information; and a version of our OMR method where the full topology information is available (OMR–FF), as a benchmark. OMR is a fully distributed protocol, while OMR–FF is centralized. Three acoustic PHY technologies are used by the network nodes: a low-frequency, low-rate technology (LF), a faster technology working at intermediate frequency (MF) and a high-frequency high-rate technology (HF). In parentheses, we show the obtained transmission rates in bytes/s. We remark that there is no conceptual limit to the number of technologies that a node can incorporate: we consider three technologies in this example in order to fix ideas.

From Fig. 5.1 we observe that, with respect to the flooding case (Fig. 5.1a), the transmission rates are much less intense and more balanced with our approach (Fig. 5.1b/c). In the ideal case of OMR–FF where full topology information is available (e.g., because the topology has been tested in advance, and does not change over time), the algorithm can better organize transmissions across all links compared to OMR. For example, OMR–FF redistributes part of the traffic of node 4 through node 5, resulting in better utilization of the LF link from node 3 to node 6, as can be seen by comparing Figs. 5.1b and 5.1c. In the following, we describe the routing algorithm in detail.

Table 5.1: Explanation of the employed notation

Symbol	**Meaning**	**Requires**	**Shared with**
$\mathcal{N}$	Set of the network nodes	—	—
D	Destination node	Known by all nodes	—
$\mathcal{Y}_i$	Set of upstream neighbors of node i	—	One-hop neighbors
$\widetilde{\mathcal{Y}}_i$	Set of all one-hop neighbors of node i	—	One-hop neighbors
$\mathcal{T}_i$	Set of PHY technologies available at node i	—	—
$\mathcal{T}_{i,j}^{\tau}$	Set of PHY technologies through which i can transmit to j at time τ	Technology availability signaled by MAC protocol	—
$P_{j,\tau}$	Number of bits in node j's queue at time τ	$P_{j,\tau'}$ for $\tau' < \tau$, $\widehat{R}_j^{\tau}(k,t)$ $\forall k \in \mathcal{Y}_j$	One-hop neighbors
$C_{i,t}^{(u)}$	Total number of bits that can be transmitted by i using technology t over a time period of duration u	Technology availability signaled by MAC protocol	—
$L_j^{(i)}$	Number of node-disjoint routes towards the destination D available to i when routing through j	Topology information or $\mathcal{Y}_\ell$ $\forall \ell \in \mathcal{Y}_i \cup \widetilde{\mathcal{Y}}_i$	—
$F_j(i)$	Fair share of j's upstream transmission resources that can be dedicated to node i	$L_j^{(i)}$, $\mathcal{Y}_\ell$ $\forall \ell \in \mathcal{Y}_i \cup \widetilde{\mathcal{Y}}_i$	—
$R_i^{\tau}(j,t)$	Number of bits in node i's queue sent to node j using technology t at time τ	$P_{i,\tau}$, Δ_j^{τ}, $C_{i,\tau}^{(u)}$, $F_j(i)$	—
Δ_j^{τ}	Amount of upstream transmission resources of node j that can be secured for node i's transmissions	$C_{j,t}^{(u)} \forall t \in \mathcal{T}_{j,k}^{\tau}$, $R_j^{\tau}(k,t)$ $\forall k \in \mathcal{Y}_j$	Nodes ℓ s.t. $i \in \mathcal{Y}_\ell$

5.2.2 Preliminary definitions and assumptions

We assume that our underwater network is composed of a set $\mathcal{N}$ of multimodal nodes, where $|\mathcal{N}| = N$. The network implements a converge-casting scenario, where all nodes send their information over multiple hops to a common sink (denoted as D, e.g., node 6 in Fig. 5.1). We assume that the network topology has been already discovered.[1] While the implementation of a topology discovery algorithm is outside the scope of this chapter, we do assume that the process can be subject to errors, or to inaccuracies caused by slow topology changes over time. We will take these errors into account in the design of the routing protocol. Given the outcome of the routing structure discovery, we assume that each node knows the available alternatives to forward a packet towards the sink D. Accordingly, for each node, we call $\mathcal{Y}_i$ the set of upstream neighbors of i, i.e., $\mathcal{Y}_i$ contains all one-hop neighbors of i that can advance packets one further hop towards D (for example,

---

[1] This can be done, e.g., by sending beacon packets downstream from the sink to the network nodes [173], or by carrying out processes aimed at discovering either the topology itself [116] or at least the available routes [174]. The discovered structure can be maintained by tracking transmission successes over each link over time [175]. These processes are out of the scope of this work.

$\mathcal{Y}_5 = \{2,3\}$ in Fig. 5.1).[2] We also call $\widetilde{\mathcal{Y}}_i$ the list of *all* one-hop neighbors of i.

Each multimodal node incorporates a number of PHY technologies, listed in the set $\mathcal{T}_i$ (e.g. $\mathcal{T}_5 = \{\mathrm{LF}, \mathrm{MF}\}$ in Fig. 5.1). A node can communicate using any subset of technologies available to it and to the addressed receiver. Note that the list of available technologies may vary over time, e.g., due to channel variations or mobility. Let $\mathcal{T}_{i,j}^{\tau}$ be the set of technologies that i can use to transmit to j at time τ. We assume that this set of technologies is known to the routing protocol, e.g., because some underlying MAC protocol forwards a notification when a given technology is available. This process is outside the scope of this chapter, and can be implemented, e.g., through the schemes in [72, 73].

Each node maintains a queue with a list of packets to transmit. Denote the bits in node i's queue at time τ as $P_{i,\tau}$. Define $R_i^{\tau}(j,t)$ as the number of bits in $P_{i,\tau}$ that will be sent by node i to node $j \in \mathcal{Y}_i$ using technology t at time τ. The objective of the routing algorithm is to find optimal values for $R_i^{\tau}(j,t)$, under a constraint on the total number of bits that can be transmitted by i using technology t over a user-defined time span u, denoted as $C_{i,t}^{(u)}$. We will indicate these optimal values as $\widehat{R}_i^{\tau}(j,t)$. A summary of the employed notation is provided in Table 5.1. The table also reports the inter-dependencies among the quantities introduced above, and the nodes each quantity is shared with. This is meant as a reference for the algorithm description below.

The optimization is to be carried out using the information available at node i or passed on by its upstream neighbors. In particular, we assume that node i knows: $\mathcal{Y}_i$ and $\mathcal{Y}_j$ $\forall j \in \mathcal{Y}_i$; $P_{i,\tau}$ and $P_{j,\tau'}$ $\forall j \in \mathcal{Y}_i$, where $\tau' < \tau$ is a time epoch that refers to a transmission carried out by node j immediately preceding the current epoch τ; and $C_{j,t}^{(u)}$ $\forall j \in \mathcal{Y}_i$.

5.2.3 Routing algorithm

We are now ready to describe the steps of the routing optimization algorithm executed by node $i \in \mathcal{N}$. Node i has to decide how many bits to transmit through each of its available technologies, and carries out the following steps for each upstream neighbor in $\mathcal{Y}_i$. For clarity, we will illustrate the algorithm by referring to one of these upstream nodes, j. The optimal transmitted bit

---

[2] We remark that routing in the network is never performed downstream, i.e., no relaying operation will bring a packet one hop farther from the destination.

allocation for node i is obtained by solving the following problem:

$$\widehat{R}_i^{\tau}(j,t) = \underset{R_i^{\tau}(j,t)}{\arg\max} \sum_{j\in\mathcal{Y}_i} \sum_{t\in\mathcal{T}_{i,j}^{\tau}} R_i^{\tau}(j,t) \tag{5.1a}$$

$$\text{s.t.} \quad \sum_{j\in\mathcal{Y}_i} \sum_{t\in\mathcal{T}_{i,j}^{\tau}} R_i^{\tau}(j,t) \leq P_{i,\tau}\,; \tag{5.1b}$$

$$\sum_{t\in\mathcal{T}_{i,j}^{\tau}} R_i^{\tau}(j,t) \leq \Delta_j^{\tau}\,; \tag{5.1c}$$

$$R_i^{\tau}(j,t) \leq C_{i,t}^{(u)} F_j(i)\,. \tag{5.1d}$$

Constraint (5.1b) means that the bits transmitted across all technologies shall not exceed the remaining number of bits in the queue at node i. Constraint (5.1c) takes into account that i's upstream neighbor j may have a backlog of packets to be transmitted, and that node j would give priority to these bits in a FIFO fashion. Assuming that the remaining portion of j's upstream transmission resources after the transmission of the backlog is sufficient to transmit Δ_j^{τ} bits from node i, constraint (5.1c) makes sure that i transmits no more than Δ_j^{τ} bits to j, aggregate over all technologies. Finally, constraint (5.1d) means that the number of bits transmitted through either technology should not exceed a certain limit, defined as i's fair share of j's upstream link capacity, where $F_{\ell}(j) = 0$ if node ℓ has nothing to transmit.

Note that, for a given node j, $\sum_i F_j(i)$ can exceed 1. This is because condition (5.1d) only applies if a node i has more possible relays to the sink than node j: in this case, it should divide its transmissions while considering the relay options of other neighbors of j. Also note that since we limit ourselves to a distributed solution, node i has typically no way to ascertain the technology used over link $j \to k$, $k \in \mathcal{Y}_j$. Instead, we perform technology allocation only hop-by-hop. As a result, the term $F_j(i)$ is not related to the used technology t.

The quantities required to evaluate the constraints are fully determined by node i. Node i is assumed to know the capacity of its one-hop links, its available technologies, and its different paths to the sink. However, Δ_j^{τ} and $F_j(i)$ must still be computed, as will be detailed in the following.

Calculation of the fair share of node j's resources

We start with the computation of $F_j(i)$. The upstream transmission resources of node j are assigned to a downstream neighbor i depending on the number of node-disjoint routes towards the destination D available to i, indicated with $L_j^{(i)}$, where the subscript j indicates that $j \in \mathcal{Y}_i$, and that it is being considered as a next hop. The rationale behind the resource assignment strategy is that if some downstream neighbors m of j can reach the destination only via a route that passes through node j, such nodes m should be given a higher priority in the use of j's upstream transmission resources. Formally, define

$$\widetilde{L}_j^{(i)} = \sum_{\ell \in \mathcal{Y}_j} L_j^{(\ell)} - L_j^{(i)} \, . \tag{5.2}$$

If $\widetilde{L}_j^{(i)} = 0$, then we immediately set $F_j(i) = 1$, as j is the only neighbor of i that can relay packets towards D (e.g., $F_5(1) = 1$ in Fig. 5.1). Otherwise, $F_j(i)$ is computed as

$$F_j(i) = \frac{\widetilde{L}_j^{(i)}}{\sum_{\ell \in \mathcal{Y}_j} \widetilde{L}_j^{(\ell)}} \, , \tag{5.3}$$

where it is understood that $i \notin \mathcal{Y}_j$, i.e., i is not an upstream neighbor of j. Note that this is a way of "fairly" allotting more resources to nodes with fewer available routes, not a means to split the capacity of node j's links towards its upstream neighbors, which is instead taken care of distributedly via constraint (5.1c). Instead, we allow nodes with a single forwarding opportunity to convey all traffic there, while nodes with additional opportunities should split their traffic through all available routes.[3] For example, in Fig. 5.1, node 1 can only forward to node 5, so $F_5(1) = 1$, and because of constraint (5.1d), all of node 1's traffic will be conveyed through the link 1→5, which can transport $C_{5,\mathrm{LF}}^{(u)}$ bits over a time span u. Conversely, node 4 shares node 5 as a potential relay, but has an additional opportunity to forward to node 2: for this reason, $F_5(4) = 1/3$ and $F_2(4) = 2/3$, hence node 4 will send up to $C_{4,\mathrm{LF}}^{(u)} F_5(4)$ to node 5 and $C_{4,\mathrm{LF}}^{(u)} F_2(4)$ to node 2, as per constraint (5.1d).

$L_j^{(i)}$ in (5.2) is computed differently depending on the network topology information available to node i. We hereby distinguish between two cases: a) full topology-informed fair share computation, in case perfect topology information is available to i; and b) one-hop topology-informed fair share computation, otherwise.

In the case of the benchmark OMR–FF, where the nodes are aware of the full network graph, each node exactly computes the number of disjoint routes available to itself and to its neighbors. Clearly, this is not possible in the distributed case of our OMR algorithm. Here, only one-hop topology information is available to each node i. In this condition, every one-hop neighbor is a potential relay on a disjoint route to the destination. However, if some relays have common relays upstream, the number of disjoint routes available to i would be overestimated: in turn, i would be allotted a lower share of j's resources.

In order to minimize the route overestimation problem in OMR, we consider the nodes that are upstream neighbors of i (in set $\mathcal{Y}_i$) and neighbors

---

[3] We remark that fair splitting is mainly needed in high traffic conditions. If the network traffic is sufficiently low, no bottlenecks will appear and the allocation will still be efficient.

of its considered upstream relay j (in set $\widetilde{\mathcal{Y}}_j$). We then eliminate at least the cases where a node $w \in \mathcal{Y}_i \cap \widetilde{\mathcal{Y}}_j$ has either i, j, or both as its only upstream neighbors. In fact, none of these cases would lead to a disjoint route. Formally, $L_j^{(i)}$ is estimated as

$$L_j^{(i)} = |\mathcal{Y}_i| - \sum_{w \in \mathcal{Y}_i \cap \widetilde{\mathcal{Y}}_j} \mathbb{1}\left[\mathcal{Y}_w \subseteq \{i, j\}\right] \tag{5.4}$$

where $\mathbb{1}[\mathsf{p}]$ evaluates to 1 whenever the predicate p is true. We note that the computation of $L_j^{(i)}$ in (5.4) is not carried out if the destination $D \in \mathcal{Y}_j$. In this case, the traffic is always directed to the sink, without passing through other 1-hop neighbors.

Our fair resource splitting eliminates bottlenecks at the expense of favoring nodes with fewer routes to the sink by setting their fairness index, $F_j(i)$, to a high value. This fair splitting automatically adjusts to the network topology to optimize the channel utilization. Yet, due to this splitting, the performance may decrease in networks with low traffic, where allocation based only on link capacity is preferred. Moreover, in large networks, topology mismatches may lead to a wrong setting of the fairness index and thus to a performance degradation. Hence, our protocol mostly fits small underwater networks with a few hops to the sink (a scenario that occurs in the majority of underwater network applications), and those cases where either the network traffic is moderate to high, or when the traffic is unknown.

Calculation of upstream resources

We proceed with the computation of Δ_j^τ from (5.1c), which represents the amount of j's upstream transmission resources that can be assigned to node i. This computation is made based on an estimate (obtained by i) of the quantities $\widehat{R}_j^\tau(k, t)$ $\forall k \in \mathcal{Y}_j$. These quantities estimate the outcome of the allocation problem as may be solved by j to compute how many bits it should transmit to its own upstream neighbors with each technology $t \in \mathcal{T}_{j,k}^\tau$. We have

$$\Delta_j^\tau = \sum_{k \in \mathcal{Y}_j} \sum_{t \in \mathcal{T}_{j,k}^\tau} \left(C_{j,t}^{(u)} - \widehat{R}_j^\tau(k, t) \right) . \tag{5.5}$$

Note that we still indicate the current time τ as a reminder that the current solution to i's problem depends on j's solution for its current transmission allocation. The quantities $\widehat{R}_j^\tau(k, t)$ are obtained by i by solving the following problem:

$$\widehat{R}_j^\tau(k,t) = \underset{R_j^\tau(k,t)}{\arg\max} \sum_{k\in\mathcal{Y}_i} \sum_{t\in\mathcal{T}_{j,k}^\tau(k,t)} R_j^\tau(k,t) \tag{5.6a}$$

$$\text{s.t.} \quad \sum_{k\in\mathcal{Y}_j} \sum_{t\in\mathcal{T}_{j,k}^\tau} R_j^\tau(k,t) \leq P_{j,\tau}\,; \tag{5.6b}$$

$$R_j^\tau(k,t) \leq C_{j,t}^{(u)}\, F_k(j)\,, \tag{5.6c}$$

where $F_k(j)$ is the share of node k's resources that can be devoted to transport node j's traffic. Constraint (5.6b) means that the bits transmitted through all technologies shall not exceed the remaining number of bits in node j's queue, whereas constraint (5.6c) implies that the number of bits transmitted by j via either technology shall not exceed its share of the upstream capacity of its relay k over a time period of length u. No constraint is imposed based on the terms Δ_k^τ, as i does not know them and it would take too many resources for j to transmit the corresponding information, especially over slow acoustic links. Note that (5.5) enforces congestion control in the network, by avoiding that a downstream node transmits more data than the receiving relay can advance towards D.

We note that the same procedure described in Section 5.2.3 above is employed to compute the fairness values $F_k(j)$ $\forall k \in \mathcal{Y}_j$. When full topology information is available, i.e., in the case of the benchmark OMR–FF, this procedure is trivial. However, since OMR is a distributed solution, node i cannot calculate $F_k(j)$ without knowledge of $\mathcal{Y}_k$ $\forall k \in \mathcal{Y}_j$, and therefore must rely on node j to transmit the $F_k(j)$ values. Similarly, since node i is not aware of $P_{j,\tau}$, we let j piggyback this value into each transmission. As a result, the overhead of this information is in the order of only a few bits. Assume that j communicated $P_{j,\tau'}$ at some preceding instant $\tau' < \tau$: $P_{j,\tau}$ can be readily derived as

$$P_{j,\tau} = P_{j,\tau'} - \sum_{k\in\mathcal{Y}_j} \sum_{t\in\mathcal{T}_{j,k}^{\tau'}} \widehat{R}_j^\tau(k,t)\,. \tag{5.7}$$

5.2.4 Complexity and overhead of OMR

To obtain the routing solution with OMR, each node i needs to solve (5.1) and (5.6). Since both $\widehat{R}_i^\tau(j,t)$ and $\widehat{R}_j^\tau(k,t)$ can take any value, these two optimization problems are solved through linear programming. The average complexity of OMR is therefore polynomial with $|\mathcal{Y}_i| \cdot \max_j |\mathcal{T}_{i,j}^\tau|$.

In terms of overhead, OMR requires the transmission of the size of the queue of one-hop neighbors, $P_{j,\tau}$. Representing $P_{j,\tau}$ as one byte, the total overhead of OMR is therefore $N^2 + N^2\log(N) + 8N$ bits. OMR is fully distributed and requires information only from one-hop links to transfer $\mathcal{Y}_j$, $F_k(j)$, $\forall k \in \mathcal{Y}_j$, and $P_{j,\tau}$. This information is piggybacked to node i within

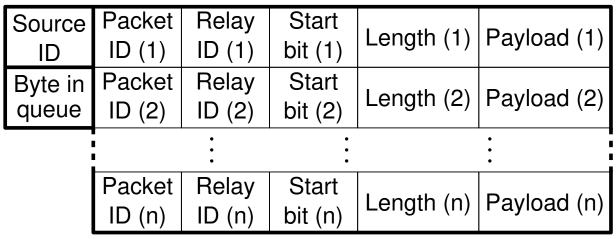

Source ID	Packet ID (1)	Relay ID (1)	Start bit (1)	Length (1)	Payload (1)
Byte in queue	Packet ID (2)	Relay ID (2)	Start bit (2)	Length (2)	Payload (2)
		⋮	⋮		⋮
	Packet ID (n)	Relay ID (n)	Start bit (n)	Length (n)	Payload (n)

Figure 5.2: Format of a typical transmitted datagram formed by fragments taken from n packets.

the packet transmitted by its one-hop neighbor j only when the values change. Since the network topology changes very slowly, $\mathcal{Y}_j$ and $F_k(j)$ are rarely transmitted, and only $P_{j,\tau}$ must be updated after each packet transmission. The communication overhead of OMR is therefore only $8N$ bits.

5.2.5 Implementation details

OMR operates at the network layer. For node i, OMR receives original packets from the application layer, and packets to relay from $|\mathcal{T}_i|$ multimodal MAC layers, one for each communication technology. The packets are saved in a *routing buffer*, implemented as a FIFO queue, which advances based on notifications received from the multimodal MAC layers. Once these layers notify node i about the possibility to transmit, OMR calculates (5.1), and reads $\widehat{R}_i^{\tau}(j,t)$ bytes from its queue. To optimize channel use, we allow byte allocation from part of various awaiting packets. If $\widehat{R}_i^{\tau}(j,t)$ is smaller than the size of the next packet, then the packet is segmented. Otherwise, if $\widehat{R}_i^{\tau}(j,t)$ is larger than the size of the next packet, bytes belonging to multiple packets are transmitted. In both cases, the packets are rebuilt at the sink based on an identification number added as a header. Fig. 5.2 shows a typical packet format. Note that, to support OMR decisions in the neighborhood of a transmitting node, the header includes the number of remaining bytes in the sender's queue.

To solve problems (5.1) and (5.6), we use the simplex algorithm [176]. Both (5.1) and the techniques to obtain its parameters (for example, (5.3) and (5.6)) are formalized as linear optimization problems with convex lower bound constraints, and the solution found is globally optimal. The average complexity is polynomial [177], and the solution is thus scalable. For reproducibility, we publish the implementation of OMR.

5.3 Simulations

We now evaluate the performance of our OMR routing scheme through numerical simulations.

5.3.1 Benchmark methods

We compare the performance of OMR with the following benchmarks.
Flooding — A node broadcasts all incoming packets through all available technologies. The flooding method will generate multiple copies of each packet. The result is high link utilization and, in the absence of packet collisions, small end-to-end delay as well as high goodput. As a result, flooding is a preferred choice in contention-free environments where the highest reliability is sought. However, the performance of this scheme is expected to decrease considerably when a contention-based MAC is used. Moreover, due to the many transmissions, energy efficiency is expected to be low.
RND — A node allocates the bits of an incoming packet uniformly at random across the available outgoing links. Like OMR, the RND scheme fragments packets for simultaneous transmission through different links. The main strength of the method is that it is simple and fully distributed with no need for any topology information. However, the allocation does not consider the flow constraints of upstream nodes.
OMR–FF — A version of OMR where the fair share of the transmission resources to be allotted to each node is calculated based on full topology information. OMR–FF stands in contrast to OMR, where the fair share computation is based only on the knowledge of one-hop links. This difference affects the way resources are allocated to different nodes over a multi-hop path: with only local topology information, OMR is more conservative in terms of link capacity usage than OMR–FF.
ETT — A packet is sent through a chosen link following the procedure in [80], modified to manage the case of multiple technologies available per link. Specifically, instead of the expected transmission time (ETT) metric $\mathrm{ETT}_{k,i}$ for the kth path and the ith link along path k, we employ $\mathrm{ETT}_{k,i,t}$ for technology t over the ith link. Therefore, we modified [80] as follows. To choose the path, we compute the weighted cumulative ETT (WCETT) metric as

$$\mathrm{WCETT} = (1-\beta)\sum_i \left(\min_t\,[\mathrm{ETT}_{k,i,t}]\right) + \beta \max(X_k)\,, \tag{5.8}$$

where X_k is the accumulated delay over path k. Once a path k to the destination is chosen based on its WCETT metric, the technology t whose $\mathrm{ETT}_{k,i,t}$ is maximum is chosen to transmit over the ith link. Different than our distributed OMR solution but similar to the centralized benchmark OMR–FF, the ETT scheme requires global topology information. The ETT scheme finds the best route in terms of delivery time but neglects bottlenecks created due to the extensive use of such best routes by all nodes. The result is a less fair routing scheme, whose delivery time is expected to be high for high traffic, and whose performance is expected to deteriorate in the presence of packet collisions. Moreover, the strategy of ETT leads to high topology dependence, as bottlenecks are mostly expected in sparse networks.

To avoid loops in the flooding and RND schemes, we include in each packet the routing path it has traveled. With flooding, a receiver will avoid broadcasting a packet if the routing path shows that the packet has already traveled through all of the node's one-hop neighbors. In the RND scheme, no bit will be allocated to a given link if the packet has already traveled through the other endpoint of such link. In all benchmark methods, packets are fragmented according to the maximum length allowed by the technology through which the packet is sent. Last, the performance of the ETT method depends on the parameter $0 \leq \beta \leq 1$, which trades off accumulated delay vs. maximum delay. In the simulation results below, we explored the performance for various values of β, and show the results for the β value that leads to the best performance for each of the metrics introduced in the following subsection.

5.3.2 Quality metrics

We measure the performance in terms of end-to-end transmission delay, per-node goodput, message success rate, transmission efficiency, and link throughput. Once all fragments of a packet i of node n have been successfully received by the sink, we measure the message's end-to-end transmission delay as

$$\rho_d = \frac{1}{N-1} \sum_{n=1}^{N-1} \frac{1}{R_n} \sum_{i=1}^{R_n} (T^r_{n,i} - T^s_{n,i}) \;, \tag{5.9}$$

where $T^r_{n,i}$ is the time when the full message was received, $T^s_{n,i}$ is the time when the message reached the network layer for routing, and R_n is the number of messages sent by node n and received in full by the sink node. For a network run time T_{net}, the per-node goodput is defined by

$$\rho_g = \frac{1}{N-1} \sum_{n=1}^{N-1} \sum_{i=1}^{I_n} \frac{M^r_{n,i}}{T_{\text{net}}} \;, \tag{5.10}$$

where $M^r_{n,i}$ is the number of bytes received by the sink for a message i originated from node n, and I_n is the number of messages originated by node n. The average per-node message success rate is

$$\rho_s = \frac{1}{N-1} \sum_{n=1}^{N-1} \frac{R_n}{I_n} \;. \tag{5.11}$$

Note that $M^r_{n,i}$ from (5.10) can exceed the number of bytes transmitted by node n, denoted by $M^s_{n,i}$. This case happens when message i or parts of it are sent through several links such that the sink may receive multiple copies of some message chunks. We consider these cases as a waste of resources, and call overhead the fraction of messages for which extra copies of any parts of the message are received by the sink. Formally:

$$\rho_o = \frac{1}{N-1} \sum_{n=1}^{N-1} \sum_{i=1}^{I_n} U\left(\frac{M^r_{n,i}}{M^s_{n,i}} - 1\right) , \tag{5.12}$$

where $U(x)$ is a step function whose value equals 1 if $x > 0$, and zero otherwise. We also consider an energy efficiency metric: this is defined by

$$\rho_e^{\text{tot}} = \sum_{n=1}^{N-1} \left(\sum_{i=1}^{I_n} B_{i,n} T_{\text{tx}}^{\text{byte}} W_{\text{tx}}\right) + T_{\text{idle}}(n) W_{\text{idle}} , \tag{5.13}$$

where $B_{i,n}$ is the total number of bytes transmitted for message i originated from node n, $T_{\text{tx}}^{\text{byte}}$ and $T_{\text{idle}}(n)$ are respectively the time spent in the transmission and idle state by node n, whereas W_{tx} and W_{idle} represent the power consumption in either state. As in this study we will mainly focus on multimodal acoustic networks (where a node integrates different acoustic PHYs), the transmit power outweighs the idle listening power. Considering also that W_{tx}, W_{idle} and $T_{\text{tx}}^{\text{byte}}$ are constants, we normalize our efficiency metric to the total number of transmitted bytes and to the total network operation time, and define it as the total number of transmitted bytes across the network for a single message:

$$\rho_e = \frac{1}{(N-1)\sum_{n=1}^{N-1} I_n} \sum_{n=1}^{N-1} \sum_{i=1}^{I_n} \frac{B_{i,n}}{T_{\text{net}}} , \tag{5.14}$$

Finally, the throughput of the link from node n to node m using communication technology t is defined as the ratio between the number of bytes successfully transmitted through the link, $R^t_{n,m}$, and the run time. Formally, the average link throughput is

$$\rho_u = \frac{1}{N^t} \sum_{n \in \mathcal{N}^t} \frac{1}{D^t_n} \sum_{m \in \mathcal{D}^t_n} \frac{R^t_{n,m}}{T_{\text{net}}} , \tag{5.15}$$

where $\mathcal{N}^t$ is the set of the nodes that hold communication technology t, and $\mathcal{D}^t_n$ is the set of the nodes that share a communication link with node n via technology t. Moreover, $|\mathcal{N}^t| = N^t$ and $|\mathcal{D}^t_n| = D^t_n$.

As mentioned in Section 5.2.1, we aim at minimizing ρ_d, and at maximizing ρ_g and ρ_s. Yet, for energy conservation, we are also interested in minimizing ρ_o and ρ_e. Finally, for better fairness and to avoid congestion, we are interested in a large ρ_u.

5.3.3 Simulation setup

Our simulation setup is based on a Monte-Carlo set of 1000 network topologies. In each simulation run, $N = 10$ nodes are placed uniformly at random

Table 5.2: Simulations: characteristics of the simulated communication technologies

Technology	Bit rate [bps]	Max range [m]
Low-rate acoustics	1000	3000
Mid-rate acoustics	32000	300
High-rate acoustics	64000	100

over an area of 500×500 m^2 with water depth of 100 m. The line of sight between the nodes may be interrupted by four horizontal obstacles and one vertical obstacle at uniformly distributed locations with uniformly distributed length in the range $[10, 50]$ m. Node 10 is defined as the sink node. Each of the other nine nodes is equipped with one or more communication technologies at random between low-frequency, mid-frequency, and high-frequency acoustic communications. The characteristics of the three acoustic systems are based on the three EvoLogics modems working in the 18–34 kHz, 48–78 kHz, and 120–200 kHz bands [135]. A summary of these characteristics is provided in Table 5.2, where the communication range of each model has been conservatively set. We remark that all acoustic technologies operate on mutually orthogonal bands, making the nodes multimodal. We run each simulation for $T_{\text{net}} = 600$ s. At the beginning of each simulation, each of the nine nodes generates its own packets according to a Poisson process of rate $\lambda = 3$ packets per minute per node. The size of each packet is drawn uniformly at random between 0 and 64 kbits. At any given time, the node is either idle, or serving a self-generated message or a packet received by another node. For each served packet, the node solves the routing allocation problem, as discussed in Section 5.2. The packet is then segmented according to the solution of the routing problem and sent over the different links according to the determined routing allocation. Besides the information-bearing bytes, each packet segment includes the ID of the original message, the location of the packet segment within the original message, and the routing path the packet segment has gone through. Once received at the sink node, the various packet segments belonging to the same message are combined together.

We consider a binary phase-shift-keying modulation, and a scheduling protocol where a node holding a packet transmits it as soon as all its communication technologies are free. Once a packet is received, an acknowledgment is transmitted. To form the full topology information required for the OMR–FF method and the one-hop link information required for OMR, we refer to the communication ranges in Table 5.2. For example, for mid-frequency acoustic communications, a link would be assumed to exist if the distance between the two nodes is smaller than 300 m, and this distance is continuously measured in our simulations by an underlying PHY mechanism. To calculate the route on the way to the sink (i.e., the sets $\mathcal{Y}_i$, $\forall i$), we carry out a preliminary route discovery phase, where the sink propagates a discovery packet through the network. The discovered routes are kept stable throughout each simulation run.

While in the OMR scheme the one-hop links are assumed to be known, in reality links would vary from the communication range set in Table 5.2. To simulate this, we calculate the instantaneous packet error rate (PER) for each link used by transmitted packet segments. Once a packet transmission fails and/or no acknowledgment is received, the packet is shifted to the end of the message queue and is re-transmitted at a later time. The PER is computed based on the simulated signal-to-noise ratio (SNR) and on the packet size. The SNR of the low-rate and high-rate acoustic links is calculated using the Bellhop framework [124, Ch. 3] for shallow waters of depth 100 m, flat sandy bottom, fixed sound speed of 1500 m/s, and considering a source level of 170 dB re (1 μPa at 1 m). The ambient noise level is set to 40 dB re (1μPa^2/Hz) for low-frequency acoustics, as 30 dB re (1μPa^2/Hz) for mid-frequency acoustics, and 10 dB re (1μPa^2/Hz) for high-frequency acoustics.

We consider two MAC schemes. With the first, named *Ideal*, no packet collisions occur and acknowledgments are always received with no errors. This ideal protocol works in favor of the flooding scheme, where the links are expected to be utilized in full. The second (*Immediate*) is a MAC protocol in which packets are transmitted immediately upon arriving to the MAC layer, unless another transmission or reception is already taking place, and the reception of packets and acknowledgments is determined based on the link SNR and only when no collision occurs with another packet or acknowledgment. The Immediate MAC models the protocol [178] employed by the modems in the lake experiment (see Section 5.4). In both the Ideal and Immediate MAC approaches, packets that need to be re-transmitted are re-inserted as new packets at the end of the queue.

5.3.4 Simulation results

In Figs. 5.3a and 5.3b, we show the cumulative distribution function (CDF) of the delay ρ_d for the Ideal MAC and the Immediate (realistic) MAC, respectively, computed over the ensemble of results from the whole Monte-Carlo simulation set. The CDF enables us to evaluate the entire distribution of the results. For the RND and ETT benchmarks, we observe a very wide span of results. This span suggests that these methods lack robustness, or in other words that thay do not provide sufficient performance guarantees over different topologies. By way of contrast, the distributions of the end-to-end delay of OMR and of its ideal benchmark OMR-FF (which counts on full network topology knowledge), span a much narrower set of values. We therefore conclude that these methods are robust to the network setup. The fact that the results span more than 100 s of delay is due to low-capacity

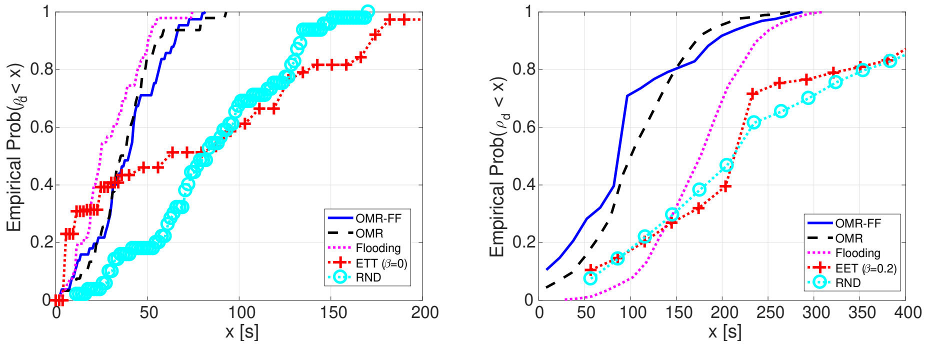

(a) Ideal MAC.

(b) Immediate MAC.

Figure 5.3: Simulations: CDF of end-to-end transmission delay, ρ_d, from (5.9). Flooding achieves the best results with the Ideal MAC, which neglects collisions. With the more realistic Immediate MAC, OMR achieves the best results.

links requiring packets to be segmented into small fragments. This tends to increase the backlog of the nodes, which in turn increases the delay. From Fig. 5.3a, we observe that with Ideal MAC the delay of the flooding scheme is better than that of OMR–FF and OMR and so is some of the performance of ETT. This result is obtained since in Ideal MAC we neglect multiple-access interference, hence flooding and ETT can propagate messages very fast through the network. Yet, the advantage of ETT is achieved in only 40% of the cases with an average of roughly 110 s compared to 39 s and 38 s for OMR–FF and OMR, respectively. This is because ETT obtains good results mostly in dense topologies. In terms of end-to-end delay, the performance of RND is the worst, since it does not optimize the packet allocation and generates bottlenecks with high probability. When the realistic Immediate MAC is used (Fig. 5.3b), we observe that all methods are affected. Yet, as noted above, the performance span of RND and ETT shows that these methods are less robust to varying topologies than the flooding scheme and our OMR method. As expected, the delay of OMR–FF is better than the delay of OMR for the realistic MAC case. This is because the availability of topology information in OMR–FF makes it possible for the nodes to optimally allocate transmission resources. However, we remark that the delay of our distributed OMR solution is almost as good as that of the benchmark centralized OMR-FF solution, which is remarkable given the limited topology information.

Next, in Figs. 5.4a and 5.4b, we show the complementary CDF (C-CDF) of the goodput, ρ_g, for the Ideal MAC and the Immediate MAC, respectively. The random bit allocation of RND yields low goodput values, since it does not give priority to less stable links. Yet, with Ideal MAC, ETT obtains high

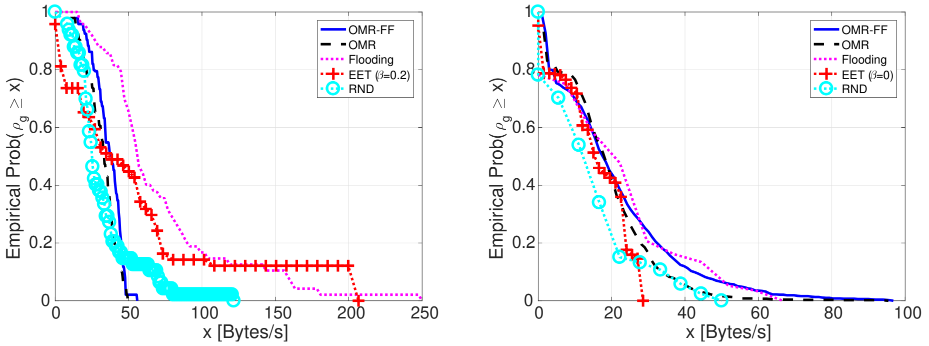

(a) Ideal MAC.

(b) Immediate MAC.

Figure 5.4: Simulations: C-CDF of per-node goodput, ρ_g, from (5.10). The results show that OMR achieves similar performance as OMR–FF, and that when collisions are considered, the goodput of OMR is better than ETT and similar to flooding.

goodput that is comparable to the energy-wasting flooding scheme. However, the performance of both ETT and flooding is more dispersed compared to OMR (meaning that OMR's performance is more predictable). Moreover, while the performance of ETT and flooding decreases much when packet collisions are considered (Fig. 5.4b), our OMR scheme achieves almost the same performance with either MAC, implying a good level of robustness. The results confirm that flooding and ETT outperform OMR only when packet collisions are ignored (Fig. 5.4a), otherwise the performance of ETT is worse than OMR's, and flooding achieves results similar to OMR (Fig. 5.4b). The reason for the former is the bottlenecks created by ETT, whereas the latter is due to the large number of packet collisions caused by the many transmissions of flooding. This is confirmed by the results of the lake experiment given further below.

When comparing the goodput of the five schemes, it is also of interest to examine the packet delivery ratio, ρ_s from (5.11), as shown in Fig. 5.5a for the Ideal and the Immediate MACs, respectively. Since the link utilization of RND is low, OMR outperforms RND. When the Ideal MAC is considered, the success rate of the flooding scheme is the highest, while the performance of ETT is slightly less than OMR's. In fact, flooding transmits each packet many times through different links, thus increasing the probability of correct delivery, whereas ETT creates several bottlenecks along the best path. However, for the immediate MAC, we observe that packet collisions reduce the delivery ratio of flooding (despite the high transmission redundancy of the scheme) and of ETT considerably. In fact, the increased load imposed on the queues of the nodes by the redundancy of flooding and the single chosen path of ETT actually contributes to the poor delivery ratios of these two

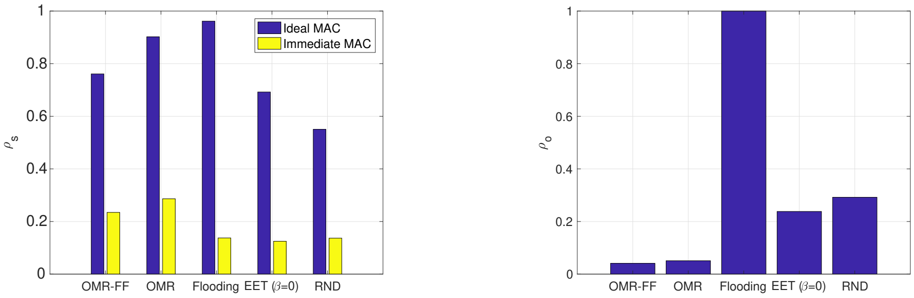

(a) Average success ratio ρ_s from (5.11).

(b) Average overhead ratio ρ_o from (5.12).

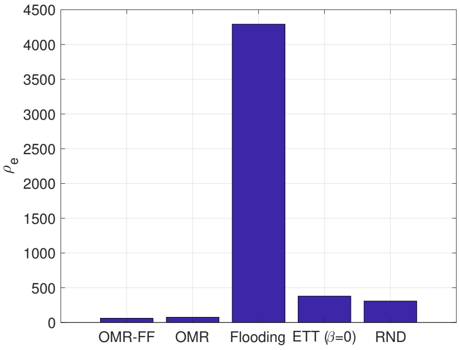

(c) Average ρ_e from (5.14).

Figure 5.5: Simulations. Success rate and energy efficiency for the Immediate MAC protocol. OMR is more efficient than flooding, ETT, and RND. OMR–FF and OMR perform similarly.

schemes.

To comment on the energy efficiency of the three methods, in Figs. 5.5b and 5.5c we show the overhead ρ_o, and the total number of transmitted bytes, ρ_e, respectively, for the case of Immediate MAC. While multiple (redundant) copies of all messages are received with the flooding scheme, in the two OMR versions the sink receives extra copies only for about 8% of the messages. We also observe that although ETT sends packets along a single path, its overhead exceeds that of OMR. This is because the load on the path chosen by ETT tends to create many collisions also on the feedback channel, thereby leading to the retransmission of many unnecessary packets. Similarly, while RND does not issue redundant packets, its sub-optimal link utilization leads to the transmission of many more packets than required, and thereby to an increase of the number of collisions affecting acknowledgment packets. The advantage of OMR in terms of overhead is further emphasized by the huge difference in the energy efficiency measured as the total number of bytes sent by the three benchmark methods compared to OMR, and shown in Fig. 5.5c. Also here, this result slightly favors OMR, which requires much less knowledge and is thus more distributed.

To summarize, the simulation results show that OMR can deliver packets effectively to their destination, and at the same time it is an energy efficient method, that does not originate a large amount of overhead and that keeps the number of transmitted bits limited. Compared to the three benchmark schemes, the performance of OMR is less sensitive to the network topology. When a realistic MAC protocol is considered, where packet collisions can occur, OMR outperforms the three benchmark schemes in almost all categories. We also note that the above advantages are obtained without ETT's assumption that the packet error rate in the network are known. This is a hard assumption, that requires knowledge of the SNR at the receiver and likely of the transmission range in each link. Equally important, the advantage of OMR over ETT is obtained with only 1-hop topology information, compared to global topology information in ETT. Hence, OMR is also a more practical scheme than ETT.

5.4 Field experiment

Our simulations revealed that the results of the comparison between OMR and the other benchmark schemes depend on whether packet collisions are considered or not. To support and complement these conclusions, we carried out an experiment in a real underwater environment. Experimenting with real systems includes non-ideal modem hardware behaviors, multipath propagation, actual packet collisions, the impact of finite memory in each node, and delays due to the management of multimodal technologies. In the following, we describe the setup of our field trial and the results obtained.

5.4.1 Setup of the experiment

The trial took place in June 2016, in the Werbellin lake, north of Berlin, Germany. The lake is narrow and long, with a maximum depth of 55 m. The resulting acoustic channel is characterized by a long delay spread and location-dependent ambient noise, which poses a significant challenge for underwater acoustic networks. The experiment included six nodes deployed at four different geographical locations. Three locations were reached using small vessels: two motorized inflatable boats, and one motorboat. The fourth location was one of the lake's docks. Throughout the experiment, the boats tended to drift at an approximate speed of 0.25 m/s.

The multimodal functionality was obtained via three types of EvoLogics acoustic modems [135], These integrated underwater communication systems include an acoustic transducer, driving electronics, a DSP/FPGA implementing the S2C modulation scheme [179], and a communications stack running

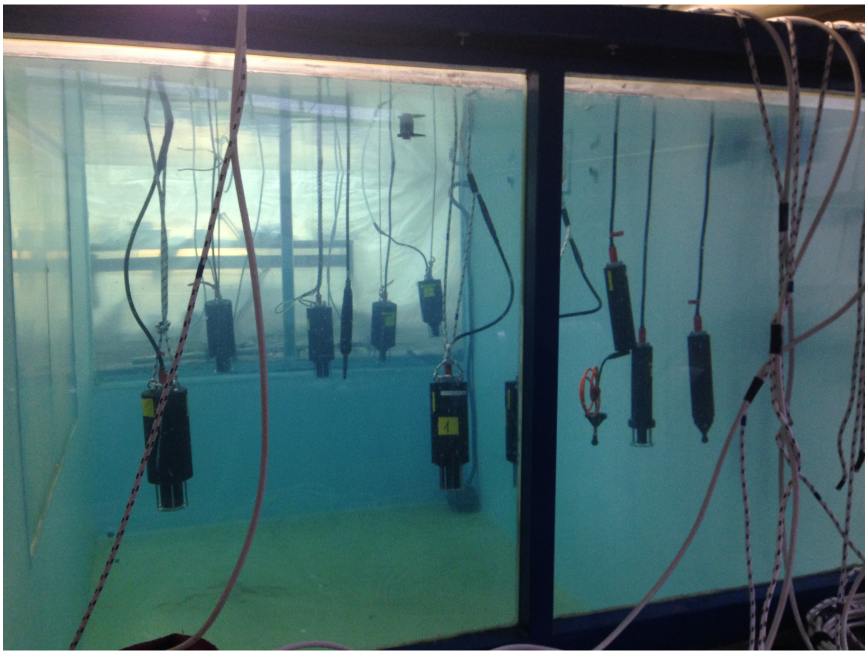

Figure 5.6: Experiment: A picture taken in a water tank showing the ten underwater acoustic modems during preliminary system tests.

on an ARM processor. The S2C scheme modulates a linear frequency-swept carrier signal through phase keying. The receiver is thus able to decouple delayed multipath arrivals in the frequency domain, reducing or eliminating frequency-selective fading.

A low-rate, low-frequency (LF) technology was incorporated by the S2C 18-34 modem, having a maximum transmission range of 3.5 km. A mid-frequency (MF) technology was obtained via the S2C 48-78 modem, which has a maximum range of 1 km. Finally, high-frequency (HF) communications were represented by the S2CM HS model, which is employed over short links of up to 300 m.

All modems were configured to transmit in instant message (IM) mode: this enacts the Immediate MAC protocol discussed in Section 5.3. Moreover, it allows us to customize both the header and the payload of all packets. We interfaced the modems to our software through the Matlab-to-Modem extension of DESERT Underwater [180], which is composed of a background C++ process and a foreground Matlab instance. For each technology, the C++ process manages an output buffer that contains data for the modem to transmit, and an input buffer that contains the payload of the instant messages received from the modem. Transmission and reception from each modem are performed via the EvoLogics drivers of DESERT Underwater [74]. We configure the native acknowledge (ACK) transmission feature of the

Table 5.3: Technologies available to each node in each topology and approximate deployment depth (between parentheses)

	Topology 1	**Topology 2**	**Topology 3**	**Topology 4**	**Topology 5**
Node 1	MF, HF (3 m)	MF, HF (3 m)	LF, MF (3 m)	MF (3 m)	MF (3 m)
Node 2	LF, HF (10 m)	LF, MF (10 m)	LF, MF, HF (10 m)	LF, MF, HF (10 m)	LF, MF, HF (10 m)
Node 3	LF, MF (10 m)	LF, HF (10 m)	LF, MF (10 m)	LF, MF (10 m)	LF, MF (10 m)
Node 4	LF (10 m)	LF, MF (10 m)	HF (10 m)	HF (10 m)	HF (10 m)
Node 5	LF (5 m)	LF (10 m)	LF (5 m)	LF (10 m)	LF (10 m)
Node 6	LF (10 m)	LF (10 m)	LF (10 m)	LF (10 m)	LF (5 m)

modem IMs, allowing up to one retransmission. If this procedure fails, we re-insert the data in the queue for a later attempt. The Matlab process generates traffic, runs the routing protocol, and issues transmissions by writing output buffers and triggering the C++ process. It also processes input buffers and manages the received data according to the OMR rules. System pre-tests in a tank using the minimum source level allowed (see Fig. 5.6) revealed that the modems could work in parallel without generating any significant outband interference. Therefore, a proof-of-concept demonstration of our multimodal routing scheme is feasible using these modems. In total, we employed ten systems: five LF, three MF, and two HF modems. We remark that the HF acoustic technology closely resembles optical communications, in that HF modems provide a higher bit rate than common acoustic systems. Moreover, they can only be operated at close distances, such as encountered during AUV docking operations, or during close interactions among divers.

The performance of the routing schemes was tested in five different network topologies, illustrated in Fig. 5.7, where solid lines represent a communication link, and we mark the LF, MF, and/or HF communication technologies available to each node. In order to deploy the nodes, the boats moved to several waypoints in the lake as shown in Fig. 5.7. The figure also shows the location of each of the four stations, the respective distances, and the ID of the nodes in each station. As shown in the figure, node 1 was always deployed on the pier, nodes 5 and 6 were hosted in one inflatable boat each, whereas nodes 2, 3 and 4 were deployed from opposite ends of the motorboat.

In all topologies, node 6 served as the sink node. The modems were deployed at roughly one half of the local water column depth. Table 5.3 shows the mapping between the nodes and the available technologies in each scenario, along with the approximate deployment depth. Most of the

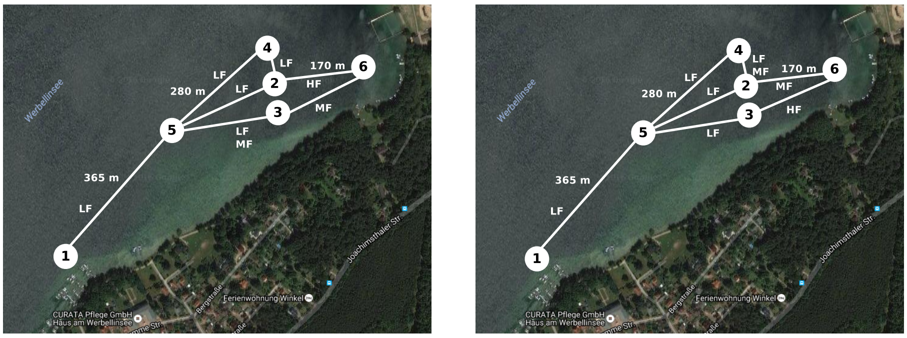

(a) Topology 1 (b) Topology 2

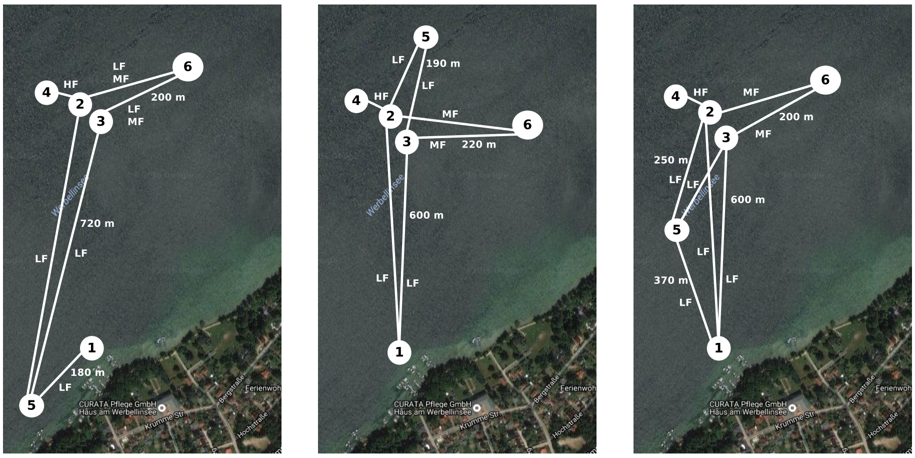

(c) Topology 3 (d) Topology 4 (e) Topology 5

Figure 5.7: Logical network topology configurations and locations of the nodes in the five scenarios considered in our lake experiment. Each link is tagged with the technologies that can be used over that link.

required reconfigurations involve the shorter-range technologies MF and HF available to nodes 2, 3 and 4.

The topologies were designed to offer different routing scenarios by varying connectivity options over different technologies. This diversifies the routing opportunities available to each node. For example, in Topology 2, nodes 2, 3 and 4 have two technologies each. The resulting network configuration allows node 4 to forward packets across the following four different routes: a) $4 \xrightarrow{\text{LF/MF}} 2 \xrightarrow{\text{MF}} 6$; b) $4 \xrightarrow{\text{LF}} 5 \xrightarrow{\text{LF}} 2 \xrightarrow{\text{MF}} 6$; c) $4 \xrightarrow{\text{LF}} 5 \xrightarrow{\text{LF}} 3 \xrightarrow{\text{HF}} 6$; and d) $4 \xrightarrow{\text{LF/MF}} 2 \xrightarrow{\text{LF}} 5 \xrightarrow{\text{LF}} 3 \xrightarrow{\text{HF}} 6$, where above each arrow we indicate the technology used over the corresponding link. The availability of different opportunities for different nodes can be easily verified for each topology. Each node was driven by a laptop which ran the routing logic and drove the modems. Note that routing was performed in a distributed fashion.

For each of the five topologies, we conducted three experiments of 10 minutes each, one employing OMR, one with the centralized benchmark OMR–FF, and one with the benchmark flooding scheme described in Section 5.3.1. The information regarding the communication technologies available in each topology (one-hop links for OMR, or full topology information for OMR–FF) was obtained via a preliminary link discovery phase [116].[4]

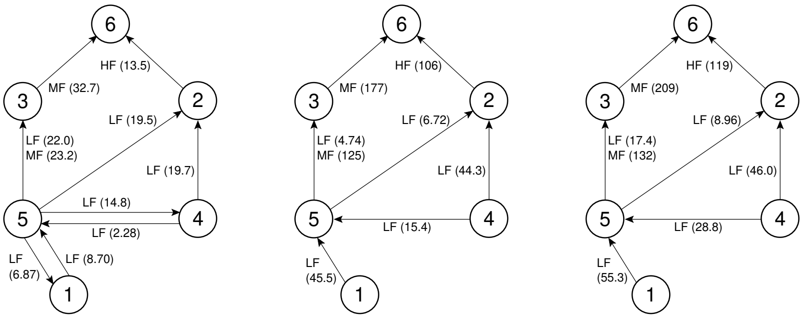

(a) Flooding (b) OMR (c) OMR–FF

Figure 5.9: Per-link transmission rates in bytes/s for all protocols run in the experiment, Topology 1.

Implementing the five experiment topologies required the coordination of the three boats and the pier in order to establish the required links and at the same time avoid unwanted interference. While logical topology configurations can be practically achieved by grouping the nodes close to one another, and using software filters to remove unwanted links [174], this solution would not remove unwanted interference. For this reason, we preferred to move the boats to suitable locations and check the topology discovered through the method in [116] until the desired topology was achieved. The environment was leveraged to facilitate the process whenever possible. For example, we hid unwanted links by lowering modems behind underwater slopes, or by moving boats inside harbors.

We lightly anchored the boats while carrying out each experiment. Upon the occurrence of significant drifts that would disrupt the desired topology, we repeated the corresponding experiment. We remark that meteorological conditions also have an impact on the obtained results. Strong wind and rain can inject unwanted noise in the water and constrain the nodes to remain physically closer in order to establish a link. To reduce the impact of these conditions on our results, we repeated all experiments for all topologies over two subsequent days. Fig. 5.8 shows two pictures taken during the experiment: on the left, a connectivity check is being performed between the

---

[4] As we assume a MAC protocol that handles both link discovery and transmissions, neither adds to the routing overhead.

boat with nodes 2, 3 and 4 to verify the communication of the modems in the water; on the right, nodes 2, 3 and 4 are controlled from a semi-rugged laptop computer.

Figure 5.8: Pictures taken during the lake experiment. (Left) Coordination between the boat containing nodes 2, 3 and 4, and the boat with node 6; (Right) Control of nodes 2, 3 and 4 through a semi-rugged laptop computer.

In each experiment, each node generated its own set of data packets according to a Poisson process of rate $\lambda = 2$ packets per minute per node. This set was equal throughout all experiments. The size of each packet was drawn uniformly at random between 0 and 64 kbits. During each experiment, the nodes sent the data packets through multiple hops towards the sink, abiding to the rules of the OMR protocol presented in Section 5.2 or the flooding scheme described in Section 5.3. Periodically, the nodes exchanged information related to the number of packets in their queue, their neighbor lists and the remaining information needed to run the protocol. When operating OMR, the reception of each data packet was separately acknowledged. In case an ACK was not received, the packet was retransmitted once by the modem's MAC protocol. Broadcast packets (e.g., reporting the queue status in the OMR protocol and the hop history in the flooding protocol) were not acknowledged.

5.4.2 Results

With five topologies tested, we measure the performance of the experiment in terms of the end-to-end transmission delay ρ_d in (5.9), the goodput ρ_g in (5.10), and the link throughput ρ_u in (5.15). The end-to-end delay of each message was calculated only once the sink (node 1) received the message in full, while the goodput was calculated for each message segment received by the sink. For the link throughput, we considered any successful transmission in the link regardless of whether the packet segment was ultimately received

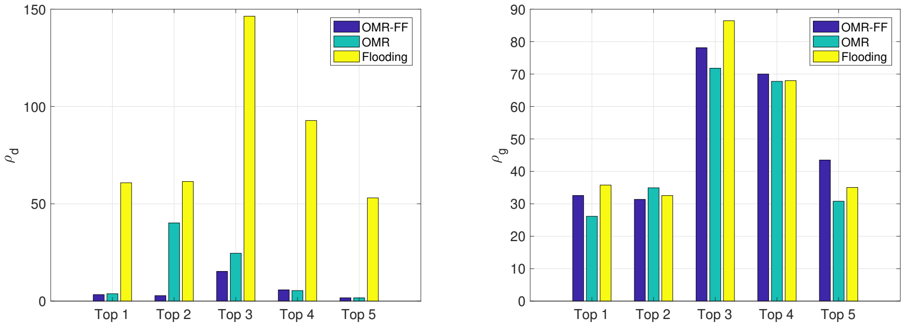

(a) ρ_d (see Eq. (5.9))

(b) ρ_g (see Eq. (5.10))

Figure 5.10: Experiment: ρ_d and ρ_g. Flooding performs worse compared to the simulations. The centralized benchmark OMR–FF performs only slightly better than our distributed OMR.

by the sink or not.

We initially focus on Topology 1 (see Fig. 5.7), and start by discussing a per-link transmission rate sample in Fig. 5.9. We observe that flooding (Fig 5.9a) is too aggressive in transmitting packets over all available links, and results in poor rates (e.g., over the link from node 4 to node 5) or unnecessarily high rates (e.g., from node 5 to node 2). By cross-checking transmission and reception logs we noted that the main reason is that flooding is subject to a high chance of collisions, and to the high bit error rate that results. On the contrary, the two OMR versions convey traffic more reliably through the network, resulting in an optimized utilization of the network link. In particular, OMR (that has no access to topology information beyond first-hop neighbors) tends to be more conservative (Fig 5.9b). As a consequence, the transmission rates of node 3's MF link and of the LF links of nodes 1, 4 and 5 are limited. Full topology awareness in OMR–FF makes nodes 1 and 4 aware of the capacity of node 5's upstream links, so that they can push more traffic through their LF links to node 5. In turn, node 5 will convey this to node 3 through both the MF and the LF links, and finally to node 6 through node 3's MF link. The overall result is higher transmission rates over all technologies (Fig 5.9c), and a lower amount of time required for a given number of packets to reach the sink (node 6) correctly.

In Fig. 5.10a, we show the measured end-to-end delay ρ_d (see (5.9)) for flooding and OMR in each topology. We observe that the end-to-end delay of flooding is significant, due to the many collisions (and subsequent retransmissions) caused by the forwarding of every packet over every available technology. While the centralized benchmark OMR-FF achieves better results than OMR, in some cases our distributed OMR achieved shorter transmission delay than OMR–FF. This is because OMR in general uses

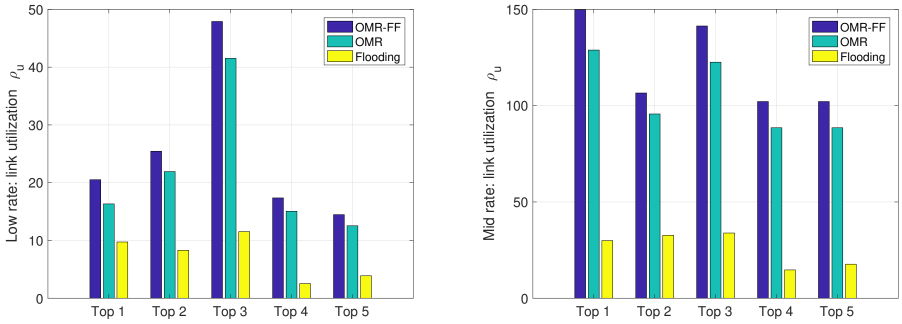

(a) LF links.

(b) MF links.

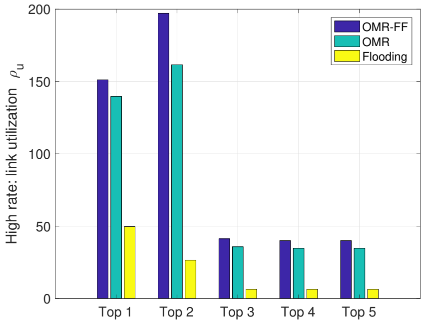

(c) HF links.

Figure 5.11: Experiment: ρ_u. Flooding performs worse compared to the simulations. The centralized benchmark OMR–FF performs only slightly better than our distributed OMR.

more links than OMR–FF, which tends to be an advantage in the presence of many collisions. The delay performance in Fig. 5.10a show that OMR achieves roughly the same results for topologies 1, 4, and 5, which are significantly better than the performance for topologies 2 and 3. Yet, the OMR-FF benchmark achieved about the same performance throughout the experiment. This is mostly because in the latter group of topologies there are many bottleneck nodes. Since OMR is a distributed scheme, it may not always find routes that circumvent bottlenecks. As a result, packets were delayed in bottlenecks before arriving to their destinations. Conversely, the global topology knowledge of the ideal benchmark OMR-FF makes it possible to find alternative routes.

Fig. 5.10b shows the goodput ρ_g from (5.10). We observe that due to the higher number of packet collisions in a real environment, the goodput of flooding decreased compared to the simulations, becoming similar and sometimes lower than that of OMR–FF. Due to the use of full topology information, the goodput of the centralized OMR–FF is higher than that of our distributed OMR. An exception to the latter result is seen in Topology 2: the reason is that this topology offers many similar routes from each node to the sink, and thus spreading the transmissions over multiple links has a positive effect.

The per-topology link throughput ρ_u, (see (5.15)), is shown in Fig. 5.11 for each of the three communication technologies. In all cases, we observe that the centralized benchmark OMR–FF delivers the best performance and that, although flooding produces many more transmissions over each link, the link throughput of OMR is significantly higher. Again, this is a consequence of the many packet collisions that occur. For the same reason, the link throughput of the centralized benchmark OMR–FF is better than that of OMR. Comparing the link throughput for the three communication types, we observe that OMR channels more transmissions through links with higher capacity. As a result, the network adapts itself to the topology, as confirmed by the changes in the link throughput for the five topologies tested in the experiment, each having a different configuration of multimodal links.

5.5 Conclusions

In this chapter, we considered the network operation of multimodal underwater systems. We proposed OMR that, to the best of our knowledge, is the first optimal distributed routing protocol to be specifically designed for multimodal underwater networks and to be experimented in the field. Our protocol leverages local topology knowledge to decide how traffic should be distributed over available links using different communication technologies. This is achieved in a way that does not congest the relays upstream, and reserves more resources for the nodes with fewer routing opportunities. We analyzed the performance of OMR by means of both simulations and field experiments. Our results show that our protocol leverages the available technologies to deliver data reliably without congesting the network, even in the presence of limited, one-hop topology information. This suggests that the implementation of OMR, which is fully distributed, is a good solution to the routing problem in multimodal underwater networks.

While having additional communication technologies available provides clear advantages, it also provides a broader set of alternatives for a malicious user to try compromising the network or part of its nodes. For this reason, future work on this topic will specifically exploit multimodal network resources in order to enhance the security of such networks.

Notes

Part of this work has been published in [68] and [181].

Chapter 6

Optimal scheduling in multimodal underwater networks

6.1 Introduction

With several heterogeneous nodes, employing a different sub-network for each technology may result in disconnections and poor data transfer performance. Instead, it would be possible to increase the throughput, decrease the communication delay via simultaneous transmissions splitting the load among different links, and reduce the occurrence of bottlenecks by properly leveraging the full set of PHYs. Scheduling poses different requirements in multimodal underwater networks, where the available PHYs have widely different communication capabilities, and the scheduler must account for PHY-dependent adjacency and interference matrices while avoiding bottlenecks. The main challenge, and the focus of this chapter, is how to optimally schedule the transmission of the available PHYs.

To address the above challenges, in this chapter we propose the optimal multimodal scheduling (OMS) protocol that can serve any set of multimodal underwater PHYs. OMS manages transmissions through any set of PHYs by jointly setting transmission time slots in a per-technology time-division multiple access (TDMA) fashion, and divides the data load among the PHYs to optimize link utilization and transmission delay. In addition, OMS organizes transmission slots to favor packet routing and enforce a fair number of transmission opportunities per node, by optimally maximizing the overall channel utilization while preserving flow limitations, and maintaining fairness in resource allocation.

We tested the performance of OMS against benchmark schemes in numerical simulations and in a sea experiment using multimodal nodes encompassing different acoustic PHYs. Our numerical simulations and experimental results show that OMS achieves better throughput, packet delivery delay, and fairness in resource allocation.

This chapter is organized as follows. First, the OMS algorithm is analyzed in Section 6.2. Second, OMS is evaluated in Section 6.3 and 6.4 via simulations and sea test, respectively. Finally, our concluding remarks are presented in Section 6.5.

6.2 The OMS algorithm

In this section, we describe the OMS algorithm. Specifically, in Section 6.2.1 we present the details of the system model and the assumptions, and in Section 6.2.2 the solutions of the OMS algorithm.

6.2.1 System model

Our system consists of N network nodes equipped with one or more of T underwater PHYs. The set of PHYs is arranged in the $N \times T$ technology matrix $\mathbf{T}$ such that $\mathbf{T}_{i,n} = 1$ if node i has PHY n. Call $\mathbf{M}$ the adjacency matrix, where $\mathbf{M}_{i,j,n} = 1$ if node i is connected to node j via PHY n. The number of neighbors of i through technology n is $\mathbf{D}_{i,n} = \sum_j \mathbf{M}_{i,j,n}$. We assume that $\mathbf{T}$ is given, and that $\mathbf{M}$ can be obtained via preliminary link probing [182]. We remark that the difference between the communication and interference range is limited in underwater networks, due to the very fast power decay incurred for increasing range by any PHY technology [28]. Hence, to harness spatial reuse for performance gain, we allow collisions in OMS.

OMS organizes orthogonal multimodal PHYs via per-technology TDMA frames. As different PHYs are characterized by diverse transmission rates, operate on different frequencies and may incur different propagation delays (e.g., optics vs. acoustics), the duration of the time slots is also set per-technology. We choose TDMA since it allows a simple time slot alignment via guard intervals. This is specifically important in multimodal systems, where different PHYs have diverse outage capacity. Additionally, in TDMA-based schemes the transmission delay is known in advance, making it possible to plan the load allocated to each PHY. This is in contrast to handshake-based schemes (where the delay depends also on the receiver) and to fully random access (where collisions may trigger an unpredictable number of retransmissions). The synchronization of the low latency technologies can be achieved either via atomic clocks or through the network time protocol (NTP). For acoustics, however, we can simply rely on guard times: as the time slot duration is at least as long as the maximum propagation delay, such guard times are negligible.

We impose traffic constraints by allowing a node i to transmit in at least $c_i > C$ time slots. Calling R_i the number of bits transmitted in each time slot of the slowest communication technology of node i, constraint c_i ensures the transmission of at least $c_i R_i$ bits within a given frame. Fairness then results from setting c_i such that nodes with lower R_i receive a higher c_i value.

6.2.2 OMS scheduling solution

Our solution allocates transmission time slots, organized in n TDMA frames of N slots and duration τ_n^{sl}: one frame for each PHY. We synchronize transmissions by considering a TDMA super-frame of length τ^{fr}, such that for some PHYs several (not necessarily full) TDMA cycles are possible per τ^{fr} s. The input to OMS is the PHY matrix $\mathbf{T}$, the adjacency matrix $\mathbf{M}$, the per-PHY communication capacity, and the number of slots N and time slot duration τ_n^{sl}. The output is the minimum allowed value of τ^{fr}, and a matrix $\mathbf{S}$, where $\mathbf{S}_{i,t,n} = 1$ if node i can transmit in slot t via PHY n. The transmission slot indices are arranged in a vector $\mathbf{t}_{i,n}^{\mathrm{Tx}} = \{r : \mathbf{S}_{i,r,n} = 1\}$ for node i over technology n. Our objective is to maximize channel utilization, measured via the total number of transmissions over a given time period. The schedule also considers collisions among neighboring nodes and facilitates the forwarding of packets across multiple hops. OMS requires the knowledge of the adjacency matrix $\mathbf{M}$ obtained, e.g., via [182]. This includes the existing connections and the available per-node PHY technologies.

Let $\vee$ be the logical “or” and $\wedge$ the logical “and” operators. The optimal schedule $\mathbf{S}^\star$ with time frame length $\widehat{\tau^{\mathrm{fr}}}$ is the solution of the following problem:

$$\mathbf{S}^\star, \widehat{\tau^{\mathrm{fr}}} = \arg\min_{\tau^{\mathrm{fr}}} \Big(\max \sum_i \sum_t \sum_n c_i \, \mathbf{S}_{i,t,n} \Big) \tag{6.1a}$$

$$\text{s.t.} \quad \mathbf{T}_{i,n} = 0 \Longrightarrow \mathbf{S}_{i,t,n} = 0 \tag{6.1b}$$

$$\begin{aligned} &\mathbf{S}_{i,t,n} = 1 \wedge \mathbf{S}_{j,t,n} = 1 \implies \\ &(\mathbf{M}_{i,p,n} + \mathbf{M}_{j,p,n} = 0) \\ &\quad \vee \ (\mathbf{M}_{i,p,n} + \mathbf{M}_{j,p,n} = 1 \ \wedge \ \mathbf{S}_{p,t,n} = 0) \\ &\quad \vee \ (\mathbf{M}_{i,p,n} + \mathbf{M}_{j,p,n} = 2 \ \wedge \ \mathbf{S}_{p,t,n} = 1) \ \forall p \neq i,j \end{aligned} \tag{6.1c}$$

$$\sum_t \sum_n \frac{\mathbf{S}_{i,t,n}}{\mathbf{D}_{i,n}} \geq c_i \geq C \quad \forall i, n \tag{6.1d}$$

$$\exists\, t \text{ s.t. } \mathbf{S}_{i,t,n} = 1, \mathbf{S}_{j,t,n} = 0 \ \forall i,j,n \text{ s.t. } \mathbf{M}_{i,j,n} = 1 \tag{6.1e}$$

$$\begin{aligned} &\exists\, n \text{ s.t. } \mathbf{M}_{p,j,n} = 1 \ \wedge \ \mathbf{M}_{j,i,n} = 1 \ \wedge \ \mathbf{M}_{p,i,n} = 0 \\ &\quad \wedge \ \max(\mathbf{t}_{j,n}^{\mathrm{Tx}}) > \min(\mathbf{t}_{p,n}^{\mathrm{Tx}}) \, . \end{aligned} \tag{6.1f}$$

The solution can be obtained via branch-and-bound, which completes in polynomial time on average [122].

Constraint (6.1b) prevents transmissions on technology n if node i does not have it. Constraint (6.1c) allows simultaneous transmissions by two nodes i and j in the same slot using technology n only if: $\forall p \neq i, j$, the links $i \leftrightarrow p$ and $j \leftrightarrow p$ do not exist for technology n; or if one of the two links exists and p does not transmit in the same slot (lest p would be deaf to i's or j's transmission); or otherwise, if both links exist, p also transmits in the same slot (so that i and j's transmissions would not collide at p). Constraint (6.1d) specifies that more slots are given to nodes with more neighbors, so that the total number of slots per neighbor is at least $c_i \geq C$. Constraint (6.1e) imposes that node i be the only transmitter in at least one slot t over each technology n. Hence, although (6.1c) allows primary conflicts, there exists at least one slot for each node to transmit free from interference. Finally, constraint (6.1f) facilitates that the same packet can propagate further than one hop within the same frame, and is achieved by allowing a node j located at an intermediate position between two nodes p and i to have at least one transmission slot later than node p's slot, i.e.,

$$\max(\mathbf{t}^{\mathrm{Tx}}_{j,n}) > \min(\mathbf{t}^{\mathrm{Tx}}_{p,n}). \tag{6.2}$$

The formalization in (6.1) shows that OMS optimizes link utilization by allocating the data flows across all PHYs of a node, while considering possible bottlenecks and packet delays due to the different capabilities of the various PHYs. However, OMS is a centralized solution and thus fits the case of small networks. Still, by sharing the adjacency matrix $\mathbf{M}$, OMS avoids the use of a centralized hub.

6.3 Simulation results

Unlike many other scheduling solutions [183],OMS focuses on managing transmissions effectively through diverse PHYs. We therefore compare the performance of OMS with the only two benchmark schemes we found to be appropriate for multimodal underwater scheduling: the Aloha protocol [184, Section 4.2], where a packet is sent as soon as it becomes available (except that no transmission can start if a reception is in progress, in order to replicate the behavior of actual acoustic transceivers); and the TDMA scheme in [28]. In both cases, to transmit on a given link, a node employs the PHY providing the highest bit rate, among those integrated by both itself and the receiver. We consider the packet delivery ratio,

$$PDR = \frac{N^{rx}}{N^{tx}} , \tag{6.3}$$

where N^{tx} and N^{rx} are the total number of packets transmitted and received, respectively; the packet delivery delay (PDD) that is calculated as the time elapsed from the packet generation until its reception; and the service fairness, which we define by Jain's fairness index [117] for the PDR,

$$J = \frac{\left(\sum_{i=1}^{N} PDR_i\right)^2}{N \cdot \sum_{i=1}^{N} PDR_i)^2} , \tag{6.4}$$

where

$$PDR_i = \frac{N_i^{rx}}{\sum_{i=1}^{N} N_{k,i}^{tx}} \tag{6.5}$$

is the PDR of the packets received by node i, and $N_{k,i}^{tx}$ is the number of packets transmitted by node k to node i. For L_p bits in a packet, we also consider the network throughput

$$THR = \frac{N^{rx} \cdot L_p}{T_s} \ , \tag{6.6}$$

where T_s is the duration of the simulation.

6.3.1 Simulation setup

We deploy a multimodal network of 4 nodes uniformly at random over an area of 2×2 km^2 and depth 100 m. We consider three PHYs, based on low-, mid- and high-frequency acoustics (respectively LF, MF and HF for short). The PHY characteristics are summarized in Table 6.1. Due to the random deployment, the MF and HF modems may not form fully connected subnetworks. Every node incorporates an LF modem. At random, two nodes also have an MF modem, and three nodes have an HF modem.

Table 6.1: Simulations: characteristics of the PHY technologies

Technology	Bit rate [bps]	Max range [m]	Band [kHz]
LF acoustics	3000	4000	7–17
MF acoustics	6000	1500	18–34
HF acoustics	15000	500	48–78

We perform a Monte-Carlo set of 600 runs, each with a different random topology realization, using DESERT Underwater [74]. At the beginning, we solve (6.1a) by passing topology data to Matlab via a TCP connection. The simulated operation time for each network configuration is 6 days. We set $L_p = 1000$ bytes, and the number of slots $N = 12$. Guard times have been chosen according to the propagation time and the bit rate of each PHY.

6.3.2 Simulation results

In Fig. 6.1, we show the cumulative distribution function (CDF) of the throughput for each technology and for their combination (“Total”). The poor performance of TDMA proves that it is unable to exploit all technologies. Since OMS optimally utilizes all available links, in total its throughput performance always exceeds that of Aloha, with a gain of roughly 100% in more than 50% of the cases. We also observe that the gain increases with

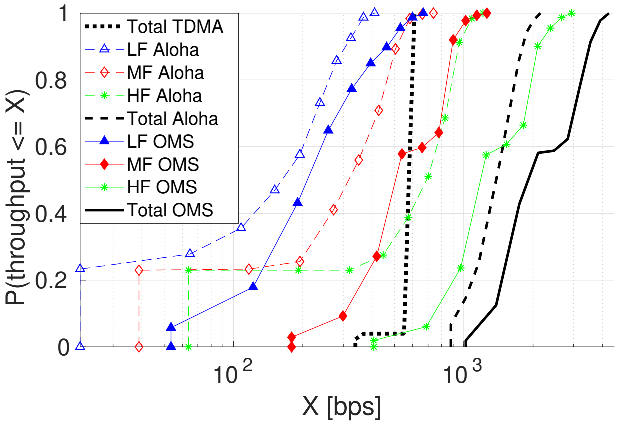

Figure 6.1: CDF of the throughput (6.6) for OMS and Aloha.

frequency, since high frequency translates into a higher bit rate, and the link utilization becomes more effective.

From the CDF of the PDD (Fig. 6.2), we observe that OMS outperforms both Aloha and TDMA by a significant figure of 3 s and 4 s, respectively, providing a delay that is 50% and 66% lower than the other two MAC schemes. Moreover, OMS proves less sensitive to specific topologies than Aloha and TDMA. This is due to constraint (6.1d), that enforces interference-free slots for all nodes.

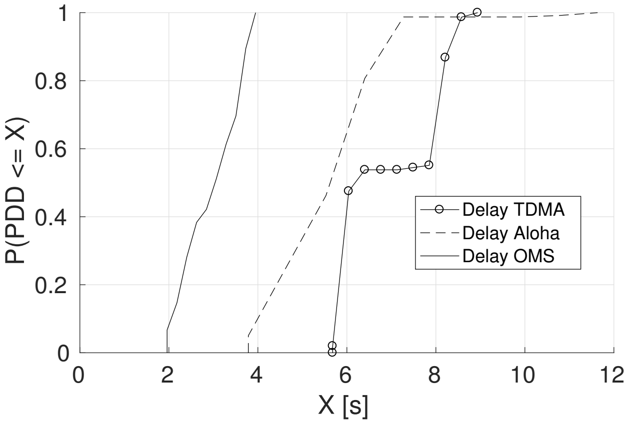

Figure 6.2: CDF of packet delivery delay for OMS and Aloha. Total case.

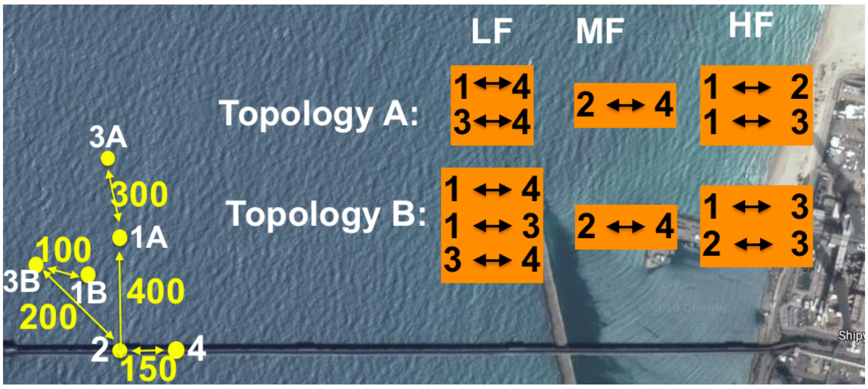

Figure 6.3: Sketch of the network deployment in Hadera, Israel.

6.4 Sea experiment

6.4.1 Experiment setup

We demonstrated OMS in a sea experiment on May 2017 in Hadera, Israel. The deployment (see Fig. 6.3) involved four stations: nodes 2 and 4 lowered from a pier stretching 2 km eastwards from the shore, and nodes 1 and 3 placed on boats. The water depth was 25 m.

The deployment setup is depicted in Fig. 6.4, where the position of each node is marked with a red ellipse.

We used EvoLogics underwater modems operating in three frequency bands: 7–17 kHz (LF, up to 6.9 kbps), 18–34 kHz (MF, up to 13.9 kbps), and 48–78 kHz (HF, up to 31.2 kbps). To transmit, we employed the modem's "instant messaging" option, which transmits as soon as a request arrives to the modem. Each node lowered its modems from the same place and to the same depth.The modems are cased separately and directly deployed from each stations. In each station, all the modems of a multimodal node are connected to a laptop with an Ethernet switch. A sea state of 3 resulted in a low PDR.

By changing the locations of nodes 1 and 3, we tested two network topologies, each for a total of 20 min. To achieve intense network traffic, we let each node transmit a packet whenever possible. Transmissions were unicast to a destination node chosen uniformly at random among the sender's one-hop neighbors. Considering the poor performance of TDMA in the simulations, we only focused on the OMS and Aloha protocols in the experiment.

6.4.2 Experimental results

In Fig. 6.5, we show the PDR, fairness, and throughput performance for Topology A. The differences between nodes are mostly due to the sparse topology, where nodes have a different number of one-hop neighbors. We

Figure 6.4: Picture of the Hadera deployment during topology 2. The position of each node is marked with a red ellipse.

observe that, except for the LF case, OMS's PDR is consistently better than Aloha's. Similarly, the bottom panels of Fig. 6.5 show that OMS's transmission fairness and throughput are also better. We note that, due to its channel utilization, the experimental results of OMS also exceed those of an ideal (theoretical) TDMA with perfect PDR.

Fig. 6.6 shows the performance for Topology B. Compared to Topology A, more LF links are available. This diversity is utilized by OMS. Thus, unlike in Fig. 6.5, here the PDR of OMS is better than Aloha's also for the LF case. While the fairness performance follows the same trend, OMS's throughput gain decreases. This is mostly because in Topology A there are fewer connection possibilities. Hence, Aloha experienced more collisions than in Topology B. Still, relative to Aloha, in the sea experiment OMS demonstrated a significant performance gain in all metrics.

Based on the data sheets of the manufacturer, the transmission power of the LF, MF, and HF modems is $P_{tx,LF} = 40$ W, $P_{tx,MF} = 35$ W, and $P_{tx,LF} = 18$ W, respectively. Thus for the transmissions executed during the experiment, where the packet duration was $t = 0.4$ s, the power consumed

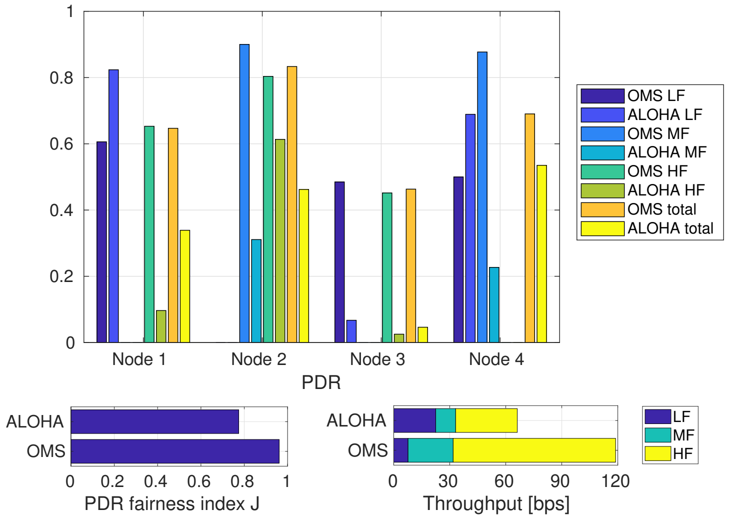

Figure 6.5: Topology A: PDR (6.3), PDR fairness (6.4), and throughput (6.6).

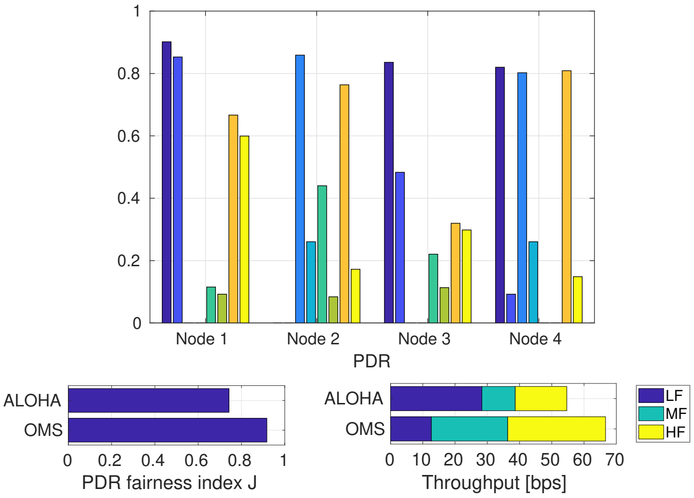

Figure 6.6: Topology B: PDR (6.3), PDR fairness (6.4), and throughput (6.6).

for a single packet transmission is

$$E = \frac{t \cdot (P_{tx,LF} \cdot N_{tx,LF} + P_{tx,MF} \cdot N_{tx,MF} + P_{tx,HF} \cdot N_{tx,HF})}{3600}. \tag{6.7}$$

Considering the number of packets transmitted, we calculate for Topology 1 a power consumption of 2.2 Wh by OMS and 4.0 W/h by Aloha. This power consumption gain of OMS increased for Topology 2, where OMS consumed 2.3 Wh, and Aloha consumed 5.1 Wh.

6.5 Conclusions

We described OMS, a new scheduling protocol for multimodal underwater networks. OMS maximizes the channel utilization while providing a fair quality of service to all nodes, and guaranteeing that at least some of the slots will be free from interference. We have tested OMS both in simulations and in a sea experiment. The results show that OMS fully utilizes the multimodal network, and thus achieves gains in both throughput and packet delivery delay. Future work will include the adaptation of multimodal PHY technologies to network flow requirements.

Notes

The content of this chapter has been published in [67].

Chapter 7

Wireless remote control for underwater vehicles

7.1 Introduction

Nowadays, ROVs are used in order to monitor the underwater environment and man-made assets. Usually, ROVs are controlled through a cable, called umbilical, which conveys power supply and data connections to the ROV, making it possible to manage the system in real time. While the umbilical cable is a mandatory requirement for supplying workclass ROVs, it inherently limits the mobility of general and inspection class ROVs due to cable strain and entanglement risks. Wireless ROV control would help avoid such issues by removing the need for a physical cable, at the price of an increased need for ROV power autonomy and smaller data rates. This chapter offers our view on the feasibility of wireless ROV management. In particular, we start by relating typical services offered by ROVs (along with their required application-layer data rates) against the rates typically offered by optical, acoustic and radio-frequency (RF) communication technologies available to date. We proceed by identifying a number of operational modes which can be chosen as a function of range to support a given set of ROV services, from simple guidance and positioning, to tool control, up to real-time video streaming. Finally we focus on remote control via acoustic communications, and extend the DESERT Underwater framework [74] to reproduce the communication patterns between the controller and an ROV, and measure the capability of the ROV to follow a prescribed path as a function of the operational mode.

The remote control of underwater autonomous systems (both ROVs and AUVs) has received increasing interest recently. One of the systems to achieve a practical rate of several tens of kbps is the FAU Hermes modem [38], which has been experimented for some years in ports and in very shallow water environments, which are among the typical scenarios for remotely-controlled

ROVs. In [185] the authors investigate the acoustic networking of an AUVs with Autonomous Surface Vehicles (ASVs) to accomplish a common mission. After introducing the vehicle control architecture, the authors describe the acoustic communication and ranging capabilities of each node and finally show some experimental results obtained with two vehicles in the Douro river in Portugal.

Optical technologies for underwater real-time video transmissions were surveyed in Chapters 1 and 3, where the achievement of a 10-Mbps bit rate in a real experiment also in case of sunlight noise is reported. Also the use of RF communications in underwater scenarios with short-range monitoring and control purposes was discussed in Chapter 1, where RF systems were compared to acoustic and optical systems. However, the distance allowed by the RF technology is very limited, as even typical levels of salinity can heavily limit the propagation of RF signals [186].

In Section 7.2, we summarize the requirements of an ROV control system, and in Section 7.3 the feasibility of its wireless implementation in light of the capabilities of underwater wireless transmission technologies analyzed in Chapter 1. Section 7.4 presents the simulation of an acoustic ROV control system designed in accordance with the observations in Sections 7.2 and 7.3, while the whole multimodal optical and acoustic system is analyzed and evaluated in Section 7.5. Finally, Section 7.6 draws some concluding remarks.

7.2 Requirements for ROV Control

We start by introducing some realistic requirements for operational ROV control. These requirements will be checked against the capabilities of current wireless communications technologies in the next section, in order to infer an empirical relationship between distance and bit rate available for controller commands and ROV reports. We assume that control features can be divided into two classes, namely mandatory and optional features. Mandatory features include movement commands (both absolute and relative to the current position), management of the ROV's mechanical tools, feature toggling (e.g., lighting, sensing, etc.) and feedback from the ROV to the controller. In particular, the mandatory portion of the latter encompasses the ROV position estimate, tools status and sensor readings. Optional features include communication-intensive services. As a representative of this kind of services, we will refer below to live video streaming, which is a typically required ROV feature.

The encoding format for the information listed above is diversely implemented in different ROV models and control systems, which makes it difficult to find proper references for the amount of information transferred between the ROV and its controller. For this reason, we had to make some practical assumptions on the data representation format and on link-layer features such as coding redundancy for forward error correction. Based on these assumptions,[1] we define the following operational modes:

- **Mode HD** provides full control capabilities (movement, ROV tools, etc.) and comprehensive feedback from the ROV, including a HD-quality video streaming from the ROV to the controller; the required bit rate for this service level is on the order of 1.4 Mbps;
- **Mode 3** maintains full control over the ROV movement and tools, but entails a significant decrease of the video quality, so that the required bit rate decreases to 66 kbps;
- **Mode 2** downgrades the video streaming into the transmission of an image slide-show, and requires a bit rate of 48 kbps;
- **Mode 1** further downgrades the quality of the image slide-show, and requires a bit rate of 30 kbps [187];
- **Mode 0** drops video streaming and maintains only the mandatory control of the movement and of the tools of the ROV, thus requiring a reduced bit rate of about 2 kpbs.

The data rates reported above refer to the transmission of color images and videos. However, some ROVs, such as the Ageotec models Pegaso and Perseo [188], can also transmit black and white video, which sometimes can provide better contrast than color streams. While it is true that black and white videos imply a lower data rate, we decided to design and evaluate the control system for the more demanding of the two cases, and therefore to consider the transmission of color videos in the computation of the minimum bit rate in each mode. Of course, this system would be able to support the transmission of black and white video streams as well. Morover, in **Mode 0** the transmission of low-quality images might still be possible if considering, for instance, black and white pictures with 8 bits per pixel. However, this increse in monitoring traffic would result on the increasing of the control traffic latency: for this reason in this chapter we do not consider any image transmission in **Mode 0**.

In the following section, we will discuss which underwater communication technologies make it possible to achieve the bit rate requirements defined above.

7.3 Selection of wireless underwater technologies

As presented in Chapter 1, the prominent technologies for underwater wireless transmission to date are acoustics, RF and optics. In this section, we select

---

[1] The interested reader is referred to [187, Ch. 2] for more details.

the best of them among the commercial products and research prototypes presented in Chapter 1. We consider a typical ROV control scenario where the ROV is located within about 150 m from the controller, and identify the transmission bit rate figures of each technology by relying on each system's data sheet. In doing so, we disregard those products that are explicitly targeted at some idealistic scenario[2] and rather focus on the ones that support normal operational conditions. In addition, among research prototypes, which often provide good performance and a high level of reliability but cannot be easily purchased, we will consider only those models that yield comparable or better performance with respect to commercial ones.

In light of the requirements in Section 7.2 and of the technologies comparison in Section 1.1, we may conclude that acoustic communications are mainly useful because they support mandatory ROV features over long ranges. In addition, the prototype Hermes modem may be able to transmit a low-quality video over a range of about 100 to 150 m. In any event, the controller can operate between middle and long ranges, but only in modes 0 to 2.

The need for high speed communications under water has pushed the realization of optical devices that can transmit data within short distances at a bit rate on the order of one or more Mbps, e.g., [17]. High turbidity scatters and attenuates the optical field, whereas ambient light may become a significant source of noise, making transmissions close to the sea surface more difficult. In order to design a stable remote control, in the selection performed in this chapter we considered only the optical modems that have been tested in these conditions. For what concerns the requirements of our ROV control system, the commercial Sonardyne BlueComm 100 modem (previously described in Section 1.1) allows HD video monitoring for short range (Mode Video HD).

Although the performance of RF modems is immune to most environmental conditions that affect the propagation of acoustic waves, RF communications suffer from RF interference and are prone to very strong attenuation in salted waters, where the conducibility of the medium is larger than in fresh waters [189]. In addition, RF modems are outperformed by optical modems at all typical operational RF ranges (see Section 1.1), with the only understanding that RF communications are omnidirectional, whereas optical communications are not.

After the considerations above and in light of the requirements in Section 7.2, we can conclude that a fully wireless ROV control system should be based on optical communications at short range, and on acoustic communications at intermediate and long ranges. More specifically, Mode HD can be supported by an optical link which, however, offers a limited coverage range of only a few meters. When the optical link cannot be used, the connection

---

[2] This includes, for example, fresh water RF modems, optical modems working in dark and clear waters, and acoustic modems for only-vertical links.

Table 7.1: System modes and modems employed

Mode	**Manufacturer/model**	**Range**	**Bit rate [kbps]**[a]
Mode 0	EvoLogics S2CR 18-34 [135]	3.5 km	13.9
Mode 1	EvoLogics S2CR 48-78 [135]	1 km	31.2 [b]
Mode 2	EvoLogics S2CM HS [135]	300 m	62.5 [c]
Mode 3	FAU Hermes modem [38]	120 m	87.7 [d]
Mode HD	Sonardyne BlueComm 100 [17]	20 m	5000 [c]

[a] Bit rate and range as declared in the data sheets of the devices. They should be taken as an upper bound.

[b] Worse results were achieved in Singapore's warm shallow waters [190].

[c] Recently released, no experimental results have been reported yet.

[d] These values for the bit rate and range have been demonstrated in [38].

is enabled by one of the acoustic communication systems, thereby striking a trade-off between coverage range and bit rate. The FAU Hermes modem [38] achieves a bit rate of 87.7 kbps within a maximum communications range of 120 m, thereby supporting mode 3; the recently released EvoLogics [135] S2C M HS supports mode 2 via a bit rate of 62.5 kbps at a maximum distance of 300 m; Mode 1 is achieved through EvoLogics' S2C R 48/78 modem, which supports communications at 31.2 kbps up to 1 km; finally, Mode 0 would be achieved by EvoLogics S2C R 18/34 modem. Table 7.1 provides a summary of the communications equipment employed in each mode and a few notes on the achieved performance. We stress that all the manufacturers declare to achieve the reported performance in shallow or very shallow water environments. In our scenario, the maximum distance that separates the controller and the ROV is about 180 m, therefore only Modes HD, 3 and 2 will be considered. In Section 7.5.2, we will detail how the communication stack implemented in the ROV and in the controller makes it possible to automatically switch among these modes.

7.4 An acoustic-piloted vehicle

In this section, we analyze the system while working either in Mode 0 or in Mode 3, i.e., when the ROV is piloted by employing the FAU Hermes acoustic modem prototype, in order to inspect which QoS can be obtained when controlling an ROV with an acoustic modem.

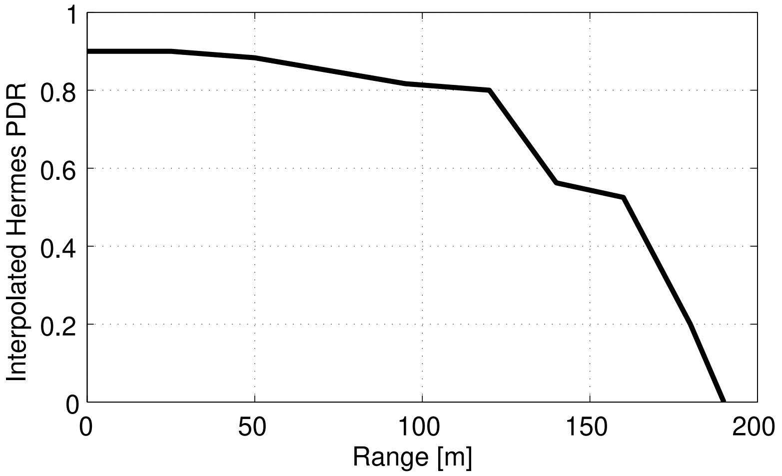

Figure 7.1: Hermes frame PDR vs. distance between transmitter and receiver as implemented in our Hermes PHY model.

7.4.1 Hermes PHY layer model

We modeled the performance of the Hermes PHY layer by making the following assumptions: *i*) the transmissions of 12380-bit Hermes frames (corresponding to 9120 information bits + 32 bits of CRC, coded with a $(15, 11, 1)$ BCH code) is subject to the error rate performance reported in [191, Table III], where the probability that a packet is received correctly (or packet delivery ratio, PDR), is considered to be equal to the product of the packet authentication probability (representing the ratio of packets actually recognized as Hermes frames) times the probability that the fraction of erroneous bits in an authenticated frame is less than 1/10. This is akin to the observations in [191]. Linear interpolation is employed between subsequent Hermes PDR samples, and we assume that the PDR drops to 0 at a range of 190 m. The resulting PDR vs. range graph is reported in Fig. 7.1. These numbers, however, refer to 12380-bit frames, which may not necessarily be the best packet length choice in our setting. To obviate this, we assume that the nodes can transmit any number k of 15-bit chunks, where $m = 832$ chunks form a full Hermes frame, and that the error process is iid across chunks. Under these assumptions, we approximate the PDR of a generic k-chunk packet as $p_c(k) = q_c^{k/m}$, where q_c is the PDR of a full Hermes frame, as shown in Fig. 7.1.

7.4.2 Scenario and parameters

We consider the task of remotely driving the movement of an ROV over a lawnmower-like trajectory spanning a 200 m × 200 m area, where the controller is centrally placed. This leads to a maximum distance of 145 m between the controller and the ROV, and requires to employ acoustic communications using the Hermes modem. This entitles the system to modes 0 to 2. The bit rate set for the system is the same as the Hermes modem's, i.e., 87.768 kbps. The sound speed is assumed to be constant and equal to 1500 m/s. Command packets sent by the controller have a total size of 1024 bits, whereas the monitoring packets sent by the ROV to the controller have a length equal to L_{mon}, which can be varied depending on the operational mode in order to balance between packet delivery ratio (PDR), efficiency and ROV reporting frequency.

The controller drives the ROV along the desired trajectory by sending absolute movement commands in the form of subsequent waypoints to be covered. In this respect, a key design choice regards the time t_k^{wp} between two subsequent waypoint transmissions. Assuming that the ROV moves at constant speed equal to v, we have $t_{\text{min},k}^{\text{wp}} \geq \|\mathbf{x}_k - \mathbf{x}_{k+1}\|/v$, where $\mathbf{x}_k$ is the absolute position of the kth waypoint. However, such minimum time gap cannot ensure the correct reception of new waypoints, as a real system also incurs additional delays due, e.g., to queuing, processing and retransmissions. In fact, the latter are a major source of delay and should be explicitly accounted for when choosing the timing of waypoint transmissions. Given that the actual number of retransmissions required for a given waypoint is not known a priori, we choose to set $t_k^{\text{wp}} = t_{\text{min},k}^{\text{wp}} + t_g$, where t_g is a guard time that can be acted upon to trade off the rate of the movement commands for the probability that the ROV actually received them and had time to act accordingly.

Given the presence of only two nodes, the communication stack set up in DESERT Underwater can be simplified to involve: a PHY layer that reproduces the error rate performance of the Hermes modem as a function of distance (details in Section 7.4.1); a CSMA or TDMA MAC protocol; static routing; UDP transport; a CBR application layer. The controller is configured to transmit packets at a fixed rate equal to $1/t_k^{\text{wp}}$: this corresponds to assuming that the ROV moves at constant speed (set here to $v = 1$ m/s) and that subsequent waypoints are equally spaced along the desired route. At the ROV side, the application layer is set to transmit monitoring packets (including the information briefly summarized in Section 7.2). Such packets, when appropriate, can piggyback an ACK packet reporting the last waypoint correctly received. Movement commands not correctly received for any reason can be retransmitted until they are preempted by newer commands, which cause the controller to drop older ones.

7.4.3 Simulation results

As a specific example, we will now focus on acoustic communication technologies, and test an acoustic wireless ROV control system using the DESERT Underwater framework [74]. The simulation engine has been modified so that the trajectory of the moving ROV can be controlled at run time based on the reception of messages from the controller. The following subsections introduce the simulation scenario, the details of our model of the Hermes physical layer [38], and the simulation results obtained via a simple CSMA as well as a more efficient TDMA MAC layer.

Results—CSMA MAC scheme

We start by considering the case where communications are handled at the MAC layer by means of a simple CSMA MAC protocol. This choice may be suboptimal, but translates into a largely simplified system implementation, as there is no need to enable additional services such as localization or time synchronization between the controller and the ROV. Our main concern at this time is how well the ROV can follow a desired trajectory while at the same time reporting back to the controller in accordance to the operational mode. The desired trajectory for the ROV is depicted using a bold black line in all the following figures. We start from Fig. 7.2, which refers to mode 0. The top pane shows the desired trajectory superimposed to the simulated ROV trajectory in two cases, $t_g = 2$ s and $t_g = 5$ s. The former enables better responsiveness to the ROV by sending waypoints more frequently; at the same time, it does not leave much room for error control, which may lead

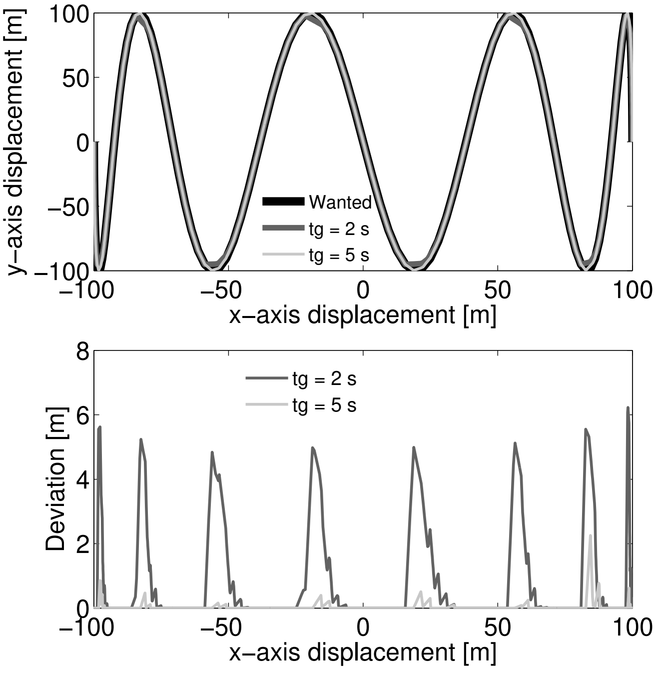

Figure 7.2: CSMA, mode 0: route followed by the ROV (top) and deviation from the desired route (bottom) as a function of the position of the ROV along the x-axis.

to uncompensated packet losses. Conversely, setting $t_g = 5$ s leaves more time to retransmit lost waypoints, at the price of slower ROV responsiveness. The net result is that the deviation from the desired trajectory is acceptably small (almost always lower than 1 m for $t_g = 5$ s, whereas the maximum deviation increases to about 6 m for $t_g = 2$ s. The main reason here is that CSMA transmissions are not coordinated, and packet reception errors may occur due to the deafness of a transmitting node to the reception of packets from its peer.

This same reason leads to even larger deviations if mode 2 is employed. In this case, the amount of information that the ROV is supposed to transmit is much larger, and the chance that control packets are not heard by the transmitting ROV is much larger than in mode 0. In particular, Fig. 7.3 shows that even with the larger guard time $t_g = 5$ s between subsequent waypoints, the maximum deviation of the ROV from the desired trajectory in the points farther from the controller is quite significant, typically below 20 m but with one peak around 30 m. With the shorter guard time $t_g = 2$ s, which leaves even less time for retransmissions, 30 m becomes the typical deviation incurred in all portions of the trajectory farthest from the controller. The results motivate the consideration of a deterministic access scheme for channel sharing between the ROV and the controller. In particular, a TDMA scheme will be considered in the following section.

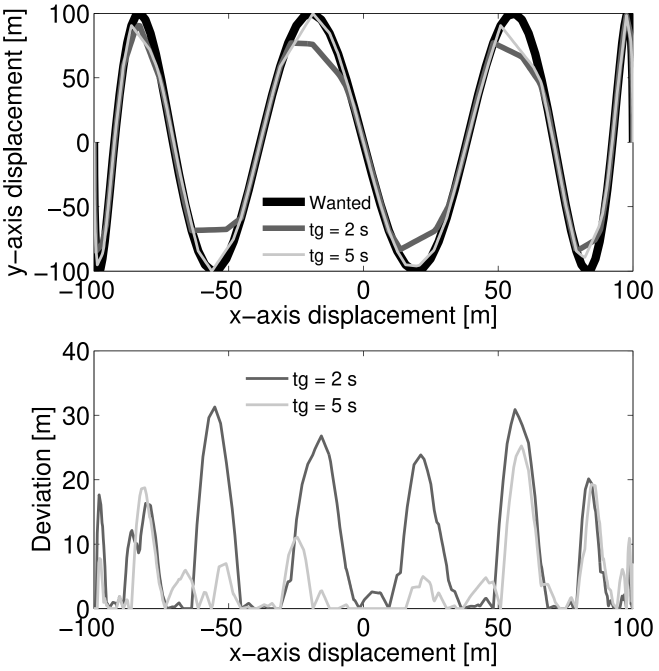

Figure 7.3: CSMA, mode 2: route followed by the ROV (top) and deviation from the desired route (bottom) as a function of the position of the ROV along the x-axis.

Results—TDMA MAC scheme

In this section, we discuss the performance of the ROV control system in the presence of a TDMA MAC layer. We will not perform an explicit simulation of the clock synchronization between the ROV and the controller, but we observe that the continuous transmission of messages from both sides expectedly facilitates the estimation and correction of clock offsets and skews. The TDMA slot durations t_{rov} and t_{ctr} and the guard interval t_i are set so that both the ROV and the controller have sufficient room to send their packets. While for mode 0 and mode 1 this can be achieved via an equal time division ($t_{\mathrm{rov}} = t_{\mathrm{ctr}} = 0.6$ s, and $t_{\mathrm{rov}} = t_{\mathrm{ctr}} = 0.8$ s, respectively), in mode 3 the ROV must send a larger amount of data and needs a larger time share. This has been provided by setting $t_{\mathrm{rov}} = 0.8$ s and $t_{\mathrm{ctr}} = 4.8$ s. In all modes, $t_i = 0.2$ s.

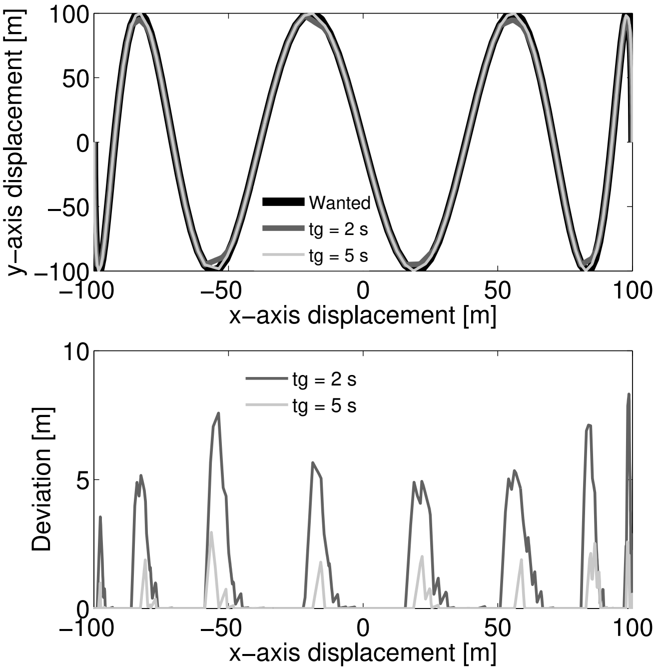

Figure 7.4: TDMA, mode 2: route followed by the ROV (top) and deviation from the desired route (bottom) as a function of the position of the ROV along the x-axis.

Fig. 7.4 reports the performance of the control system in mode 2. We observe that the multiplexing of control messages and ROV data in time improves the performance of the control system considerably. In particular, the ROV no longer has very large deviations from the desired route, and if a guard time $t_g = 5$ s is considered, the ROV never deviates more than 3 m from the expected route. Although the results in Fig. 7.4 already show promisingly good performance, these results could be further improved by

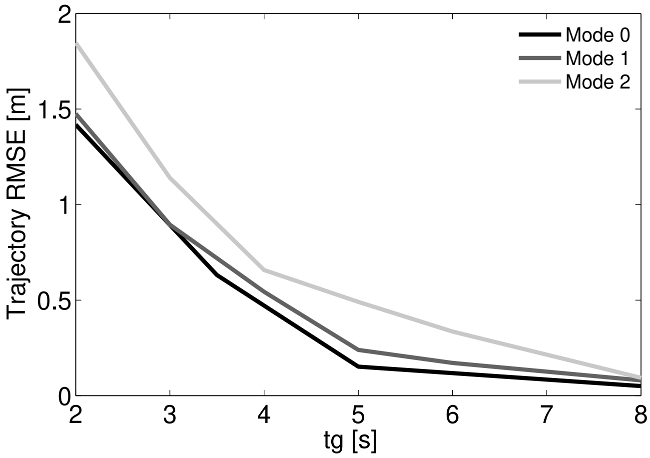

Figure 7.5: RMSE of the trajectory followed by the ROV as a function of t_g for modes 0, 1 and 2. TDMA is employed at the MAC layer.

increasing t_g, with the understanding that the operator will have to accept some additional lag when controlling the ROV at points farthest from the controller.

As a final comparison, in Fig. 7.5 we show the root-mean square error (RMSE) of the actual trajectory followed by the ROV against the desired trajectory. We consider the TDMA MAC scheme and all modes 0 to 2. The curves are plotted against the guard interval t_g, and help set t_g in order to reduce the average trajectory deviation under either operational mode. We observe that the RMSE is lowest in modes 0 and 1, which incur almost the same variation with t_g. In mode 3, the RMSE becomes expectedly higher, although increasing t_g to about 8 s reduces the error down to values comparable with modes 0 and 1. This is in line with the results in Figs. 7.2–7.4.

7.5 Multi-Modal wireless remote control for ROVs

In this section we analyze the behavior of the complete multimodal system during a use-case operation, where it switches between modes according to the available technology.

7.5.1 Early mode switching via signaling

Multimodal communication systems require a strategy to switch between different PHYs according to the channel conditions, e.g., to maximize the instantaneous throughput at any given time. For applications requiring a continuous flow of traffic through a point-to-point connection, a straightforward strategy is to quantize the use of any PHY down to a fixed amount of time, at the end of which the PHY choice is reevaluated. While a PHY is in use, the received power level over this PHY is continuously monitored: once a preset threshold is exceeded, the system switches to a different PHY at the beginning of the next PHY evaluation period. The PHY layer switch algorithm implemented in [192] follows. We calculate the transmission range d corresponding to an optical Signal-to-Noise Ratio (SNR) of 20 dB, and define θ_{opt} as the received *optical* power at a distance $d + 0.5$ m. We then define θ_{ac} as the received *acoustic* power at a distance $d - 0.5$ m. The hysteresis of 0.5 m provides a sufficient margin to avoid continuous switching between acoustic and optical communications. The switch from the acoustic to the optical PHY is operated after the reception of packet k whenever $\bar{P}_{r,ac}(k) > \theta_{ac}$, where $\bar{P}_{r,ac}(k)$ is the average receiver-side acoustic power after the reception of packet k: this value is updated at every received packet i according to the relationship

$$\bar{P}_{r,ac}(i) = \alpha P_{r,ac}(i) + (1 - \alpha)\bar{P}_{r,ac}(i - 1), \tag{7.1}$$

where $P_{r,ac}(i)$ is the received power of packet i, and it is understood that $\bar{P}_{r,ac}(0) = 0$ and $\bar{P}_{r,ac}(1) = P_{r,ac}(1)$. The switch between physical layers is similarly triggered after the reception of packet ℓ as $\bar{P}_{r,opt}(\ell) < \theta_{opt}$, where $\bar{P}_{r,opt}(\ell)$ is the average receiver-side optical power after the reception of packet ℓ, and is filtered over time analogously to (7.1).

However, this system may not be sufficiently fast to react at the speed at which the conditions of the communication vary [192]. Therefore, in this chapter we also introduce an explicit PHY changing mechanism based on the transmission of specific control messages between the controller (or master) and the ROV (or slave). In particular, we prescribe that the master sends a packet in unicast to the slave in order to command an immediate PHY switch triggered by the received-power metric at the master node. At the price of a small overhead (which will be quantified in Section 7.5.3), the signaling mechanism relieves the slave from having to wait for the beginning of the next fixed transmission period before the PHY layer can be actually changed. This results in a much more agile behavior in the presence of optical communications, which offers very high throughput within a very limited coverage range, and must therefore be exploited as soon as it becomes available.

When the slave receives the signaling packet, it switches PHY according to the master's indication. In addition, if the slave is also in signaling mode, it replies with another signaling packet, allowing the master to re-compute the power metric immediately after the switch. After the PHY switch command, the master expects to start receiving data over the new PHY. If this is not the case, after a Signaling Timeout (STO) interval of prescribed duration, the master signals the slave nodes, in broadcast, to switch to a more robust physical layer, in order to avoid losing an excessive number of transmissions and wasting the corresponding transmission energy. Both the STO and the slave signaling mode are useful for systems experiencing bursty traffic, where the collected time series of the received power do not provide sufficiently timely information about the channel conditions. A relevant example is when the slave is transmitting a burst of packets through the optical PHY, but a number of packets at the beginning of the burst are sent while the distance between the two nodes is too long in order to allow any packet reception, thus preventing the master from computing the power metric. Furthermore, without the STO, the system would lose all the subsequent incoming packets.

7.5.2 Simulation parameters and settings

All simulation results have been obtained using a set of C/C++ libraries that simulate multimodal communications in underwater networks. They have been implemented as part of the DESERT Underwater v2 software [74] and released as open-source software [148]. The proposed scenario has two nodes: the ROV and its remote controller. The protocol stack implemented in each node is organized as follows:

- `ROV CONTROL` [28] application layer
- Either `CSMA` or `TDMA` MAC
- `MULTI–STACK–CONTROLLER` layer that coordinates multiple PHY, either with or without signaling
- `ACOUSTIC PHY LAYER` model that simulates the Evologics' S2C M HS device [135]
- `HERMES PHY LAYER` [28] model that simulates the Hermes acoustic modem
- `OPTICAL PHY LAYER` [192] model that simulates optical communications.

The `ROV CONTROL` application layer has two primary operating modes: `ROV` and `ROV–CONTROLLER`. In the former, the module implements the ROV behavior, by receiving command packets, performing the request and sending monitoring packets to the controller. The `ROV` module is configured to continuously generate monitoring packets of length 1000 bytes at a fixed generation rate, preventing the node's transmission queue from becoming empty. The `ROV–CONTROLLER` implements the ROV remote control behavior, by dispatching command packets to the ROV in order to control its position and to receive monitoring packets. The controller drives the ROV along the desired path by sending absolute movement commands in the form of a waypoint list. The path has been sampled in 101 way-points and the guard time between the transmission of subsequent waypoints has been set to $t_g = 2.5$ s. The command packets' size is 125 bytes.

Given the presence of only two nodes, we employed the UDP transport layer, static routing and either the CSMA or the TDMA MAC protocol. The choice of two different MAC protocols will allow us to verify if the performance trends and conclusions stemming from the analysis of a single-PHY remote control system in [28] extend to the multimodal case. The mechanism used to switch among the different PHY layers conforms to the description given in Section 7.5.1. We set the STO to 3 s, as this value has resulted in the highest throughput in an extensive set of preliminary simulations.

In Section 7.5.3 we show the comparison of the system with and without signaling, in order to assess the benefits provided by this feature. A signaling packet has a size of 5 bytes. In our simulations, the `OPTICAL PHY LAYER` module [192] is configured as follows: transmission power equal to 100 W, 200 kHz of bandwidth,[3] 2-Mbps PHY bit rate, an SNR threshold to ensure correct reception equal to 20 dB, optical wavelength $\lambda = 532$ nm and a divergence angle $\theta = 0.5$ rad. In this configuration the optical transmission range is 14 m.

The `HERMES PHY LAYER`'s source level is 180.0 dB re μPa^2 at 1 m from the source. The transmission rate is 87768 bps, the carrier frequency is 375 kHz and the bandwidth is 76 kHz. The transmission range of the Hermes acoustic modem is 120 m.

Unfortunately no detailed information has been published on the performance of the new Evologics' S2C M HS acoustic modem, therefore we employed the default DESERT `ACOUSTIC PHY LAYER` in order to simulate it. The modem's source level is set to 177 dB re μPa^2 at 1 m from the source [4], whereas the carrier frequency and the bandwidth available for communications are 160 kHz and 80 kHz, respectively.

The threshold model employed in the master switching system is described in [192] and in Chapter7.5.1. The switching thresholds are chosen so as to ensure the proper operation of each PHY technology while in use. For example, this means that the thresholds for switching from the Hermes modem to the optical modem and vice-versa depend on the conditions of the water in terms of turbidity and ambient light noise. Similar considerations apply to the acoustic PHYs. The power thresholds are reported in the following list:

- Evologics HS → Hermes: 139.95 dB re μPa^2 at 1 m
- Hermes → Evologics HS: 138.04 dB re μPa^2 at 1 m
- Hermes → Optical Modem: 161.70 dB re μPa^2 at 1 m

---

[3] These parameters correspond to our own understanding of the Sonardyne BlueComm 100 optical transceiver, as its datasheet reports neither its transmission power nor its bandwidth.

[4] Value declared by the manufacturer.

- Optical Modem → Hermes: $1.08{\cdot}10^{-8}$ W

In our simulations, the ROV moves at a speed of 1 m/s, at a depth of 40 m in a water column of 100 m, whereas the controller has fixed position and is deployed at a depth of 38.5 m. We implement the empirical underwater sound propagation and noise models in [193], with a spreading coefficient equal to 1.5 in the spreading loss component, no shipping activity and speed of wind of 1 m/s. The speed of sound under water is assumed to be constant and equal to 1500 m/s. The underwater speed of light is set to $2.25{\cdot}10^{8}$ m/s. For assessing the impact of the solar irradiance on the optical communications component of the multimodal control system, we assume environmental conditions that are typical of a coastal ocean scenario. In particular, the attenuation coefficient is set to $c = 0.4$ m^{-1}, equally subdivided between the absorption coefficient a and the scattering coefficient b, where $c = a + b$. Furthermore, we assume the absence of clouds, and a solar zenith angle of 0 rad, which is obtained during solar noon at the equatorial line. In these conditions, the solar irradiance perceived by the controller is $1.9{\cdot}10^{-4}$ W/m^2.

7.5.3 Results

In this section we analyze the system performance in order to assess which configuration is best for the remote control of an underwater vehicle over a wireless link in our scenario. In particular, we focus on the achievement of the minimum required bit rate for each mode (see Section 7.5.2), the speed of the switching between modes, the ROV's deviation from the path commanded by the controller, and the signaling overhead, which is defined as the number of signaling bits sent divided by the total number of bits transmitted.

Results–CSMA MAC scheme

First we analyze the performance achieved by the control mechanism when using a CSMA MAC protocol without signaling for prompt switching. This configuration may be suboptimal, but entails a simplified system implementation, as there is no need to enable additional services such as localization and time synchronization between the controller and the ROV; moreover, no signaling overhead is required. However, the performance of the control system does not achieve the expected targets in terms of desired monitoring data throughput in each system mode defined in Section 7.5.2. The latter, in particular, can be observed from Fig. 7.6, which shows one realization of the instantaneous throughput achieved by the system as a function of the simulation time. The figure is focused on the part of the simulation where the ROV is closest to the controller (represented as a triangle centered at the bottom of the figure), which in turn triggers the shift from Mode 2 to 3 (around 275 s), then to Mode HD (at about 400 s), and back to 3 (about

430 s) and 2 (540 s). Three dashed lines mark the minimum throughput that should be achieved in Mode HD (red), Mode 3 (blue) and Mode 2 (green).

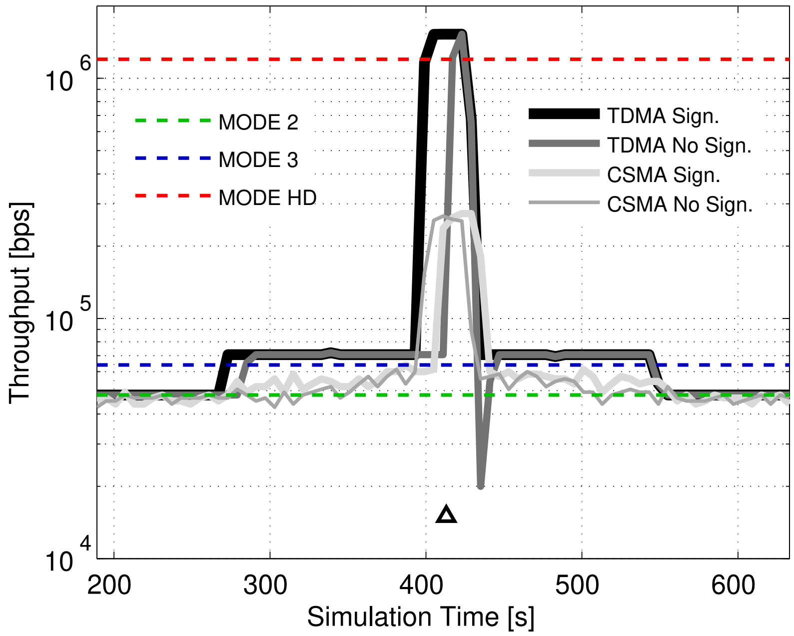

Figure 7.6: Throughput achieved by the four MAC and PHY switching configurations considered in this chapter as a function of the simulation time.

We observe that the throughput for the case of CSMA with no signaling, represented by a thin, dark-gray line, correctly remains around the prescribed level in Mode 2, but fails to achieve the level prescribed by Mode 3, and cannot even exploit optical communications properly when it becomes available. The main reason for this is the lack of coordination between the transmissions of commands by the controller and the transmission of monitoring data by the ROV. There is a high chance that these transmissions take place while the other node is also transmitting, which results in significant packet losses. The resulting metrics are as follows: PDR of control packets: 84%; average path deviation: 2.0 m; path RMSE: 2.7 m; average throughput of 56.1 kbps; no signaling overhead.

We now turn to the case where the switching mechanism is employed to notify that the choice of the PHY should be changed. It turns out that this mechanism yields little if any significant improvement with respect to the case without signaling: in fact, the ROV deviation from the intended path gets smaller (on average, about 28% with respect to the case without signaling), but despite the faster PHY switch, the monitoring traffic requirement is not

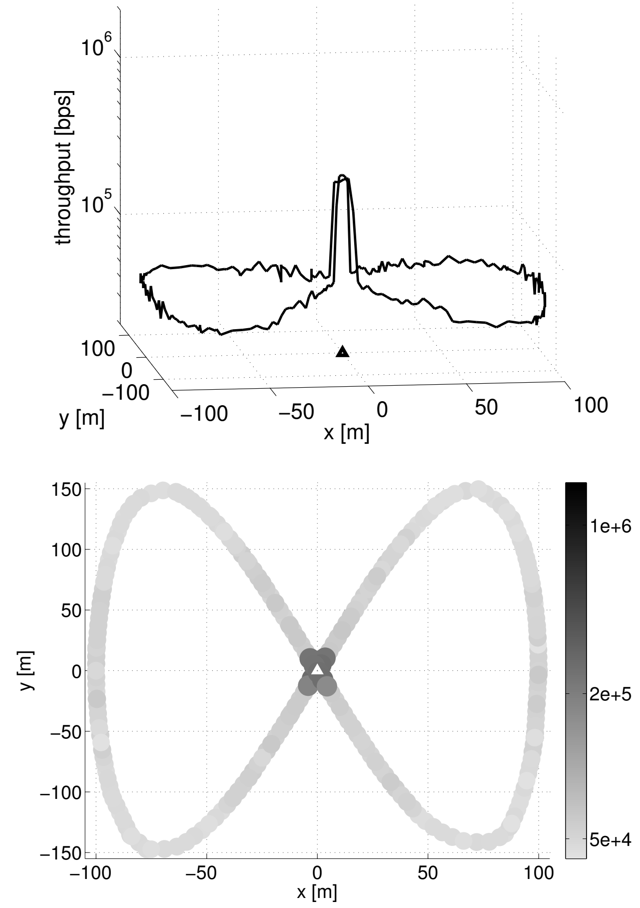

Figure 7.7: CSMA with signaling: 3D (top) and 2D projection (bottom) of the throughput against the position of the ROV along one lap.

achieved, as can be seen from the light-gray line in Fig. 7.6. In particular, we note that the peak throughput during optical communications is negligibly higher than the maximum achieved in the no signaling case, and in any event it is one order of magnitude lower than the requirement of 1.4 Mbps. When TDMA is employed, the achieved throughput is generally much more stable and higher. Signaling helps TDMA improve the PHY switching efficiency as well. In particular, we note that the low value of the TDMA throughput around 440 m in the no signaling case (dark grey line) is due to a late switch, whereby the optical PHY technology is suboptimally employed beyond its coverage range. This causes the optical link to fade and the average throughput to decrease, before a link with the Hermes modem (the fastest of the two acoustic technologies considered here) is finally established at about 450 m. Such an event is prevented by the signaling mechanism (black line).

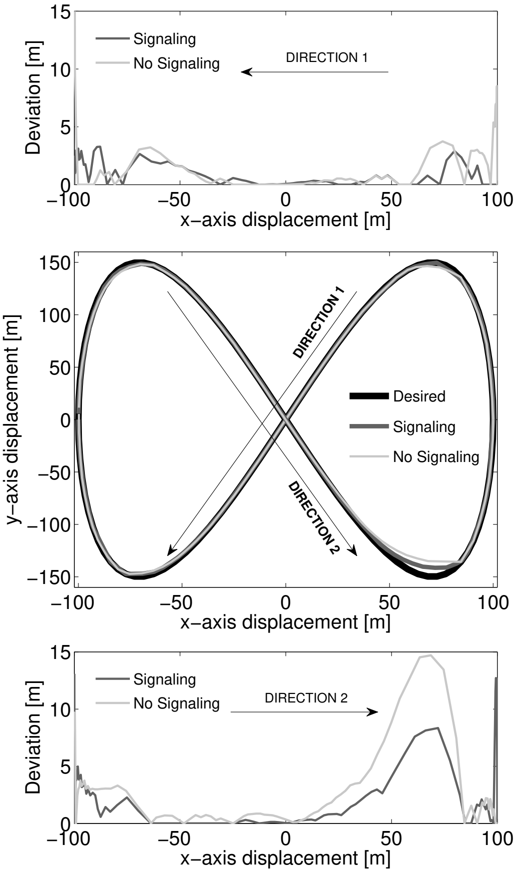

Figure 7.8: CSMA: route followed by the ROV and deviation from the desired route as a function of the position of the ROV along the x-axis.

The behavior of the control system along the trajectory commanded by the controller is presented in Fig. 7.7 in terms of monitoring throughput versus ROV position, both in a 3D plot (top pane) and in a 2D projection seen from above (bottom pane). In the latter, the performance metric is represented using gray-scale points, with a circle area and gray shade level proportional to the throughput values along that portion of the trajectory. The position of the remote controller is represented by a triangle. The PHY switch occurs correctly, however, the throughput of the monitoring traffic varies broadly in every mode and the optical throughput does not increase above 250 kbps. In the case of no signaling the system behavior is very similar, with the exception of a longer PHY switch time.

To summarize, the main reason for the monitoring performance degradation is the CSMA protocol configuration, in terms of listening and back-off timing which causes packet collision and deafness states. This setup can dramatically reduce the maximum throughput and the PDR of the control packets sent by the controller. The low control packet PDR is the main cause of ROV deviation from the desired path: the higher the PDR, the smaller the deviation. Due to this trade-off, the system cannot meet the monitoring traffic constraint. Other system performance figures are control packet PDR: 85%; average path deviation: 1.4 m; path RMSE: 2.1 m; average throughput: 57.9 kbps; signaling overhead: $3.3{\cdot}10^{-6}$.

A detailed analysis of the deviation of the ROV from the desired path is provided in Fig. 7.8 for the CSMA case. In particular, the middle pane shows a superimposition of the desired trajectory (black) to the actual ones followed by the ROV, both in the presence (dark gray) and in the absence (light gray) of signaling. The figure-of-eight trajectory has been split into two legs in order to make the analysis simpler. The first leg goes from point $(100, 0)$ to point $(-100, 0)$ following direction 1. The deviation of this part of the trajectory from the desired path is shown in the top pane. The second leg goes from $(-100, 0)$ to $(100, 0)$ following direction 2. The deviation of this trajectory from the wanted one is reported in the bottom pane.

We observe that the maximum path deviation is 15 m in the case of no signaling, and is suffered near point $(70, -150)$, which corresponds to one of the farthest distances between the ROV and the controller. The maximum deviation decreases to about 12.5 m in the case of PHY switch with signaling, and is observed towards the end of the trajectory, when the ROV is almost back at its original position. Also in this case, a deviation peak (albeit slightly lower than in the no signaling case) is observed near the point $(70, -150)$. The peaks are due to lack of reception of some waypoint, either due to errors over the signaling channel (in turn most likely due to untimely PHY switching) or due to deafness at the ROV induced by a ROV transmission. Either event makes the ROV lose some of the required waypoints along the route. When an ensuing waypoint is finally received, the ROV will then head towards the most recently received waypoint, and skip all lost ones. In the remaining portions of the path, the deviation is typically less than 5 m, and becomes larger when the distance between the ROV and the controller increases. The ROV, in both system configurations, follows the trajectory with very similar reliability. This confirms that the PHY signaling system does not provide significant advantages in terms of throughput or path deviation. We note that errors and deafness take place randomly in each realization of our simulation setup, and therefore the behavior of the ROV along a trajectory is not necessarily symmetric, nor identically equal to the realization shown in Fig. 7.8.

7.5.4 Results–TDMA MAC scheme

In this section, we discuss the performance of the multimodal ROV control system with a TDMA MAC layer. First of all, we note that our TDMA channel access mechanism subdivides time into frames, which in turn are divided into four time slots: a slot dedicated to the monitoring feedback from the ROV (of length t_{rov}), a guard time interval of length t_i, a slot dedicated to the control messages from the controller (of length t_{ctr}) and a second guard interval t_i. We stress that the slot durations and the guard interval are set so that both the ROV and the controller have sufficient time to send their monitoring and control packets, respectively. In particular, the ROV must send a large amount of data, and to do so it needs a time slot larger than the controller's. This has been achieved by setting $t_{\mathrm{rov}} = 4.8$ s, $t_{\mathrm{ctr}} = 0.8$ s and $t_i = 0.2$ s.

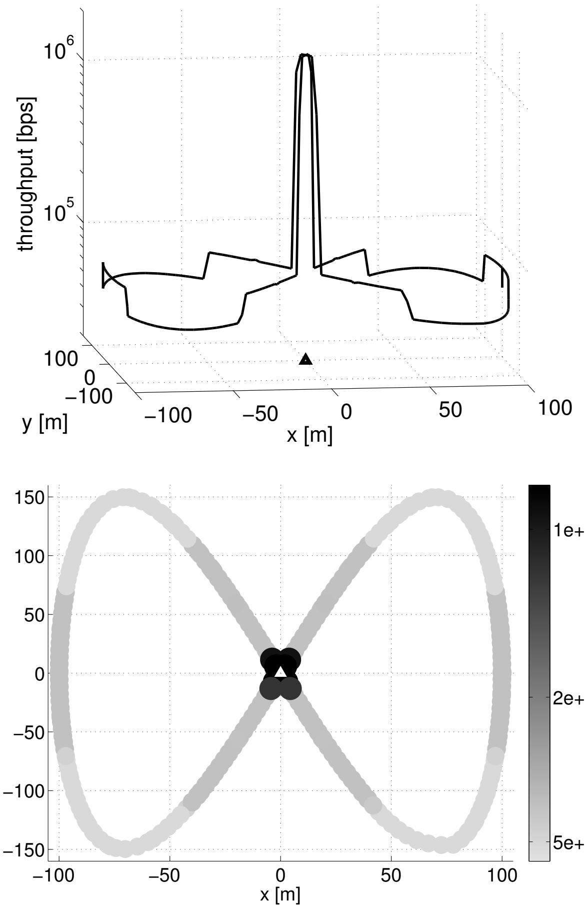

Figure 7.9: TDMA with signaling: 3D (top) and 2D projection (bottom) of the throughput against the position of the ROV along one lap.

We first consider the case where no signaling is employed by the PHY switching mechanism. The observed performance metrics are as follows; control packet PDR: 100%; average path deviation: 0.6 m; path RMSE:

1.50 m; average throughput: 83.4 kbps; signaling overhead = 0. The TDMA protocol provides two main advantages. First, no collisions and deafness occur, as the ROV correctly receives all the waypoints, thus following its path with a small deviation (the average path deviation is four times smaller than the CSMA case). Second, the system experiences a higher throughput, and consistently achieves the monitoring target in each control Mode, as seen from the bold gray line in Fig. 7.6. This configuration is not very reactive. Although the PHY switch occurs correctly, the observed delay causes a decrease of the measured throughput, as well as of the average throughput along the path. For instance, if the switch from the Hermes (acoustic) to the optical PHY occurs with a delay of 3 seconds, the system can transmit 3.3 Mb less than in the optimal case.

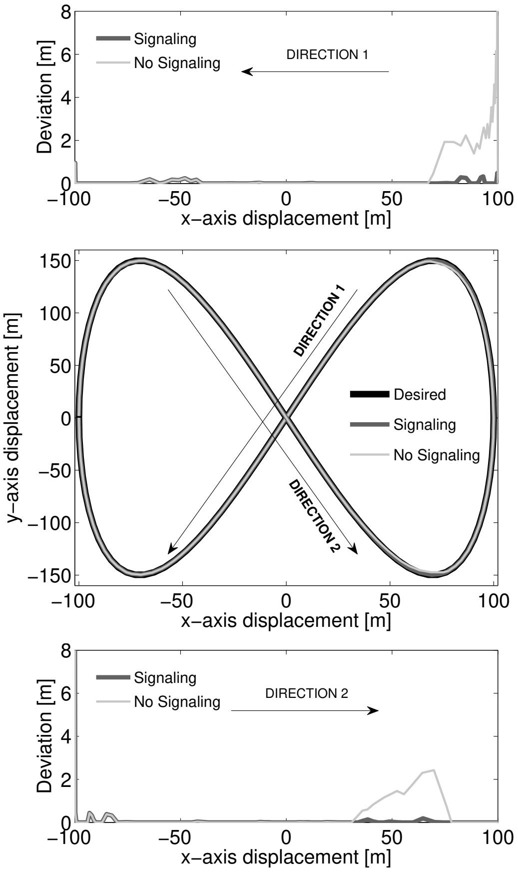

Figure 7.10: TDMA: route followed by the ROV and deviation from the desired route as a function of the position of the ROV along the x-axis.

Employing the signaling mechanism to switch PHY solves this issue (black curve of Fig. 7.6). In this case, the performance of the control system improves even further as indicated by the following metrics; control

PDR: 100%, average path deviation: 0.2 m, path RMSE: 1.0 m, average throughput: 117.6 kbps, signaling overhead = $1.7{\cdot}10^{-6}$. For this case, we report the monitoring throughput versus the ROV position in Fig. 7.9, both in a 3D plot (top pane) and in a 2D projection (bottom) We observe that the switch occurs correctly, the monitoring traffic flows smoothly and constantly, and the bit rate targets in each mode are consistently achieved. In particular, the bottom pane shows that only the farthest portions of the trajectory have to fall back to Mode 2, whereas the sections immediately closer to the controller can already use Mode 3, and the points in its immediate proximity enjoy the high bit rate allowed by the optical connection. In the case of no PHY signaling the system behavior is very similar, but the switch among different PHYs is delayed, thus causing a performance loss.

The comparison of the ROV path deviation (top and bottom panes) against the commanded route (intermediate pane) is shown in Fig. 7.10. The maximum path deviation is 4 m in the case of no PHY signaling and 0.5 m in the case of PHY switch with signaling. The ROV, in both system configurations, follows the trajectory with significant reliability, and when the PHY signaling is active the deviation from the requested path is almost zero. In this case, the PHY signaling technique provides a reduction of path deviation and a large improvement in terms of monitoring traffic, at the cost of a negligible signaling overhead.

7.6 Conclusions

We discussed the feasibility of wireless ROV control in light of the capabilities offered by current optical, RF and acoustic modem technologies. For each technology, we focused on the available modems that report performance figures measured in the presence of realistic operational conditions, including turbidity, shallow-water channels, and distances on the order of 150 m, which are of interest for the remote control application. We then identified a number of operational modes based on the amount of data to be transferred between the controller and the ROV, and defined the range at which current modems can support each operational mode. We first focused on acoustic communications and implemented a remote control system in the DESERT Underwater network simulator, which we used to test the capability of an ROV to follow a desired trajectory. In doing so, we compared the CSMA and TDMA approaches for sharing the half-duplex acoustic channel between the ROV and the controller. The results show that TDMA increases the chance that commands and ROV reports are correctly received; in addition, the accuracy of the actual trajectory relative to the desired one can be improved by increasing the guard time between subsequent commands.

Then, we demonstrated the effectiveness of a multimodal optical and acoustic wireless remote control system for underwater mobile vehicles, by comparing the performance of different system configurations. Also in this case the TDMA MAC layer is more robust than CSMA, in terms of both throughput and ROV deviation from the desired trajectory. This is due to the fact that coordinating the transmissions of the ROV and of the controller avoids the occurrence of deafness and collisions. Finally, we have shown the effectiveness of a PHY switching signaling mechanism, which makes moving from a PHY to another in the multimodal system faster and more reliable, at the cost of a negligible overhead.

Notes

Part of this work has been published in [28] and in [140].

Chapter 8

Multi-hop range extension of a wireless remote control for AUVs

8.1 Introduction

In this chapter, we analyze a multimodal multi-hop network scenario, where both mid-frequency (MF) and low-frequency (LF) acoustic modems are employed in the same network, used to remotely control an AUV that moves inside a certain area. The AUV follows the path sent by a control station (CTR) and sends back monitoring packets containing information about its status and its position to the CTR. In our analysis, we compare the performance in terms of throughput, packet delivery delay (PDD) and packet error rate (PER), of two different multi-hop networks with a linear topology that cover more or less the same distance between AUV and CTR. First, we analyze a multi-hop single technology (`ST`) network, akin to the one described in [194], where all the nodes are equipped with the same MF acoustic modem. Then, we propose a multimodal (`MM`) network solution with two acoustic modems, operating at different frequencies, where both contention-free (TDMA-based) and contention-based (CSMA-based) MAC protocols are evaluated. The `ST` network is used as a benchmark to evaluate the performance of the proposed solution.

The rest of the chapter is organized as follows: in Section 8.2.1 and Section 8.2.2 we describe topologies and MAC layer solutions of the `ST` and `MM` networks, respectively. In Section 8.3 we talk about the protocol stack designed for the DESERT underwater network simulator [195], freely available at [148], and used in our simulations. Section 8.4 introduces the simulation scenario and the system parameters. In Section 8.5 we depict the results of the simulations and compare the performance of the proposed `MM` scenario with respect to the `ST` configuration. Finally, in Section 8.6 we draw

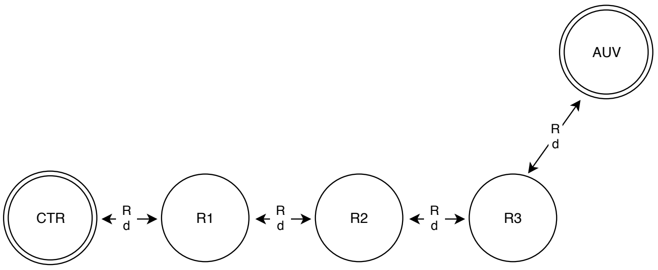

Figure 8.1: Single technology network topology.

some conclusions.

8.2 AUV control range extension approaches

The main purpose of this chapter is a performance-oriented comparison of different acoustic networks configured to extend the working range of an AUV during a patrol mission of a certain area. This coverage problem is typically solved through the deployment of multiple intermediate single technology (`ST`) acoustic relays that forward the packets coming from the CTR and destined to the AUV and vice-versa. This first approach, presented in Section 8.2.1, is used as a benchmark for a more advanced solution, that requires the use of a two-hop hybrid multimodal network (`MM`) that combines different acoustic modems. This second approach is presented in Section 8.2.2.

8.2.1 Range extension via single technology networks

The `ST` network topology used in this chapter for extending the AUV control range is presented in Fig. 8.1. In this case, all the nodes are equipped with the same acoustic modem and, therefore, use the same bandwidth for packet transmission. The MAC layer strategy employed in this scenario is an advanced TDMA-based protocol, similar to the one presented in [125], that implements a customized time division multiple access where it is possible to control the frame duration (number of slots in each frame) and also the slots assignment. For example, it is possible to schedule more than one slot to the same node within a single frame. Moreover, in the case of multi-hop networks with a sufficient number of nodes, this configuration presents the possibility of using both the pipeline mechanism and the near-far effect, exploiting the high propagation delays, and scheduling simultaneous transmissions in different parts of the network [115]. Two adjacent nodes can transmit simultaneously without interfering with each other if the propagation delay is larger than the time needed to transmit a packet. Therefore, once the distance between consecutive nodes is fixed, we have implicitly imposed also the maximum packet length that can be successfully transmitted. This protocol is included in the DESERT Underwater simulator as a MAC layer module, called `TDMA_FRAME`.

The frame of the TDMA scheme needs to be specifically designed in order to ensure network stability and avoid traffic congestion. Indeed, the nodes generating traffic, i.e., CTR and AUV, must have a total cumulative number of transmission opportunities smaller than or equal to that of each relay. Thus, if in a time frame T_{Frame} both CTR and AUV transmit once, each relay must transmit at least twice within T_{Frame}. The frame allocation used in our simulations is reported in Table 8.1. R_1 and AUV can transmit in the same slots, since they are sufficiently separated in space to not interfere with each other. Moreover, R_2 and R_3 transmit simultaneously exploiting the long propagation time. Each node can transmit up to one packet in each assigned time slot. It might be argued that in slot 1, when both R_1 and AUV are transmitting, they may collide at R_2, as AUV is moving around the coverage area of R_3. In Table 8.2 we prove that the presented frame avoids this issue as during slot 1 R_1 transmits only packets for CTR, while it transmits the packets for R_2 in slot 2, where the transmission is not parallelized and, therefore, the collision cannot occur. This Table shows the node queues evolution in three consecutive time frames, where `CXX` is a control packet generated from CTR to AUV, and `MYY` is a monitoring packet generated from AUV to CTR, with `XX` and `YY` the sequence number of the `C` and `M` packets, respectively.

Table 8.1: Frame of the single technology scenario.

Slot N°	1	2	3	4
Node	CTR R_1 AUV	R_1	R_2 R_3	R_2 R_3

Although this MAC configuration is very efficient when the AUV moves around R_3, it does not work in the case where the AUV patrols all the area spanning from CTR to R_3. This is a different scenario, where the network topology changes in time, and static routing cannot be employed. Such situation has already been addressed in [194], where a different time frame is used and a specific routing protocol is presented. Such routing protocol, called Estimate-Position Based Routing (EPBR), uses information related to the AUV position to decide the next hop. In this chapter we only consider a static topology with the goal to extend the control range of an AUV through a predefined route, thus, in this case a static routing can be employed, because the vehicle always moves near R_3, the farthest relay from the control station.

Table 8.2: Time frame evolution of the node queues in the single technology scenario

Slot N°	CTR	R_1	$R2$	$R3$	AUV
1	C1				M1
2		C1		M1	
3			C1	M1	
4			M1	C1	
5	C2	M1			M2 **C1**
6	**M1**	C2		M2	
7			C2	M2	
8			M2	C2	
9	C3	M2			M3 **C2**
10	**M3**	C3		M3	**C2**
11			C3	M3	
12			M3	C3	

8.2.2 Range extension via multimodal networks

The `MM` network topology used in this chapter to extend the AUV control range is depicted in Fig. 8.2. In this scenario only one intermediate relay is used, equipped with two different acoustic modems. Specifically, the relay is a multimodal node equipped with two technologies working on non-overlapped bands, e.g., one operating at low-frequency (LF), and the other at mid-frequency (MF), such as [196]. CTR, instead, is equipped with only an acoustic LF modem, and AUV with acoustic MF. This smart design choice provides an interesting degree of freedom from the channel access point of view. In fact, the relay can communicate at the same time with both CTR and AUV without dealing with any interference problems. In particular, we can consider this network as the composition of two very simple independent networks, one composed by CTR and the relay connected through the LF modem, the other composed by the relay and AUV connected through the MF modem. In this chapter we refer to the former network as `NET_LF` and to the latter as `NET_MF`.

This channel access freedom significantly simplifies the MAC layer design and opens the possibilities for hybrid MAC solutions such as a contention-based protocol for nodes transmitting with LF, and a contention-free MAC for nodes transmitting with MF. In the following we describe the four different MAC combinations that will be analyzed in Section 8.5.

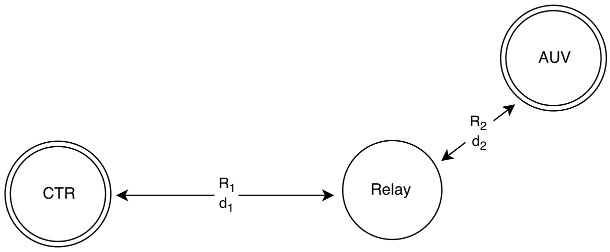

Figure 8.2: Multimodal network topology

TDMA - TDMA

This is the simplest case, in fact, it is our starting point for the evaluation of the proposed scenario. Here, both subnetworks use a standard TDMA strategy, the only difference between `NET_LF` and `NET_MF` is the length of the time slots t_{slot}. Indeed, in `NET_LF` the distance between the nodes is twice that in `NET_MF`, hence, the propagation delay in `NET_LF` is two times that experienced in `NET_MF`. Moreover, also the transmission time changes because the bit rate of the two networks is not the same. Details on the frame size and the parameter configuration are presented in Section 8.4.

In each subnetwork we choose to implement a TDMA MAC layer with only two time slots: the structure of these basic frames is reported in Table 8.3. In our configuration, only one packet per slot can be sent, like in the `ST` scenario.

Table 8.3: Slot assignments in the LF network and in the MF network.

Slot N°	1	2
Node	CTR	Relay

Slot N°	1	2
Node	AUV	Relay

CSMA - TDMA

Moving to a slightly more complicated solution, we have a hybrid configuration that combines a contention-based and a contention-free protocol. The contention-based protocol selected for this analysis is CSMA 1-persistent [197], available in the DESERT Underwater simulator as a MAC module, called `CSMA_ALOHA`. This module is adopted in `NET_LF` while in `NET_MF` we use again standard TDMA with two slots. The frame structure is presented in Table 8.4.

TDMA Frame - TDMA

In this configuration, we adopt two contention-free protocols. More precisely, in `NET_LF` we use the `TDMA_FRAME` module already presented in Sec 8.2.1,

Table 8.4: Slot assignments in MF network

Slot N°	1	2
Node	AUV	Relay

while for `NET_MF` we choose a standard TDMA protocol with only 2 time slots. During the simulations of the simplest case with two independent TDMA described in Sec. 8.2.2, we observed that many slots reserved for the CTR are not actually used. This situation happens because the control station sends a packet containing the waypoint every T_{CTR} seconds while a reserved slot is available every T_{FRAME} seconds, with $T_{FRAME} < T_{CTR}$. A smarter solution, that aims to manage this inefficiency, consists in the design of a suitable frame with $T_{FRAME} \simeq T_{CTR}$. For instance, this requirement can be achieved with a frame where only one slot is reserved for the CTR and all the remaining slots are assigned to the relay. The frame structure considered in this chapter is reported in Table 8.5.

This particular mechanism greatly increases the number of packets per frame generated by the AUV, that can be received by the CTR. This happens because the relay has more transmission opportunities to transfer the monitoring packets received from the AUV.

Table 8.5: Slot assignments in LF network

Slot N°	1	2	3	4	5	6	7
Node	CTR	Relay	Relay	Relay	Relay	Relay	Relay

TDMA Frame-CSMA

We close the overview of the proposed solutions describing this last configuration. Again, we have a hybrid solution like in Section 8.2.2. In this case, in `NET_LF` we use a `TDMA_FRAME` module with the time frame described in Table 8.5, while in `NET_MF` we adopt the CSMA 1-persistent MAC presented in Section 8.2.2.

Excluded MAC configurations

Also other MAC combinations could be inspected, such as employing CSMA in both `NET_LF` and `NET_MF`, or `TDMA_FRAME` in both `NET_LF` and `NET_MF`. The former solution has been excluded due to the high probability of deafness in long range low frequency networks, such as `NET_LF`, while the former solution provides benefits only if the TDMA frames of both technologies are synchronized. This is in general not easy (or not even possible), as the time slots duration differ per technology according to packet size and distance between nodes.

8.3 DESERT Underwater simulator

All the simulation results described in this chapter are obtained using a set of C/C++ libraries that reproduce underwater communications through different transmission technologies. In this case we have used only acoustic modems, but also optical and radio-frequency physical layers are available for testing. In principle, the simulator allows the definition of customized network scenarios in terms of number, location and mobility of the nodes, MAC addresses and, more importantly, the protocol stack implemented in every single node.

As an example, in Table 8.6 we report the protocol stack used for the simulation of the multimodal relay described in Section 8.4.2.

In the relay the application layer does not generate traffic as the relay only forwards packets to extend the transmission range of the control station, while CTR transmits periodic control packets and AUV generates monitoring packets according to a Poisson process. Given the relatively simple topology, we choose a static routing approach. The most important part of the `MM` relay communication stack starts with the `MULTI_DESTINATION` layer, presented in Section 8.3.1. More precisely, we can observe that the lower layers (`MAC` and `PHY`) are duplicated. In general we will have as many copies as the number of different physical layers we want to simulate. Using this particular structure, it is possible to have simultaneous transmissions on the two physical layers. Finally, for each acoustic physical layer we can define transmission frequency, bandwidth, transmission power, transmission bit rate and interference model. The implemented acoustic propagation and noise models are presented in [198].

Table 8.6: Multimodal protocol stack.

<table>
<tr><td colspan="2">UW APPLICATION LAYER</td></tr>
<tr><td colspan="2">UW STATIC ROUTING</td></tr>
<tr><td colspan="2">UW MULTI_DESTINATION</td></tr>
<tr><td>UW MAC 1</td><td>UW MAC 2</td></tr>
<tr><td>ACOUSTIC PHY 1</td><td>ACOUSTIC PHY 2</td></tr>
</table>

8.3.1 Implementation of the MULTI_DESTINATION module

In order to implement the behavior of the multimodal relay, we developed a new module in the DESERT Underwater simulator, called `MULTI_DESTINATION`. The basic idea is a switching mechanism that performs the following operations. For each packet ready to be transmitted, it first checks the IP address of the packet destination, and then chooses the right physical layer technology to use for the transmission. The selection is performed through a technology per node map, where the `MULTI_DESTINATION` stores the list of physical layers available in each node, and selects the best performing one within range. In our case this list is assumed to be known at network deployment, however, a periodic topology discovery mechanism [182] might be employed to update this list periodically. For example, in the `MM` network with the three nodes used for our simulations, we defined an address map where CTR, relay and AUV have IP address 1, 2 and 3, respectively. The relay hence has two possibilities: if the destination address is 1, it chooses the LF technology to reach the CTR, while if the destination is 3, it chooses the MF technology. The complete protocol stack is described in Table 8.6.

8.4 System scenario and simulation settings

In our simulations, we analyze a scenario where the control station (CTR) commands at distance the AUV sending waypoints at a constant rate, one packet every $T_{CTR} = 50$ seconds. On the other side, the AUV moves at a fixed speed ($v_{AUV} = 1$ m/s) towards the last received waypoint, and sends back monitoring packets generated according to a Poisson process with average generation time equal to T_{AUV} seconds. In Section 8.5, the network performance will be evaluated in different traffic conditions, varying T_{AUV} within a suitable range.

In all the TDMA-based configurations, the length of each slot t_{slot} is computed from Eq. (8.1):

$$t_{slot} = \frac{d_{max}}{c} + \frac{8 \cdot L_{max}}{R} \tag{8.1}$$

where the first term is the propagation delay, computed as the ratio between the maximum distance between two adjacent nodes (d_{max}) and the sound speed underwater ($c = 1500$ m/s), while the second term is the time needed to send a packet of L_{max} bytes at bit rate R. This slot duration guarantees that each single packet has enough time to reach the intended destination and takes into account that acoustic underwater communications are affected by very high propagation delays. Moreover, in each slot, we identify a guard time exactly equal to the propagation delay during which the node can not transmit, to avoid collision between transmissions in consecutive slots. In our simulation we assume nodes to be perfectly synchronized. This assumption can be relaxed by adding an additional guard time, however, modern atomic clocks can be employed in the submerged nodes to ensure an almost perfect synchronization between them [199]. Since we want a fair comparison, the length of the packets (L_{CTR} and L_{AUV} respectively), T_{CTR} and the range of possible values for T_{AUV} are the same in both the considered scenarios. The parameters are listed in Table 8.7.

Table 8.7: Simulation parameters.

Parameter	**Value**
L_{CTR}	1000 byte
T_{CTR}	50 s
L_{AUV}	1000 byte
T_{AUV}	[4, 60] s
v_{AUV}	1 m/s
f_{LF}	12 kHz
BW_{LF}	5 kHz
P_{LF}	187.8 dB Re μPa
R_{LF}	3500 bps
$d_{max,LF}$	7000 m
t_{LF}	7 s
f_{MF}	26 kHz
BW_{MF}	8 kHz
P_{MF}	184 dB Re μPa
R_{MF}	4800 bps
$d_{max,MF}$	3500 m
d_{ST}	3000 m
t_{MF}	4 s

All the node positions are defined in the three-dimensional space using three coordinates (x, y, z) where z is the depth with respect to the sea level and by definition is always negative, i.e., $z = -1000$ m. In a similar way, also the waypoint consists of a triplet (x, y, z) that defines the next position where the AUV needs to go to continue its mission. The control station and the relays are fixed nodes anchored to the sea-floor to maintain a stable position.

8.4.1 Single technology scenario

The `ST` scenario has a linear topology, depicted in Fig. 8.1, with five nodes: CTR, AUV and three intermediate relays (R_i with i = 1, 2, 3). In this case, the AUV moves around the last relay (R_3). The distance between consecutive nodes is d_{ST} = 3 km, while the number of relays is set to 3 and the AUV moves around an area 1.5 km apart from R_3, thus, the maximum distance between CTR and AUV is 10.5 km. Each node is equipped with the same MF acoustic physical layer, used to simulate the behavior of real acoustic modems, such as the Evologics S2CR 18/34 [36]. It transmits at a frequency f_{MF} 26 kHz with bandwidth BW_{MF} = 8 kHz, transmission power P_{MF} = 184 dB Re 1μPa at 1 m, bit rate R_{MF} = 4800 bps, and maximum transmission range of $d_{max,MF}$ = 3.5 km. The slot duration, obtained with Eq. (8.1), is set to t_{MF} = 4 s. The parameters are summarized in Table 8.7.

8.4.2 Multimodal scenario

The `MM` scenario, designed to evaluate all the MAC layer protocols proposed in this chapter, is reported in Fig. 8.2. The topology is again linear but this time we have only 3 nodes: the control station (CTR), a single intermediate relay R and the AUV. This new layout is possible thanks to the longer transmission range of the LF modem.

The total distance covered by this network is the same as in the `ST` network, i.e., 10.5 km, in order to have a similar use-case scenario. The distance between CTR and relay is equal to $d_{max,LF}$ = 7 km while the AUV moves around the relay within a maximum distance of $d_{max,LF}$ = 3.5 km. In this case we have two different types of transmission technologies: an MF acoustic physical layer, used to simulate the behavior of an Evologics S2CR 18/34 (already presented in Section 8.4.1), and an LF acoustic physical layer, used to simulate the behavior of an Evologics S2CR 7/17 [30]. This second physical layer is set to transmit at a frequency f_{LF} = 12 kHz, with bandwidth BW_{LF} = 5 kHz, transmission power P_{LF} = 187.8 dB Re 1μPa at 1 m and bit rate R_{LF} = 3500 bps (see Table 8.7). In this scenario, not all the nodes have the same equipment. Specifically, the CTR is equipped only with LF, the AUV only with MF and, finally, the relay is a multimodal node equipped with both LF and MF, in order to communicate with both the CTR and the AUV. The two transmission bands BW_{LF} and BW_{MF}, centered in f_{LF} and f_{MF} respectively, do not overlap.

8.5 Results and performance comparison

All the results presented in this section are obtained by averaging over 35 independent simulation runs, where every single run simulates an AUV mission of 50 hours.

The results analysis is divided in two parts: the first part, presented in Section 8.5.1, focuses on the network performance considering 6 different metrics, i.e., AUV delay, AUV throughput, AUV packet error rate, CTR delay, CTR throughput and CTR packet error rate; the second part, instead, analyzes the power consumption of the two networks.

8.5.1 Network performance

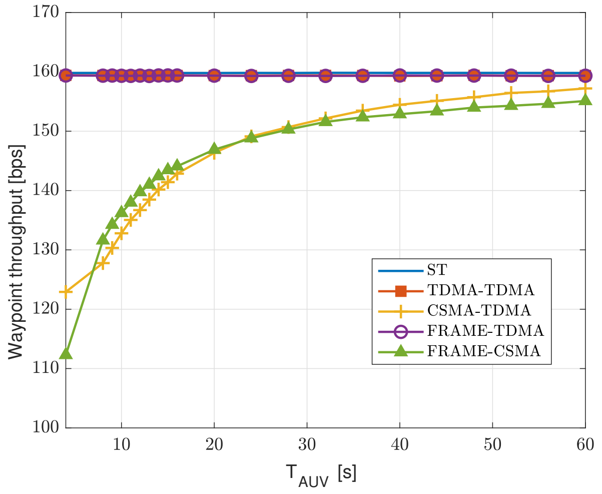

Figure 8.3: Average throughput received by the AUV.

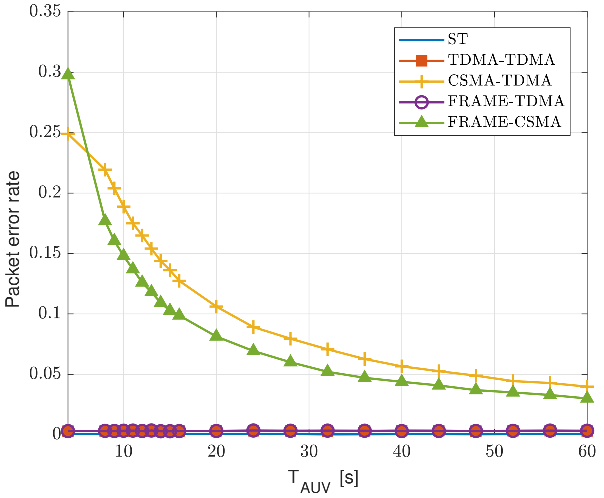

Figure 8.4: Packet error rate of the waypoints.

Fig. 8.3 depicts the throughput received by the AUV, i.e., the throughput related to the waypoints sent by the control station. We can observe that in the two configurations with the CSMA-based protocol the throughput is lower than in the other cases. In particular, the throughput decreases as the monitoring traffic generated by the AUV increases. That is because in contention-based protocols deafness can occur and, therefore, some packets may be lost. Indeed, as reported in Fig. 8.4, in the configurations with the CSMA-based protocol, the PER for the waypoints is non-negligible and increases as the generation of the monitoring traffic increases.

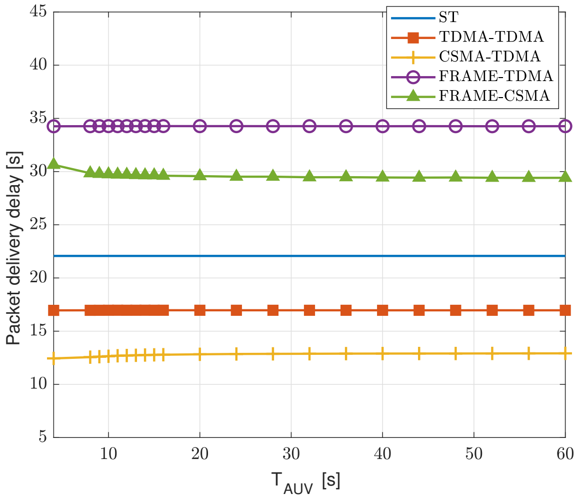

Figure 8.5: Average packet delivery delay of the waypoints.

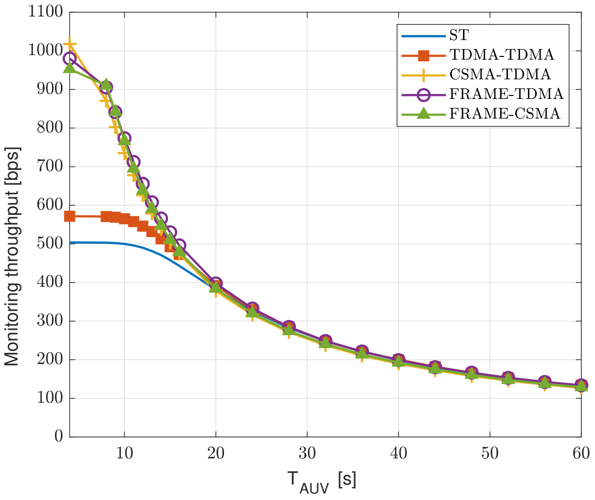

Figure 8.6: Average throughput received by the control station.

Fig. 8.5 reports the average PDD for the waypoints sent by the CTR to the AUV. The highest PDD has been obtained in the two configurations of the `MM` network that use the `TDMA_FRAME` reported in Table 8.5. That is because with this configuration the control station has fewer transmission opportunities than in the other cases and the packets sent by the CTR wait, on average, more time for their transmission slot. Moreover, we highlight that the PDD is almost independent of the average generation time of the monitoring packets, T_{AUV}.

In general, for all the configurations based on a contention-free MAC protocol, we can observe that the value of T_{AUV} does not affect the performance related to the transmission of the waypoints. Differently, for contention-based protocols, a higher monitoring traffic also affects the transmission of the waypoints, because deafness can cause packet loss.

The monitoring throughput received by the control station is presented in Fig. 8.6. For values of $T_{AUV} \geq 20$ s, the throughput is similar in all the configurations. For $T_{AUV} < 20$ s, the `ST` solution has the worst results in terms of throughput with respect to all the other configurations of the `MM` scenario. The highest throughput is achieved using the TDMA Frame-TDMA configuration or using the two configurations with the CSMA protocol combined with TDMA or TDMA Frame. However, as reported in Fig 8.7, we can observe that the CSMA-based configurations have a higher PER with respect to the TDMA Frame-TDMA configuration. The PER is computed at the application layer, i.e., it takes into account also the packets lost due to buffer overflow. In the `ST` scenario, the PER starts to increase for values of $T_{AUV} < 30$ s. This means that the network is not able to support an average packet generation time lower than 30 s. In the TDMA Frame-TDMA configuration, the network is able to support a minimum value of T_{AUV} equal to 15 s. Fig. 8.8 reports the PDD of the monitoring traffic. The `ST` configuration has the biggest PDD for all the values of $T_{AUV} > 7$ s. For

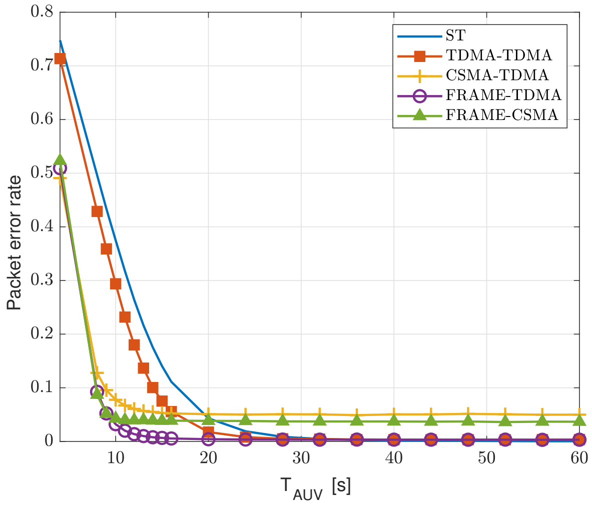

Figure 8.7: Packet error rate of monitoring packets.

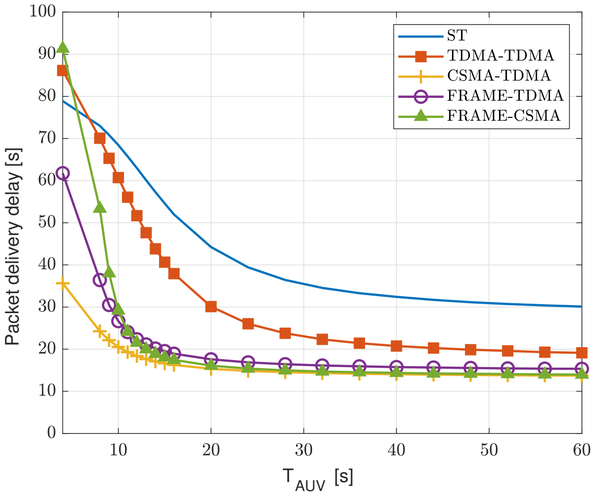

Figure 8.8: Average packet delivery delay of the monitoring traffic.

smaller values of T_{AUV} only the TDMA-TDMA and the TDMA Frame-CSMA configurations have a higher delay than the `ST`.
In general, we can observe that the TDMA Frame-TDMA configuration is the best solution in terms of monitoring packet throughput, PER and PDD. Moreover, this configuration is able to support the highest monitoring traffic without making the network unstable. The drawback of this configuration is that it experiences the highest control packet PDD.

8.5.2 Power budget

In this section we compute the overall energy consumption of the `ST` approach and the `MM` approach. The `MM` scenario is analyzed considering the TDMA Frame-TDMA configuration. In both cases we considered an average generation period for the monitoring traffic equal to $T_{AUV} = 20$ s. We supposed to use the EvoLogics S2CR 18/34 as the MF modem and the EvoLogics S2CR 7/17 as the LF modem. In particular, for the MF modem we considered a power consumption equal to $P_{MF} = 35$ W [36] and for the LF modem equal to $P_{LF} = 65$ W [30]. During the full mission the overall number of packets sent in the `ST` and `MM` scenarios is equal to $N_{ST} = 11883$ and $N_{MM} = 12093$, respectively.

In the `ST` scenario each packet needs to be transmitted $N_{tx}^{ST} = 4$ times to reach the destination. Each transmission has a duration t_{tx}^{MF} equal to

$$t_{tx}^{MF} = \frac{packet\ length}{R_{MF}} = \frac{8000}{4800} = 1.67 \text{ s.} \tag{8.2}$$

The overall amount of time each modem is involved in the transmission is equal to

$$t^{ST}_{totTx} = N_{ST} \cdot t^{MF}_{tx} = 19844.61 \text{ s}. \tag{8.3}$$

The overall energy consumed by a single node for packet transmission during the AUV mission is equal to

$$E^{ST}_{modem} = P_{MF} \cdot t^{ST}_{totTx} = 192.93 \text{ Wh}. \tag{8.4}$$

Therefore, the energy consumption of the `ST` network is given by

$$E_{ST} = E^{ST}_{modem} \cdot N^{ST}_{tx} = 771.73 \text{ Wh}. \tag{8.5}$$

In the `MM` scenario each packet is transmitted 2 times before it reaches the destination: one time with the LF modem and one time with the MF modem. The transmission time for a packet with the LF modem is equal to

$$t^{LF}_{tx} = \frac{packet\ length}{R_{LF}} = \frac{8000}{3500} = 2.29 \text{ s}. \tag{8.6}$$

Since in this scenario the number of transmitted packets is equal to N_{MM}, the overall energy consumption of the network is given by

$$E_{MM} = (t^{LF}_{tx} \cdot N_{MM})P_{LF} + (t^{MF}_{tx} \cdot N_{MM})P_{MF} = 696.36 \text{ Wh}, \tag{8.7}$$

where the first term of the sum is the overall energy consumption for the LF modem and the second term is the overall energy consumption for the MF modem.

From this analysis, we can observe that the energy consumption of the `MM` scenario is lower than in the `ST` scenario, even if the number of packets sent in the `MM` network is slightly higher than in the `ST` network.

8.6 Conclusions

In this chapter we presented a comparison of the performance of different networks employed to extend the range in which an AUV can be driven during a patrol mission. The performance of different MAC protocols employed in a multimodal and multi-hop network has been compared with the performance of a single technology multi-hop network used as benchmark. The different configurations have been simulated with the DESERT Underwater network simulator. The `MULTI_DESTINATION` module has been implemented in the network simulator to deal with the multimodal network scenario. Simulation results showed that the `ST` scenario is outperformed by some configurations of the `MM` network. Moreover, an ad hoc solution for the `MM` scenario can greatly improve the performance in terms of monitoring throughput when the network load increases, while in low traffic conditions there are no large differences between the configurations, as expected.

Notes

Part of this work has been published in [194] and [200].

Chapter 9

Other works performed during the PhD activity

This chapter presents an overview of the other research activities and the related publications I have performed during my PhD program that are not directly related to the main focus of this thesis, i.e., underwater multimodal networks.

9.1 Design and evaluation of a low-cost acoustic chamber for underwater experiments

Testing acoustic equipment before sea experiments is a necessary step, which usually requires large and expensive facilities. In this paper, published in [201], we present the design guidelines, structure and details of a small-scale, low-cost acoustic chamber for in-lab testing of underwater acoustic networks. The chamber has been assembled with the objective to be of low cost and limited size: therefore, its installation fits small university laboratories that cannot afford large testing pools. The chamber was designed to mitigate the extreme multipath which, in a small chamber, makes communications unreliable. Considering this challenge, our chamber includes a phono-absorbing coating on the walls and floor, to be optionally complemented by a panel of the same coating material, to be installed at the water surface level. After providing the details of several phono-absorbing materials to motivate our specific choice, we carry out a number of transmission experiments with EvoLogics modems, proving that our design substantially reduces the severe multipath and thereby improves the communications quality.

To this purpose, we first presented a detailed survey of phonoabsorbing materials suitable to be employed for multipath mitigation in a small-sized and low-cost high-density polyethylene (HDPE) tank for preliminary in-lab experimentation of underwater networking protocols and systems. After a balance of pros and cons, we then chose to employ neoprene rubber for its good echo reduction and internal absorption properties. Finally, we measured the performance of the coating in terms of the packet delivery ratio achieved by underwater acoustic modems placed submerged in the tank in three cases: no coating; tank walls and bottom coating; full coating, including a subsurface layer. From our experimental results, we can conclude that the neoprene rubber serves well the purpose of mitigating multipath inside the tank, and considerably increases the reliability of the acoustic links. We believe this makes our solution a good low-cost alternative to larger and more expensive tanks or pools, which would require a sizeable investment. Future work includes mitigating the echo originating at the interface between the outer walls of the HDPE tank and air.

9.2 Development of a submerged hub for monitoring the deep sea

Understanding the ever-changing oceans, biota and atmosphere is one of the great global challenges of the next several decades. The future of measuring and forecasting long-term trends and variability in coastal ecosystems, weather, acoustics, and climate lies in sustained measurements of key ocean indicators from ocean observing systems. A new era in ocean observing has begun, one of an integrated, organized approach to gathering and sharing information. The University of Haifa and the University of Padova have joined forces and developed a submerged hub on top of the Texas A&M - University of Haifa Eastern Mediterranean Observatory (THEMO). THEMO is located in the Levant Basin of the Mediterranean Sea at a depth of 125 m. The developed hub includes processing units, energy cells and interfaces to various sensors, and is designed to connect any underwater sensor to a cloud service in real time. In its first stage, the hub serves as a remotely accessed underwater acoustic modem for the aim of long-range underwater acoustic communication and to actively detect marine mammals and large predators. The hub conserves power and is suitable for long-term deployments (several months). By combining the RF communication capability of THEMO with a wired transmission from deep water to surface, the hub transfers the collected data to a shore station. This communication link is two-way and allows updating of the processing software onboard the hub from the shore. The communication between the hub and the shore station is managed to avoid bottlenecks. Moreover, the processing burden is divided between the submerged hub and a processor onboard the surface buoy.

In this paper, published in [202], we share some design details of the submerged hub, and discuss its capabilities. We then demonstrate the usage of the submerged hub, and invite the research community to use its data.

9.3 Full reconfiguration of underwater acoustic networks through low-Level physical layer access

Underwater acoustic communications experiments often involve custom implementations of schemes and protocols for the physical and data link layers. However, most commercial modems focus on providing reliable or optimized communication links, rather than on allowing low-level reconfiguration or reprogramming of modulation and coding schemes. As a result, the physical layer is typically provided as a closed, non-reprogrammable black box, accessible by the user only through a specific interface. While software-defined modems [203] would be the ultimate solution to overcome this issue, having access to the symbols transmitted by the modems using a proprietary modulation format already opens up a number of research opportunities, e.g., aimed at the cross-layer design and optimization of channel coding schemes and communication protocols.

In this work, published in [204], we take the latter approach. We consider the commercial EvoLogics modem, driven by a custom firmware version that bypasses the channel coding methods applied by the modem, and allows the user to set the transmit bit rate to any desired value within a given set. This makes it possible to evaluate different coding schemes in the presence of different bit rates. The higher flexibility does not require the user to know specialized programming languages (e.g., for FPGA and DSP programming), and still makes it possible to experiment with user-defined physical layer algorithms, such as channel coding schemes and data compression strategies. More generally, the user can force the modem to transmit any arbitrary bit stream, by turning off the PHY coding and bit rate adjustments. We tested this capability using the DESERT Underwater framework and its tool-to-modem extensions [180], in addition to a software implementation of Hamming and Reed-Solomon codes. This setting was employed to test the performance of the codes over in-water and in-air acoustic links. We also extended the test scenario to simple network and MAC protocol tests. While we conducted the tests in a laboratory tank [201], the signals propagating in this tank are subject to harsh multipath distorsion, especially if the tank walls and the water surfaces are not insulated with phono-absorbing materials. This is representative of highly reflective harbor environments, and is typically harsher than horizontal transmissions in open waters, except for the fact that it is impossible to reproduce Doppler distortion in a small tank. Our experiments demonstrate the flexibility of low-level PHY access and the potential of this setting as an intermediate step between black-box and fully software-defined modem setup. For example, unlike many other hardware and software settings, our system makes it possible to directly experiment with adaptive coding techniques, hybrid ARQ, and adaptive medium access control with tunable bit rate.

9.4 On the feasibility of video streaming through underwater acoustic links

While live video streaming is already mature through media such as coaxial cables, optical fibers and radio links, real-time live video streaming through underwater acoustic communication is still in its infancy. The underdevelopment of underwater live streaming is due to both the unstable nature and the long propagation delay of the acoustic channel. The former poses several obstacles to reaching the needed bit rate capabilities, while the latter causes a non-negligible video latency proportional to the distance between transmitter and receiver. Despite these obstacles, a lot of research on advanced video codecs is conducted to reduce the required bit rates of a video stream. In addition, modem manufactures recently developed short range high rate acoustic modems. Among the new video codecs released in the last years, H.265 [205] and VP9 [206] are the mostly widely used and aim to replace H.264 [207] and VP8 [208], respectively.

This work, published in [209], discusses the feasibility of underwater acoustic live video streaming, in light of the capabilities offered by the EvoLogics S2CM HS commercial off the shelf acoustic modems and these new standard video codecs (in addition, the H264 video codec has been considered as a benchmark). With each codec, we streamed the video with different settings, in order to define which configuration can be used to perform video streaming over an underwater acoustic channel. The codec selection was constrained by the acoustic modem's bit rate, however, other objective parameters have been analyzed. Specifically, for each video configuration, we observed the peak signal to noise ratio, the video quality metric and the similarity index measure [210]. During a tank test, we employed the VP9 video codec to stream a quasi-real-time low quality video successfully.

Future tests will regard the further inspection of VP9 and H.265, testing them with different codec implementations and low latency configurations, to reduce the reception delay. In addition, the new standard AOMedia Video 1 (AV1) seems very promising [205], and it will be interesting to evaluate it in this scenario as soon as it is released. Performing the same test in the open sea or in a larger tank would help to obtain a better acoustic channel, and possibly stream the video at the maximum bit rate allowed by the modem.

9.5 Implementation of AUV and ship noise for link quality evaluation in the DESERT Underwater

The underwater acoustic channel exhibits many challenges for communications. Since the underwater environment is becoming crowded with both static and mobile users, additional noise is produced in the channel by the physical components of the nodes. In particular, the noise generated by vessels causes interference to the packets transmitted by the acoustic modems, with a consequent increase in packet loss.

This work, published in [211], proposes methods for the simulation of the additive noise introduced by vessels traveling near or inside the network area. Specifically, the simulations include the presence of an AUV and a cargo ship, distinguished by their own noise patterns, in an underwater acoustic sensor network. The noise was introduced through a lookup table, where each entry corresponds to a noise level for a specific carrier frequency for the AUV crafts, and via mathematical models for ship vessels. The ship models were obtained from the research of the AQUO Project [212]; instead, for characterizing the AUVs, we used Zimmerman's data trials [213]. The results revealed that the lower frequencies react worse than the mid frequencies to the noise caused by a cargo ship, but better to the noise caused by an AUV. Further works will inspect how a multimodal network can be employed in this scenario to overcome the noise issue, by switching between LF and MF according to the surrounding noise sources. Other interesting items for future work include the enhancement of the noise representation as a set of interfering packets by adapting their length to the mobility pattern of the nodes, as well as the addition to the noise model of the mechanical noise which is generated by collisions or banging of metal parts, such as the banging between chainrings around the acoustic modem. All simulations have been performed with the DESERT Underwater framework.

9.6 On the feasibility of an anti-grounding service with autonomous surface vessels

Grounding of ships is as of today one of the most common causes of maritime accidents. An effective antigrounding service, where updated bathymetry data is sent in real time to a ship, can improve maritime and human safety. The bathymetry data is collected by an autonomous surface vessel equipped with a multi-beam sonar while the ship is approaching the port. This data is then conveyed immediately to the ship, by employing a wireless communication link.

In this work, published in [214], a study on the enabling technologies for an effective antigrounding service is provided, with special focus on the wireless communication devices to employ for the real-time bathymetry data transmission. The results proved the feasibility of an anti-grounding service, where an ASV, traveling ahead of a ship approaching a port area, maps the seabed with the EM 2040 MKII Kongsberg multi-beam echosounder [215]. The feasibility has been proved by simulating the RF channel behavior in a marine environment, by employing a two to three-rays path-loss model [216]. Our preliminary study reveals that the transmission of the complete real-time bathymetry data can be performed with an LTE [217] communication link, when the ship is up to 25 km from shore. Wimax and WiFi instead are good options for a direct link scenario. Satellite communication can also support the service without coverage limit, but at a very high price per MB transmitted. Finally, although a LoRa backup channel cannot be employed to transmit the full bathymetry data, it can effectively transmit status and alarm messages whenever under keel clearance is not assured. In this case, we showed that in order to compensate for the delay in the propagation of the alarm signal caused by the LoRa [218] network, an additional guard distance should be allowed between the ASV and the ship.

9.7 Underwater acoustic sensors data collection in the Robotic Vessels as-a-Service project

The Robotic Vessels as-a-Service (RoboVaaS) [219] project aims to provide innovative services for the shipping activities and near-shore maritime operations such as ship-hull and quay walls inspection, anti-grounding service and environmental data collection. To this end, both underwater and above water communications will be employed.

In this work, published in [220] and in [221], we focus on the study of the underwater environmental data collection service, performed by one or more autonomous vehicles equipped with an acoustic modem and moving along submerged acoustic sensor nodes. This study analyzes the feasibility of such service in the scenario of the port of Hamburg, characterized by shallow turbid fresh water, where the RoboVaaS concept will be demonstrated as part of the project. To this end, an underwater acoustic network composed by both static and moving nodes has been designed and simulated with the DESERT Underwater Network Simulation Framework and the World Ocean Simulation System (WOSS) [222].

In this work we presented an enhancement of the UW-POLLING MAC protocol [223]. Specifically, we introduced the capability of a mobile node to collect data from sensor nodes and then forward them to a sink node directly connected to shore with a radio link. In this protocol, a moving node first probes the channel in order to identify which of its neighbors that need to transmit data are in range, and then polls each of them in order according to a fair policy. Finally, it forwards the collected data to the sink node. First, we analyzed how the maximum backoff time affects the network performance, and then we simulated the protocols in the scenario of the port of Hamburg. To this purpose we performed the simulations introducing the Hamburg port bathymetry in the WOSS framework, to employ the Bellhop ray-tracer [224]. In addition, we mapped the performance of the low cost smartPORT acoustic modem (AHOI) [225] (developed by the Technical University of Hamburg) in the DESERT Underwater simulator, in order to prove the effectiveness of the UW-POLLING protocol also when employing a low cost device. The AHOI modem will be employed for the final demonstration of the RoboVaas project. We analyzed the maximum offered traffic that can be supported employing the UW-POLLING protocol in this scenario. Future works will include the possibility to use multiple sink nodes at the same time, to automatically adapt the backoff time according to the number of nodes in the AUV range and to enhance the policy used to POLL the nodes in order to improve the fairness also with a large offered traffic.

9.8 Jamming the underwater: a game-theoretic analysis of energy-depleting jamming attacks

Underwater sensor networks can be employed in both military and environmental remote coastal monitoring applications, such as enemy targeting and identification, and tsunami prevention. Jamming can be a serious issue in these networks, typically composed by battery-powered nodes, as an attacker can not only disrupt packet delivery, but also reduce the lifetime of energy-constrained nodes.

In this work, accepted in [226], we consider a malicious jammer with the dual objective of preventing communication and depleting the battery of a targeted underwater sensor node. The jammed node may use packet-level coding as the countermeasure against the attack and to increase its chances of correctly delivering its information to the legitimate receiver. We model this scenario as a multistage game, derive optimal long-term strategies for both sides, and evaluate how the position of the jammer affects the communication performance of the legitimate network. The legitimate transmitter leverages channel coding to counteract the jamming by adding redundancy. We model the attack by means of game theory and derive the optimal strategies assuming that the jammer and the legitimate transmitter are two rational players with full knowledge about the adversary, playing a zero-sum game. We studied the impact of the jamming attack on the lifetime and the packet delivery ratio of the transmitter, and in particular the role played by the length of the time horizon used to calculate the expected payoffs, the distance of the jammer from the receiver, and the importance of the energy consumption in the payoff functions. The simulation results highlight three regions where the jamming attack is almost always successful, depends on the strategies of the two players, or is ineffective, respectively. Although the analytical solution is based on the simplifying assumption of complete information available at the two players, it still sheds light on the dynamics in this scenario. It may also serve as a guideline for more realistic scenarios, which we plan to investigate as future work, possibly including a more realistic characterization of the acoustic channel, based on real field measurements, and relaxing the full information assumption, i.e., considering a Bayesian incomplete information game.

Chapter 10

Conclusions

This thesis presented the concept of multimodal underwater networks, where different communication technologies are combined to increase the system performance. After reviewing the state of the art of all underwater communication technologies in Chapter 1, underwater acoustic and optical modems have been selected as the best performing and most mature technologies available off the shelf. Specifically, acoustics can be employed for long range long latency communications, while optical modems can provide short range broadband communication links.

The acoustic channel is characterized by a long propagation delay that makes carrier-sense MAC layers ineffective. MAC layers, indeed, require to be specifically designed for underwater acoustic networks: in Chapter 2, for instance, the near-far effect of the acoustic channel has been exploited to design a spatial reuse time-division multiple access scheduling protocol, that outperforms the classical TDMA, thanks to a better use of the channel. This protocol has been evaluated both via simulations and in a lake test.

The optical channel, instead, is strongly affected by the alignment between the transmitter and the receiver, the turbidity of the water and noise caused by the sunlight. While existing models have been employed to simulate the acoustic channel with the DESERT Underwater framework, a dedicated module for simulating the optical channel has been implemented as part of that framework. This model, presented in Chapter 3, includes the possibility to map into the simulator both modems' beam patterns, and the the water properties that affect the optical channel in the form of lookup tables. These lookup tables can be either generated through specific simulators (i.e., Hydrolight [227]), or obtained through real field measurements. The measurements database presented in this thesis permits to simulate the optical channel in a wide set of specific scenarios.

The existence of the statistical relationship between the optical and the acoustic channel has been proved in Chapter 4, by training a support vector machine learning model with an extended dataset obtained during a field measurements campaign. These measurements have been retrieved during the Alomex'15 NATO cruise. Our results indicate a clear relation between the acoustic properties and the quality of the optical link.

Optimal multimodal routing and optimal multimodal scheduling protocols have been presented in Chapter 5 and Chapter 6, respectively. All protocols have been simulated and evaluated with dedicated field experiments. During these experiments, three different types of acoustic modems have been employed: low-frequency, mid-frequency, and high-frequency acoustic modems. The results proved that, in all cases, employing an algorithm that optimally chooses which subset of the available technologies to employ time by time, is better than simply employing all the available technologies simultaneously.

In Chapter 7, a multimodal remote control for underwater vehicles has been presented and analyzed as one of the applications that can be enabled by underwater multimodal networks. In this system, a multimodal protocol is used not only to switch between communication technology, but also to change the vehicle working mode and the related quality of service, according to the best performing channels in range. In Chapter 8, a pure-acoustic multihop extension of the remote control is discussed. The latter leverages both the near-far and the pipeline effects of the acoustic channel in order to extend the maximum distance between the control station and the vehicle. It proves, via simulations, that a multimodal acoustic network can provide significant benefits also in this case.

Finally, in Chapter 9, we briefly presented all the topics addressed during the PhD activity that are not directly connected to underwater multimodal networks, but still related to communications in maritime environment.

In the future, we aim to prove the effectiveness of the multimodal remote control system for underwater vehicles also with real field evaluations. Other future works will address the remaining aspects of multimodal networks, such as how combining optical and acoustic communications can significantly improve the network security of underwater assets. Indeed, perfect secrecy can be ensured by deploying through a directional laser-based optical link a long key to be used to cipher the data sent via acoustics with one-time pad, an information-theoretically secure encryption technique that cannot be cracked. Specifically, this technique requires the use of a one-time pre-shared key the same size as, or longer than, the message being sent. With an optical link a key long few megabytes can be exchanged between a sensor node and an AUV in few seconds, as soon as they are in the range of the optical modem. After the key deployment, thanks to the fact that acoustic transmissions are hundreds of times slower than optical transmissions, the AUV and the sensor node can exchange secure data between each other for the whole duration of the AUV mission, by using an acoustic link.

Acknowledgments

The datasets used in Chapters 3 and 4 were acquired with CTDs, projectors and hydrophone instruments from the anti-submarine warfare (ASW) program of CMRE. We would like to thank the captain and the crew of NRV Alliance for their kind assistance during data collection operations at sea. The author is also grateful to the EvoLogics team for their support during the Werbellinsee lake experiment. Finally, the author would like to thank Dr. Paolo Casari, Dr. Roee Diamant, Prof. Michele Zorzi, and all components of the Signet Underwater group for their support, advices and help on various technical issues examined during this last three years.

Bibliography

[1] "BlueComm - What's what?" Last time accessed: Sep. 2019. [Online]. Available: https://www.sonardyne.com/bluecomm-whats-what/

[2] P. Leon, F. Roland, L. Brignone, J. Opderbecke, J. Greer, M. Khalighi, T. Hamza, S. Bourennane, and M. Bigand, "A New Underwater Optical Modem based on Highly Sensitive Silicon Photomultipliers," in *Proc. MTS/IEEE OCEANS*, Aberdeen, UK, Oct. 2017.

[3] M. Doniec, A. Xu, and D. Rus, "Robust real-time underwater digital video streaming using optical communication," in *Proc. ICRA*, Karlsruhe, Germany, May 2013.

[4] H. S. Dol, P. Casari, T. van der Zwan, and R. Otnes, "Software-defined underwater acoustic modems: Historical review and the NILUS approach," *IEEE J. Ocean. Eng.*, vol. 42, no. 3, pp. 722–737, Jul. 2017.

[5] M. Chitre, S. Shahabudeen, and M. Stojanovic, "Underwater acoustic communications and networking: Recent advances and future challenges," *Marine Tech. Soc. Journal*, vol. 42, no. 1, pp. 103–116, spring 2008.

[6] J. Heidemann, M. Stojanovic, and M. Zorzi, "Underwater sensor networks: applications, advances and challenges," *Phil. Trans. of the Royal Soc. of London A*, vol. 370, no. 1958, pp. 158–175, 2011.

[7] T. Melodia, H. Kulhandjian, L.-C. Kuo, and E. Demirors, "Advances in underwater acoustic networking," in *Mobile Ad Hoc Networking.* Wiley, 2013, pp. 804–852.

[8] K. McCoy, "JANUS: from primitive signal to orthodox networks," in *Proc. of IACM UAM*, Nafplion, Greece, Jun. 2009.

[9] J. Potter, J. Alves, D. Green, G. Zappa, I. Nissen, and K. McCoy, "The JANUS underwater communications standard," in *Proc. UComms*, Sestri Levante, Italy, Sep. 2014.

[10] A. Nordrum, "A language for the internet of underwater things," *IEEE Spectrum*, vol. 54, no. 9, pp. 9–10, Sep. 2017.

[11] "AQUAmodem Op1 Optical Modem page," Accessed: Sep. 2019. [Online]. Available: http://www.aquatecgroup.com/aquamodem/aquamodem-op1

[12] F. Campagnaro, M. Calore, P. Casari, V. S. Calzado, G. Cupertino, C. Moriconi, and M. Zorzi, "Measurement-based simulation of underwater optical networks," in *Proc. MTS/IEEE Oceans*, Aberdeen, Scotland, Jun. 2017.

[13] Y. Ito, S. Haruyama, and M. Nakagawa, "Short-range underwater wireless communication using visible light LEDs," *WSEAS Trans. Commun.*, vol. 9, pp. 525–552, Sep. 2010.

[14] P. Gois, N. Sreekantaswamy, N. Basavaraju, M. Rufino, L. S. J. Botelho, J. Gomes, and A. Pascoal, "Development and validation of Blue Ray, an optical modem for the MEDUSA class AUVs," in *Proc. Ucomms*, Lerici, Italy, Sep. 2016.

[15] J. W. Bales and C. Chryssostomidis, "High-bandwith, low power, short range optical communication underwater," in *Int. Symp. Unmanned, Untethered Submersible Tech.*, Boston, MA, Sep. 1995.

[16] "About Penguin Automated Systems," accessed: Sep. 2019. [Online]. Available: http://www.penguinasi.com/

[17] "Sonardyne BlueComm Optical Modem ," Accessed: Sep. 2019. [Online]. Available: http://www.sonardyne.com/products/all-products/instruments/1148-bluecomm-underwater-optical-modem.html

[18] F. Hanson and S. Radic, "High bandwidth underwater optical communication," *Applied Optics*, vol. 47, no. 2, pp. 277–283, Jan. 2008.

[19] A. Caiti, E. Ciaramella, G. Conte, G. Cossu, D. Costa, S. Grechi, R. Nuti, D. Scaradozzi, and A. Sturniolo, "Optocomm: introducing a new optical underwater wireless communication modem," in *Proc. Ucomms*, Lerici, Italy, Sep. 2016.

[20] G. Ardelt, M. Mackenberg, J. Markmann, T. Esemann, and H. Hellbruck, "A flexible and modular platform for development of short-range underwater communication," in *Proc. ACM WUWNet*, Shanghai, Oct. 2016.

[21] S. I. Inacio, M. R. Pereira, H. M. Santos, L. M. Pessoa, F. B. Teixeira, M. J. Lopes, O. Aboderin, and H. M. Salgado, "Dipole antenna for underwater radio communications," in *Proc. UComms*, Lerici, Italy, Aug. 2016.

[22] "Wireless For Subsea Seatooth," accessed: Feb. 2016. [Online]. Available: http://www.wfs-tech.com/index.php/products/seatooth/

[23] N. Ahmed, J. Hoyt, A. Radchenko, D. Pommerenke, and Y. R. Zheng, "A multi-coil magneto-inductive transceiver for low-cost wireless sensor networks," in *Proc. UComms*, Sestri Levante, Italy, Sep. 2014.

[24] J.-F. Bousquet, A. A. Dobbin, and Y. Wang, "A compact low-power underwater magneto-inductive modem," in *Proc. ACM WUWNet*, Shanghai, Oct. 2016.

[25] I. Vasilescu, K. Kotay, D. Rus, P. Corke, and M. Dunbabin, "Data collection, storage and retrieval with an underwater optical and acoustical sensor network," in *Proc. ACM Sensys*, San Diego, CA, Nov. 2005.

[26] M. O'Rourke, E. Basha, and C. Detweiler, "Multi-modal communications in underwater sensor networks using depth adjustment," in *Proc. ACM WUWNet*, Los Angeles, CA, Nov. 2012.

[27] P. A. Forero, S. Lapic, C. Wakayama, and M. Zorzi, "Rollout algorithms for data storage- and energy-aware data retrieval using autonomous underwater vehicles," in *Proc. ACM WUWNet*, Rome, Italy, Nov. 2014.

[28] F. Campagnaro, F. Favaro, P. Casari, and M. Zorzi, "On the feasibility of fully wireless remote control for underwater vehicles," in *Proc. Asilomar Conf. SS&C*, Pacific Grove, CA, Nov. 2014.

[29] "Teledyne-benthos acoustic modems," accessed: Sep. 2019. [Online]. Available: http://www.teledynemarine.com/acoustic-modems/

[30] "Evologics S2C R 7/17 modem," accessed: Sep. 2019. [Online]. Available: http://www.evologics.de/en/products/acoustics/s2cr_7_17.html

[31] "Aquatec Underwater Communication," accessed: Sep. 2019. [Online]. Available: http://www.aquatecgroup.com/9-offshore-energy/12-communication

[32] "MATS 3G multi-modulation acoustic telemetry system," accessed: Sep. 2019. [Online]. Available: http://www.sercel.com/products/Pages/mats3g.aspx

[33] "Develogic Subsea Systems," Last time accessed: Sep. 2019. [Online]. Available: http://www.develogic.de/

[34] L. Freitag, K. Ball, J. Partan, P. Koski, and S. Singh, “Long range acoustic communications and navigation in the Arctic,” in *Proc. MTS/IEEE OCEANS’15*, Washington DC, US, Oct. 2015.

[35] L. Freitag, M. Grund, S. Singh, J. Partan, P. Koski, and K. Ball, “The WHOI Micro-Modem: An Acoustic Communications and Navigation System for Multiple Platforms,” http://www.whoi.edu, 2005.

[36] “S2CR 18/34 Acoustic Modem,” Last time accessed: Sep. 2019. [Online]. Available: http://www.evologics.de/en/products/acoustics/s2cr_18_34.html/

[37] “Subnero,” accessed: Sep. 2019. [Online]. Available: https://subnero.com/

[38] P.-P. Beaujean, J. Spruance, E. A. Carlson, and D. Kriel, “HERMES - A high-speed acoustic modem for real-time transmission of uncompressed image and status transmission in port environment and very shallow water,” in *Proc. MTS/IEEE OCEANS*, Québec City, Canada, Sep. 2008.

[39] C. Pelekanakis, M. Stojanovic, and L. Freitag, “High rate acoustic link for underwater video transmission,” in *Proceedings MTS/IEEE OCEANS.* IEEE, 2003.

[40] E. Demirors, B. G. Shankar, G. E. Santagati, and T. Melodia, “Seanet: A software-defined acoustic networking framework for reconfigurable underwater networking,” in *Proc. ACM WUWNet*, Washington DC, US, Oct. 2015.

[41] “Underwater Wireless Acoustic Video Communications Channel,” accessed: Sep. 2019. [Online]. Available: http://www.baltrobotics.com/index.php/products-services-mnu/item/269-underwater-wireless-acoustic-video-communications-channel

[42] “Evologics S2C M HS modem,” accessed: Sep. 2019. [Online]. Available: http://www.evologics.de/en/products/acoustics/s2cm_hs.html

[43] AQUATEC group, “AQUAmodem Op1 Optical Modem,” Accessed: Sep. 2019. [Online]. Available: http://www.aquatecgroup.com/images/datasheets/aquamodemop1opticalmodem.pdf

[44] “LinkQuest Underwater Acoustic Modems,” accessed: Sep. 2019. [Online]. Available: http://www.link-quest.com/html/models1.htm

[45] M.-A. Khalighi, T. Hamza, S. Bourennane, P. Léon, and J. Opderbecke, “Underwater Wireless Optical Communications Using Silicon Photo-Multipliers,” *IEEE Photonics Journal*, vol. 9, no. 4, pp. 1–14, Aug. 2017.

[46] “WFS Technologies,” Last accessed: Sep. 2019. [Online]. Available: http://www.wfs-tech.com/

[47] B. W. Hobson, R. S. McEwen, J. Erickson, T. Hoover, L. McBride, F. Shane, and J. G. Bellingham, “The development and ocean testing of an auv docking station for a 21” auv,” in *Proc. IEEE/OES Oceans*, Vancouver, Canada., Sep. 2007.

[48] G. Baiden and Y. Bissiri, “High bandwidth optical networking for underwater untethered telerobotic operation,” in *Proc. MTS/IEEE Oceans*, Vancouver, Canada, Sep. 2007.

[49] C. Moriconi, G. Cupertino, S. Betti, and M. Tabacchiera, “Hybrid acoustic/optic communications in underwater swarms,” in *Proc. MTS/IEEE OCEANS*, Genova, Italy, May 2015.

[50] M. Stojanovic and J. Preisig, “Underwater acoustic communication channels: Propagation models and statistical characterization,” *”IEEE” communications magazine*, vol. 47, no. 1, pp. 84–89, 2009.

[51] P. Casari and M. Zorzi, “Protocol design issues in underwater acoustic networks,” *Elsevier Computer Communications*, vol. 34, no. 17, pp. 2013–2025, Nov. 2011.

[52] J. G. Proakis, *Digital Communications*, 3rd ed. McGraw-Hill, 1995.

[53] K. G. Kebkal, O. Kebkal, and R. Petroccia, "Assessment of underwater acoustic channel during payload data exchange with hydro-acoustic modems of the S2C series," in *Proc. MTS/IEEE OCEANS*, Genova, Italy, may 2015.

[54] R. Diamant, A. Feuer, and L. Lampe, "Choosing the right signal: Doppler shift estimation for underwater acoustic signals," in *ACM Conference on UnderWater Networks and Systems (WUWNet)*, Los Angeles, USA, Nov. 2012.

[55] B. Katsnelson, V. Petnikov, and J. Lynch, *Fundamentals of shallow water acoustics.* Springer Science & Business Media, 2012, ch. 3, 4.

[56] M. Ainslie, P. Dahl, C. de Jong, and R. Laws, "Practical spreading laws: The snakes and ladders of shallow water acoustics," in *Proc. UA2014 - 2nd International Conference and Exhibition on Underwater Acoustics*, Rhodes, Greece, Jun. 2014, pp. 879–886.

[57] R. Urick, *Sound propagation in the sea.* Peninsula Publishing Newport Beach, 1982.

[58] ——, *Principles of Underwater Sound.* New York: McGraw-Hill, 1983.

[59] M. Legg, A. Zaknich, A. Duncan, and M. Greening, "Analysis of impulsive biological noise due to snapping shrimp as a point process in time," in *IEEE OCEANS*, Aberdeen, Scotland, United Kingdom, june 2007.

[60] R. Spinrad, K. Carder, and M. J. Perry, *Ocean Optics. Oxford Monographs on Geology and Geophysics.* Oxford University Press, USA, 1994.

[61] C. Mobley, *Light and water: radiative transfer in natural waters.* Academic Press, 1994.

[62] R. Kastner, A. Lin, C. Schurgers, J. Jaffe, P. Franks, and B. S. Stewart, "Sensor platforms for multimodal underwater monitoring," in *Proc. IGCC*, San Jose, CA, Jun. 2012.

[63] B. Benson, Y. Li, B. Faunce, K. Domond, D. Kimball, C. Schurgers, and R. Kastner, "Design of a low-cost underwater acoustic modem," *IEEE Embedded Syst. Lett.*, vol. 2, no. 3, pp. 58–61, Sep. 2010.

[64] A. Tennenbaum, M. Dyakiw, J. H. Cui, and Z. Peng, "Application of low cost optical communication systems to underwater acoustic networks," in *Proc. IEEE MASS*, Philadelphia, PA, Oct. 2014.

[65] R. Kastner, A. Lin, C. Schurgers, J. Jaffe, P. Franks, and B. S. Stewart, "MURAO: A multi-level routing protocol for acoustic-optical hybrid underwater wireless sensor networks," in *Proc. IEEE SECON*, Seoul, South Korea, Jun. 2012.

[66] C. J. C. H. Watkins and P. Dayan, "Q-learning," *Machine Learning*, vol. 8, no. 3, pp. 279–292, May 1992.

[67] F. Campagnaro, P. Casari, M. Zorzi, and R. Diamant, "Optimal transmission scheduling in small multimodal underwater networks," *IEEE Wireless Communications Letters*, vol. 8, no. 2, pp. 368–371, Oct. 2018.

[68] R. Diamant, P. Casari, F. Campagnaro, and M. Zorzi, "Routing in multi-modal underwater networks: a throughput-optimal approach," in *Proc. WCNEE (IEEE INFOCOM wkshp.)*, Atlanta, GA, May 2017.

[69] S. Basagni, V. Di Valerio, P. Gjanci, and C. Petrioli, "Finding MARLIN: Exploiting multi-modal communications for reliable and low-latency underwater networking," in *Proc. IEEE INFOCOM*, Atlanta, GA, May 2017.

[70] S. Han, R. Chen, Y. Noh, and M. Gerla, "Real-time video streaming from mobile underwater sensors," in *Proc. ACM WUWNet*, Rome, Italy, Nov. 2014.

[71] S. Basagni, L. Bölöni, P. Gjanci, C. Petrioli, C. A. Phillips, and D. Turgut, "Maximizing the value of sensed information in underwater wireless sensor networks via an autonomous underwater vehicle," in *Proc. IEEE INFOCOM*, Toronto, Canada, Apr. 2014, pp. 988–996.

[72] F. Campagnaro *et al.*, "Simulation of multimodal optical and acoustic communications in underwater networks," in *Proc. MTS/IEEE OCEANS*, Genova, Italy, May 2015.

[73] F. Campagnaro, F. Guerra, R. Diamant, P. Casari, and M. Zorzi, "Implementation of a multimodal acoustic-optic underwater network protocol stack," in *Proc. MTS/IEEE OCEANS*, Shanghai, China, Apr. 2016.

[74] P. Casari, C. Tapparello, F. Guerra, F. Favaro, I. Calabrese, G. Toso, S. Azad, R. Masiero, and M. Zorzi, "Open-source suites for the underwater networking community: WOSS and DESERT Underwater," *IEEE Network, special issue on "Open Source for Networking: Development and Experimentation"*, vol. 28, no. 5, pp. 38–46, Sep. 2014.

[75] R. Petroccia, G. Cario, M. Lupia, V. Djapic, and C. Petrioli, "First in-field experiments with a bilingual underwater acoustic modem supporting the JANUS standard," in *Proc. MTS/IEEE OCEANS*, Genova, Italy, May 2015.

[76] M. Radi, B. Dezfouli, K. A. Bakar, and M. Lee, "Multipath routing in wireless sensor networks: Survey and research challenges," *MDPI Sensors*, vol. 12, no. 1, pp. 650–685, Jan. 2012. [Online]. Available: http://www.mdpi.com/1424-8220/12/1/650

[77] P. Kyasanur and N. H. Vaidya, "Routing and interface assignment in multi-channel multi-interface wireless networks," in *Proc. IEEE WCNC*, New Orleans, LA, Mar. 2005.

[78] M. X. Gong and S. F. Midkiff, "Distributed channel assignment protocols: a cross-layer approach," in *Proc. IEEE WCNC*, New Orleans, LA, Mar. 2005.

[79] A. Raniwala and T. Chiueh, "Architecture and algorithms for an IEEE 802.11-based multi-channel wireless mesh network," in *Proc. IEEE INFOCOM*, Miami, FL, Mar. 2005.

[80] R. Draves, J. Padhye, and B. Zill, "Routing in multi-radio, multi-hop wireless mesh networks," in *Proc. ACM MobiCom*, Philadelphia, PA, Sep. 2004.

[81] C. E. Perkins and E. M. Royer, "Ad-hoc on-demand distance vector routing," in *Proc. IEEE WMCSA*, New Orleans, LA, 1999.

[82] C. Pan, B. Liu, H. Zhou, and L. Gui, "Multi-path routing for video streaming in multi-radio multi-channel wireless mesh networks," in *Proc. IEEE ICC*, Kuala Lumpur, Malaysia, May 2016.

[83] F. Campagnaro, R. Francescon, P. Casari, R. Diamant, and M. Zorzi, "Multimodal underwater networks: Recent advances and a look ahead," in *Proc. ACM WUWNet*, Halifax, Canada, Nov. 2017.

[84] J. Heidemann, M. Stojanovic, and M. Zorzi, "Underwater sensor networks: applications, advances and challenges," *Philosophical Transactions of the Royal Society A*, vol. 370, no. 1958, pp. 158–175, 2012.

[85] C. Fullmer and J.-J. Garcia-Luna-Aceves, "Solutions to hidden terminal problems in wireless networks," in *Proc. ACM SIGCOMM*, Cannes, France, Sep. 1997.

[86] N. Chirdchoo, W.-S. Soh, and K. Chua, "RIPT: A receiver-initiated reservation-based protocol for underwater acoustic networks," *IEEE J. Sel. Areas Commun.*, vol. 26, no. 9, pp. 1744–1753, Dec. 2008.

[87] Y. Noh, U. Lee, S. Han, P. Wang, D. Torres, J. Kim, and M. Gerla, "DOTS: A propagation delay-aware opportunistic MAC protocol for mobile underwater networks," *IEEE Trans. Mobile Comput.*, vol. 13, no. 4, pp. 766–782, Apr. 2014.

[88] R. Diamant, G. Shirazi, and L. Lampe, “Robust spatial reuse scheduling in underwater acoustic communication networks,” *IEEE J. Ocean. Eng.*, vol. 39, no. 1, pp. 32–46, Jan. 2014.

[89] D. Pompili, T. Melodia, and I. F. Akyildiz, “A CDMA-based medium access control for underwater acoustic sensor networks,” *IEEE Trans. Wireless Commun.*, vol. 8, no. 4, pp. 1899–1909, Apr. 2009.

[90] M. Zuba, Z. Shi, Z. Peng, J.-H. Cui, and S. Zhou, “Vulnerabilities of underwater acoustic networks to denial-of-service jamming attacks,” *Wiley Security and Communication Networks*, vol. 8, no. 16, pp. 2635–2645, Nov. 2015.

[91] J. McGee, J. Catipovic, and P. Swaszek, “Leveraging spatial diversity to mitigate partial band interference in undersea networks through waveform reconstruction,” in *Proc. MTS/IEEE OCEANS*, St.John’s, NL, Canada, Sep. 2014.

[92] P. Pandey, M. Hajimirsadeghi, and D. Pompili, “Region of feasibility of interference alignment in underwater sensor networks,” *IEEE J. Ocean. Eng.*, vol. 39, no. 1, pp. 189–202, Jan. 2014.

[93] R. Diamant, P. Casari, F. Campagnaro, and M. Zorzi, “A handshake-based protocol exploiting the near-far effect in underwater acoustic networks,” *IEEE Wireless Comm. Lett.*, vol. 5, no. 3, pp. 308–311, June 2016.

[94] M. K. Park and V. Rodoplu, “UWAN-MAC: an energy-efficient MAC protocol for underwater acoustic wireless sensor networks,” *IEEE J. Ocean. Eng.*, vol. 32, pp. 710–720, Jul. 2007.

[95] Y. Zhong, J. Huang, and J. Han, “A TDMA MAC protocol for underwater acoustic sensor networks,” in *Proc. IEEE YC-ICT*, Beijing, China, Sep. 2009.

[96] P. Casari, F. E. Lapiccirella, and M. Zorzi, “A detailed simulation study of the UWAN-MAC protocol for underwater acoustic networks,” in *Proc. MTS/IEEE Oceans*, Vancouver, Canada, 2007.

[97] W. van Kleunen, N. Meratnia, and P. J. Havinga, “Simplified scheduling for underwater acoustic networks,” *Journal of Networks*, vol. 8, no. 1, pp. 4–14, Jan. 2013.

[98] C. Yun, A.-R. Cho, S.-G. Kim, J.-W. Park, and Y.-K. Lim, “A hierarchical time division multiple access medium access control protocol for clustered underwater acoustic networks,” *Journal of Information and Communication Convergence Engineering*, vol. 3, no. 3, pp. 153–166, Sep. 2013.

[99] Z. Li, Z. Guo, H. Qu, F. Hong, P. Chen, and M. Yang, “UD-TDMA: A distributed TDMA protocol for underwater acoustic sensor network,” in *Proc. IEEE MASS*, Macau, China, Oct. 2009.

[100] L. Hong, F. Hong, Z. Guo, and Z. Li, “ECS: Efficient communication scheduling for underwater sensor networks,” *MDPI Sensors*, vol. 3, no. 3, pp. 2920–2938, Mar. 2011.

[101] P.-H. Huang, Y. Chen, B. Krishnamachari, and A. Kumar, “Link scheduling in a single broadcast domain underwater networks,” in *Proc. IEEE SUTC*, Newport Beach, CA, Jun. 2010.

[102] D. Marinakis, K. Wu, N. Ye, and S. Whitesides, “Network optimization for lightweight stochastic scheduling in underwater sensor networks,” *IEEE Trans. Wireless Commun.*, vol. 11, no. 8, pp. 2786–2795, Aug. 2012.

[103] K. B. Kredo II and P. Mohapatra, “A hybrid medium access control protocol for underwater wireless networks,” in *Proc. ACM WUWNet*, Montreal, Quebec, Canada, Sep. 2007.

[104] L. Badia *et al.*, "An optimization framework for joint sensor deployment, link scheduling and routing in underwater sensor networks," in *Proc. of ACM WUWNet*, Los Angeles, CA, Sep. 2006.

[105] K. Kredo, P. Djukic, and P. Mohapatra, "STUMP: Exploiting position diversity in the staggered TDMA underwater MAC protocol," in *Proc. IEEE INFOCOM*, Rio de Janeiro, Brazil, Apr. 2009.

[106] K. Kredo and P. Mohapatra, "Distributed scheduling and routing in underwater wireless networks," in *Proc. IEEE GLOBECOM*, Miami, FL, Dec. 2010.

[107] C.-C. Hsu, K.-F. Lai, C.-F. Chou, and K. Ching-Ju Lin, "ST-MAC: Spatial-temporal MAC scheduling for underwater sensor networks," in *Proc. IEEE INFOCOM*, Rio de Janeiro, Brazil, Apr. 2009.

[108] Y. Zhu, S. N. Le, Z. Peng, and J.-H. Cui, "DOS: Distributed on-demand scheduling for high performance MAC in underwater acoustic networks," UCONN CSE, Tech. Rep. UbiNet-TR13-07, Jul. 2013.

[109] J. Ma and W. Lou, "Interference-aware spatio-temporal link scheduling for long delay underwater sensor networks," in *Proc. IEEE SECON*, Salt Lake City, UT, Jun. 2011.

[110] L. Hong, F. Hong, B. Yang, and Z. Guo, "ROSS: Receiver oriented sleep scheduling for underwater sensor networks," in *Proc. ACM WUWNet*, Kaohsiung, Taiwan, Nov. 2013.

[111] Z. Wu, C. Tian, H. Jiang, and W. Liu, "Minimum-latency aggregation scheduling in underwater wireless sensor networks," in *Proc. IEEE ICC*, Kyoto, Japan, Jun. 2011.

[112] A. Shashaj, R. Petroccia, and C. Petrioli, "Energy efficient interference-aware routing and scheduling in underwater sensor networks," in *Proc. MTS/IEEE OCEANS*, St. John's, Canada, Sep. 2014.

[113] M. Chitre, M. Motani, and S. Shahabudeen, "Throughput of networks with large propagation delays," *IEEE J. Ocean. Eng.*, vol. 37, no. 4, pp. 645–658, Oct. 2012.

[114] P. Anjangi and M. Chitre, "Scheduling algorithm with transmission power control for random underwater acoustic networks," in *Proc. MTS/IEEE OCEANS*, Genova, Italy, May 2015.

[115] ——, "Design and implementation of super-TDMA: A MAC protocol exploiting large propagation delays for underwater acoustic networks," in *Proc. ACM WUWNet*, Washington, DC, Oct. 2015.

[116] R. Diamant, R. Francescon, and M. Zorzi, "Efficient link discovery for underwater networks," in *Proc. UCOMMS*, Lerici, Italy, Aug. 2016.

[117] R. Jain, W. Hawe, and D. Chiu, "A quantitative measure of fairness and discrimination for resource allocation in shared computer systems," Washington University, Sant Louis, Tech. Rep. DEC-TR-301, Sep. 1984.

[118] A. Othman, W. Abidin, H. Zen, K. Ping, and N. Zamhari, "Performance evaluation for network set up and nodes discovery protocol in underwater grid topology networks," in *Proc. APSITT*, Kuching, Malaysia, Jun. 2010.

[119] R. Diamant and L. Lampe, "Spatial reuse time-division multiple access for broadcast ad hoc underwater acoustic communication networks," *IEEE J. Ocean. Eng.*, vol. 36, no. 2, pp. 172–185, Apr. 2011.

[120] R. Otnes, P. van Walree, H. Buen, and H. Song, "Underwater acoustic network simulation with lookup tables from physical-layer replay," *IEEE J. Ocean. Eng.*, vol. 40, no. 4, pp. 822–840, Oct. 2015.

[121] B. Bollobas, *Random Graphs*, 2nd ed. Cambridge University Press, 2001, pp. 34–74.

[122] W. Zhang and R. E. Korf, "An average-case analysis of branch-and-bound with applications: Summary of results," in *Proceedings of the National Conference on AI (AAAI)*, 1992, pp. 545–550.

[123] D. R. Smith, "Random trees and the analysis of branch and bound procedures," *Journal of the ACM (JACM)*, vol. 31, no. 1, pp. 163–188, Jan. 1984.

[124] F. Jensen, W. Kuperman, M. Porter, and H. Schmidt, *Computational Ocean Acoustics*, 2nd ed. New York: Springer-Verlag, 1984, 2nd printing 2000.

[125] R. Diamant, P. Casari, F. Campagnaro, and M. Zorzi, "Leveraging the near–far effect for improved spatial-reuse scheduling in underwater acoustic networks," *IEEE Transactions on Wireless Communications*, vol. 16, no. 3, pp. 1480–1493, March 2017.

[126] "Neptune underwater optical communications," accessed: Sep. 2019. [Online]. Available: https://www.saphotonics.com/communications-sensing/optical-communications/

[127] D. Anguita, D. Brizzolara, G. Parodi, and Q. Hu, "Optical wireless underwater communication for AUV: Preliminary simulation and experimental results," in *Proc. IEEE/OES Oceans*, Santander, Spain, Jun. 2011.

[128] F. R. Dalgleish, J. J. Shirron, D. Rashkin, T. E. Giddings, A. K. V. Dalgleish, I. Cardei, B. Ouyang, F. M. Caimi, and M. Cardei, "Physical layer simulator for undersea free-space laser communications," *Optical Engineering*, vol. 53, no. 5, pp. 1–14, May 2014.

[129] C. Gabriel, M.-A. Khalighi, S. Bourennane, P. Leon, , and V. Rigaud, "Monte-carlo-based channel characterization for underwater optical communication systems," *IEEE/OSA Journal of Optical Communications and Networking*, vol. 5, no. 1, pp. 1–12, Jan. 2013.

[130] N. Farr, J. Ware, C. Pontbriand, and T. Hammar, "Optical communication system expands CORK seafloor observatory's bandwidth," in *Proc. MTS/IEEE Oceans*, Seattle, US, Sep. 2010.

[131] N. Farr, A. D. Chave, L. Freitag, J. Preisig, S. N. White, D. Yoerger, and F. Sonnichsen, "Optical modem technology for seafloor observatories," in *Proc. MTS/IEEE Oceans*, Boston, MA, Sep. 2006.

[132] C. Pontbriand, N. Farr, J. Ware, J. Preisig, and H. Popenoe, "Diffuse high-bandwidth optical communications," in *Proc. MTS/IEEE Oceans*, Quebec City, Canada, Sep. 2008.

[133] N. Farr, A. Bowen, J. Ware, C. Pontbriand, and M. Tivey, "An integrated, underwater optical/acoustic communications system," in *Proc. MTS/IEEE Oceans*, Sydney, Australia, May 2010.

[134] F. Campagnaro *et al.*, "The DESERT underwater framework v2: Improved capabilities and extension tools," in *Proc. Ucomms*, Lerici, Italy, Sep. 2016.

[135] "Underwater acoustic modems," accessed: Sep. 2019. [Online]. Available: https://evologics.de/acoustic-modems

[136] "Absorption and attenuation meter ac-9," Last time accessed: Sep. 2019. [Online]. Available: http://www.comm-tec.com/Prods/mfgs/Wetlabs/Manuals/ac-9_manual.pdf

[137] "Free-falling optical profiler," Last time accessed: Sep. 2019. [Online]. Available: http://hahana.soest.hawaii.edu/hot/methods/hyperpro.html

[138] J. t.o. Kirk, *Light and Photosynthesis in Aquatic Ecosystems.* Cambridge University Press, 2007.

[139] M. Doniec, I. Topor, M. Chitre, and D. Rus, *Experimental Robotics – Autonomous, Localization-Free Underwater Data Muling Using Acoustic and Optical Communication*, ser. Springer Tracts in Advanced Robotics. Springer, 2013. [Online]. Available: https://link.springer.com/chapter/10.1007/978-3-319-00065-7_56

[140] F. Campagnaro, F. Guerra, F. Favaro, V. S. Calzado, P. Forero, M. Zorzi, and P. Casari, "Simulation of a multimodal wireless remote control system for underwater vehicles," in *Proc. ACM WUWNet*, Washington, DC, Oct. 2015.

[141] "Arduino mega 2560," accessed: Sep. 2019. [Online]. Available: https://www.arduino.cc/en/Main/arduinoBoardMega2560

[142] "Si PIN photodiode S5971," accessed: Sep. 2019. [Online]. Available: http://www.hamamatsu.com/eu/en/product/category/3100/4001/4103/S5971/index.html

[143] "Cooled Large Area 5mm Blue Enhanced Silicon APD Module SD 192-70-74-661," Last time accessed: Sep. 2019. [Online]. Available: http://datasheet.octopart.com/SD197-70-74-661-Advanced-Photonix-datasheet-146440.pdf

[144] "Photomultiplier tubes - basics and applications," accessed: Sep. 2019. [Online]. Available: https://www.hamamatsu.com/resources/pdf/etd/PMT_handbook_v3aE.pdf

[145] "A technical guide to silicon photomultipliers (SiPM)," accessed: Sep. 2019. [Online]. Available: https://hub.hamamatsu.com/jp/en/technical-note/sipm-mppc-technical-note/index.html

[146] F. Campagnaro, M. Calore, P. Casari, V. S. Calzado, G. Cupertino, C. Moriconi, and M. Zorzi, "Measurement-based Simulation of Underwater Optical Networks," in *Proc. MTS/IEEE OCEANS*, Aberdeen, UK, Oct. 2017.

[147] B. Cochenour, A. Laux, and L. Mullen, "Temporal dispersion in underwater laser communication links: Closing the loop between model and experiment," in *Proc. UCOMMS*, Lerici, Italy, Sep. 2016.

[148] "DESERT Underwater github repository," Last time accessed: Sep. 2019. [Online]. Available: https://github.com/uwsignet/DESERT_Underwater

[149] "Piecewise cubic hermite interpolating polynomial (pchip)," accessed: Sep. 2019. [Online]. Available: https://it.mathworks.com/help/matlab/ref/pchip.html

[150] A. Signori, F. Campagnaro, and M. Zorzi, "Modeling the performance of optical modems in the desert underwater network simulator," in *Proc. IEEE UComms*, Lerici, Italy, Aug. 2018.

[151] X. Lurton, *An introduction to underwater acoustics - Principles and applications*. Springer Praxis, 2002.

[152] N. Farr, A. Bowen, J. Ware, C. Pontbriand, and M. Tivey, "An integrated, underwater optical/acoustic communications system," in *Proc. IEEE/OES OCEANS*, Sydney, Australia, May 2010.

[153] C. Cortes and V. Vapnik, "Support-vector networks," *Machine learning*, vol. 20, no. 3, pp. 273–297, 1995.

[154] V. N. Vapnik, "An overview of statistical learning theory," *IEEE Transactions on Neural Networks*, vol. 10, no. 5, pp. 988–999, 1999.

[155] A. J. Smola and B. Schölkopf, "A tutorial on support vector regression," *Statistics and computing*, vol. 14, no. 3, pp. 199–222, 2004.

[156] R. Diamant and L. Chorev, "Emulation system for underwater acoustic channel," in *International Undersea Defence Technology Europe conference (UDT)*, vol. 2, Amsterdam, the Netherlands, Jun. 2005, pp. 1043–1046.

[157] R. Diamant, “A normalized matched filter detector for hydroacoustic signals,” *Elsevier Ocean Engineering*, 2016.

[158] “Beta function,” accessed: Sep. 2019. [Online]. Available: https://en.wikipedia.org/wiki/Beta_function

[159] M. Pal and P. Mather, “Support vector machines for classification in remote sensing,” *International Journal of Remote Sensing*, vol. 26, no. 5, pp. 1007–1011, 2005.

[160] G. M. Foody and A. Mathur, “Toward intelligent training of supervised image classifications: directing training data acquisition for SVM classification,” *Remote Sensing of Environment*, vol. 93, no. 1, pp. 107–117, 2004.

[161] John T. O. Kirk, *Light and Photosynthesis in Aquatic Ecosystems*, 3rd ed. Cambridge University Press, 2011.

[162] M. Stojanovic, “Absorption and attenuation of visible and near-infrared light in water: dependence on temperature and salinity,” *Applied Optics*, vol. 36, no. 24, pp. 6035–6046, Aug. 1997.

[163] J. Huang, J. Lu, and C. X. Ling, “Comparing Naive Bayes, Decision Trees, and SVM with AUC and Accuracy,” in *Third IEEE International Conference on Data Mining, 2003. ICDM 2003.* IEEE, 2003, pp. 553–556.

[164] M. Sokolova and G. Lapalme, “A systematic analysis of performance measures for classification tasks,” *Information Processing & Management*, vol. 45, no. 4, pp. 427–437, 2009.

[165] G. E. Hinton, S. Osindero, and Y.-W. Teh, “A fast learning algorithm for deep belief nets,” *Neural computation*, vol. 18, no. 7, pp. 1527–1554, 2006.

[166] M. Zorzi, A. Testolin, and I. P. Stoianov, “Modeling language and cognition with deep unsupervised learning: a tutorial overview,” *Frontiers in Psychology*, vol. 4, pp. 65–78, 2013.

[167] M. Zorzi, A. Zanella, A. Testolin, M. De Filippo De Grazia, and M. Zorzi, “Cognition-based networks: A new perspective on network optimization using learning and distributed intelligence,” *IEEE Access*, vol. 3, pp. 1512–1530, 2015.

[168] A. Testolin, M. Zanforlin, M. De Filippo De Grazia, D. Munaretto, A. Zanella, and M. Zorzi, “A machine learning approach to QoE-based video admission control and resource allocation in wireless systems,” in *Ad Hoc Networking Workshop (MED-HOC-NET), 2014 13th Annual Mediterranean.* IEEE, 2014, pp. 31–38.

[169] R. Diamant, F. Campagnaro, M. D. F. D. Grazia, P. Casari, A. Testolin, V. S. Calzado, and M. Zorzi, “On the relationship between the underwater acoustic and optical channels,” *IEEE Transactions on Wireless Communications*, vol. 16, no. 12, pp. 8037–8051, September 2017.

[170] ——, “Exploring the statistical relation between the underwater acoustic and optical channels,” in *UACE*, Skiathos, Greece, September 2017.

[171] I. Akyildiz, D. Pompili, and T. Melodia, “Underwater acoustic sensor networks: research challenges,” *Elsevier's Ad Hoc Networks*, vol. 3, no. 3, 2005.

[172] Y. Sun and T. Melodia, “The internet underwater: An IP-compatible protocol stack for commercial undersea modems,” in *Proc. ACM WUWNet*, Kaohsiung, Taiwan, Nov. 2013.

[173] A. Camillò, M. Nati, C. Petrioli, M. Rossi, and M. Zorzi, “IRIS: Integrated data gathering and interest dissemination system for wireless sensor networks,” *Elsevier Ad Hoc Networks*, vol. 11, no. 2, pp. 654–671, Mar. 2013.

[174] G. Toso, R. Masiero, P. Casari, O. Kebkal, M. Komar, and M. Zorzi, “Field experiments for dynamic source routing: S2C evologics modems run the SUN protocol using the DESERT Underwater libraries,” in *Proc. MTS/IEEE Oceans*, Hampton Roads, VA, Oct. 2012.

[175] S. Basagni, C. Petrioli, R. Petroccia, and D. Spaccini, “CARP: A channel-aware routing protocol for underwater acoustic wireless networks,” *Elsevier Ad Hoc Networks*, vol. 34, pp. 92–104, Nov. 2015.

[176] J. Nelder and R. Mead, “A simplex method for function minimization,” *The computer journal*, vol. 7, no. 4, 1965.

[177] A. Schrijver, *Theory of linear and integer programming.* John Wiley & Sons, 1998.

[178] O. Kebkal, M. Komar, and K. Kebkal, “D-MAC: Hybrid media access control for underwater acoustic sensor networks,” in *Proc. IEEE ICC*, Cape Town, South Africa, May 2010.

[179] K. G. Kebkal and R. Bannasch, “Sweep-spread carrier for underwater communication over acoustic channels with strong multipath propagation,” *The Journal of the Acoustical Society of America*, vol. 112, no. 5, pp. 2043–2052, 2002.

[180] F. Campagnaro, R. Francescon, F. Favaro, F. Guerra, R. Diamant, P. Casari, and M. Zorzi, “The DESERT Underwater framework v2: Improved capabilities and extension tools,” in *Proc. UComms*, Lerici, Italy, Sep. 2016.

[181] R. Diamant, P. Casari, F. Campagnaro, O. Kebkal, V. Kebkal, and M. Zorzi, “Fair and Throughput-Optimal Routing in Multimodal Underwater Networks,” *IEEE Transactions on Wireless Communications*, vol. 17, no. 3, pp. 1738–1754, Jan. 2018.

[182] R. Diamant, R. Francescon, and M. Zorzi, “Topology-efficient discovery: A topology discovery algorithm for underwater acoustic networks,” *IEEE J. Ocean. Eng.*, vol. PP, no. 99, pp. 1–15, Jun. 2017.

[183] V. Gabale, B. Raman, P. Dutta, and S. Kalyanraman, “A classification framework for scheduling algorithms in wireless mesh networks,” *IEEE Commun. Surveys Tuts.*, vol. 15, no. 1, pp. 199–222, First quarter 2013.

[184] A. S. Tanenbaum, *Computer Networks.* Prentice Hall, 2002.

[185] N. A. Cruz *et al.*, “Investigation of Underwater Acoustic Networking Enabling the Cooperative Operation of Multiple Heterogeneous Vehicles,” *Marine Tech. Society Journal*, vol. 47, no. 2, pp. 43–58, Mar./Apr. 2013.

[186] X. Che, I. Wells, G. Dickers, P. Kear, and X. Gong, “Re-evaluation of RF electromagnetic communication in underwater sensor networks,” *IEEE Commun. Mag.*, vol. 48, no. 12, pp. 143–151, Dec. 2010.

[187] F. Campagnaro, “Design of a wireless remote control for underwater equipment,” Master’s thesis, University of Padova, Italy, 2014, accessed: Sep. 2019. [Online]. Available: http://tesi.cab.unipd.it/46709/1/MasterThesis.pdf

[188] L3, “ROV,” Accessed: Sep. 2019. [Online]. Available: http://www.lighthouse-geo.com/equipment/rov/

[189] A. Palmeiro, M. Martín, I. Crowther, and M. Rhodes, “Underwater radio frequency communications,” in *Proc. IEEE/OES Oceans*, Santander, Spain, Jun. 2011.

[190] M. Chitre, “Underwater acoustic communications in warm shallow water channels,” 2006, accessed: Sep. 2019. [Online]. Available: http://scholarbank.nus.edu.sg/handle/10635/27859

[191] P.-P. Beaujean and J. Spruance, “A very high bit rate broadband acoustic modem for short-to-medium range data transmission in ports and shallow water using spread spectrum modulation and decision feedback equalizing,” Florida Atlantic University, Tech. Rep. ONR project N00014-06-C-0368, Sep. 2008, Accessed: Oct. 2014.

[192] F. Campagnaro, F. Favaro, F. Guerra, V. Sanjuan, P. Casari, and M. Zorzi, “Simulation of multimodal optical and acoustic communications in underwater networks,” in *Proc. MTS/IEEE Oceans*, Genova, Italy, May 2015.

[193] M. Stojanovic, “On the relationship between capacity and distance in an underwater acoustic communication channel,” *ACM Mobile Comput. and Commun. Review*, vol. 11, no. 4, pp. 34–43, Oct. 2007.

[194] A. Signori, F. Campagnaro, and M. Zorzi, “Multi-hop range extension of a wireless remote control for underwater vehicles,” in *Proc. IEEE/MTS OCEANS*, Kobe, Japan, May 2018.

[195] R. Masiero, S. Azad, F. Favaro, M. Petrani, G. Toso, F. Guerra, P. Casari, and M. Zorzi, “DESERT Underwater: An NS-Miracle-based framework to design, simulate, emulate and realize test-beds for underwater network protocols,” *2012 Oceans - Yeosu*, pp. 1–10, May 2012.

[196] H. Dol, M. Colin, P. van Walree, and R. Otnes, “Field experiments with a dual-frequency-band underwater acoustic network,” in *Proc. Ucomms*, Lerici, Italy, Sep. 2018.

[197] A. Olivier, M. Zorzi, and P. Casari, “Modeling the throughput of 1-persistent CSMA in underwater networks,” in *Proc. MTS/IEEE Oceans*, Genova, Italy, May 2015.

[198] M. Stojanovic, “On the relationship between capacity and distance in an underwater acoustic communication channel,” *SIGMOBILE Mob. Comput. Commun. Rev.*, vol. 11, no. 4, pp. 34–43, Oct. 2007.

[199] K. Kebkal, O. Kebkal, E. Glushko, V. Kebkal, L. Sebastião, A. Pascoal, J. Gomes, J. Ribeiro, H. Silva, M. Ribeiro, and G. Indivery, “Underwater acoustic modems with integrated atomic clocks for one-way travel-time underwater vehicle positioning,” in *Proc. UACE*, Skiathos, Greece, Jun. 2017.

[200] W. Rizzo, A. Signori, F. Campagnaro, and M. Zorzi, “Auvs telemetry range extension through a multimodal underwater acoustic network,” in *Proc. IEEE/MTS OCEANS*, Charleston, US, 2018.

[201] F. Meneghello, F. Campagnaro, R. Diamant, P. Casari, and M. Zorzi, “Design and evaluation of a low-cost acoustic chamber for underwater networking experiments,” in *Proc. ACM WUWNet*, Shanghai, China, Oct. 2016.

[202] R. Diamant, F. Campagnaro, S. Dahan, R. Francesconb, and M. Zorzi, “Development of a submerged hub for monitoring the deep sea,” in *Proc. UACE*, Skiathos, Greece, July 2017.

[203] The NUS ARL and SubNero, “UNET–The Underwater NETworks project,” Last time accessed: Sep. 2019. [Online]. Available: http://www.unetstack.net

[204] F. Campagnaro, R. Francescon, O. Kebkal, P. Casari, K. Kebkal, and M. Zorzi, “Full reconfiguration of underwater acoustic networks through low-level physical layer access,” in *Proc. ACM WUWNet*, Halifax, Canada, Nov. 2017.

[205] G. J. Sullivan, J.-R. Ohm, W.-J. Han, and T. Wiegand, “Overview of the High Efficiency Video Coding (HEVC) Standard,” *IEEE Transactions on Circuits and Systems for Video Technology*, vol. 22, no. 12, pp. 1649–1668, Sep. 2012.

[206] “WebM VP9 webpage,” last time accessed: Sept. 2019. [Online]. Available: https://www.webmproject.org/vp9/

[207] ITU-T Series H: Audiovisual and Multimedia Systems, *Advanced video coding for generic audiovisual services*, ITU Recommendation ITU-T H.264, Apr. 2017.

[208] “IBC2008: On2 Touts New Codec for Web Video,” Last time accessed: Sept. 2019. [Online]. Available: http://www.broadcastingcable.com/news/technology/ibc2008-on2-touts-new-codec-web-video/46250

[209] O. the Feasibility of Video Streaming through Underwater Acoustic Links, “Filippo campagnaro and roberto francescon and davide tronchin and michele zorzi,” in *Proc. UComms*, Lerici, Italy, Aug. 2018.

[210] Z. Wang, L. Lu, and A. C. Bovic, “Video quality assessment using structural distortion measurement,” in *International Conference on Image Processing*, 2002.

[211] E. Coccolo, F. Campagnaro, A. Signori, F. Favaro, and M. Zorzi, “Implementation of auv and ship noise for link quality evaluation in the desert underwater,” in *Proc. ACM WUWNet*, Shenzhen, China, Dec. 2018.

[212] C. Audoly and E. Rizzuto, “Ship underwater radiated noise patterns,” AQUO Project Consortium, final report R2.9, 06 2015.

[213] R. Zimmerman, G. L. D’Spain, and C. D. Chadwell, “Decreasing the radiated acoustic and vibration noise of a mid-size AUV,” *IEEE Journal of Oceanic Engineering*, vol. 30, no. 1, pp. 179–187, Jan 2005.

[214] D. Zordan, F. Campagnaro, and M. Zorzi, “On the feasibility of an anti-grounding service with autonomous surface vessels,” in *Proc. MTS/IEEE Oceans*, Marseille, France, Jun. 2019.

[215] “EM 2040P MKII Multibeam echo sounder,” accessed: Sept. 2019. [Online]. Available: https://www.kongsberg.com/maritime/products/mapping-systems/multibeam-echo-sounders/em-2040p-mkii-multibeam-echosounder-max.-550-m

[216] J. Wang, H. Zhou, Y. Li, Q. Sun, Y. Wu, S. Jin, T. Q. S. Quek, and C. Xu, “Wireless channel models for maritime communications,” *IEEE Access*, vol. 6, pp. 68 070 – 68 088, Nov. 2018.

[217] “Lte radio link budgeting and rf planning,” accessed: Sept. 2019. [Online]. Available: https://sites.google.com/site/lteencyclopedia/lte-radio-link-budgeting-and-rf-planning#TOC-2.4.-Propagation-Path-Loss-Models

[218] M. Capuzzo, D. Magrin, and A. Zanella, “Confirmed traffic in LoRaWAN: Pitfalls and countermeasures,” in *2018 17th Annual Mediterranean Ad Hoc Networking Workshop (Med-Hoc-Net)*, Capri, Italy, June 2018, pp. 1–7.

[219] “Robovaas - robotic vessels as-a-service,” accessed: Sep. 2019. [Online]. Available: https://www.martera.eu/projects/robovaas

[220] A. Signori, F. Campagnaro, D. Zordan, F. Favaro, and M. Zorzi, “Underwater acoustic sensors data collection in the robotic vessel as-a-service project,” in *Proc. MTS/IEEE Oceans*, Marseille, France, Jun. 2019.

[221] ——, “Data collection in shallow fresh water scenarios with low-cost underwater acoustic modems,” in *Proc. UACE*, Crete, Greece, Jul. 2019.

[222] P. Casari *et al.*, “Open-source suites for the underwater networking community: WOSS and DESERT Underwater,” *IEEE Network, special issue on “Open Source for Networking: Development and Experimentation”*, vol. 28, no. 5, pp. 38–46, Sep. 2014.

[223] F. Favaro, P. Casari, and M. Zorzi, “Data upload from a static underwater network to an auv: Polling or random access?” in *Proc. of MTS/IEEE OCEANS*, Yeosu, South Korea, May 2012.

[224] M. Porter *et al.*, “Bellhop code,” Last time accessed: Sept. 2019. [Online]. Available: http://oalib.hlsresearch.com/Rays/index.html

[225] C. Renner and A. J. Golkowski, “Acoustic modem for micro auvs: Design and practical evaluation,” in *Proc. ACM WUWNet*, Shanghai, China, Oct. 2016.

[226] A. Signori, C. Pielli, F. Chiariotti, M. Giordani, F. Campagnaro, and M. Zorzi, “Jamming the underwater: a game-theoretic analysis of energy-depleting jamming attacks,” in *accepted into Proc. ACM WUWNet*, Atlanta, US, Oct. 2019.

[227] Sequoia Scientific, “Hydrolight radiative transfer numerical model,” accessed: Sep. 2019. [Online]. Available: http://www.sequoiasci.com/product/hydrolight/

List of publications

Journals and letters

J.1 Paolo Casari, Filippo Campagnaro, Elizaveta Dubrovinskaya, Roberto Francescon, Amir Dagan, Shlomo Dahan, Michele Zorzi, Roee Diamant, “ASUNA: A Freely Shared Topology Datasetfor Underwater Network Emulation“, **submitted to** *IEEE Journal of Oceanic Engineering 2019 (under review).*

J.2 Filippo Campagnaro, Paolo Casari, Michele Zorzi, Roee Diamant, “Optimal Transmission Scheduling in Small Multimodal Underwater Networks”, *IEEE Wireless Communication Letter*, vol. 8, no. 2, pp. 368–371, Oct. 2018.

J.3 Roee Diamant, Paolo Casari, Filippo Campagnaro, Oleksiy Kebkal, Veronika Kebkal, Michele Zorzi, “Fair and Throughput-Optimal Routing in Multimodal Underwater Networks“, *IEEE Transactions on Wireless Communications*, vol. 17, no. 3, pp. 1738–1754, Jan. 2018.

J.4 Roee Diamant, Filippo Campagnaro, Michele De Filippo De Grazia, Paolo Casari, Alberto Testolin, Violeta Sanjuan Calzado, Michele Zorzi, On the Relationship between the Underwater Acoustic and Optical Channels, *IEEE Transactions on Wireless Communications*, vol. 16, no. 12, pp. 8037–8051, September 2017.

J.5 Roee Diamant, Paolo Casari, Filippo Campagnaro, and Michele Zorzi, “Leveraging the Near–Far Effect for Improved Spatial-Reuse Scheduling in Underwater Acoustic Networks”, *IEEE Transactions on Wireless Communications*, vol. 16, no. 3, pp. 1480–1493, March 2017.

Conferences and workshops

C.1 Alberto Signori, Chiara Pielli, Federico Chiariotti, Marco Giordani, Filippo Campagnaro, Nicola Laurenti and Michele Zorzi, “Jamming the Underwater: a Game-Theoretic Analysis of Energy-Depleting Jamming Attacks”, **accepted in** *ACM WUWNet 2019*, Atlanta, US.

C.2 Alberto Signori, Filippo Campagnaro, Davide Zordan, Federico Favaro and Michele Zorzi, “Underwater Acoustic Sensors Data Collection in the Robotic Vessels as-a-Service Project“, *MTS/IEEE Oceans 2019*, Marseille, France.

C.3 Davide Zordan, Filippo Campagnaro, Michele Zorzi, “On the feasibility of an Anti-grounding Servicewith Autonomous Surface Vessels”, *MTS/IEEE Oceans 2019*, Marseille, France.

C.4 Filippo Campagnaro, Fabian Steinmetz, Alberto Signori, Davide Zordan, Bernd-Christian Renner, Michele Zorzi, “Data Collection in Shallow Fresh Water Scenarios with Low-Cost Underwater Acoustic Modems”, *UACE 2019*, Crete, Greece.

C.5 Emanuele Coccolo, Filippo Campagnaro Alberto Signori, Federico Favaro, Michele Zorzi, “Implementation of AUV and Ship Noise for Link Quality Evaluation in the DESERT Underwater”, *ACM WUWNet 2018*, Shenzhen, China.

C.6 Alberto Signori, Filippo Campagnaro, Michele Zorzi, “Modeling the Performance of Optical Modems in the DESERT Underwater Network Simulator”, *IEEE Ucomms 2018*, Lerici, Italy.

C.7 Filippo Campagnaro, Roberto Francescon, Davide Tronchin, Michele Zorzi, “On the Feasibility of Video Streaming through Underwater Acoustic Links”, *IEEE Ucomms 2018*, Lerici, Italy.

C.8 William Rizzo, Alberto Signori, Filippo Campagnaro, Michele Zorzi, “AUVs Telemetry Range Extension through a Multimodal Underwater Acoustic Network”, *MTS/IEEE Oceans 2018* Charleston, US.

C.9 Alberto Signori, Filippo Campagnaro, Michele Zorzi, “Multi-Hop Range Extension of a Wireless Remote Control for Underwater Vehicles”, *MTS/IEEE Oceans 2018*, Kobe, Japan.

C.10 Roee Diamant, Paolo Casari, Filippo Campagnaro, Michele Zorzi, “Routing in Multi-Modal Underwater Networks: a Throughput-optimal Approach”, *IEEE INFOCOM Workshops 2017*, Atlanta, US.

C.11 Filippo Campagnaro, Roberto Francescon, Paolo Casari, Roee Diamant and Michele Zorzi, “Multimodal Underwater Networks: Recent Advances and a Look Ahead”, *ACM WUWNet 2017*, Halifax, Canada.

C.12 Filippo Campagnaro, Roberto Francescon, Oleksiy Kebkal, Paolo Casari, Konstantin Kebka and Michele Zorzi, “Full Reconfiguration of Underwater Acoustic Networks through Low-Level Physical Layer Access”, *ACM WUWNet 2017*, Halifax, Canada.

C.13 Roee Diamant, Filippo Campagnaro, Shlomo Dahan, Roberto Francescon and Michele Zorzi, “Development of a Submerged HUB for

Monitoring the Deep Sea", *UACE 2017, Skiathos*, Greece.

C.14 Roee Diamant, Filippo Campagnaro, Michele De Filippo de Grazia, Alberto Testolin, Violeta Sanjuan Calzado, Michele Zorzi and Paolo Casari, "Exploring the Statistical Relationship Between the Underwater Acoustic and Optical Channels", *UACE 2017*, Skiathos, Greece.

C.15 Filippo Campagnaro, Matteo Calore, Paolo Casari, Violeta Sanjuan Calzado, Giacomo Cupertino, Claudio Moriconi, Michele Zorzi, "Measurement-based Simulation of Underwater Optical Networks", *MTS/IEEE Oceans 2017*, Aberdeen, UK.

C.16 Francesca Meneghello, Filippo Campagnaro, Roee Diamant, Paolo Casari, Michele Zorzi, "Design and Evaluation of a Low-Cost Acoustic Chamber for Underwater Networking Experiments", *ACM WUWNet 2016*, Shanghai, China.

Publications before my PhD

Journals and letters

J.6 Roee Diamant, Paolo Casari, Filippo Campagnaro, Michele Zorzi, "A Handshake-based Protocol Exploiting the Near-Far Effect in Underwater Acoustic Networks", *IEEE Wireless Communications Letters*, vol. 5, no. 3, pp. 308–311, June 2016.

Conferences and workshops

C.17 Filippo Campagnaro, Roberto Francescon, Federico Guerra, Federico Favaro, Paolo Casari, Roee Diamant, Michele Zorzi, "The DESERT Underwater Framework v2: Improved Capabilities and Extension Tools", *IEEE Ucomms 2016*, Lerici, Italy.

C.18 Filippo Campagnaro, Federico Guerra, Paolo Casari, Roee Diamant, Michele Zorzi, "Implementation of a Multi-modal Acoustic-Optical Underwater Network Protocol Stack", *MTS/IEEE Oceans 2016*, Shanghai, China.

C.19 Filippo Campagnaro, Federico Guerra, Federico Favaro, Violeta Sanjuan Calzado, Pedro Forero, Michele Zorzi, Paolo Casari, "Simulation of a Multimodal Wireless Remote Control System for Underwater Vehicles", *ACM WUWNet 2015* Washington DC, US.

C.20 Filippo Campagnaro, Federico Favaro, Federico Guerra, Violeta Sanjuan Calzado, Michele Zorzi, Paolo Casari, Simulation of Multimodal Optical and Acoustic Communications in Underwater Networks, *MTS/IEEE Oceans 2015*, Genova, Italy.

C.21 Filippo Campagnaro, Paolo Casari, Federico Favaro, Michele Zorzi, “On the Feasibility of Fully Wireless Remote Control for Underwater Vehicles”, *IEEE Asilomar SS&C*, 2014, Asilomar, US.